Design and Evaluation of an Automated Experimental Test Rig for Determination of the Dynamic Characteristics of Fluid-Film Bearings

Erik Evan Swanson

Dissertation submitted to the Faculty of the
Virginia Polytechnic Institute and State University
in partial fulfillment of the requirements of the degree of

Doctor of Philosophy
in
Mechanical Engineering

R. G. Kirk, Chair
S.L. Hendricks
M.E.F. Kasarda
R.G. Leonard
R.H. Plaut

August 7, 1998
Blacksburg, VA

Keywords: Hydrodynamic, Bearing, Experimental, Journal Bearing

Design and Evaluation of an Automated Experimental Test Rig for Determination of the Dynamic Characteristics of Fluid-Film Bearings

Erik Evan Swanson

(Abstract)

Hydrodynamic journal bearings are applied in a wide range of both old and new, advanced rotating machinery designs. To maintain existing machinery, as well as to design new, state of the art machines, validated analytical models for these bearings are needed. This work documents the development and evaluation of an automated test rig for the evaluation of hydrodynamic journal bearings to provide some of the needed experimental data. This work describes the test rig in detail, including the results of experimental characterization of many of the test rig subsystems. Experimental data for a two axial groove bearing and a pressure dam bearing under steady load conditions are presented for a range of loads at two different shaft speeds. Experimental data and analytical results for dynamic loading are also discussed. The work concludes with a summary of the state of the test rig and recommendations for further work.

Acknowledgments

I would like to thank Dr. Kirk for his continued support over the course of a rather long graduate career, the Rotor Lab Affiliates members, especially Dr. John Nicholas of Rotating Machinery Technology, Inc., for their support of the lab and test rig, and Mohawk Innovative Technology Inc., for their support and understanding during the final phases of this project.

I would also like to thank my parents and many excellent teachers for giving me a curiosity about the world and their support and encouragement through the years.

I would also like to thank the members of my committee for agreeing to serve. Thanks also go to Dr. Felix Pierce, who was a member of the committee during most of this work, for convincing me it was ok to not quite accomplish everything I initially set out to accomplish.

Finally, I would like to thank my girlfriend, Kimberly, for putting-up with me during the final part of my graduate program.

Table of Contents

List of Figures

List of Tables

Nomenclature

C	Clearance
C_{ij}	Damping Coefficients
F	Frequency Domain Force
F_x	Horizontal Force
F_y	Vertical Force
K	Stiffness
$K_{nominal}$	Nominal Stiffness Value Predicted by Code
K_{ij}	Stiffness Coefficients
X	Frequency Domain Displacement
c	Damping Coefficient
f	Force
k	Stiffness Coefficient
x	Horizontal Coordinate/Displacement
y	Vertical Coordinate
Δ	Finite Perturbation
ω	Frequency

Chapter 1

Introduction

1.1 Background

Almost all industrially significant transformations of energy from one form to another involve rotating machinery in some way. Modern industry could not exist without the ubiquitous electric motor, turbine, generator, pump, or the whole host of rotating machinery we see around us every day. All of these rotating machines involve a shaft supported on some form of bearing. With few exceptions, such as aircraft engines and rolling mills, most medium to large rotating machinery is supported with some form of hydrodynamic bearing.

New machine designs for these applications feature ever higher operating speeds, longer, more flexible rotors, and higher power densities as part of the quest for higher performance and lower unit cost. These changes, which make machines more sensitive to small changes in system parameters, as well as the need to reduce time-to-market and prototype costs have created a need for ever more accurate mathematical models for use in the design stage. One of the important model elements is the bearings. Not only must the rotor weight and operating loads be supported, but the bearings also have a very strong influence on the dynamic behavior of the rotor. This need for accurate bearing models has led industry to move from approximate solutions to the governing equations and design charts, to more sophisticated models. The typical industrial journal bearing design code in use since the late 70's/early 80's is a computer implementation of a two-dimensional, finite element or finite difference solution of the governing equations. Although the models implemented in these computer codes usually gave results which worked for the majority of machines for the past ten to twenty

years, it was always apparent that there were shortcomings in the bearing models. With new, higher performance turbomachinery designs, rotor dynamic stability margins are being pushed to the limit, while shrinking research and development budgets preclude doing machine development on the test stand. Hence, these model shortcomings are going to become ever more problematical.

It is not currently clear, however, which of the many possible increases in bearing model complexity will best bring the basic model into better agreement with reality, while adding the fewest complexities. Unfortunately, there is really not an adequate collection of published, experimental data to guide analysis development efforts. The scatter within the data is frequently large, agreement between different experiments is frequently poor, and several industrially important designs have no available experimental data. Also, the range of data available does not adequately cover the range of typical industrial loads and speeds.

1.2 The Need for Experimental Data

As indicated above, there is a clear need for quality experimental measurements of bearing characteristics for a variety of journal bearing types. Unfortunately, quality measurements of journal bearing characteristics are difficult - the displacements being measured are very small (μm), the forces can be very large (kN), the hydrodynamic film necessitates a rotating shaft, the oil temperature has a significant impact on the results, etc. As a result, despite the best efforts of many researchers, there is still a real need for experimentally measured bearing characteristics. The need for measurements of the dynamic characteristics of hydrodynamic bearings over a realistic range of operating conditions is especially acute. This work details the development of a test rig intended to help provide some of the needed data.

1.3 Analytical Model For Hydrodynamic Bearings

For oil lubricated, hydrodynamic bearings, the analytical model generally used is a two-dimensional partial differential equation referred to as the “Reynolds Equation” which relates the bearing geometry, fluid viscosity and density, shaft rotation and motion to a pressure field in the oil film.

Since oil viscosity is a very strong function of temperature, this equation needs to be supplemented with an appropriate statement of the first law of thermodynamics (the energy equation), to describe the relationship between viscous dissipation in the lubricant film, and the temperature of the lubricant. In a refined model, elasticity equations are also needed to describe the deformation of the bearing and shaft due to thermal and pressure induced strains. At a given operating condition, these coupled equations can be solved for a pressure distribution, a film shape, and a temperature distribution. The solution is generally obtained through some combination of finite element and finite difference approximations to the governing partial differential equations. Dynamic characteristics are then obtained via numerical or analytical perturbations about the steady-state solution. Occasionally, full non-linear transient solutions are also examined. Ultimately, the analyst/designer needs to predict several things:

1) Load capacity
2) Film thickness
3) Operating temperature(s)
4) Dynamic characteristics
5) Power loss
6) Oil flow requirements

These characteristics then allow the machinery designer/analyst to predict whether the machine will be able to operate successfully with this bearing, and design appropriate auxiliary equipment for the machinery. Within the context of this work, the details of the analysis and the actual solution techniques employed do not need further elaboration, as the focus of the discussion will be on the measurement of these characteristics.

1.4 Bearing Dynamic Model

To model the dynamic behavior of a rotating system, a model must be assumed for the bearings which support the shaft. Unfortunately, the force versus displacement characteristics of hydrodynamic bearings are noticeably non-linear. For example, Fig. 1 presents typical calculated shaft vertical and horizontal equilibrium positions for a common fluid film bearing design as a function of applied vertical load.

Figure 1, and other analytical figures in this work were generated with a computer code called "NPADVT". This code is based on the work of Nicholas (1977). This code implements a two-dimensional, finite element, isoviscous solution of Reynolds equation, with a global energy balance to obtain an average oil temperature for fluid viscosity calculation. The code does not consider thermal deformations. It is a design oriented code, trading usability for complexity, and is currently used by industry. In Swanson (1992), a number of comparisons between NPADVT predictions and published experimental data are made. These comparisons suggest that the code is qualitatively correct, but has errors (or the experimental data are not accurate, or both). NPADVT is, however, the best analytical tool available to the author.

In addition to the visible non-linearity of the force-displacement characteristics as presented above, hydrodynamic bearings have been shown to exhibit many of the more interesting characteristics of non-linear systems, including sub and super harmonic response, Hopf bifurcations, and chaotic behavior (see, for example, Adams and Abu-Mahfouz, 1994;, Crooijmans, et al., 1990; Hollis and Taylor, 1986; Kato, T., et al., 1992; Myers, 1984; and Sundararajan and Noah, 1997). However, the range of rotor lateral motion for normal, stable operation of most rotating machinery is small enough, that linearization about an equilibrium position with a Taylor series expansion is generally adequate to describe the bearing dynamic behavior. The resulting linearized stiffness and damping model for two dimensional (vertical and horizontal), lateral shaft motion within a bearing, is as shown in equation 1.

$$\begin{bmatrix} K_{xx} & K_{xy} \\ K_{yx} & K_{yy} \end{bmatrix} \begin{bmatrix} x \\ y \end{bmatrix} + \begin{bmatrix} C_{xx} & C_{xy} \\ C_{yx} & C_{yy} \end{bmatrix} \begin{bmatrix} \dot{x} \\ \dot{y} \end{bmatrix} = \begin{bmatrix} F_x \\ F_y \end{bmatrix} \tag{1}$$

This bearing dynamic model has allowed designers to develop and build many machines which operate roughly as predicted, and has gained widespread acceptance in the rotor dynamics community. Indeed, most commercial rotor dynamic analysis codes directly accept the coefficients for this model, with a provision for varying the coefficients as a function of speed to account for some of the non-linear, shaft speed dependency of hydrodynamic bearings characteristics, as part of the process of building an overall model of the rotating system. The bearing load, oil inlet

temperature, and other effects are then assumed to be constant or vary with speed. It should be noted that this equation does not have an inertia term. For the case of hydrodynamic bearings, it is claimed that since the flow is laminar (typical Reynolds numbers for the bearings tested in this rig are 25 to 1000 depending on speed and operating clearance), and that the mass of the lubricant film is so small relative to the shaft, that the inertia terms can be eliminated. Several authors have examined the predicted effect of including the inertia terms, and show that they are not significant in typical turbomachinery. The inertia terms could be significant, however, for very light, low load rotors or for systems with very high shaft speeds (Reinhardt and Lund, 1975; Nataraj, et al., 1994; El-Shafei, 1993). There are no experimental data for journal bearings to confirm or disprove this assumption. For certain other bearing systems, such as hydrostatic bearings, hybrid (combined hydrodynamic and hydrostatic) bearings, and squeeze-film dampers, the inertia terms would need to be included (Childs and Hale, 1993; Tichy, 1983).

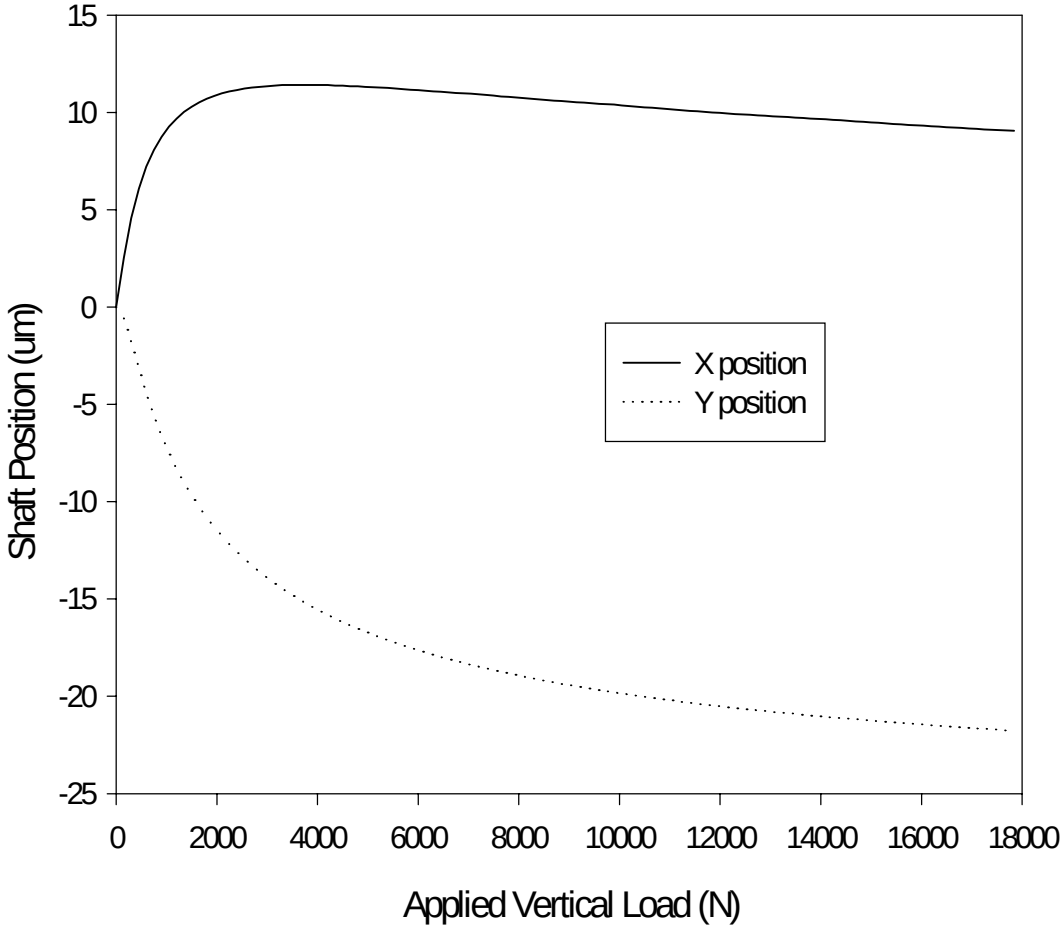

Figure 1 - Typical Shaft Position for Applied Vertical Load for a Two Axial Groove Bearing

1.5 Bearing Testing - Performance Measurement Goals

Thus, there are a wide variety of possible experimental goals in bearing testing. As a first level, experiments to validate the performance predictions of a bearing can be performed. Data gathered could include:

1) Bearing torque (power loss)
2) Shaft position
3) Lubricant temperature rise

These variables could be measured for combinations of independent parameters such as:

1) Shaft speed
2) Applied load
3) Oil inlet temperature
4) Oil flow rate/supply pressure
5) Bearing geometry (including alignment)
6) Bearing thermal environment (hot shaft, hot housing, thermal flux paths, etc.)

Another valuable testing goal is to map the thermal and or lubricant film pressure distributions in the bearing during operation. These test data can be used both to confirm code predictions, as well as directly point the way towards model improvements. For example, Pinkus (1990) points out that much of the uncertainty on how to model bearings concerns thermal boundary conditions and simplifications related to mixing of hot and cold lubricant in pockets and grooves. This work also points out the need for measurements of the actual lubricant temperature, especially in feed grooves and the recesses (pockets) cut into the operating surface of many bearings. In addition to the independent variables listed previously, Pinkus (1990) suggests a need for transient thermal data for step changes in shaft speed and load to help develop a better understanding of bearing seizure.

Other miscellaneous data which would be very useful to the analyst includes the actual operating film shape, which can be measured, for example, with displacement probes on the rotating shaft. In the case of tilting pad bearings, there is a need for data on pad motion, since the models for these bearings must account for the contact stiffness and friction coefficient/moment restraint at the pad

pivots. Tilting pad bearing researchers also need data on pad inner bore elastic and thermal deformations.

1.6 Bearing Testing - Experimental Dynamic Coefficient Estimation

The next level of performance testing would be to estimate the linearized bearing stiffness and damping characteristics described in section 1.4. These would be measured as a functions of the same independent variables as the steady load characteristics discussed in section 1.5.

In principle, this estimation task is fairly straightforward. If the model presented in equation 1 is essentially correct, there are eight well defined terms to identify in a two-input, two-output system. Hence, in principle, all that is required is to obtain at least two independent perturbations of the shaft about a steady-steady state operating position, and measure the relative displacements and the applied dynamic forces (four dynamic measurements total). However, the task is not easy. The scatter among data in the literature gives a hint of the level of difficulty. Most of the complications arise from the measurement environment. The problems include:

1) The difficulty in applying a controlled, measurable force to the bearing
2) The use of relative displacement measurements, which generally suffer from poor signal to noise ratios due to the small motions involved
3) The non-linear nature of the force-displacement characteristics of a hydrodynamic bearing

The non-linearity issue is especially vexing. The results previously presented in Fig. 1 give some indication of the effect. To highlight the effect of the bearing non-linearity on linearized stiffness coefficients, Fig. 2 shows typical analytically predicted stiffness coefficients versus load and Fig. 3 shows typical damping coefficients versus load for a 100 mm diameter, two axial groove journal bearing. It should be clear that the experimentalist is faced with a dilemma. The relative displacement measurements will be contaminated by noise from shaft unbalance, shaft motion caused by seal forces, shaft non-circularity at the sensor location, sensor noise from effects such as shaft electrical properties, drive system noise, and other external influences, etc. Hence the

displacements need to be as large as possible to improve the signal to noise ratio. However, the linearization is only valid over a very small region, so the orbits must also be small.

In the case of NPADVT, the stiffness coefficients are calculated via small displacement perturbations about the steady-state operating position. To examine the effect of the size of the perturbation, the code was modified to compare the results from the small perturbation to larger perturbations. Figures 4 through Fig. 9 present these results as percent error relative to the NPADVT default (nominal) small perturbation as the perturbation is increased. The results presented are for a two axial groove bearing with geometric parameters which match the test bearing discussed in chapter six. Based on these results, Table I enumerates the maximum normalized displacement which will give more than a 2.5 percent error relative to the indicated default perturbation. Note the perturbations shown are the peak-to-peak perturbation divided by the shaft centered radial clearance. Based on these results, a maximum experimental peak-to-peak orbit of less than 0.05 to 0.10 times the bearing radial clearance would be expected to be within a few percent of the linearized stiffness characteristics. This issue is also considered in Qiu and Tieu (1996). They conclude that the peak-to-peak orbit should be no more than 0.10 times the shaft centered bearing radial clearance for an error of 2.5 percent over a similar range of operation. For a 90 µm clearance bearing (the size of the Virginia Tech test rig test bearing), this translates to a peak-to-peak orbit size of about 9 µm. Accurate measurement of shaft displacement, with good signal to noise characteristics at this level of displacement is not a trivial task, especially in an environment where oil may splatter through the measurement zone. The mechanical problems of applying an accurately measurable, controllable static and dynamic loads to obtain the desired perturbation at a given nominal steady load with an operating bearing are also difficult.

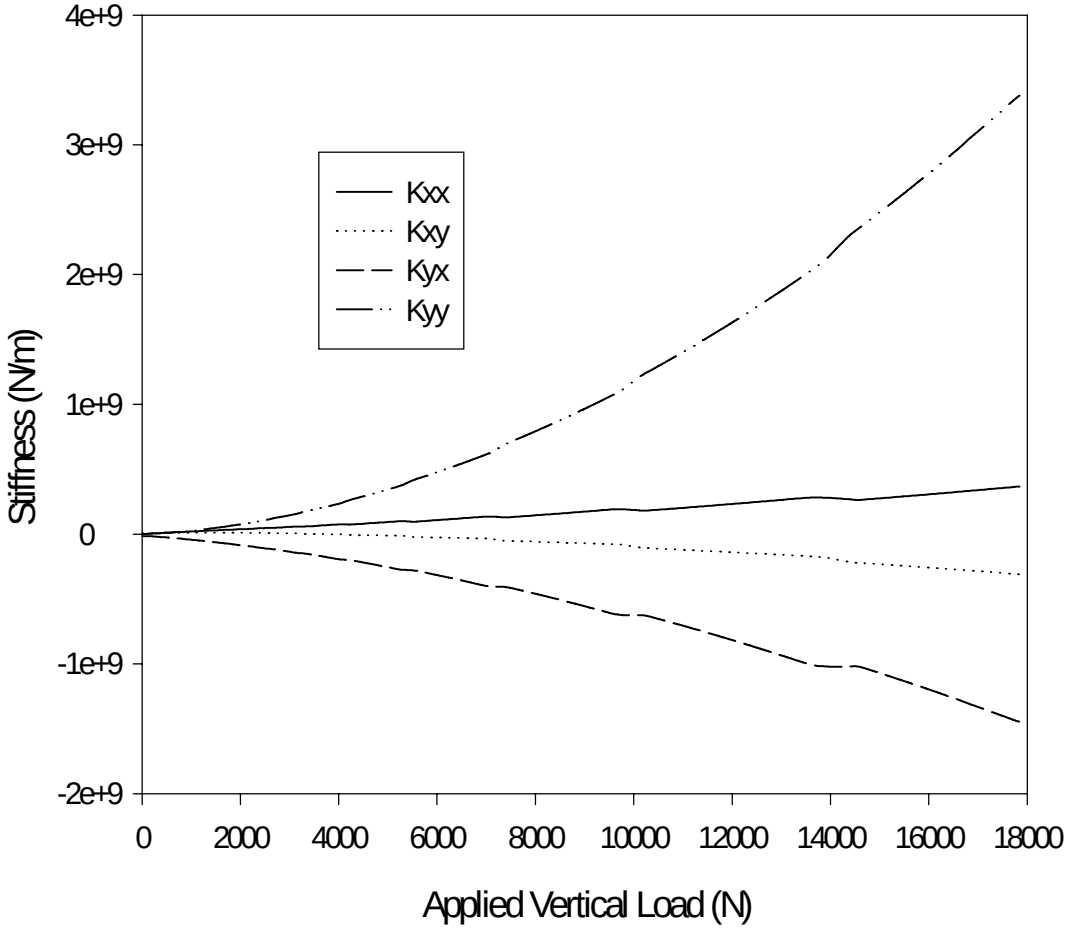

Figure 2 - Typical Two Axial Groove Linearized Stiffness Versus Load (100 mm Dia)

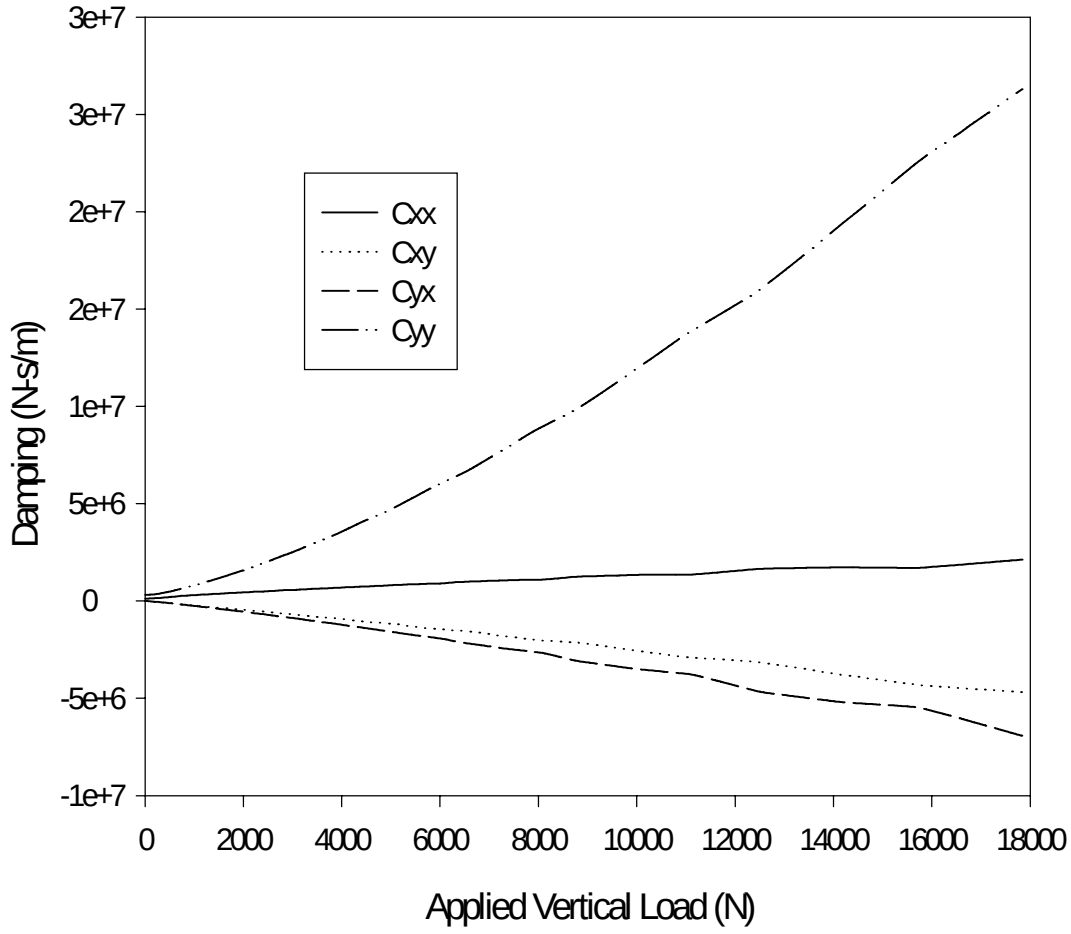

Figure 3 - Typical Two Axial Groove Bearing Linearized Damping Versus Load (100 mm Dia)

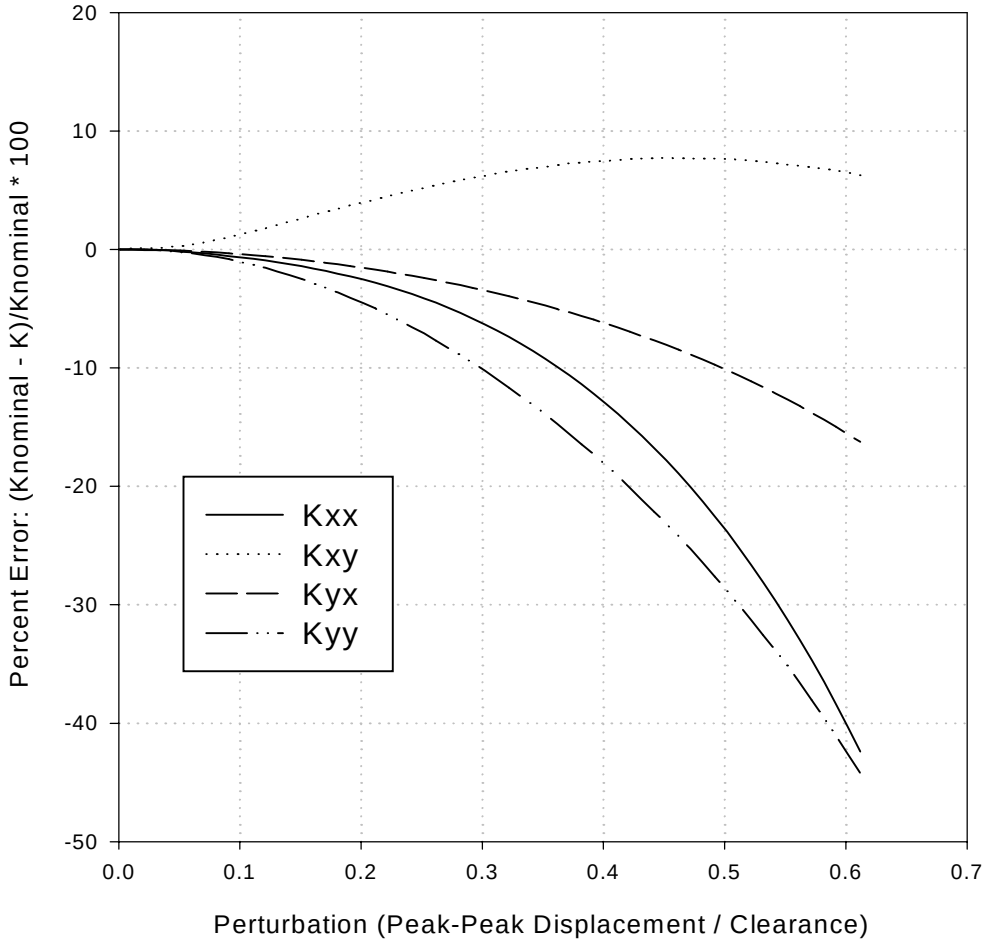

Figure 4 - Analytical Stiffness Change Versus Perturbation Size, 2 A.G., 1000 RPM, 500 N Load

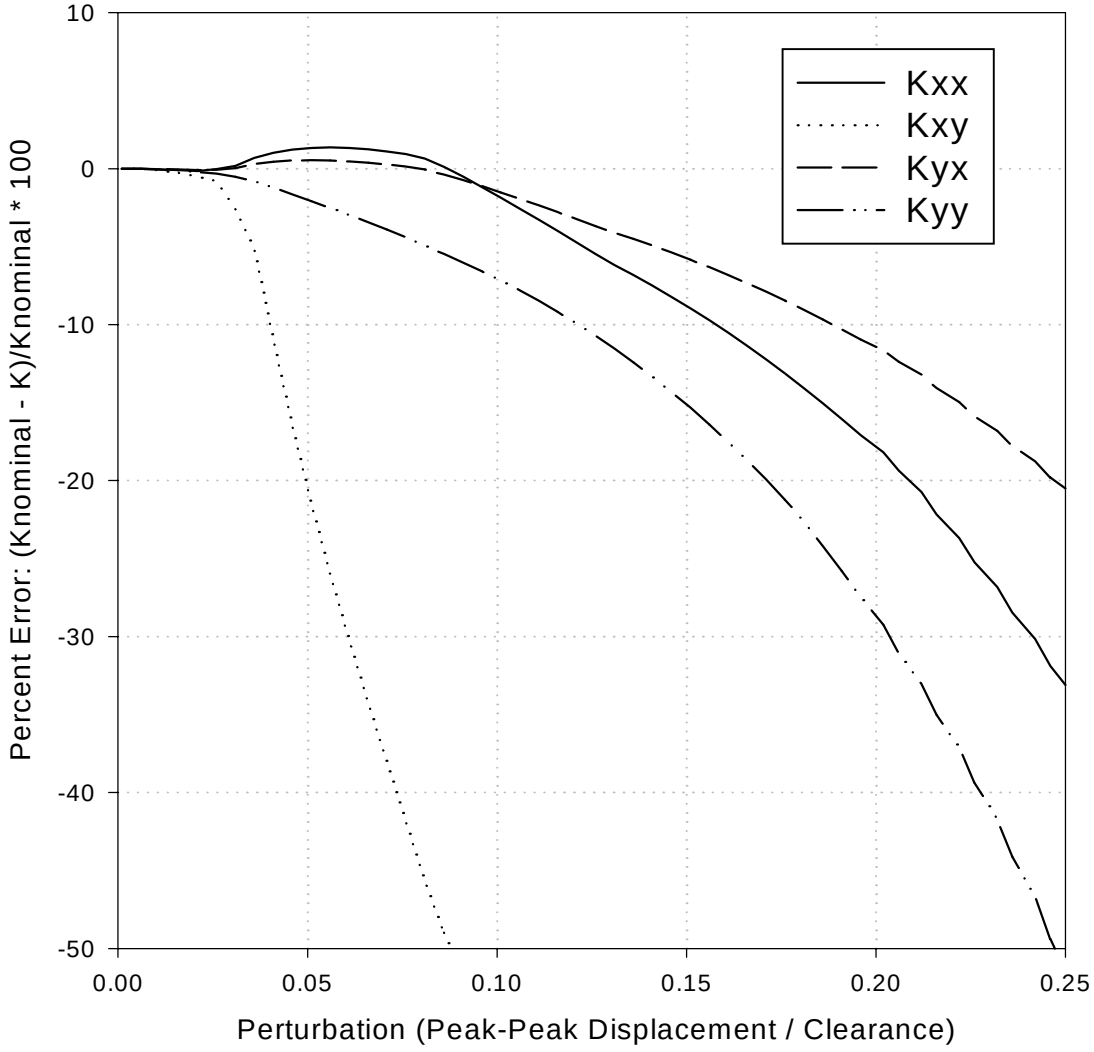

Figure 5 - Analytical Stiffness Change Versus Perturbation Size, 2 A.G. 1000 RPM, 5000 N Load

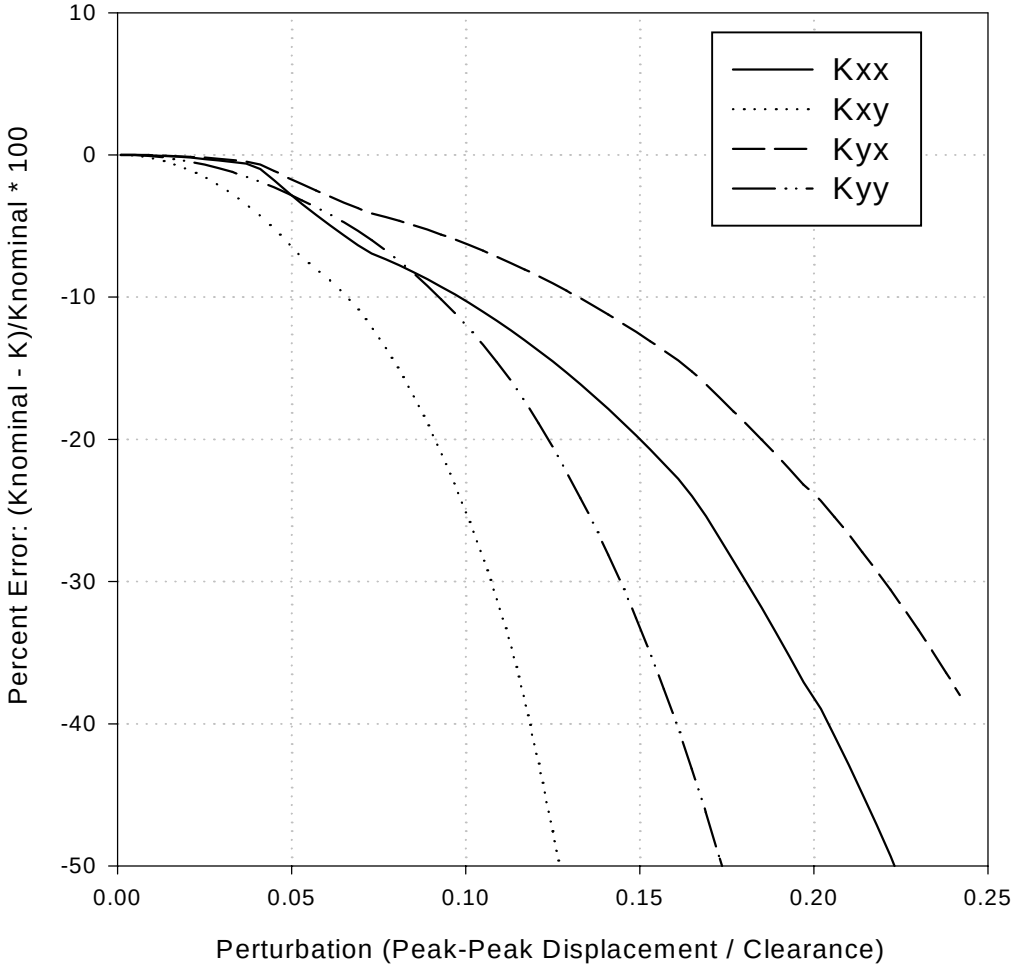

Figure 6 - Analytical Stiffness Versus Perturbation Size, 2 A.G., 1000 RPM, 8000 N Load

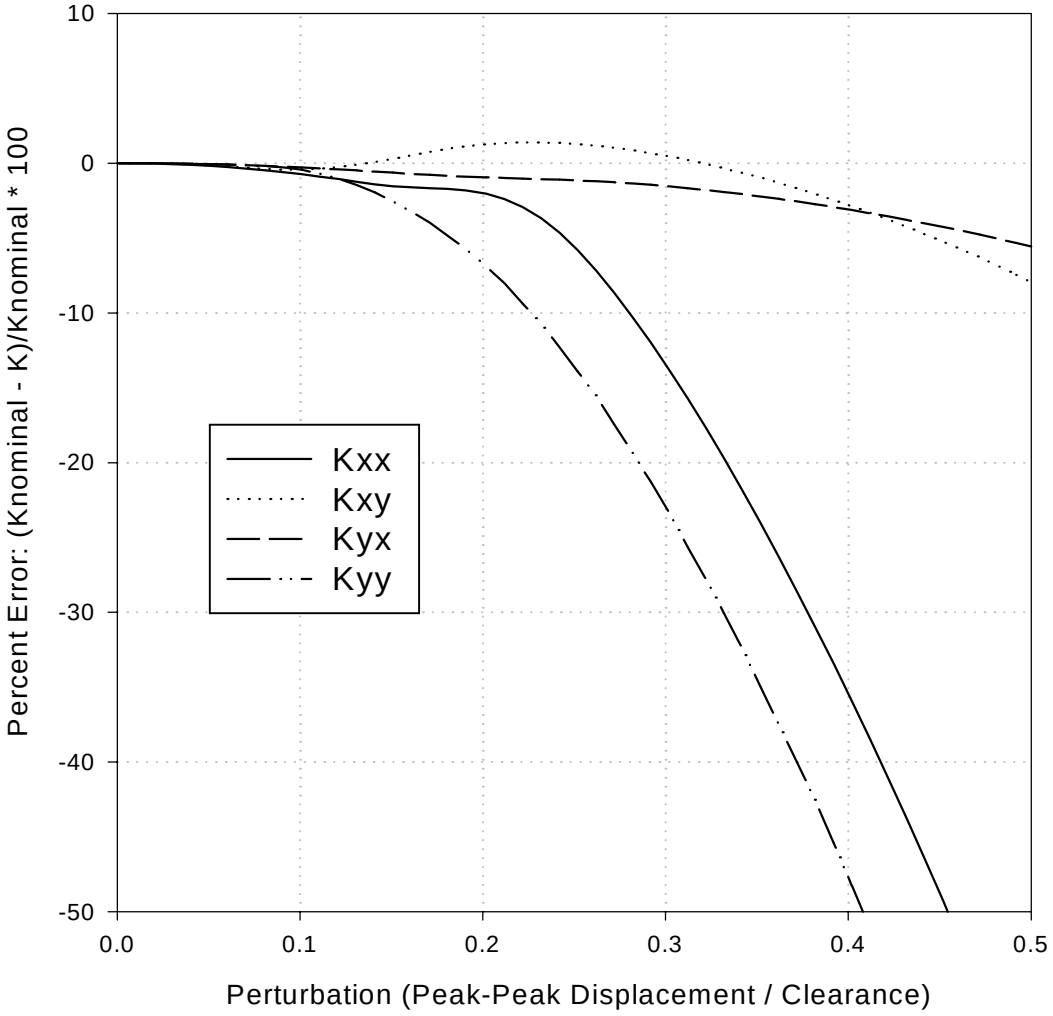

Figure 7 - Analytical Stiffness Versus Perturbation Size, 2 A.G., 5000 RPM, 500 N Load

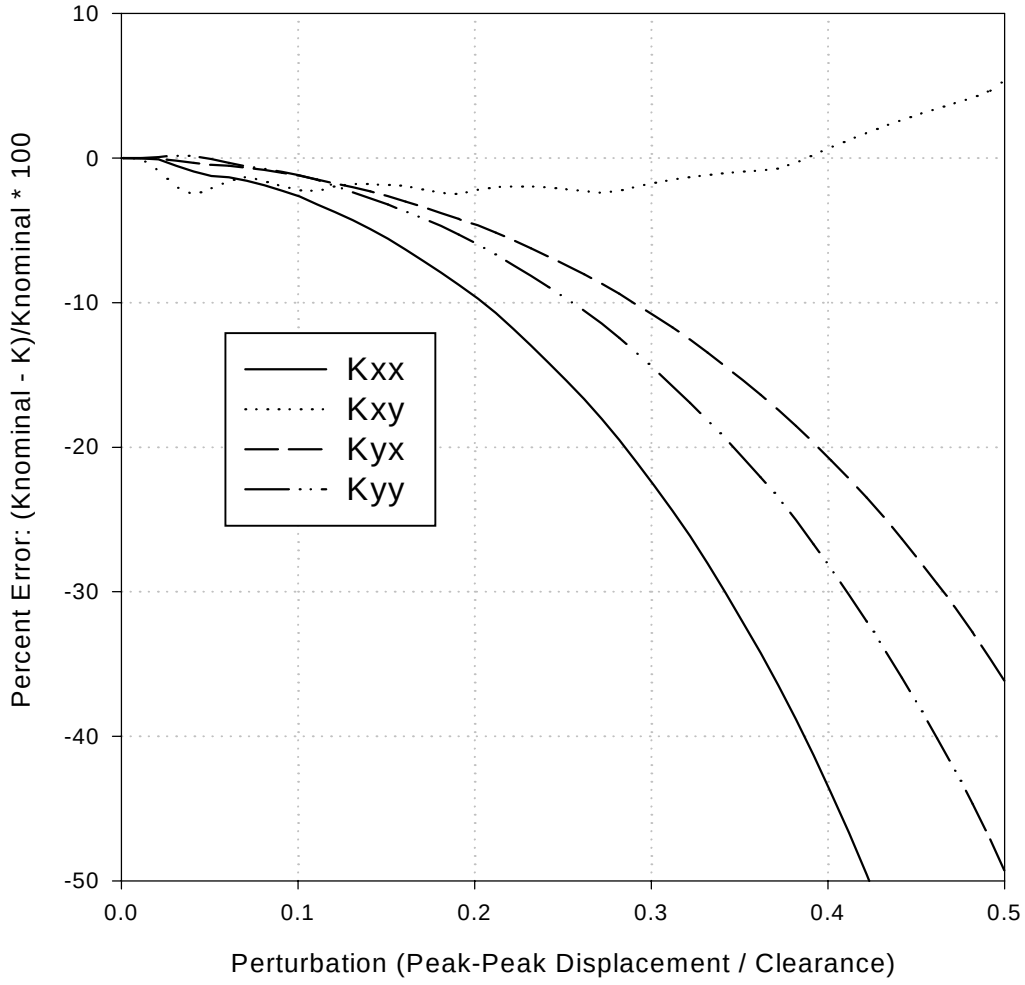

Figure 8 - Analytical Stiffness Change Versus Perturbation Size, 2 A.G., 5000 RPM, 5000 N Load

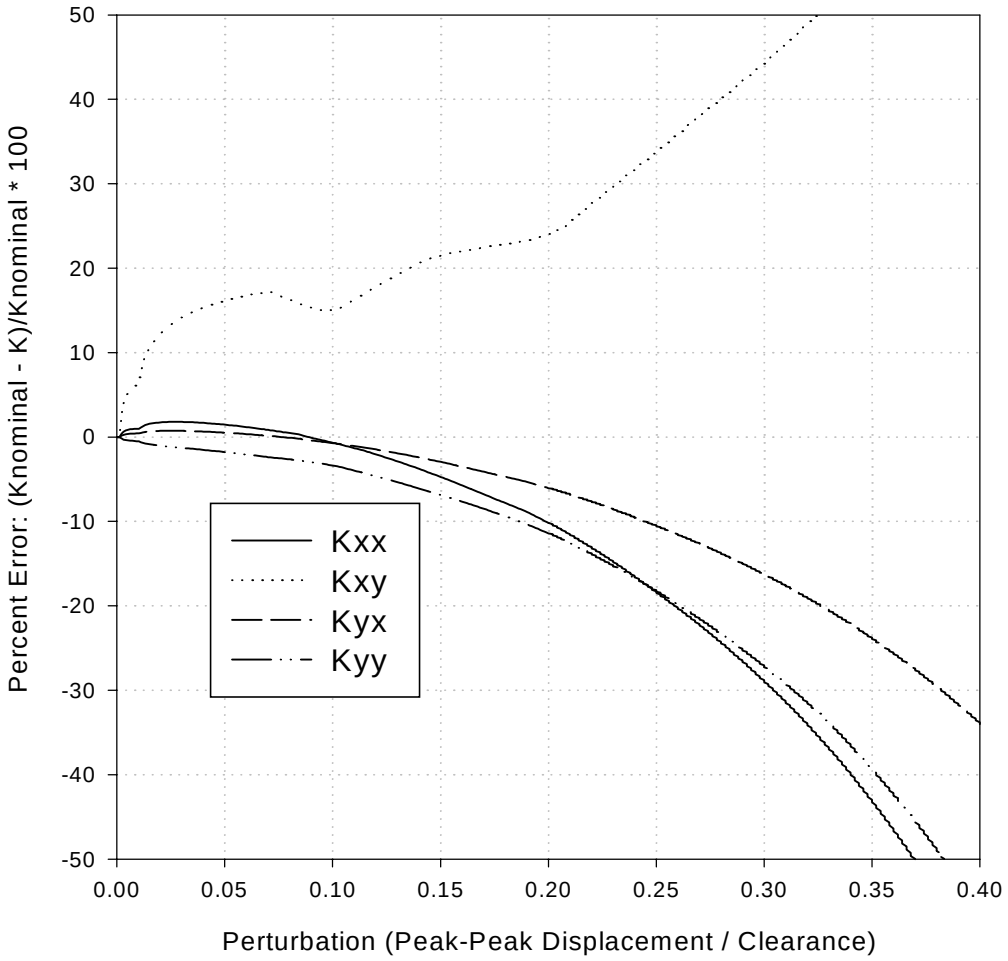

Figure 9 - Analytical Stiffness Change Versus Perturbation Size, 2 A.G., 5000 RPM, 8000 N Load

Table I - Maximum Peak-Peak Perturbations for 2.5 Percent Error in Stiffness Calculation

Case		Reference Perturbation (Δ / C)	Max. Peak-Peak Perturbation for 2.5% Error (2*Δ/C)			
Speed (RPM)	Load (N)		Kxx	Kxy	Kyx	Kyy
1000	500	0.001	0.20	0.14	0.24	0.14
	5000	0.001	0.11	0.30	0.11	0.06
	8000	0.001	0.04	0.03	0.06	0.05
5000	500	0.001	0.21	0.39	0.37	0.14
	5000	0.001	0.08	0.04	0.14	0.12
	8000	0.0002	0.13	0.002	0.14	0.07

1.7 Summary of Previous Work

Since the original goal of this test rig was primarily to test fixed geometry, hydrodynamic journal bearings, an extensive literature search was performed to examine what previous researchers had accomplished with this class of bearings. This work is summarized in Swanson (1997). This work is a guide to what is available in slightly over 100 published experimental works, ranging from 1932 through the end of 1995.

This search revealed that the several varieties of the 360 degree, circular bearing (one hole, one hole/axial groove and circumferential groove oil feeds) were the most widely tested. For these bearings almost all of the variables discussed in section 1.5 have been measured in some way by at least one researcher. There has also been a fair amount of work on bearings described as elliptical or three-lobe, with most of the basic steady load and dynamic characteristics reported by at least one researcher.

With regards to works published since this survey was completed, the results are relatively unchanged. Most of the experimental data are either for cylindrical or two axial groove bearings (Gethin, 1996; Elkholy and Elshakweer, 1995; Kostrzewsky, et al., 1996; Arumugam, et al., 1996; Tieu and Qui, 1996; Qui and Tieu, 1996; Ma and Taylor, 1996), or preloaded designs such as elliptical (Ma and Taylor, 1996), and three-lobe (Prabhu, 1997; Arumugam, et al., 1996; Arumugam, et al., 1997). One work presents results for an offset halves bearing (Makino and Taniguchi, 1996), and one work presents results for a partial arc bearing (Ogrodnik, et al., 1996). These works present a variety of data, including shaft locus or eccentricity ratio/attitude angle versus load, temperatures, dynamic coefficients, free deceleration rates, oil flow rate and data for misaligned bearings. Estimates of measurement uncertainty are presented in five of these eleven works.

The results available in the literature, however, do not provide all of the answers needed by the analyst. One of the major problems is a troubling amount of scatter, and occasionally conflicting trends. These problems occur both within a given work, as well as among results from different works which should match closely. This is especially true among the dynamic coefficients. For

example, in Someya (1988), several figures are presented which show a great deal of scatter, for similar bearings under similar conditions. Some of the damping estimates, for example, are for very similar bearings under very similar operating conditions, but differ by over 200 percent. Not only do the magnitudes differ, but some of the trends are different as well. The analyst would be hard pressed to justify using many of these results as more than order of magnitude checks. This scatter, among both dynamic and steady load characteristics, also highlights the difficulty of the measurement task.

In addition to the scatter, there are two other problems confronting the analyst who needs to use the data. The first is that less than half of the works provide information on the uncertainty of the measurements. This is especially problematical in the case of the dynamic coefficients, where the likelihood of ill-conditioned matrices in the data reduction process is very high. Without the uncertainty information, the analyst is hard pressed to quantify the idea of "good agreement" between experiment and analysis, especially given the level of scatter in the reported coefficient estimates. The second problem is a lack of adequate information of thermal boundary condition. This omission would make it difficult to build an appropriate analytical model to check against experimental data.

Another observation from the literature review concerns test rig design strategies. In most cases, the test rigs employed were configured as shown in Fig. 10. This configuration - a fixed shaft with a floating test bearing - is very appealing from a mechanical point of view. A controlled load can be readily applied to the non-rotating test bearing housing. By making the dubious assumption that the shaft is rigid (or that the shaft dynamics can be accurately and reliably estimated), a correction can be made for the housing mass, allowing for a straightforward estimate of the applied static and dynamic load. In addition to the debatable assumptions given above, there is also the problem that the shaft/bearing geometry in most actual machinery is the reverse of this test set-up. In most machinery, a relatively fixed bearing supports a moving shaft. If all of the elements of the bearing system were linear, there would not be a problem with reversing the geometry. However, the system is not linear; hence, these assumptions must be viewed with some skepticism.

One of the sources of this skepticism concerns the lubricant feed system. To the author's knowledge, there is no published system dynamic analysis which takes the whole bearing/lubricant system, including the lubricant supply system, into account and shows that it is reasonable to assume that the reversed geometry should behave the same as the normal fixed bearing geometry. In addition to the dynamics issue, another concern is the bearing thermal environment. In real machinery, the bearing supports are usually fairly substantial metal structures. As such, they will provide a thermal path from the (generally) hot bearing to a (generally) cooler foundation. In the case of the floating test bearing, this thermal path is not present. As a result, the temperatures in the bearing housing could be quite different between test rig and actual machinery. Since the viscosity of the oil is a strong function of temperature, and thermal deformations can be significant, the difference in thermal environment could cause differences between the test and actual operation (Pinkus, 1990). Even if the test bearing liner temperatures are measured and properly applied to a model with the correct thermal situation, there is also the issue of the cavitated region of the bearing. Most hydrodynamic bearings operate with a region of two-phase (cavitated) flow in some part of the unloaded half of the bearing. Some researchers have suggested that the details of this region are very strongly influenced by the difference between the shaft temperature and the temperature at the surface of the bearing (Heshmat, 1989). The ramifications of this are unclear, and ignored in most computer programs which implement a journal bearing analysis.

A second design approach, used in the Virginia Tech test rig and very few others, is to rigidly mount the test bearing and indirectly load the bearing by loading the shaft through some other means. This test rig design strategy is illustrated in Fig. 11. Although mechanically more difficult, this approach does more nearly model realistic machinery, as well as potentially eliminating the shaft dynamics from the force measurement path.

With regards to test rig designs used to obtain the published, experimental data for dynamic coefficients, 22 out of 35 works employed a test rig with a floating bearing design. Of the remaining 13 works, three used unbalance excitation, which does not allow identification of all eight coefficients in equation 1. One used incremental step loading to only identify the four stiffness

coefficients. One used incremental step loading in combination with unbalance excitation. One used multiple tests with unbalance excitation for a symmetric rotor in matched bearings, and a few assumptions to allow estimation of all eight coefficients. Two of the works employed impact excitation and the assumption of a perfectly rigid rotor. One employed a step load. One used a shaker/load sensor with the assumption of a rigid shaft and a rigid slave bearing. Finally, three works rely on a calibrated finite element model to estimate the transfer function from a non-contact magnetic excitation force to bearing force. Thus, as noted above, the Virginia Test rig design is unusual, in that a magnet bearing-like loader/exciter is used, along with a hard mounted test bearing with a stiff load sensing mount system. These elements are described in detail in later chapters.

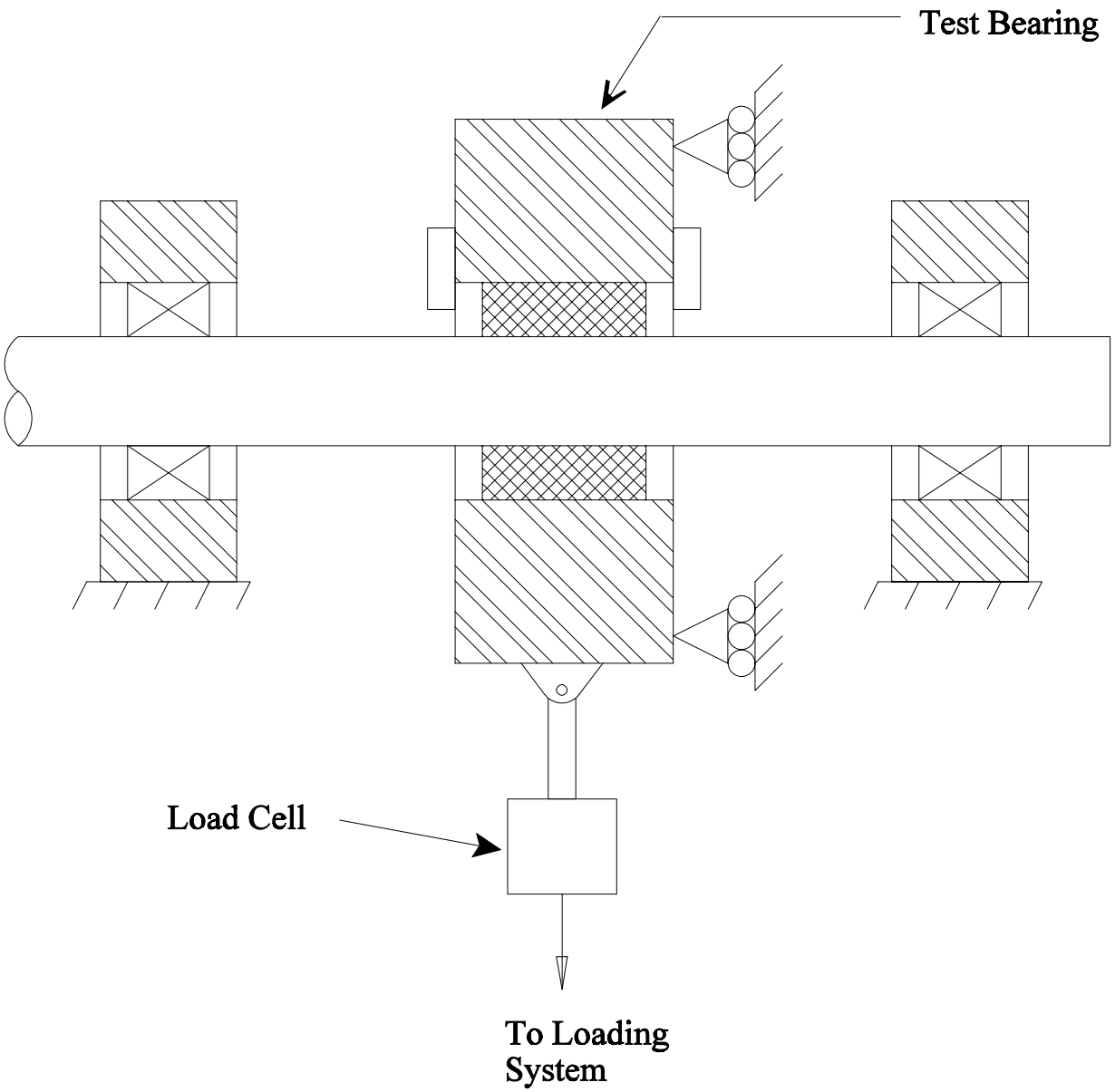

Figure 10 - Floating Bearing Test Rig

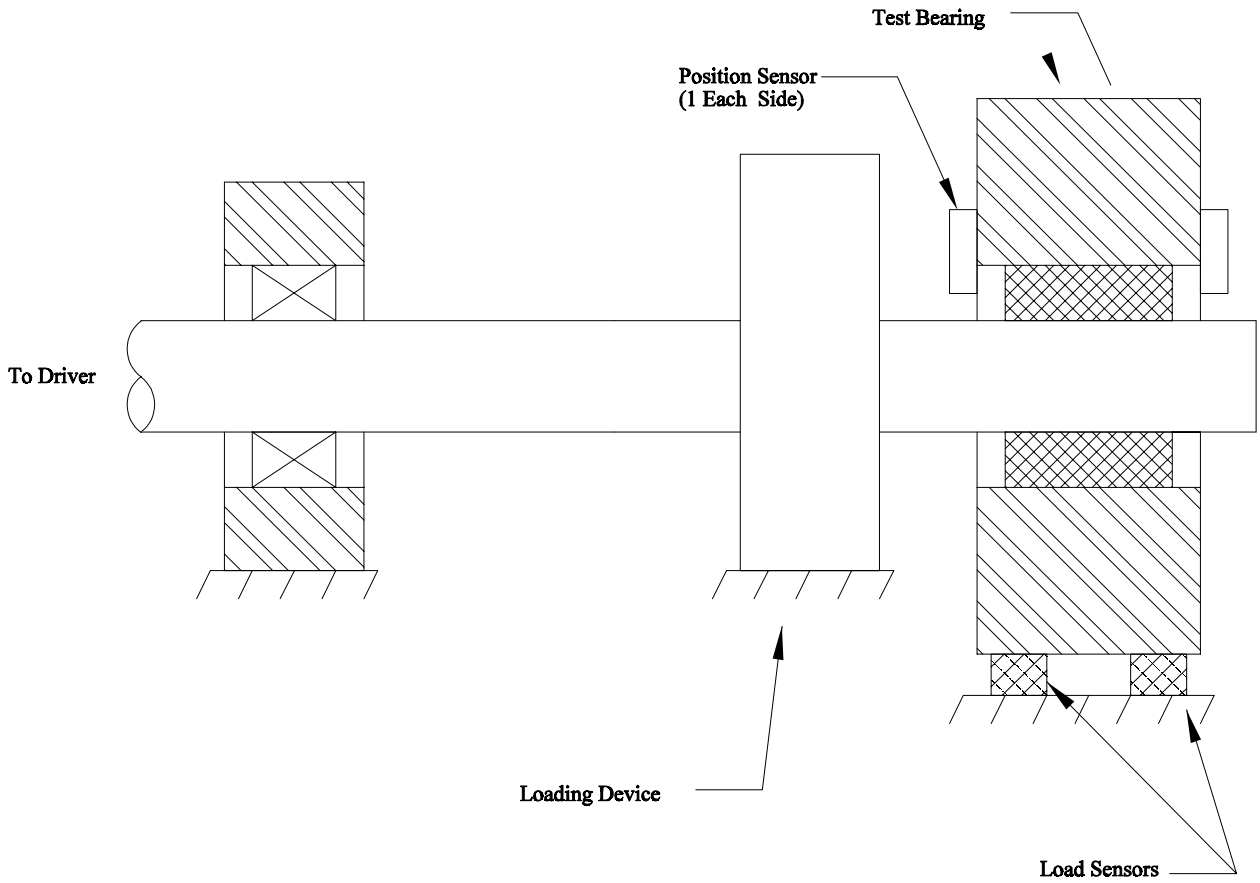

Figure 11 - Floating Shaft Test Rig Design

1.8 Purpose and Scope of Work

The remainder of this work documents the development and details of the Virginia Tech test rig. This rig was intended to allow both steady load characterization and estimation of the dynamic characteristics of oil lubricated, hydrodynamic bearings. The remainder of the chapters of this work are organized as follows:

2) A summary description of the test rig, including current capabilities
3) A detailed discussion of the magnetic loading system used
4) A detailed discussion of the test bearing system
5) A detailed discussion of several other important test rig systems
6) Presentation of some “proof of concept” test data
7) A discussion of the test rig shaft dynamics
8) A summary and some recommendations for future work

Chapter 2

Test Rig - Overview

2.1 Introduction

This chapter discusses the history of the test rig, including the initial test rig configuration and problems associated with this configuration, an overview of the test rig, and describes the current rig capabilities.

2.2 Rig History

The Virginia Tech Rotor Dynamics Research Laboratory fluid film bearing test rig is based on a test rig originally built in the mid 1980's by Ingersoll-Rand Research. This rig was constructed to allow static characterization of high speed bearings for compressor applications. After a very short career at Ingersoll-Rand, the rig eventually was donated to the Virginia Tech Rotor Dynamics Research Laboratory. Since this time, most of the rig components have been modified or replaced, with the goal of improving the test rig steady load bearing performance measurement capability, and upgrading the test rig to make the measurements required to estimate bearing dynamic characteristics. An evaluation of this test rig formed the basis for a master's thesis by the author (Swanson, 1992), which also documents the evaluation of an existing bearing code for fixed geometry journal bearings and presents comparisons between preliminary tests with the test rig and the bearing analysis code.

During the test rig reconfiguration, it was used for a project to compare the performance of various mineral based and synthetic oils in a high speed journal bearing for eventual use in a large thrust bearing at a pump storage power generation facility (Swanson, Kirk, and Mondy, 1992).

As an outgrowth of this work, a research program on the thermal distortion effects in journal bearings was developed. This program employed bearings fabricated from steel, bronze and aluminum as a vehicle to examine thermal distortions arising from the thermal gradients in an operating bearing. Several works were published showing a measurable effect (Swanson and Kirk, 1994; Swanson and Kirk, 1995).

Finally, the extensive upgrade/redesign program to give the test rig the capability of performing the measurements needed for estimation of bearing dynamic coefficients was sufficiently completed to allow preliminary testing. The capabilities of the upgraded test rig will be described following a discussion of the original test rig configuration. The results of the preliminary tests are described in two later chapters of this work.

2.3 Original Test Rig Configuration

A picture and a side view of the test rig as it arrived from Ingersoll-Rand are shown in Fig.12 and Fig. 13, respectively. This test rig is unusual in that it is based around a movable (floating) shaft which applies load to a fixed test bearing as in Fig. 11. As discussed previously, this approach most nearly models the actual arrangement in real turbomachinery. The load is applied to the shaft by electro-magnets, which provides a very flexible, non-contact loading system. The test rig as supplied, was mounted to a sturdy (but not very stiff) steel table, and included a small, dedicated oil system, as well as an oil mist lubrication system for the support bearing. The test bearing installed in the rig was a five-pad bearing manufactured by Glacier Metal Co. Also included were two DC power supplies for the upper and lower magnets which were still mounted in the test rig. The two horizontal magnets and load cells arrived with the rig; however, only one of the horizontal magnet mounting plates was present.

The rig itself was of solid construction, with a 38 mm thick, type 410 stainless steel baseplate, and magnet housings of 25 mm thick 410 stainless steel. The test bearing was mounted in a massive 330 mm x 375 mm x 127 mm type 410 stainless steel housing. The rear support bearing was mounted to a 38 mm thick mild steel support plate. The center portion of the shaft was surrounded by a 19 mm thick mild steel cover. The drive system was a 30 kW air turbine, which will be described in detail in a later section. The only instrumentation included with the rig was a once-per-rev speed pick-up, a thirty pulse-per-revolution speed pick-up in the turbine, a torque sensing, strain-gaged turbine mount, the four magnet load sensors, along with a single channel force readout and a two channel signal conditioning unit for the torque and speed sensors.

Following initial investigations to check the basic functionality of the rig, a solid foundation was designed and built for the rig, and the upgrade process was started. The basic goal of this upgrade was to develop a test rig which would be capable of making the measurements required to estimate the linearized stiffness and damping characteristics of fluid-film bearings, while re-using as many of the original test rig components as possible. Although the actual design and development of the revised test rig took place over a period of about five years, including several years of hardware fabrication frustrations, the major shortcomings of the original test rig were quickly identified in the initial two year evaluation which was summarized in Swanson (1992). Briefly, these were as follows:

1) The design of the magnets provided with the test rig was not suitable for dynamic loading
2) There was no provision to sense the applied load at the test bearing
3) The instrumentation initially used to collect data was not suitable for dynamic testing and suffered from reliability problems
4) Shaft bow under load and differential thermal growth between the test and support bearings caused alignment problems at the test bearing

5) The oil system had poor temperature regulation and rapidly became saturated with entrained air at higher shaft speeds
6) The speed regulation needed improvement
7) The shaft test bearing location did not have enough axial length for the bearings of interest
8) The shaft was designed for use with removable sleeves at the test bearing location which could not be reliably installed concentric with the shaft center of rotation
9) The shaft had excessive deflection through a seal adjacent to the test bearing

Items one through three precluded the use of the test rig for dynamic testing; hence the primary thrust of the rig modifications was to address these issues. Item four was also considered to be quite important, and was in fact addressed prior to finishing the upgrades aimed at dynamic testing. The remaining items were addressed at various stages of the upgrade process.

Over several iterations of rig design, most of the components of the rig were replaced. The only pieces of the rig as it arrived from Ingersoll-Rand which remain are:

- Rig baseplate (modified)
- Magnet housing (some modifications)
- Shaft cover pieces (minor modifications)
- Support legs (modified)
- Turbine mount (modified)
- Drive to shaft coupling
- Oil cooler
- Turbine air filters
- Air turbine (replaced by electric motor, but still usable)
- Speed/once-per-revolution pick-up

In retrospect, the constraint of remaining as faithful to the original test rig layout and speed capability was probably the wrong constraint to have maintained during the upgrade. However, lacking access

to experienced test rig designers, following the lead of a successful designer seemed a prudent thing to do at the outset of the upgrade process.

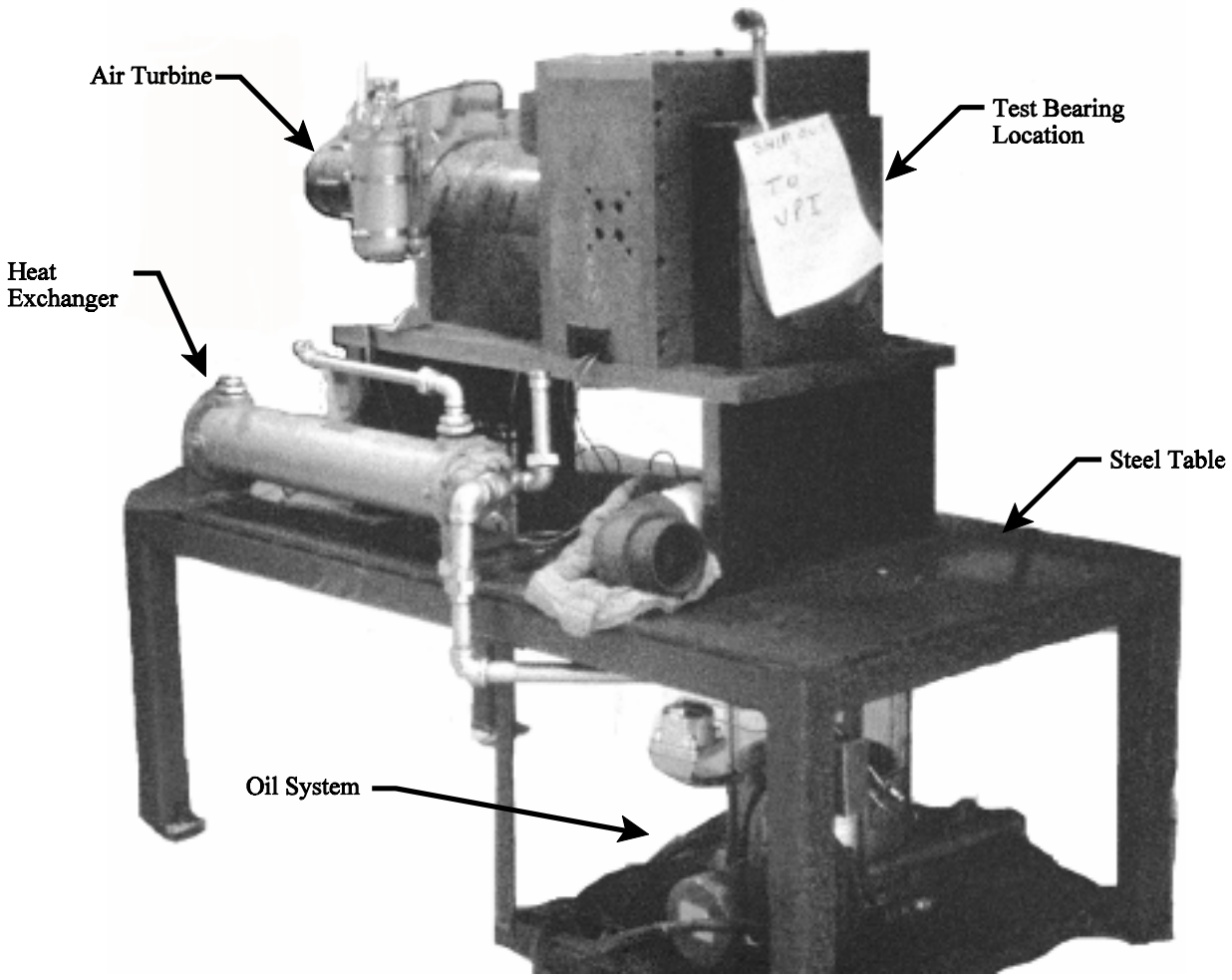

Figure 12 - Original Test Rig

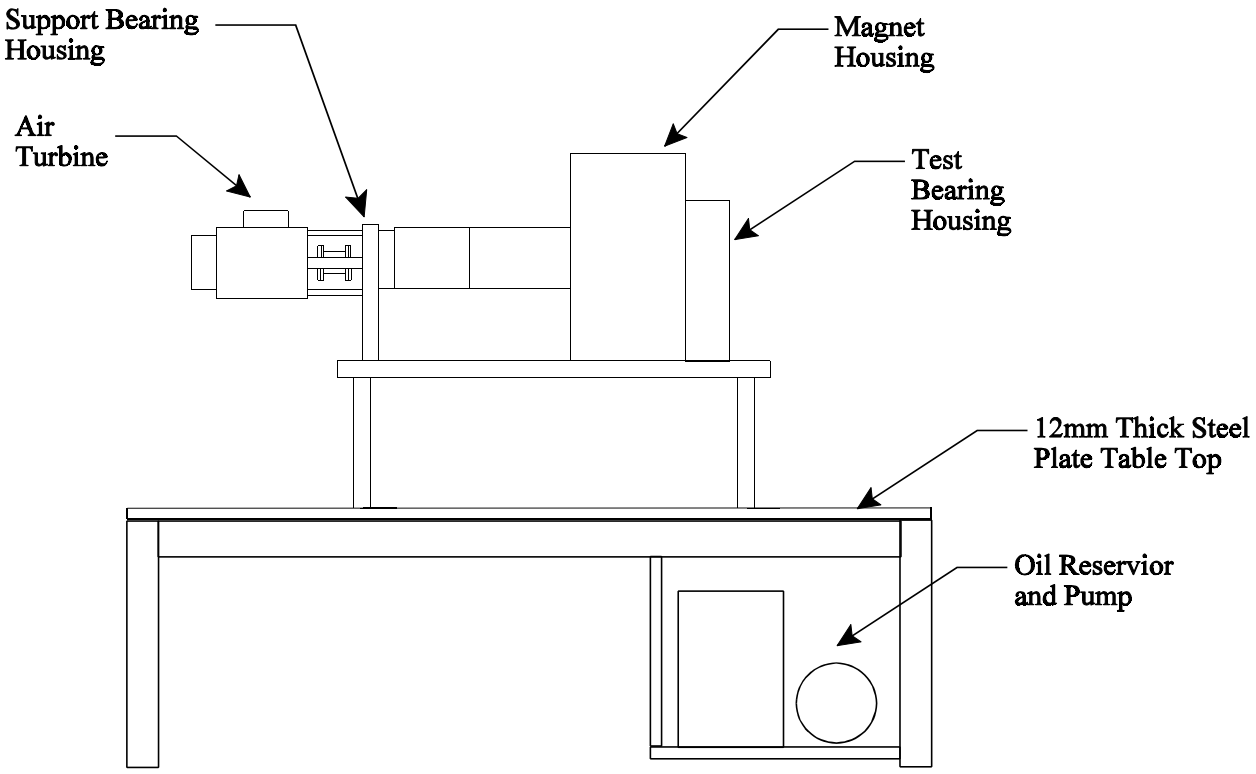

Figure 13 - Original Test Rig - Side View

2.4 Test Rig Description and Capability

The current test rig configuration is shown in Fig. 14, and schematically in Fig. 15. An overview of the rig capabilities is presented in Table II. The subsystems will be discussed in detail in the following chapters.

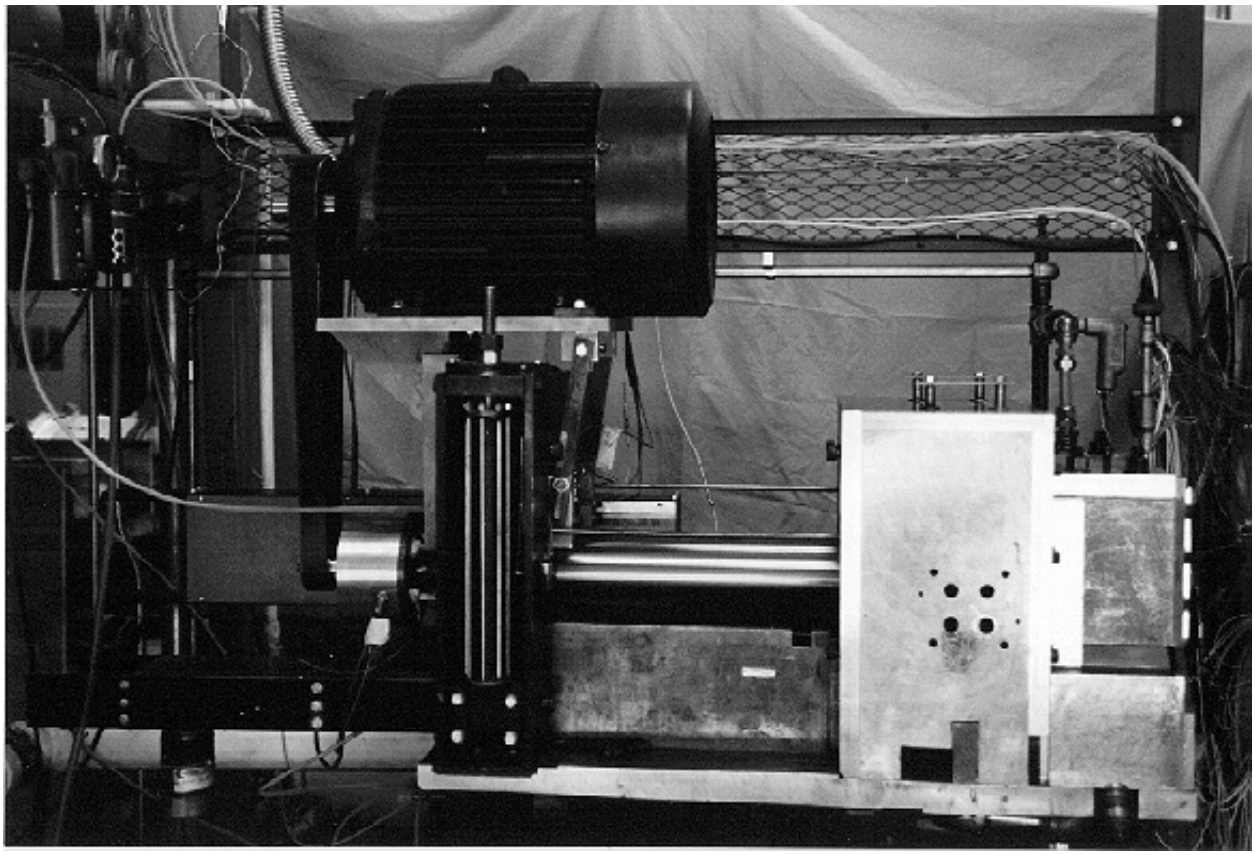

Figure 14 - Rig Side Picture

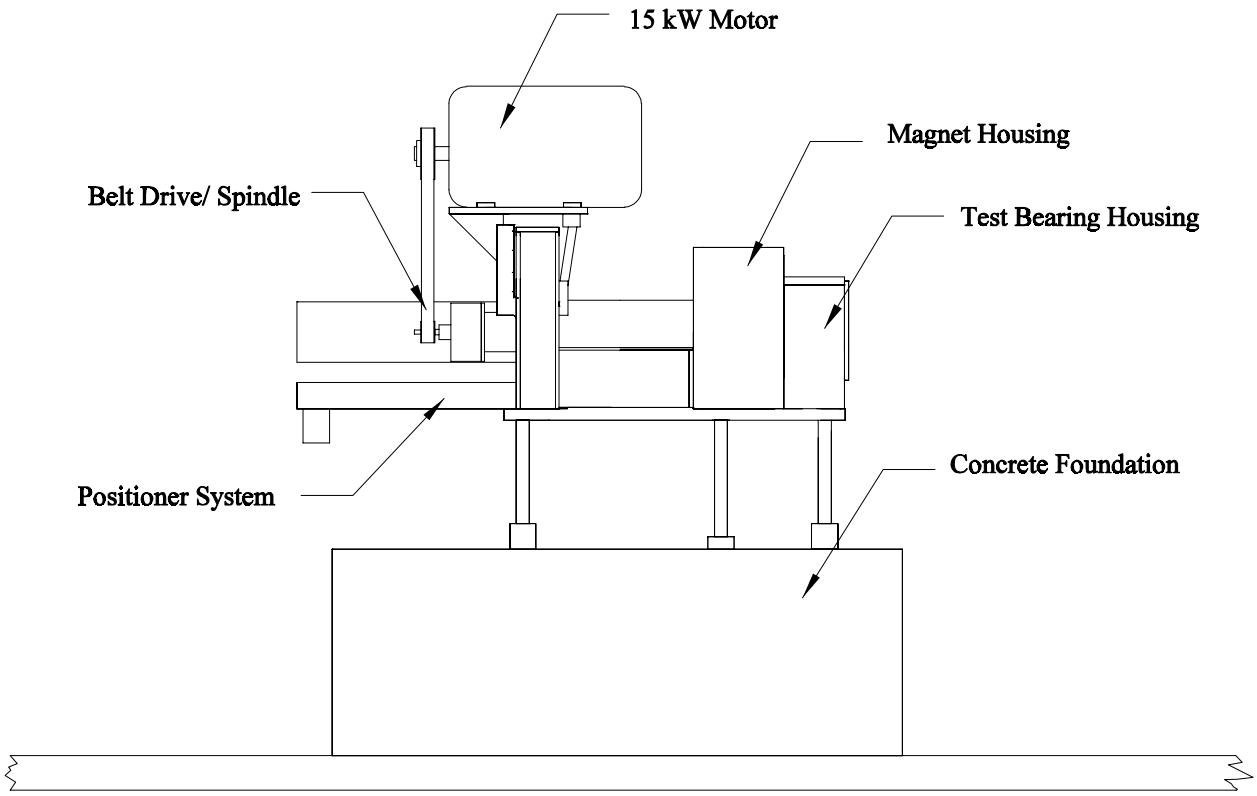

Figure 15 - Test Rig Side View

Table II - Current Test Rig Capabilities

Item	Description
Speed Range	300 RPM to 15,000 RPM (motor drive, 2.4:1 belt) 300 RPM to 35,000 RPM (air turbine)
Static Load	0 to 1600 lb, Arbitrary orientation
Dynamic Load	Frequency dependent magnitude Arbitrary orientation
Displacement Measurement	8 eddy current displacement probes (Bently-Nevada series 3300, 8 mm) arranged in opposing pairs: Test bearing inboard horizontal (2) Test bearing inboard vertical (2) Test bearing outboard horizontal (2) Test bearing outboard vertical (2) Probes are calibrated for aluminum and use aluminum rings on the shaft as targets in an attempt to reduce electrical shaft runout 2 eddy current displacement probes at support bearing for monitoring only (Bently-Nevada series 7200, 5mm)
Force Measurement	2 Low profile (strain gage) Load cells at loading magnets for radial load (GSE 4650) 4 ICP piezoelectric, compression load cells under test bearing to sense both X,Y radial load and moments (PCB 200A05)
Temperature Measurement	Type J thermocouples embedded in bearing and inserted into oil inlets, drain, etc.(15 max). Type K thermocouples embedded around bearing outer housing (15) for housing temperatures
Pressure Measurement	Pressure taps in bearing insert and oil inlet (14 max.)

Item	Description
Driver	15 kW, 5400 RPM electric motor with variable frequency drive. 2.4:1 speed-up belt drive to rig via jack shaft 30 kW, 35,000 RPM rated air turbine driven by a large diesel air compressor. Two air operated control valves in supply pipe for flow control. The speed with either system can be controlled with a PC running a custom program with a digital proportional-integral algorithm
Oil System	20 kPa, 38 L/min rated vane pump 15 micron filter 76 L tank 1000 watt heater w/ proportional controller for tank temperature Oil/water cooler with commercial process controller to regulate inlet oil temperature by controlling water flow with an air operated control valve, based on readings from a thermocouple in bearing inlet Manually operated pressure regulating valve at bearing inlet 38 L/min Rotometer for flow measurement Analog and pressure transducer for oil pressure measurement
Operating Alignment	Positioner system which allows support bearing radial motion of ±10mm during rig operation

Item	Description
Rig Control	Split between 2 PC's: Rig Operation PC controls shaft speed, monitors rig bearing temperatures, oil level, etc. Data acquisition PC controls testing. The actual testing is controlled via Matlab driver routines which allow control over applied load, speed, excitation, rear bearing position, as well as data acquisition.

Chapter 3

Magnetic Loading System

3.1 Introduction

The test rig loading system, shown in block diagram form in Fig. 16, is a non-contact, electromagnetic loading system similar to a magnetic bearing. Indeed, with displacement feedback, the system operates as a magnetic bearing. This system is the enabling design feature which makes the floating shaft/fixed test bearing arrangement of this test rig possible. The magnetic loading system was intended to be the source of the steady load, as well as the excitation force to allow bearing coefficient estimation. With regards to this function, the system works quite well. As will be described in a later chapter, were the shaft made from an infinitely stiff material, or the bearings at least an order of magnitude softer, the system would indeed allow bearing identification. Due to the shaft/bearing stiffness mismatch, however, the full capability of this system cannot really be utilized. This chapter describes the loading system in detail.

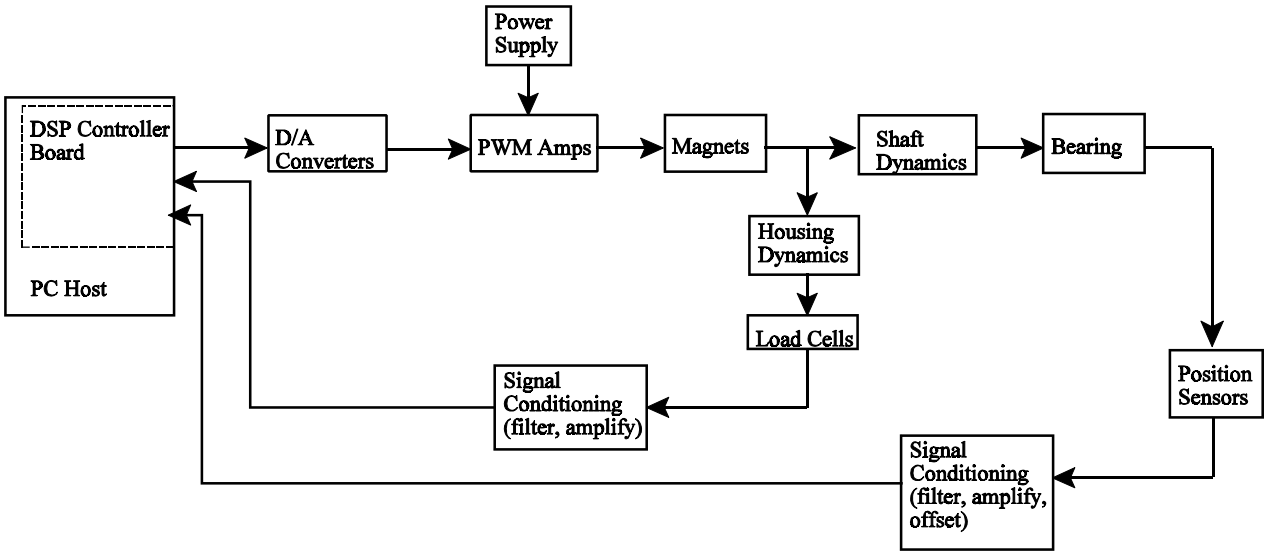

Figure 16 - Rig Loading System Block Diagram

3.2 Actuator

3.2.1 Overview

The magnetic actuator, shown in Fig. 17 and Fig. 18, consists of a stator built-up from thin (356 µm thick) laminations of silicon-steel (type M22), with windings to generate the magnetic flux, and a region of the shaft with a stack of thin (356 µm thick) disk-shaped laminations. As constructed, the stator is actually three separate magnets made into a single structure. This actuator can apply up to approximately 8900 N of steady load to the shaft with the power amplifiers currently in use. Approximately 78 percent of this load is reacted by the test bearing. The dynamic load capacity reduces with increasing frequency, but measurable force is still obtained at 500 Hz.

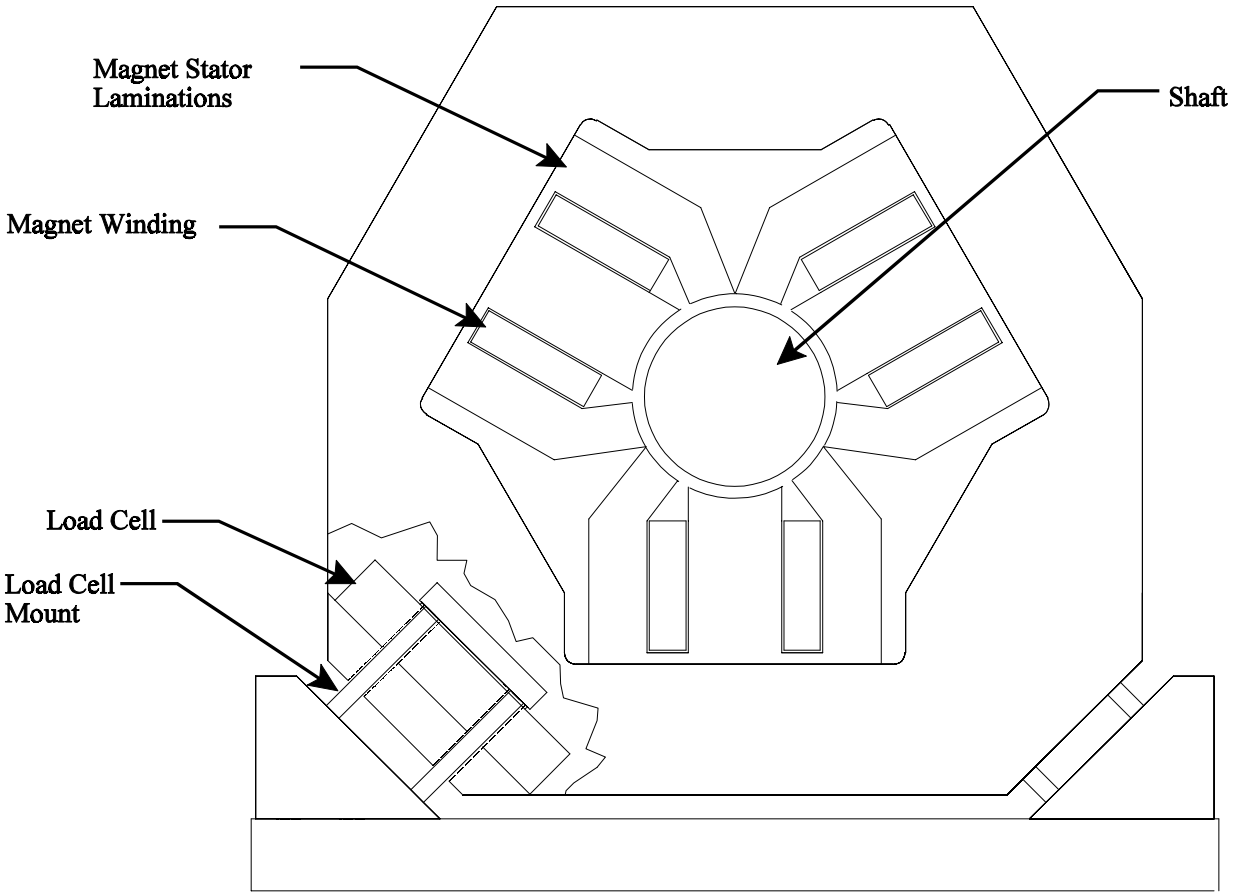

Figure 17 - Magnetic Actuator, Concept

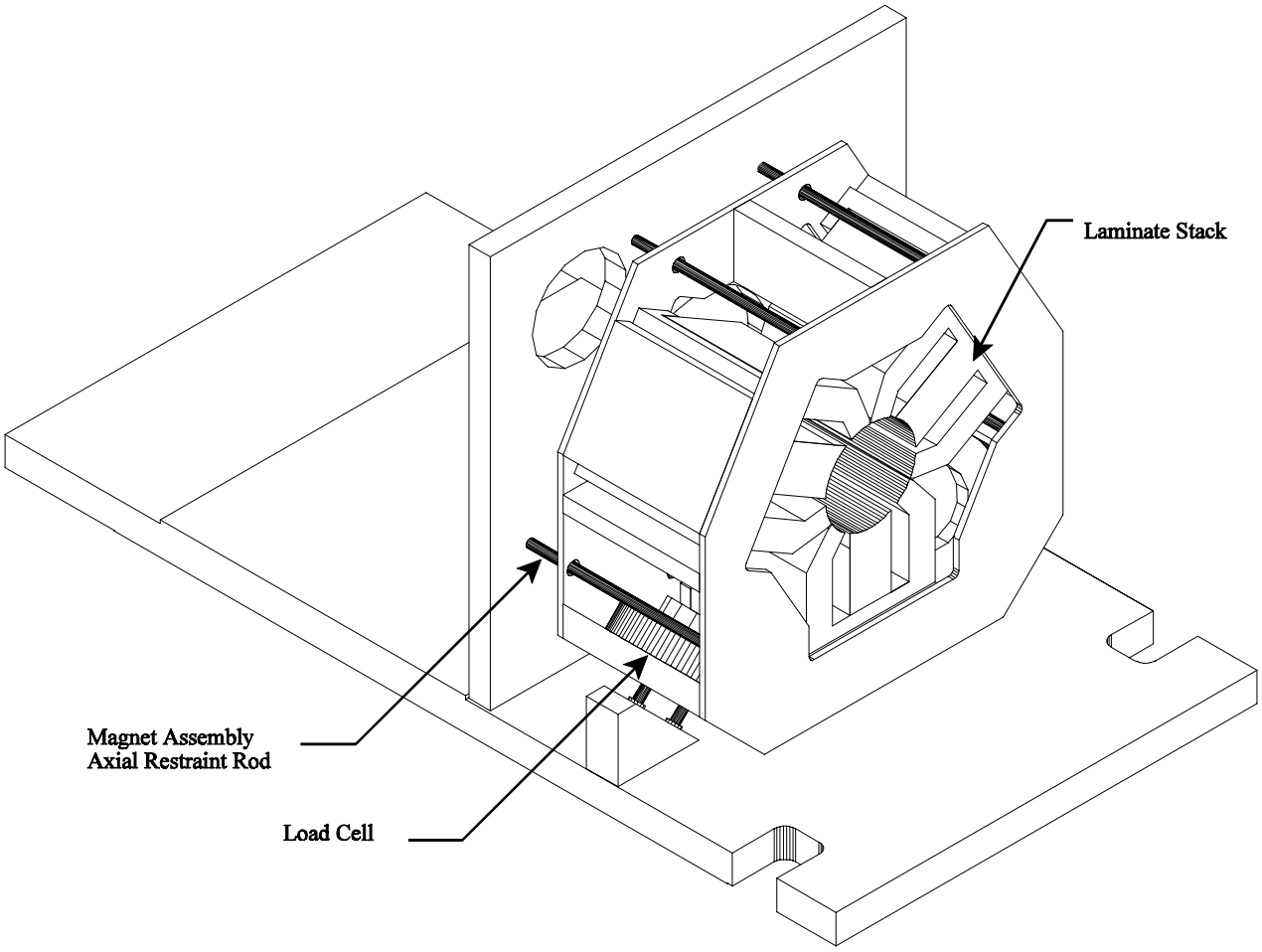

Figure 18 - Magnetic Actuator, Stator Overview

3.2.2 Actuator Design

The original test rig design used independent magnetic quadrants mounted on low profile load cells as shown in Fig. 19. In keeping with the goal of following the original rig design, this approach was also used for the development of the initial new magnet design. This design does not supply the desired load of at least 8000 N, even when driven into saturation. Figure 20 presents the measured load versus drive characteristics of one quadrant of this design (indicated by "Initial Magnet Design"). There were four possible routes to increasing load: increase the current further, change materials, decrease the air gap, or increase the projected area. Increasing the current was not likely to markedly increase the load, as the magnet material was already becoming saturated. Since the shaft had already been fabricated at a substantial cost and time investment, changes to a material with a higher magnetic saturation level were not very appealing. In addition, the candidate material, Hyperco (trade name for a high performance, iron-cobalt-vanadium magnetic alloy), is expensive and could be difficult to obtain. Decreasing the air gap was ruled out, as it would increase the probability of contact between the actuator and the shaft, with potentially disastrous consequences. Hence, the only remaining approach was to increase the projected area. Since the shaft had been fabricated at this point, increasing the length of the magnet was also not a viable option; hence a three sector design was selected. By going to this design, a somewhat greater projected area (see Fig. 21), and hence a greater load capacity was obtained. This design was inspired to some extent by the work of Gondhalekar and Holmes (1984). The drawback of this design is the slight increase in complexity of the control algorithm to convert an orthogonal vertical-horizontal desired load, into a non-orthogonal, three actuator system.

As with the original design, a scheme of one load cell per magnet was kept. Initial testing revealed a flaw in this design strategy. The combination of the large magnet wrap angle, the negative spring rate associated with a magnet, and the relatively low moment stiffness of the load cell was such that the assembly would rock, with one or the other top edge of the load cell moving in towards the shaft. This problem was identified after a high-speed rub between the corner of the load cell and the surface of the shaft.

As a result of this experience, as well as concerns with the likelihood of a tangential force component for operation with the shaft displaced from the magnet centerline due to the negative spring rate inherent in all attractive magnetic actuators, a structure to hold all three magnets, with provision for two load sensors, was fabricated. This structure (see Fig. 18) consists of two 6.4 mm thick plates, load-cell mounting plates, magnet mounting plates and spacer plates. To prevent any relative motion between the magnets, the space between the individual magnets was filled with a steel spacer and high-strength epoxy as shown in Fig. 22. This assembly is quite heavy, weighing slightly over 1000 N.

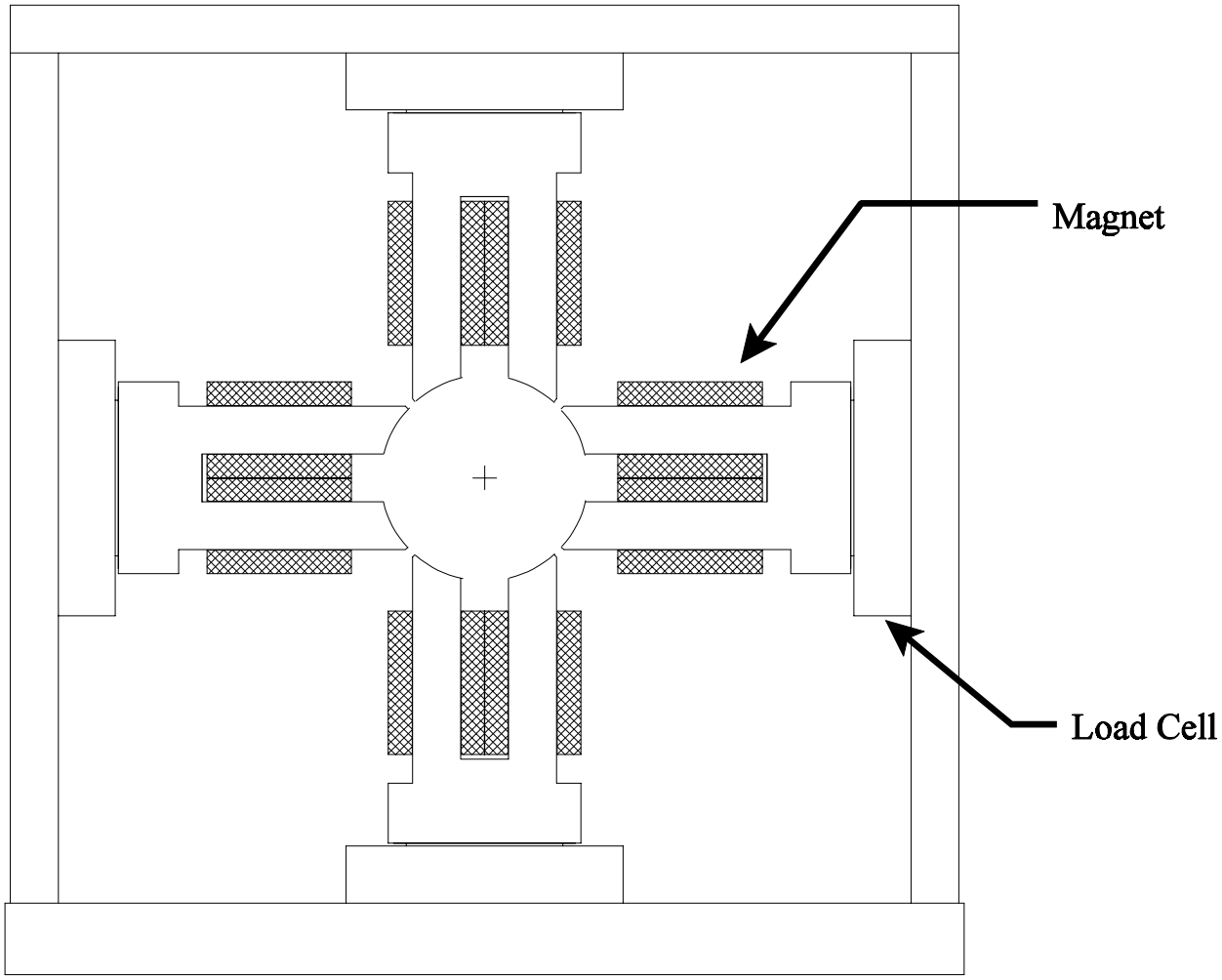

Figure 19 - Original Magnet Design

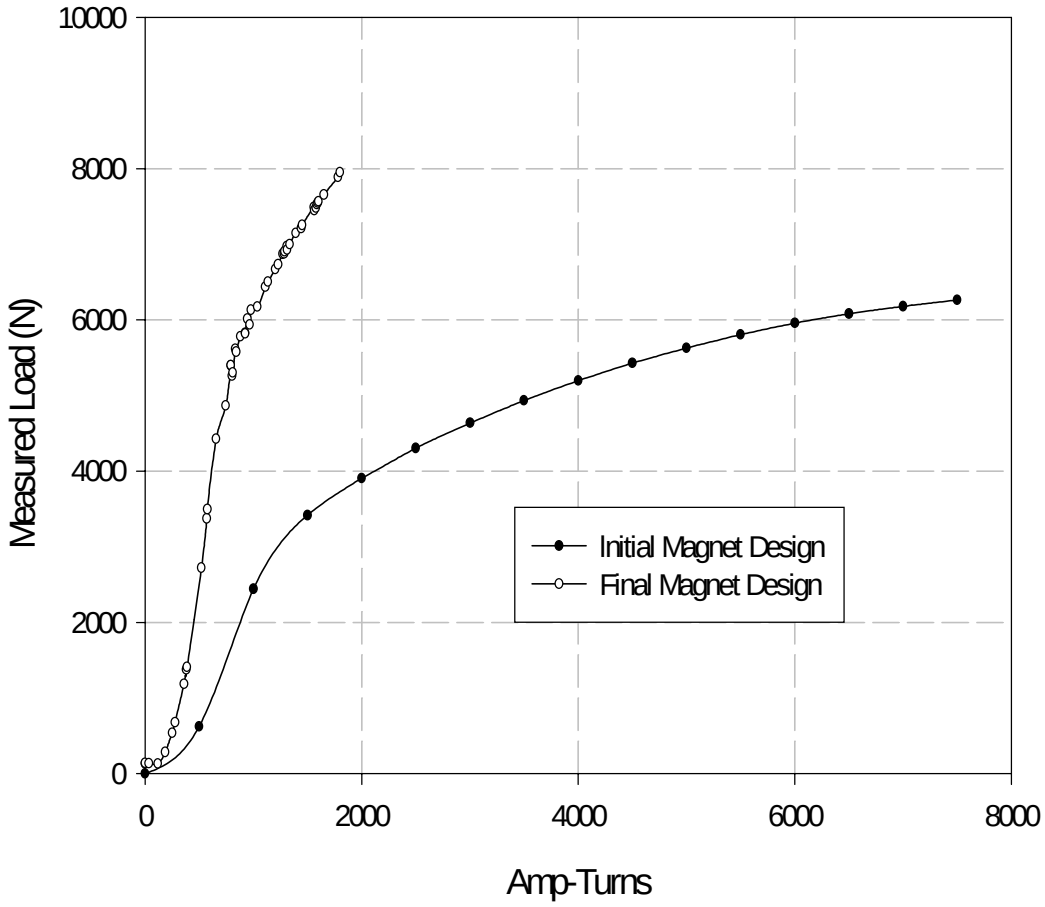

Figure 20 - Magnet Load vs Drive (amp-turns)

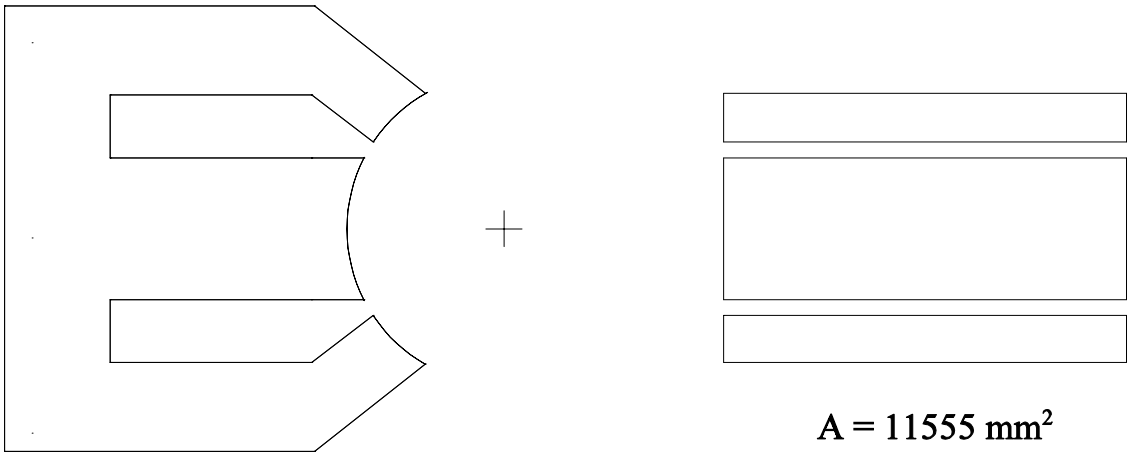

Figure 21 - Magnet Design Comparison

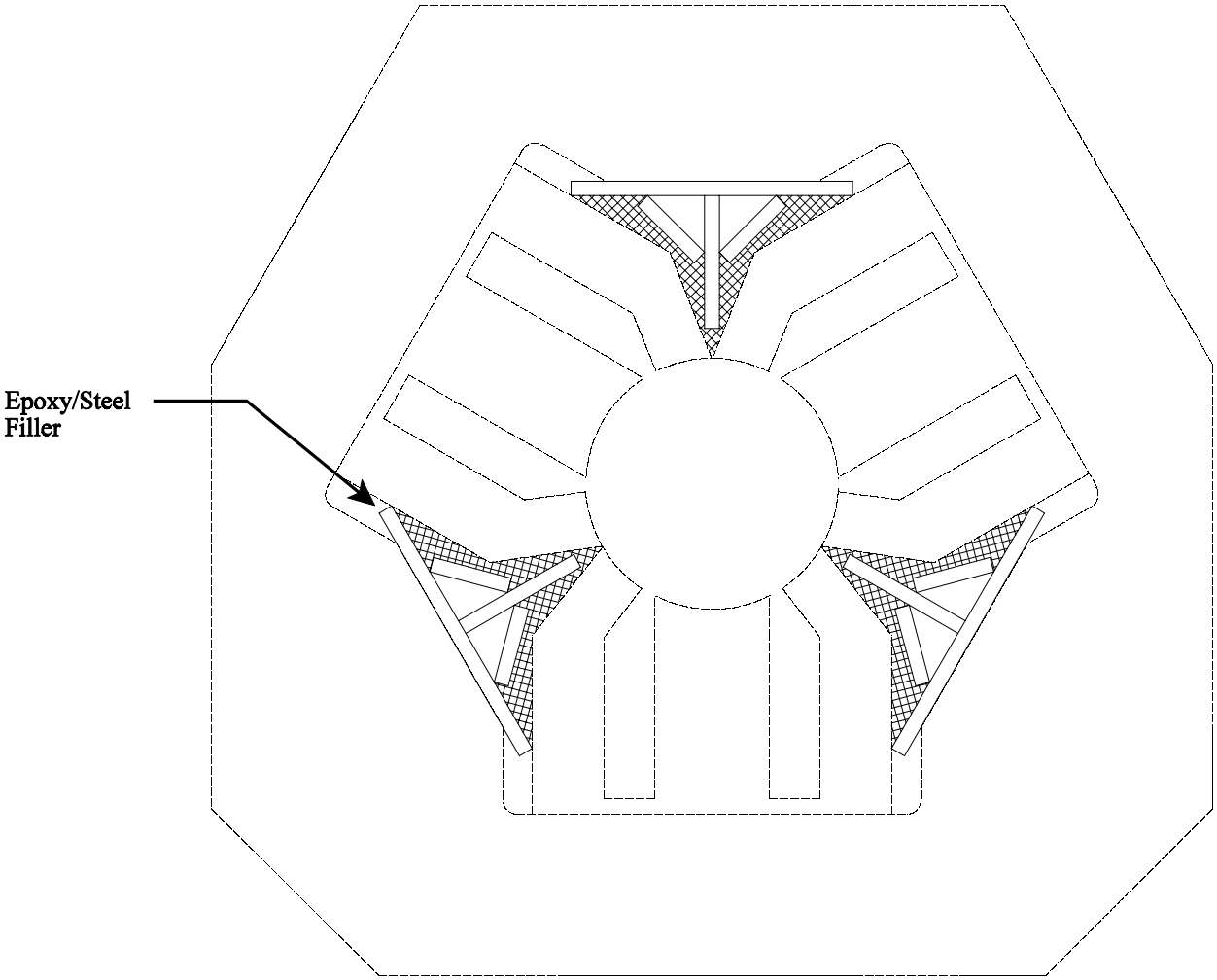

Figure 22 - Magnetic Actuator, Filler Detail

3.2.3 Actuator Electrical System

The electrical portion of the actuator consists of windings on the laminated stator, power amplifiers, and a high voltage power supply as shown previously in Fig. 16. Each winding consists of six layers of 30 turns of 12 gage, enamel insulated wire, for a total of 180 turns of wire on each magnet sector. The wire size selected is fairly conservative for the expected full load current of 10 amps. Although the magnets remain at an acceptable temperature at full load in open air, a fan is provided to keep air circulating around the magnet in the rather close confines of the test rig.

The laminate stack was wrapped with fiberglass insulating tape prior to the coils being wound. In addition, the coils are epoxy impregnated to improve resistance and heat transfer. The beginning and end of each layer are terminated on a terminal strip located on the side of the magnet to allow the winding configuration to be changed. As built, the windings are connected in series, which provides the greatest force for a given current. This configuration also has the highest inductance, which limits the dynamic response of the system, since the power amplifiers and power supply have a maximum output voltage of 160 volts. If higher frequency operation is required, the coils can be connected in series-parallel, and higher current amplifiers used. The provision for coil reconfiguration also enabled recovery when a short to the laminate stack developed in the left upper magnet windings. It was very straightforward to eliminate the shorted layer (30 turns) from the active coil.

The amplifiers selected for the loading system are Advanced Motion Controls Model 20A20 pulse-width modulated (PWM) amplifiers. The manufacturer's specifications for the 20A20 are as presented in Table III. This type of amplifier is generally selected rather than a liner amplifier for a magnetic bearing application as they are far less expensive, are more efficient (and hence much smaller) than a comparable linear amplifier, and are designed to operate with a very inductive load, such as that presented by the magnet windings. The primary reason for selecting this type of amplifier in this case was cost. Due to an inadvertent short which destroyed the amplifier for the top left coil during trouble shooting, this magnet is currently connected to a 10 amp linear power supply/amplifier.

There are several major drawbacks to these amplifiers. The first is electrical noise. These amplifiers operate essentially as a very high frequency switch, applying full voltage pulses of varying length at a high frequency to obtain the desired average current. The 20A20 amplifiers switch 160 volts DC on and off at 22 kHz. The high frequency spikes tend to couple into all of the sensors and instrumentation. The second drawback is spectral purity. The amplifier/coil combination is somewhat deficient in this regard at some current settings. Figure 23 presents the measured amplifier current power spectrum for a 25 Hz sine wave input. Figure 24 shows the spectrum of the corresponding measured dynamic load at the left magnet load cell. Figures 25 and 26, respectively, present the current and load power spectrums for the same input with a larger DC (average current) offset. Note that all of these figures present the data in decibels. As shown in the figures, significant amounts of energy at higher harmonics are present in the output at some current levels. These harmonic distortion problems can be corrected to some extent through careful iteration on the input signal to cancel-out the undesired harmonics, also closed loop operation of the loading system would improve the performance. However, the degree to which the higher frequencies can be eliminated is limited due to the maximum amplifier slew-rate due to the large inductance of the loading magnet coils. As the rig is not really suitable for dynamic testing, this issue should not really cause problems. A final problem with the amplifiers concerns stability. The amplifiers have a slight glitch at small time intervals at some current settings. This glitch results in load excursions of several Newtons. The exact source of the problem was not researched in great detail, beyond finding that changes to the amplifier internal current feedback loop could change the nature of this problem somewhat. The amplifier settings in use are a compromise between the severity of this problem and the dynamic response of the amplifiers. For future steady load testing, configurations which would reduce the frequency response, while improving stability, might be explored. However, the impact of these glitches on shaft position are fairly small, and could probably be ignored. Operating the controller in displacement mode probably also reduces the impact of these glitches.

The power supply for the amplifiers is an Advanced Motion Controls model PS16H160. This supply is a 1600 watt, 160 volt DC, unregulated supply. It should be adequate for any testing.

Table III - Advanced Motion Controls 20A20 PWM Amplifier Specifications

Parameter	Specification
Maximum Supply/Output Voltage	190 V
Maximum Continuous Current	± 10 amps
Peak Current	± 20 amps
Switching Frequency	22 kHz
Bandwidth	2.5 kHz

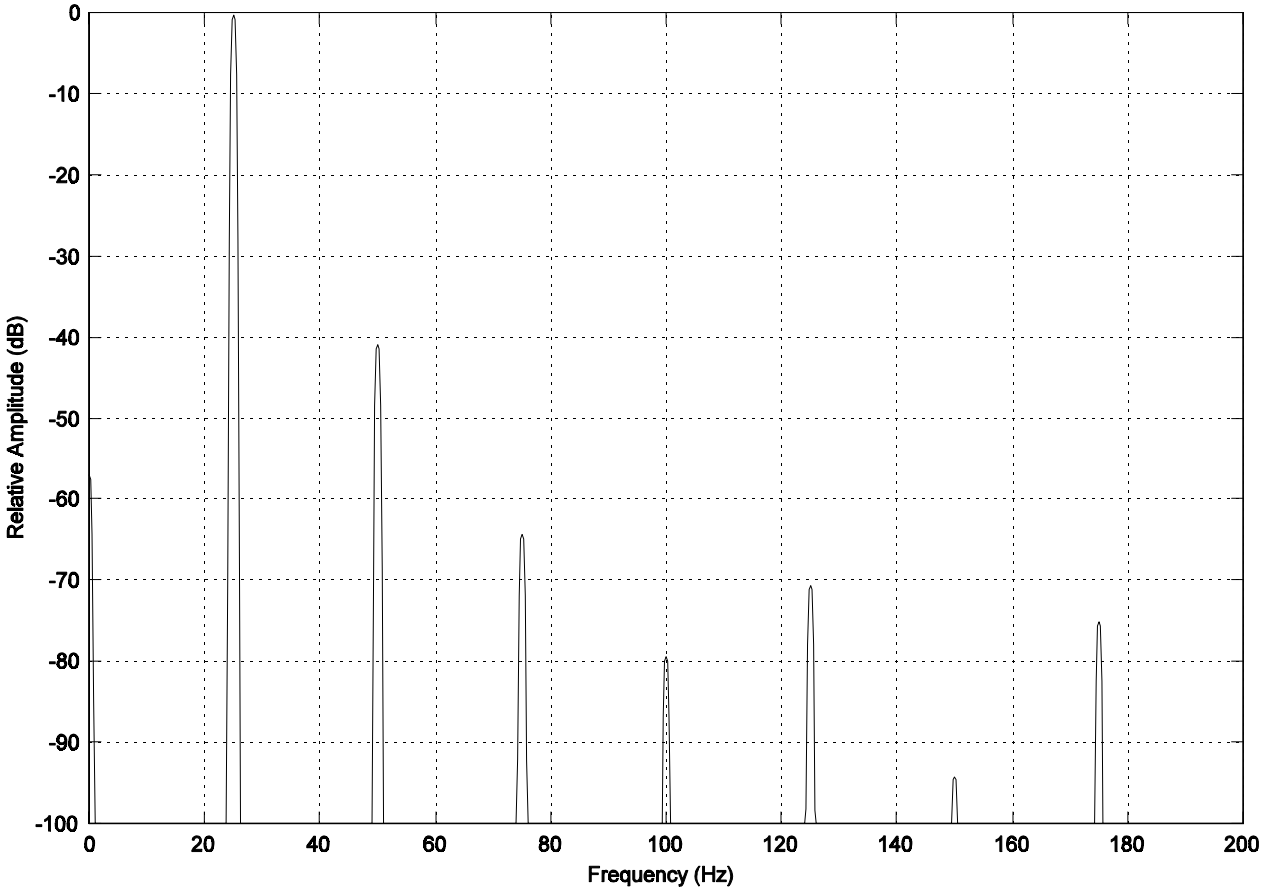

Figure 23 - 25 Hz Sine Excitation Current Power Spectrum 1 (4 Amps DC Current)

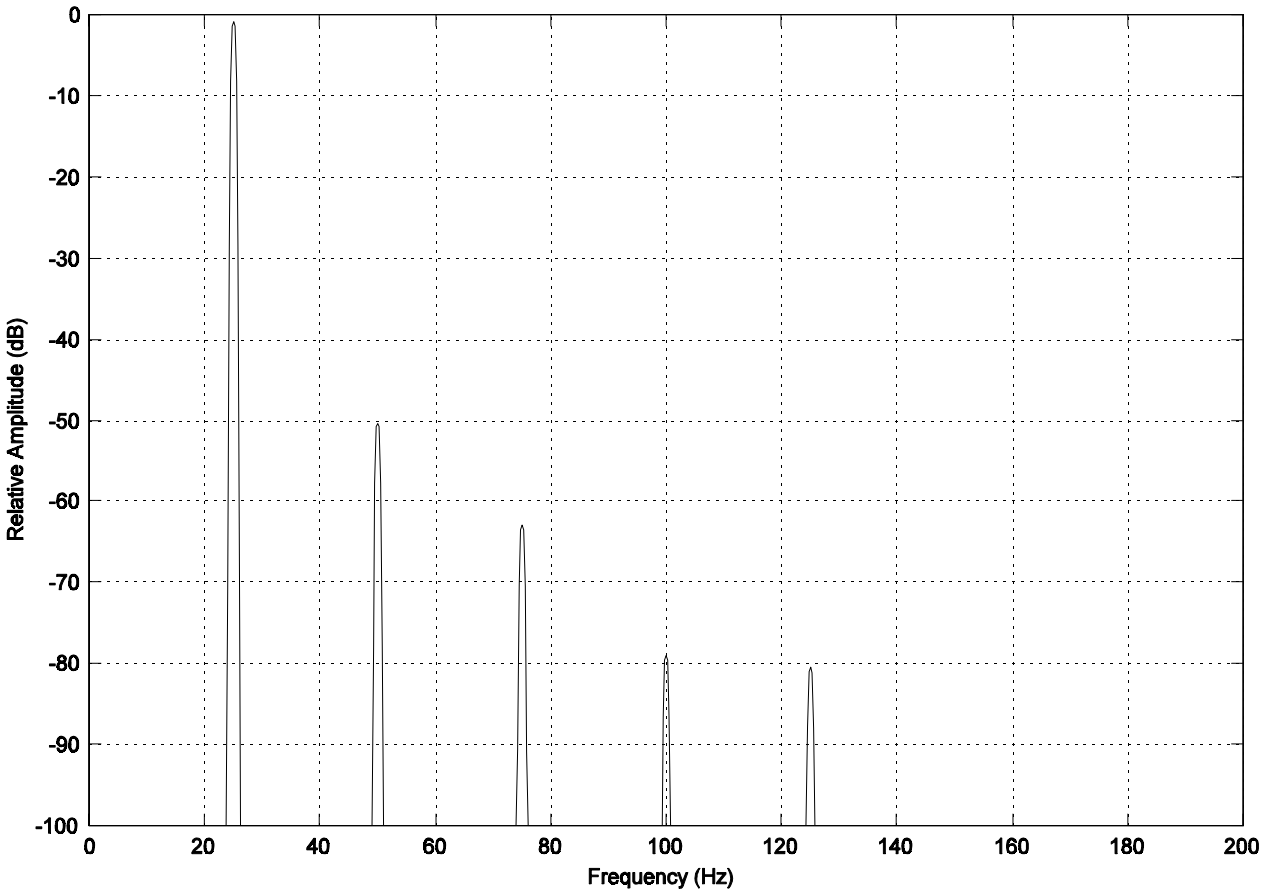

Figure 24 - 25 Hz Sine Excitation Left Magnet Load Cell Power Spectrum 1 (4 Amps DC Current)

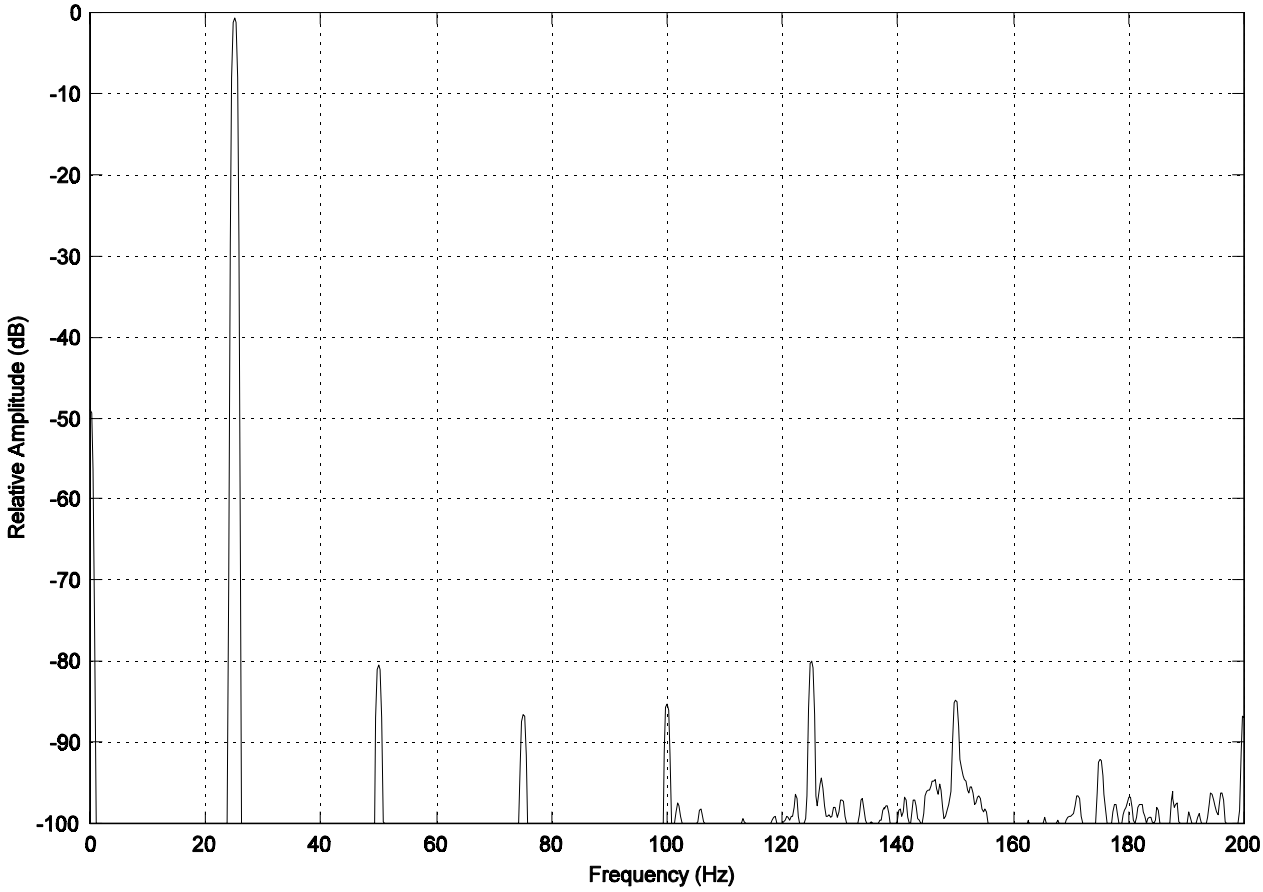

Figure 25 - 25 Hz Sine Excitation Current Power Spectrum 2 (8 Amps DC Current)

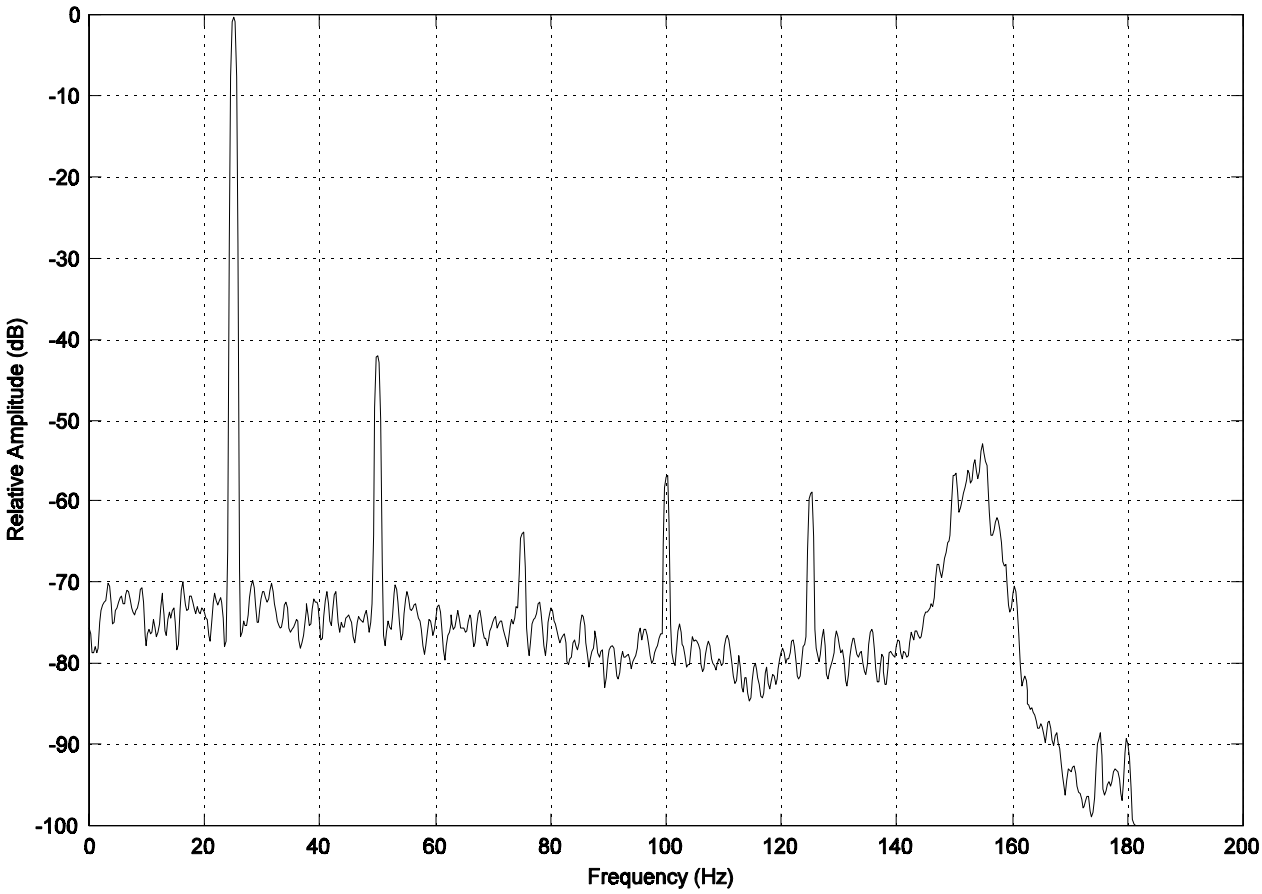

Figure 26 -25 Hz Sine Excitation Left Magnet Load Cell Power Spectrum 2 (8 Amps DC Current)

3.3 Test Rig Shaft

The shaft also must be considered as part of the actuator system. There are two basic issues associated with the shaft. The first is the dynamic behavior of the shaft as a means of transferring the magnet load to the test bearing. This issue will be discussed in a later chapter. The second concerns the shaft mechanical design required to accommodate the magnetic actuator. Since the shaft rotation within the magnets generates a changing magnetic field at the magnet location as the shaft rotates (see Fig. 27), eddy currents will be induced in the shaft. By replacing the outer portion of the shaft which is spinning in the magnetic field with thin, insulated, washer shaped pieces, the magnitude of the eddy-current losses can be significantly reduced. This technique is standard practice in magnetic bearings. The laminates used for this rotor are 107.95mm OD, 63.5 mm ID, 355 µm thick, M-19 silicon steel. Figure 28 shows the components used to allow the laminates to be mounted to the shaft at the magnet location.

The requirement for a laminated section, when coupled with the need for this shaft to be extremely stiff, made the design difficult. Typical magnetic bearing rotor lamination stacks are not required to carry a moment load. In this test rig, however, the laminated section was required to be able to carry a bending moment. To carry the moment load and maintain stiffness, the laminate stack is required to have a large axial preload to prevent the laminates from separating in the region of tensile stress due to the bending moment.

The need for an axial preload presented an assembly problem. The end piece has a heavy interference fit adjacent to the laminate stack, requiring it to be heated to approximately 250 degrees C to obtain enough clearance to go onto the shaft. As this part cooled, any axial preload obtained at assembly would have markedly decreased. Hence the interface piece (see Fig. 28) was cooled with liquid nitrogen prior to assembly. The shaft was then supported in a large hydraulic press, the hot end piece and cold interface piece were then rapidly dropped onto the shaft, and the press was pumped up to its maximum load of 200+ kN. This load was maintained as the temperatures equalized. Finally, the outer end of the end piece was welded to the shaft. Unfortunately, as will be discussed later, the shaft

currently behaves as if there is no axial preload. It is unclear if the assembly procedure did not work as desired, or if fretting wear between the laminates reduced the preload to zero.

In addition, due to growth of the disks from centrifugal forces at high speeds they must be assembled with a very precise interference fit on the shaft. This interference fit, unfortunately, causes the thin laminates to buckle into a dish shape. Despite the use of a hydraulic ram to press the laminates together while they were stacked on the rotor, some dishing still occurred. To accommodate the dishing, the interface piece was undercut and contoured to match the end of the laminate stack, as shown in Fig. 28.

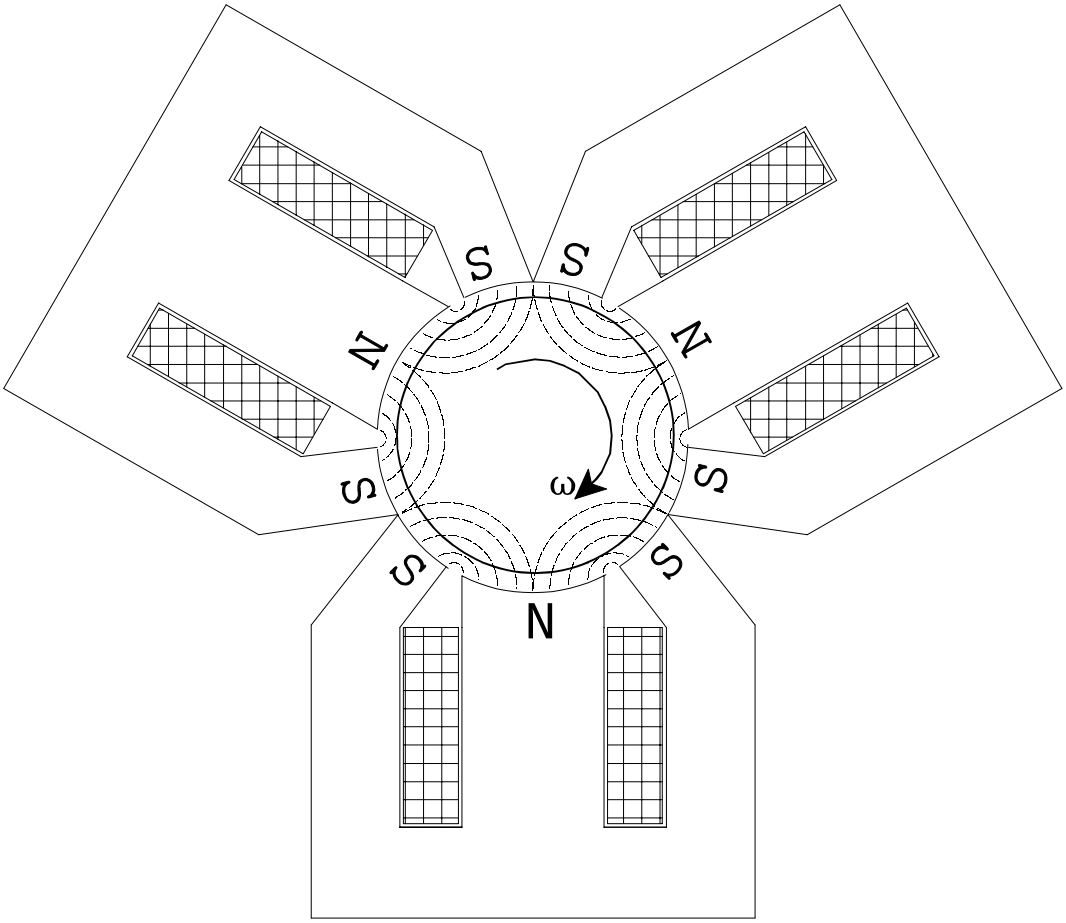

Figure 27 - Actuator Magnetic Fields

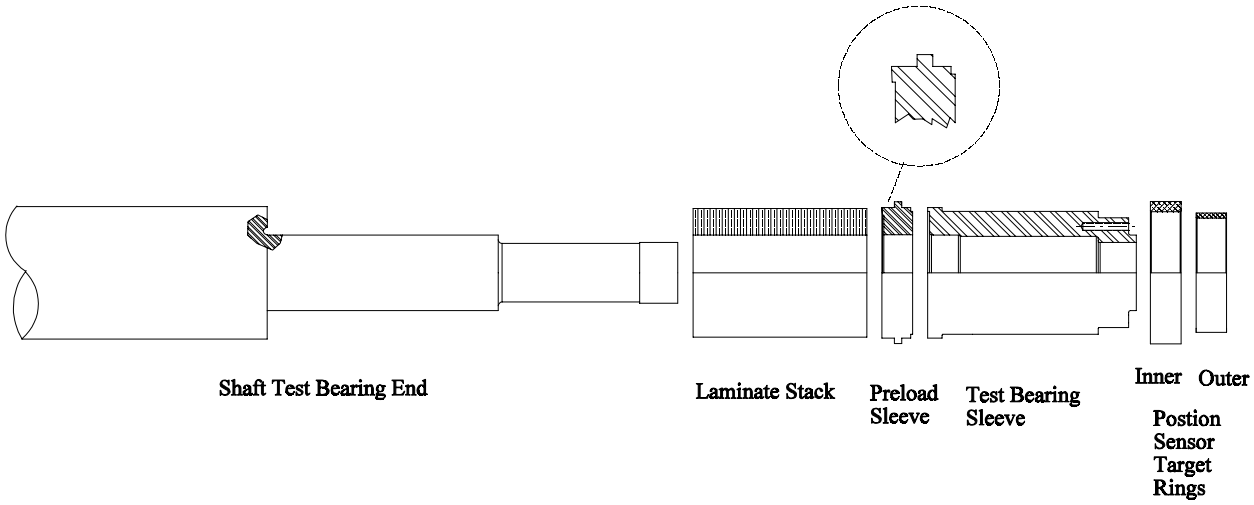

Figure 28 - Shaft Assembly

3.4 Magnet Assembly Load Measurement

3.4.1 Load Cells, Fixturing

As has been described, the original test rig design called for separate magnets, each mounted on a load cell (see Fig. 19). When the decision was made to move to a single piece magnet assembly, one of the goals was to re-use the low profile load cells supplied with the test rig if possible, as replacement precision load cells would be rather expensive. These load cells are low profile load cells, manufactured by GSE. The specifications are summarized in Table IV.

To enable the use of these load cells, a plus/minus forty-five degree orientation was selected so as to allow the load to be reacted by the relatively rigid base-plate. The resulting configuration has been shown in Fig. 17. To further increase the mount stiffness, a center support leg was added adjacent to the magnet mount location (center leg in Fig. 15). Since the load cells are single axis designs, the scheme shown in Fig. 17 was devised to allow for some compliance in the off-axis direction. This design uses two support rods at each load cell to give some torsional stiffness to the assembly, although minimal torque is expected from the loading magnets. To keep the magnet assembly from rocking or twisting, four additional axial restraint rods are provided to the housing end-plate as was shown in Fig 18.

The biggest problem with this mount design is the relatively low load cell stiffness, given the mass of the magnet assembly and desired excitation frequency range. The magnet assembly acceleration frequency response for impact loading of the assembly is as shown in Fig. 29. Figure 30 shows the corresponding measured transfer function between impact load and the load measured at the two load cells (traces overlaid). Ideally, this transfer function would be flat, with no phase shift. Due to the compliance of the load cells, there is a distinct resonance at approximately 161 Hz. The desired range of operation for this loading system was up to 500 Hz. Hence, it is not possible to use these load cells alone for either control or measurement of applied dynamic load over the full frequency range.

The difference between the load cell measurement and applied bearing load is, in fact, even more serious when the shaft dynamics are also considered. Figure 31 and Fig. 32 present the measured transfer function between the unfiltered right magnet load cell output and the two right side bearing load cells. The test rig was operating at 1000 RPM, with approximately 4225 N magnet down load. A random excitation on the bottom magnet and 50 averages were used to generate these plots. The transfer functions to the left bearing load cells are similar. All four transfer functions show a distinct null at the magnet assembly resonance, with a 180 degree phase shift. The narrow notch at approximately 212 Hz also appears in all four data sets. This notch is probably a bearing housing mode. As a result of these dynamic problems, the magnet load cells are only used to sense the magnitude of the static component of the load; all higher frequencies are filtered out. The motion at the resonance is dealt with by limiting excitation around this frequency to a value which will not damage the load cells or allow contact between the shaft and the magnet assembly.

Table IV - GSE 4650 Low Height Precision Load Cell Specifications

Parameter	Specification
Capacity (Tension/Compression)	8896 N
Non-Linearity	± 0.20% of full scale (±17.8 N)
Hysteresis	± 0.15% of full scale (±13.3 N)
Repeatability	± 0.05% of full scale (±4.4 N)
Mounted Stiffness	approx 6.6e7 N/m

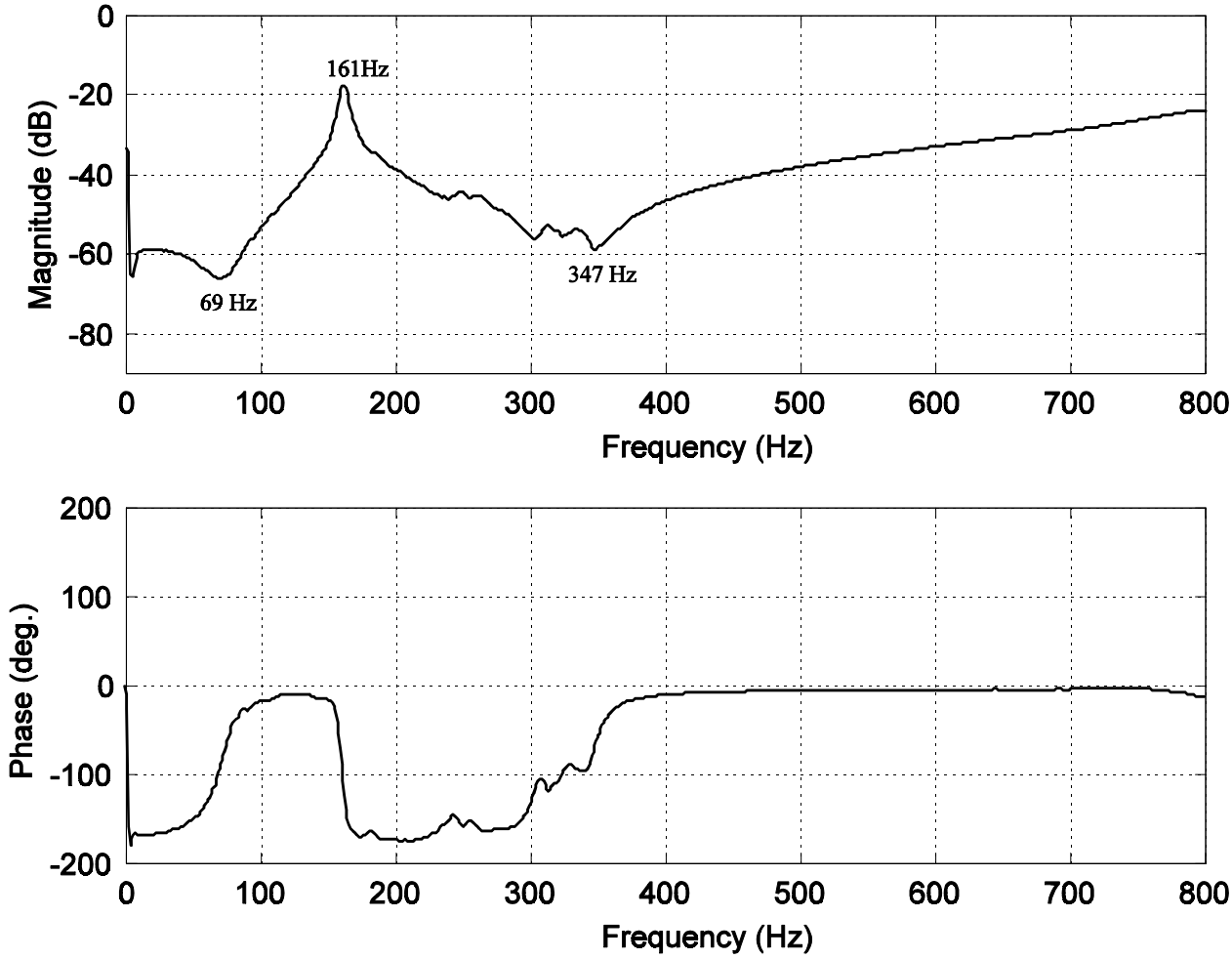

Figure 29 - Magnet Assembly Vertical Impact to Vertical Acceleration Frequency Response

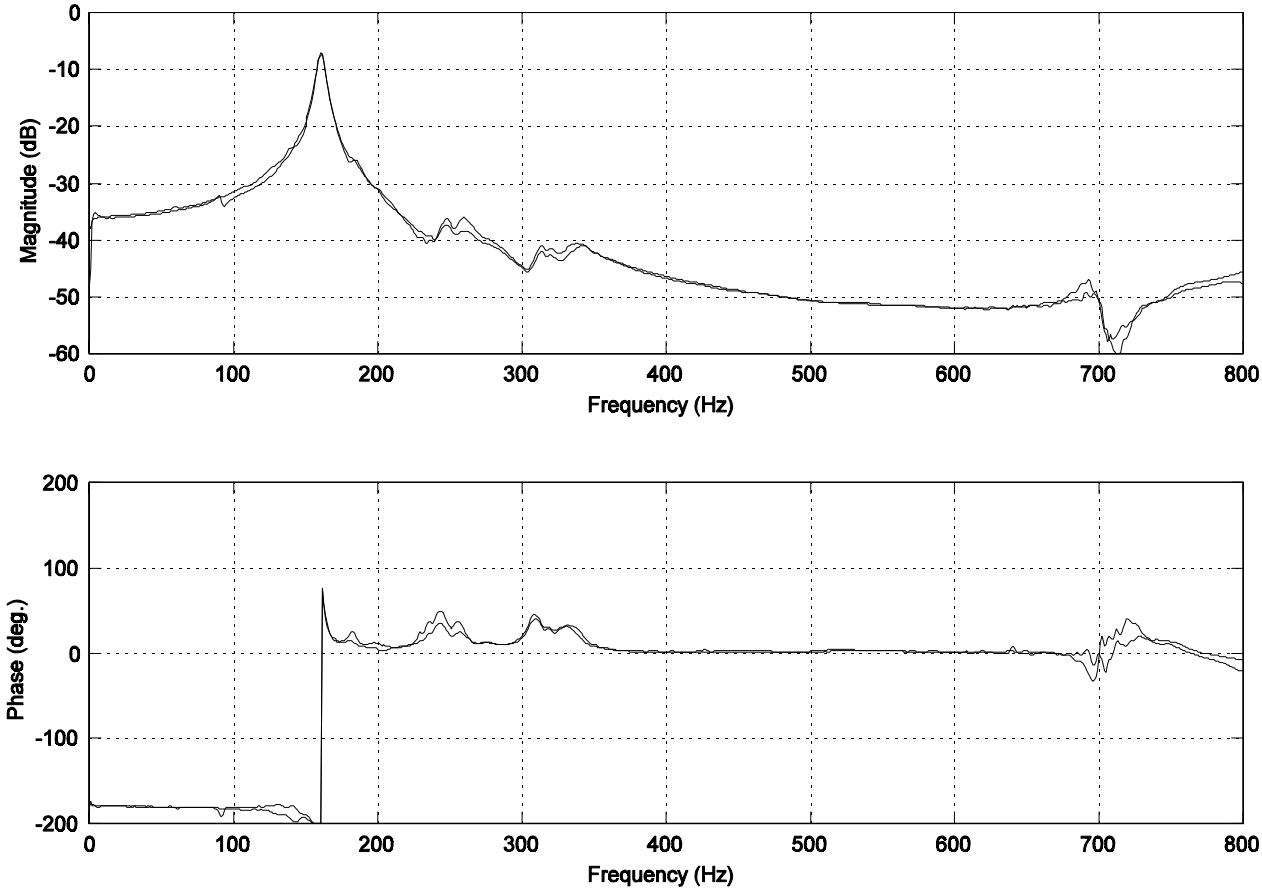

Figure 30 - Magnet Assembly Vertical Impact to Load Cell Frequency Responses

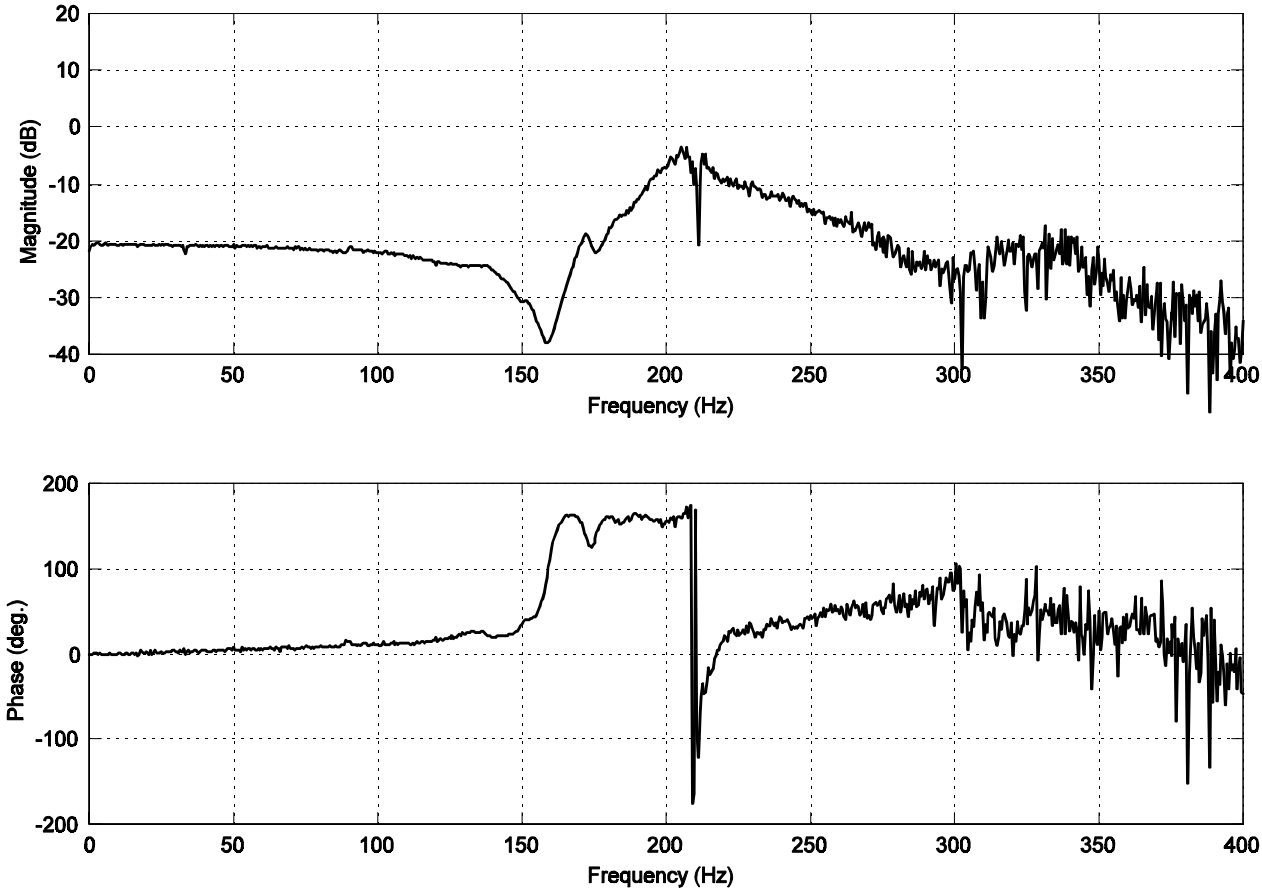

Figure 31 - Right Magnet Load Cell to Outside Right Bearing Load Cell Frequency Response

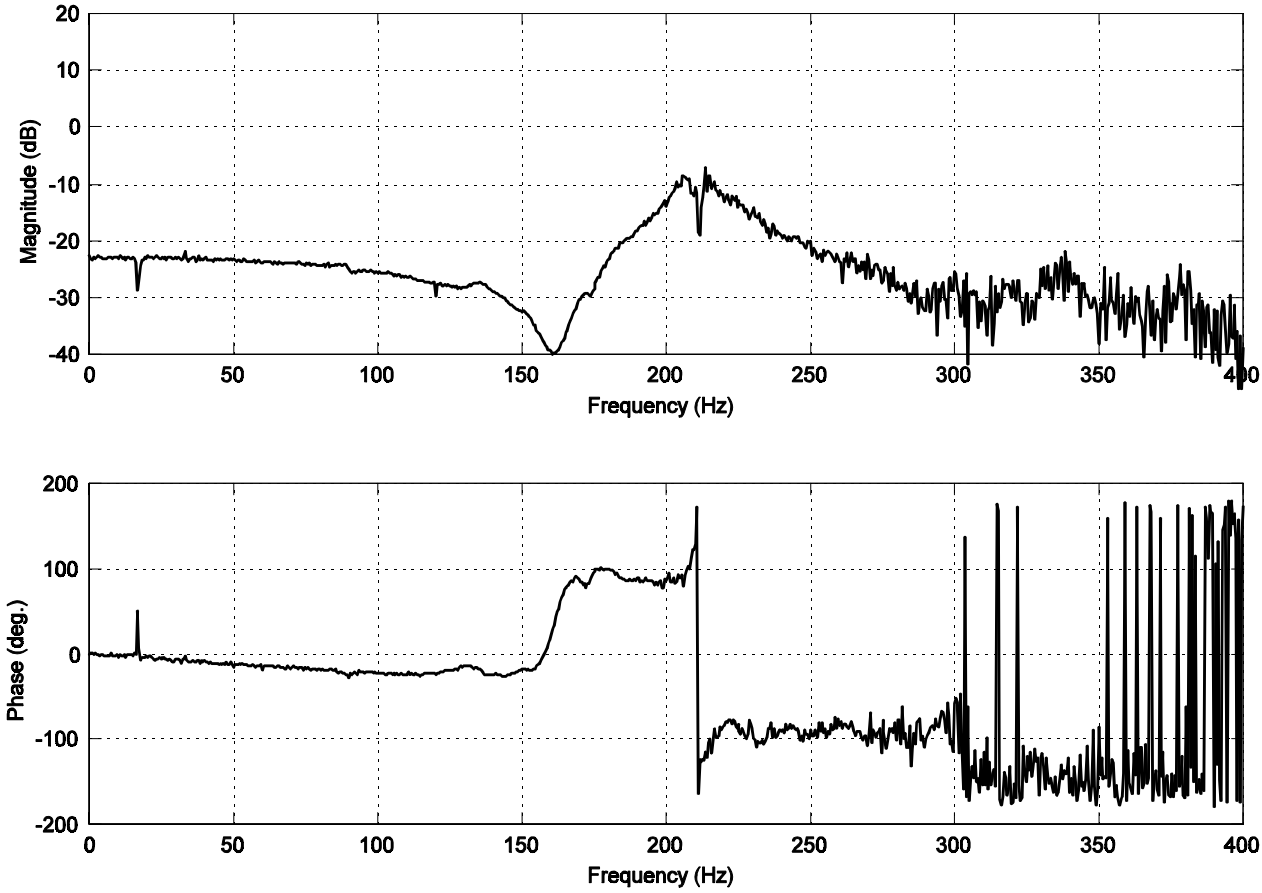

Figure 32 - Right Magnet Load Cell to Inside Right Bearing Load Cell Frequency Response

3.4.2 Load Cell Signal Conditioning

The signal conditioning system for the magnet load cells is based on a Calex Inc. model 160 MK resistive bridge signal conditioning module. This module provides the excitation voltage, amplification, and low-pass filtering for the load cell measurements. The specifications for this signal conditioner are as shown in Table V. The gain and offset voltage of this module can be varied to match the measurement system input range. This module has been augmented with a set of relays which provide (electrical) calibration inputs of zero, plus full scale, and minus full scale. These inputs are used to confirm the health and calibration of the signal conditioning and measurement system. As currently configured, these relays are manually activated by panel switches, but were designed to also allow for integration into a self-calibrating data acquisition system. Figure 33 presents a block diagram of the control system data acquisition system. The magnet load cell signal path is the bottom path.

Table V - Calex 160MK Load Cell Signal Conditioner Specifications

Parameter	Specification
Gain Range	100 V/V to 500 V/V
Gain Thermal Drift	75 ppm/°C (typical)
Offset Thermal Drift	± (4 + 100/gain) µV/°C
Non-linearity	0.002% (typical)
Low pass Filter Cut-Off	10, 100, 1000 Hz (selectable)
Low Pass Filter Roll-Off	40 dB/Decade (2 pole)
Common Mode Rejection (DC - 60 Hz)	140 dB
Maximum Output Voltage	± 10 V
Bridge Supply Stability	.05%/24 Hrs
Bridge Supply Thermal Drift	40 ppm/°C (typical)

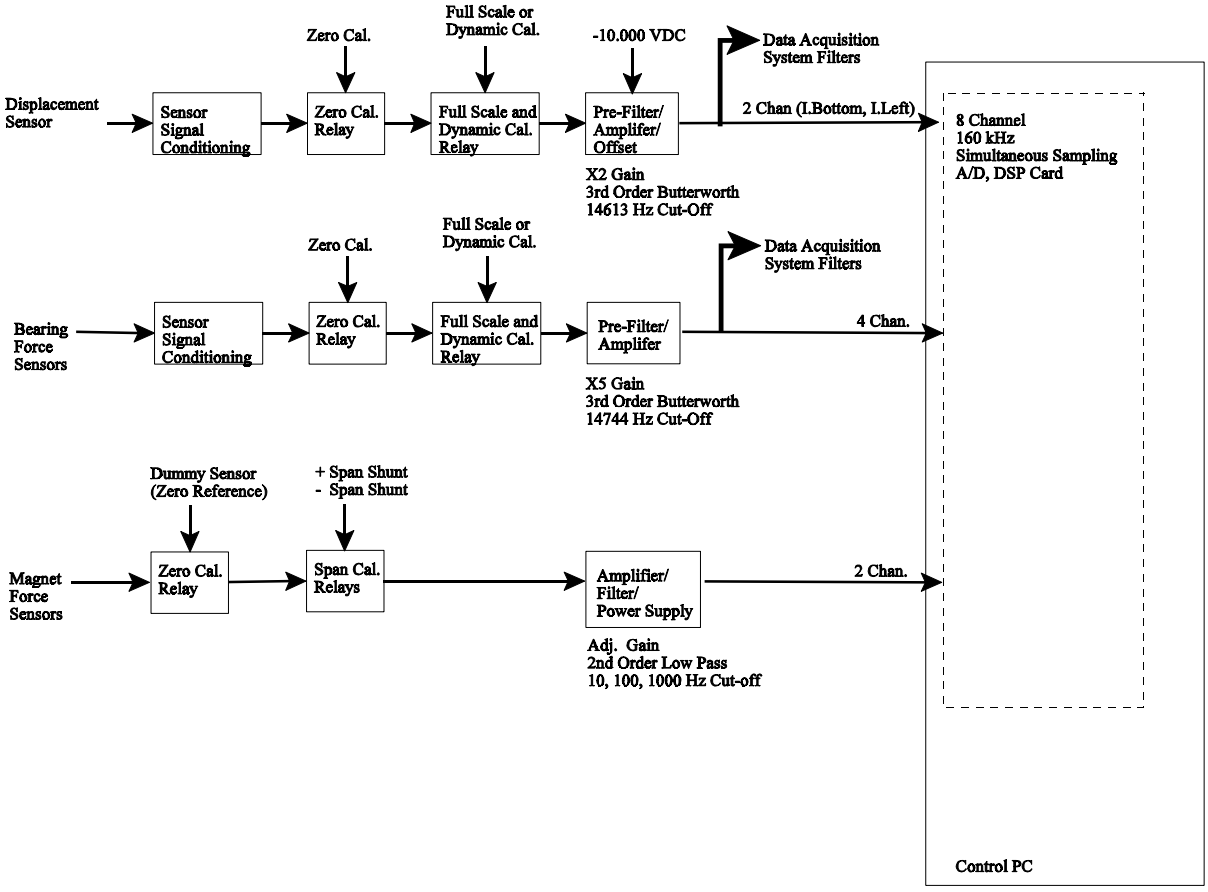

Figure 33 - Control System Signal Conditioning

3.4.3 Magnet Control System

The PC based, digital magnet control system is based on a Data Translation model DT3808, high speed digital signal processing board. The specifications of this board are as shown in Table VI. This board combines analog input, a digital signal processor and support hardware, and analog as well as digital outputs, thus allowing a complete digital control system to be implemented with a minimum of external hardware. Unfortunately, the board only has two analog outputs and three are needed to control the magnets, so an external board with digital to analog converters was fabricated. This custom board is built around three Analog Devices AD660AN's Digital to Analog (D/A) converters. These chips are configured to read a serial data stream from the DT3808 dynamic digital output port, and output three 16 bit resolution analog command signal to the PWM amplifiers. This board does not include the reconstruction (anti-image) filters generally required for a high speed D/A converter. Instead the low-pass characteristics of the amplifiers and the higher output rate of the D/A system are used to prevent image problems (2.5 kHz amplifier 3 dB vs 8.192 kHz D/A output rate). The input filtering provided for the displacement sensors is a bit marginal in terms of anti-aliasing protection, but the system works.

Table VI - Data Translation DT3808 DSP Data Acquisition System Specifications

Parameter	Specification
Number of Inputs	8, Simultaneously Sampled, Differential
Resolution	16 bit
Maximum Acquisition Rate/Channel	20 kHz (for 8 channel samples)
Accuracy	0.012%
Input Voltage	± 10 Volts
DSP Processor	TMS320C40, 40 MHz

3.4.4 Magnet Control Algorithm

The control system is based on a traditional proportional-integral-derivative (PID) approach. This algorithm was selected for its simplicity, and an expectation that it could be made to function without extensive system modeling and cost in development time. In addition, the bulk of active magnetic bearing systems the author is familiar with are operating successfully with a PID algorithm or something very close to it. As implemented, the algorithm also includes a linearization step. This is a third-order curve fit correction for the non-linear current versus load characteristics of the magnet resulting from the theoretical proportionality between force and current squared, as well as the nonlinear flux density versus applied field characteristics of silicon steel. The linearization is included as an attempt to reduce some of the harmonic distortion in loading when two or all three magnets are required to be active to create a particular excitation. For the case of steady loading, the PID algorithm and current allocation strategy are sufficiently robust for good performance to be possible without the linearization step. The algorithm also allows the user to set a DC bias for all three magnets, which will also tend to improve linearity.

3.4.4.1 Displacement Mode

With the system operating in displacement mode (magnetic bearing mode), a block diagram of the system is as shown in Fig. 34. The linearization step is not shown in this figure. The algorithm runs on the DSP controller at an input sample rate of 16384 Hz, using a two sample average for an effective sample rate of 8192 Hz. The loop output rate is 8192 Hz. Each output to the D/A board consists of a 34 element long serial data stream consisting of data, clock and update command information. This data stream is sent at 278528 Hz. Shaft excitation is provided for in the software by summing an excitation signal with the measured displacement prior to computing the control loop error. For reasons which have not been explored, this control algorithm is not stable without some damping at the test bearing. The most likely cause is a combination of the noise present at the system input, phase loss though the PWM amplifiers, and the shaft/magnet dynamics. It is also possible that the instability is the result of inappropriate controller gains, since very little tuning effort was expended. Initial attempts to increase the damping by increasing the derivative gain were not very successful. With an operating bearing, however, there is enough damping in the system for stable

operation. This is true even with a very lightly loaded bearing. As any testing would involve the presence of a test bearing, minimal effort was expended tuning the system for levitation without a test bearing.

The host program running on the PC communicates with the DSP system to allow the user or test control software to change the setpoints (horizontal and vertical position), as well as controller gains. Two types of setpoint are communicated for each axis. The first is the average setpoint, which represents the equilibrium position desired. The second is the vector of perturbations about this equilibrium position for excitation. As currently implemented, vectors of 8192 perturbation values for each axis are accommodated. These vectors correspond to one second of excitation, and are intended for use in bearing coefficient identification. This approach allows for closed loop control of the excitation. The DSP system also communicates low-pass filtered horizontal and vertical measured positions and magnet load back to the host computer.

3.4.4.2 Force Control Mode

The system could be operated in a force feedback only mode by substituting the output of the magnet load cells for the displacement probes used in the displacement mode, and running the magnetic bearing without any bias current (to reduce problems with the negative stiffness). Since both displacement and force measurements are supplied to the DSP card, this would simply be a minor change in the software. This approach could be preferred for future testing which operates the bearing in a stable region of operation. The available bandwidth, however, would be restricted due to the magnet assembly resonance at 161 Hz. This restriction would not be a problem for steady load testing.

3.4.4.3 Hybrid Control Mode

For dynamic testing, or testing with lightly loaded bearings operating without enough load for stability, a hybrid force-displacement mode was developed. As shown in Fig. 35 this mode consists of an inner displacement loop running as described above. Around this loop there is a second, lower speed control loop which adjusts the displacement setpoint as required to obtain a desired static load.

This approach works well. It also works with displacement perturbation excitation active, provided that the lowest excitation frequency is somewhat larger than the high frequency cut-off for the force measurement so as to provide a frequency separation between the passbands of the two control systems. In the case of a lightly loaded bearing, which would otherwise be unstable, the system also seems to work well, with the displacement feedback system providing stabilization.

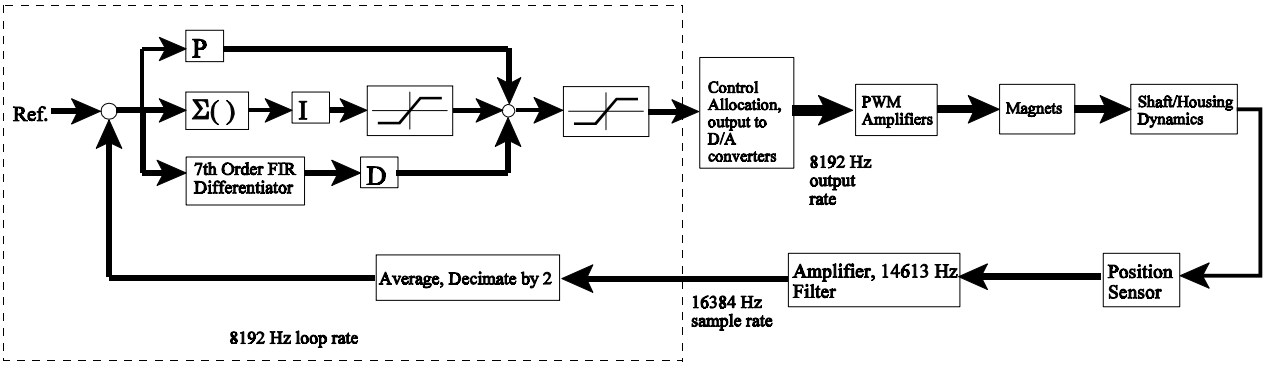

Figure 34 - Magnet Displacement Mode Control

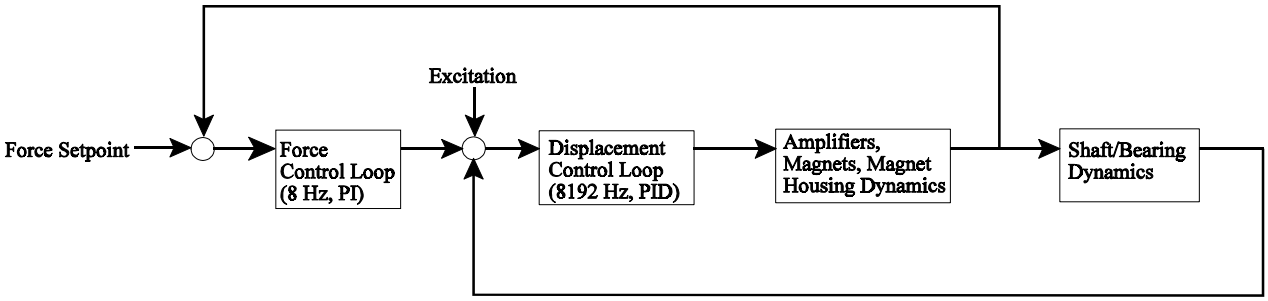

Figure 35 - Hybrid Force/Displacement Control Mode

3.5 Measured Magnet System Characteristics

To confirm that the magnet control system is functioning as desired, both step responses to a vertical load setpoint change, and steady-state responses were recorded. Figure 36 presents the closed-loop force/displacement hybrid mode step response with a typical test bearing operating at 1500 RPM. Figure 37 presents the steady-state response for this operating condition. The results presented are typical of results for other speeds and loads. These two figures indicate that the system functions well. The step response is well damped and sufficiently quick for the testing planned. The steady-state response, while not perfect, is also adequate for the testing planned.

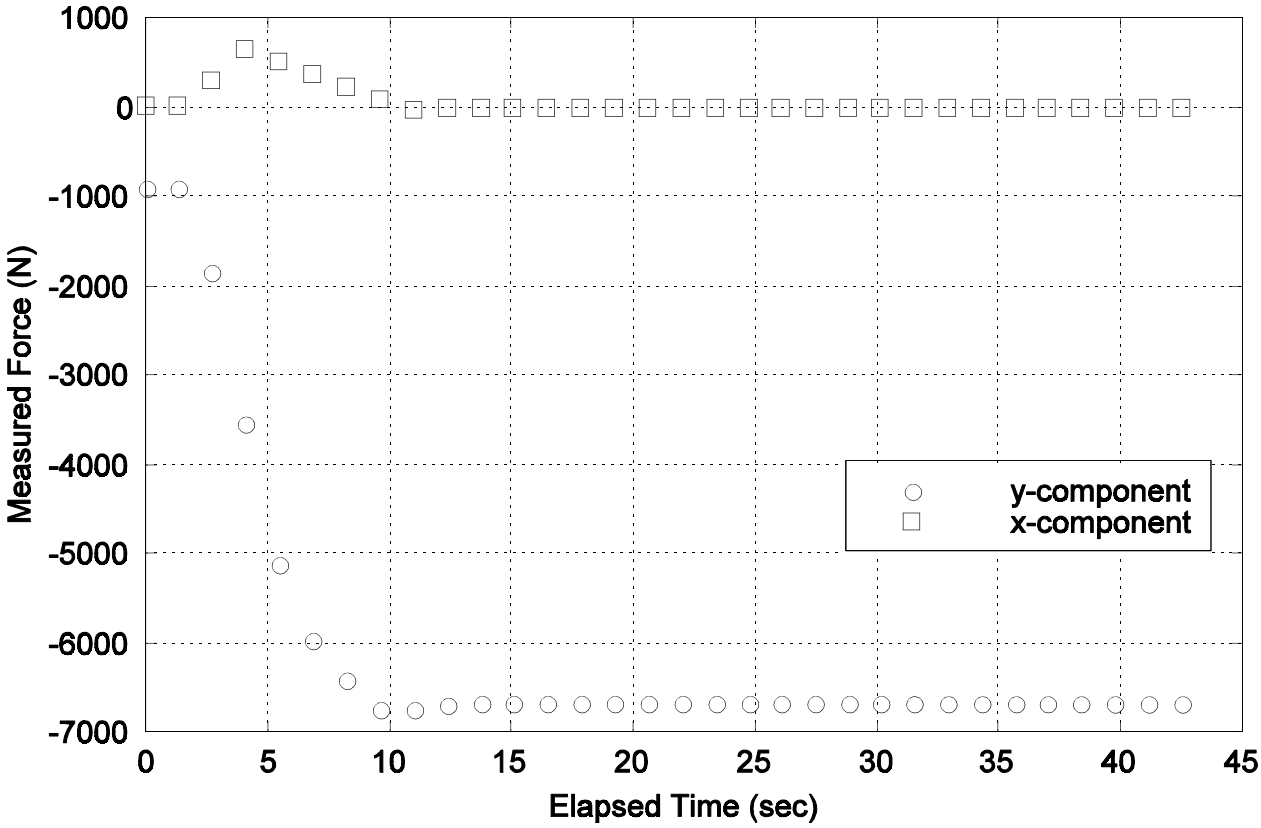

Figure 36 - Magnet Load Step Response

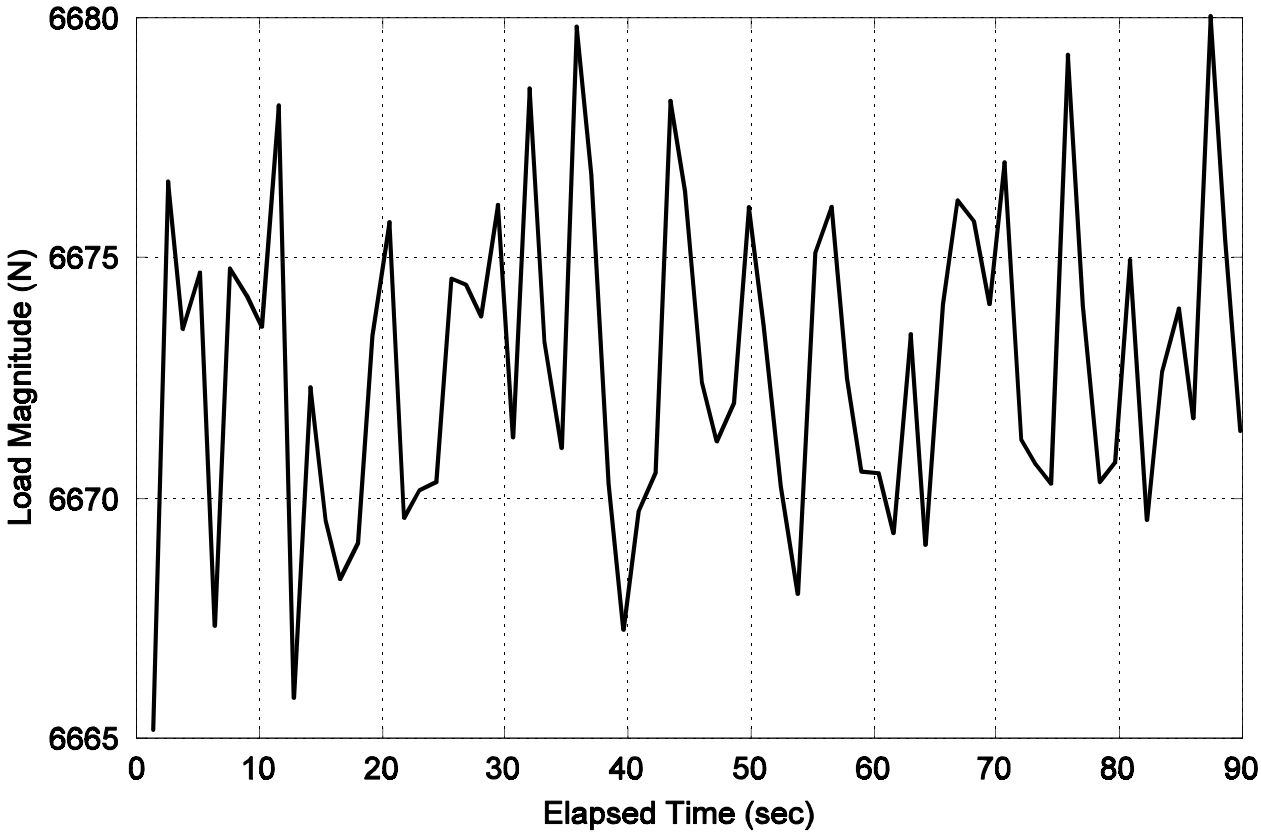

Figure 37 - Magnet Load Steady-State Response

Chapter 4

Test Bearing System, Hardware, Instrumentation and Software

4.1 Introduction

The test bearing holder and mount, shown in Fig. 38 and Fig. 39, provides a mounting location for the test bearing inserts, a system to provide oil to the test bearing, a mounting location for the test bearing shaft position sensors, and a means to measure the load applied to the test bearing. This chapter will discuss each of these functions, except for the oil distribution system, which is discussed in chapter five.

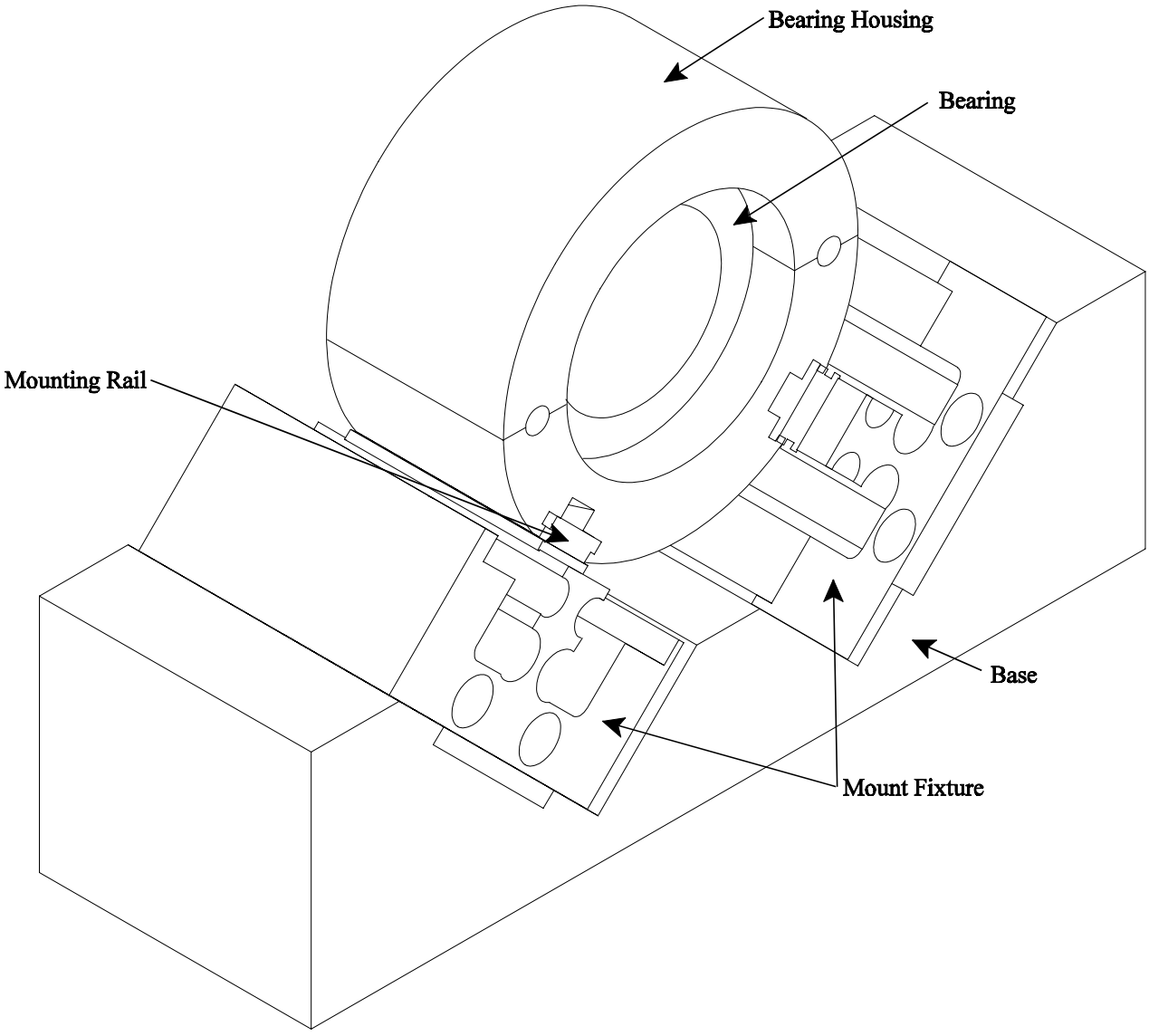

Figure 38 - Test Bearing Mount, Overall

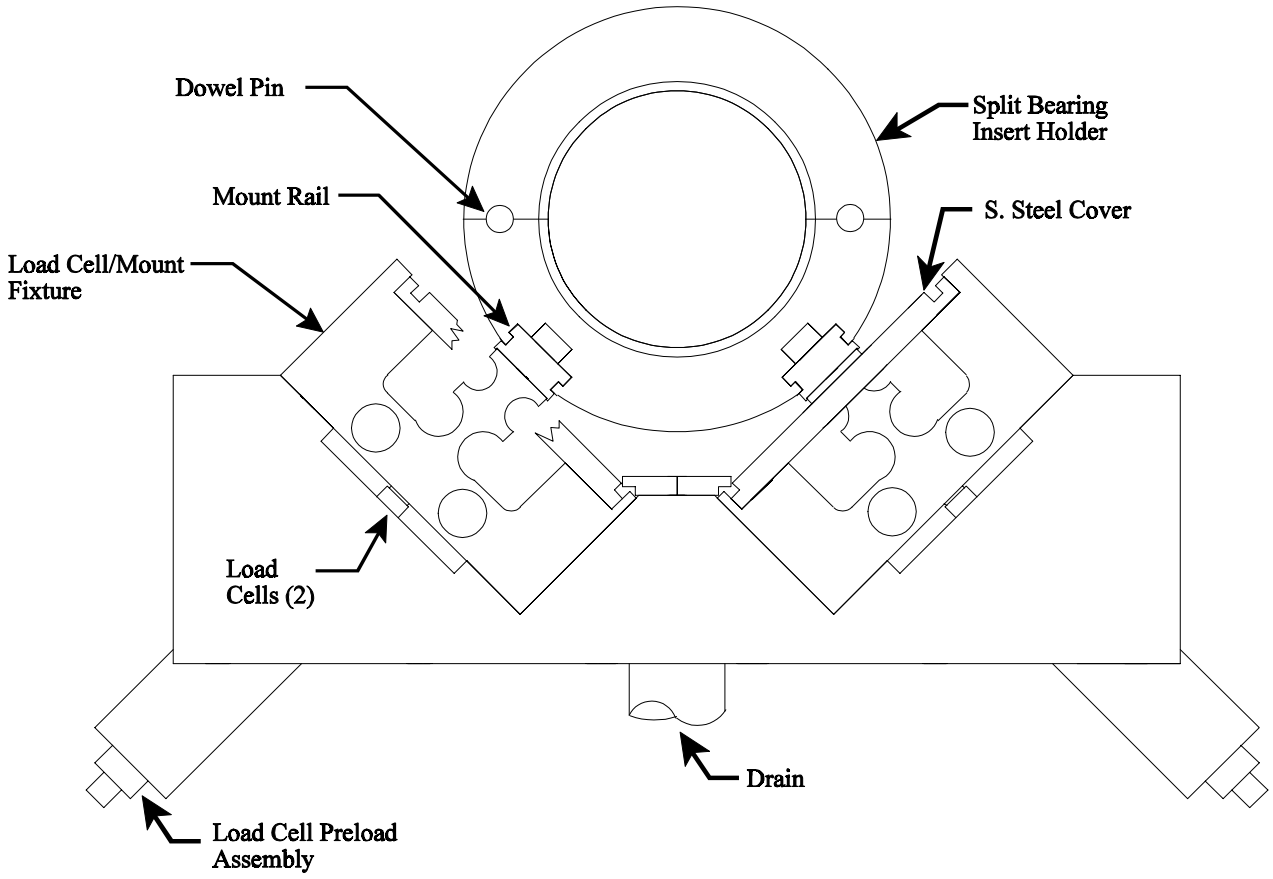

Figure 39 - Bearing Mount, Front View

4.2 Test Bearings

The test bearings are one piece, cylindrical inserts. The bore of the insert is machined to the particular bearing geometry under test. Depending on the goals of the test, the insert could have up to 15 embedded thermocouples, as well as passages for up to 14 pressure taps (these numbers represent the current data acquisition system capacity). Table VII lists the eight bearing insert designs currently available.

With the exception of the last bearing listed, all these bearings have been donated by Rotating Machinery Technology, Inc.

Table VII - Test Bearing Inserts

Bearing Type and Construction	Instrumentation
Two Axial Groove, Steel/Babbitt	Thermocouples and Pressure Taps
Two Axial Groove, Bronze/Babbitt	Thermocouples and Pressure Taps
Two Axial Groove, Aluminum	Limited Thermocouples
Three Axial Groove, Steel/Babbitt	Thermocouples and Pressure Taps
Double Pocket, Steel/Babbitt	Thermocouples and Pressure Taps
Pressure Dam, Steel/Babbitt	Thermocouples and Pressure Taps
5 Pad Tilting Pad with Various Oil Feeds	Thermocouples in Pads
5 Pad "Tilting Pad" made by Glacier Metal Co (pads actually rock)	None

4.3 Bearing Housing

Figure 41 presents a section view of the bearing housing with a bearing insert installed. The inside diameter of this housing is bored to match the outside diameter of the bearing inserts, and has a locating shoulder designed to center a 57.2 mm long test bearing insert between the displacement and force sensors. Four retainers are used to press the bearing insert firmly against the inner shoulder of the housing to maintain a consistent axial bearing location, as well as to accurately locate the top half of the bearing housing in an axial direction. The housing is split horizontally, to allow the bottom half of the housing to be very carefully located in the rig, then left undisturbed as bearing inserts are changed. The housing also has dowel pins in the horizontal split as indicated in Fig. 39 to ensure repeatable assembly. Very rapid change-over is possible with this design. A test bearing can be replaced and the shaft alignment reset in about 30 minutes. The housing also has a central, circumferential oil delivery passage to accommodate a variety of bearing oil feed configurations. The existing housing is fabricated from AISA 4140 steel, with a thin inner lining of epoxy filled with titanium powder as described below.

To allow for easy housing installation and removal, the housing attaches to two slide mount rails as shown in Fig. 40. The design provides an inner and outer clamping location on each side, with front access to the clamping bolts. Although this design makes it fairly easy to assemble the housing to the test rig, the presence of these slots, along with improper fabrication techniques by the machine shop selected to manufacture the part resulted in an out-of-round housing as received. The acceptance inspection suggests that the piece was bored to size, then the slots were cut. The internal stresses released by cutting the slots were sufficient to make the housing out of round by about 100 µm. The groove perpendicularity error was also noticeably larger than the specification on the print. To correct the geometry defects, the part was stress relieved, the bore machined oversize by approximately 1.5 mm, and coated with a thick coating of an epoxy which is heavily loaded with titanium powder and recommended for this application . The bore was then machined back to the correct diameter. Due to the abrasive nature of the powder filling, diamond tooling was required for the final few cuts. As there was no easy way to correct the distortion in the grooves, these were left as is, and the compliance in the mount fixturing used to accommodate the slightly incorrect geometry.

The housing also has fifteen embedded thermocouples permanently installed to provide data on thermal boundary conditions. These Type K thermocouples are located as shown in Fig. 42. To allow measurement of actual feed pressure, a pressure tap has been drilled through to the oil feed passage.

The housing and slide mounts are bolted to a specially designed fixture which interfaces with the load cells used to measure the bearing load (see Fig. 39). This mounting surface is also used by another similar split housing designed to accommodate a five-pad tilting pad test bearing. These fixtures are designed to provide a means of isolating off-axis loads from the load cells, which are sandwiched between the interface piece and the base piece. Conceptually, this cross-section consists of a pinned-pinned beam section and a lateral/moment restraint section (see Fig. 43). The top part provides compliance to tangential forces, while maintaining a high stiffness in the direction of the sensed load. The lower section, provides restraint against tangential and moment loads to ensure that the load actually applied to the load cell is only the desired bearing radial load. The cross section of the interface piece is the result of consideration of fabrication costs. It was built from a single piece of stress relieved material with a straightforward combination of drilling and milling, followed by final precision surface grinding on the top and bottom surfaces.

The test bearing load cells are PCB Piezotronics 200A05 voltage mode, piezo-electric, compression load cells with matching PCB power supplies. The specifications of these load cells are as shown in Table VIII. These load cells were selected in part because of availability at the lab, but more importantly due to their extremely high axial stiffness, approaching that of a solid piece of steel. Two pairs of these load cells are used at plus and minus forty-five degrees as shown in Fig. 44, for a total of four load cells. In principle, this arrangement allows sensing both the applied radial loads, as well as the applied moments (two) at the bearing. These load cells are mounted in a preloaded arrangement, with about 13 kN of axial preload provided by a soft (relative to the load cells) spring arrangement as shown in Fig. 45 .

The load cells and interface fixtures mount to a single piece base. This base was cut to shape from a piece of stress-relieved A36 steel plate in a large traveling wire, electrical discharge machine. The single piece design was selected to provide an extremely rigid and accurate mounting surface for the load cells. The mount assembly is securely bolted to the test rig baseplate, directly over the front mounting leg, thus providing a very rigid reaction surface. The components of the entire assembly are drilled and reamed for precision dowel pins to allow for repeatable assembly.

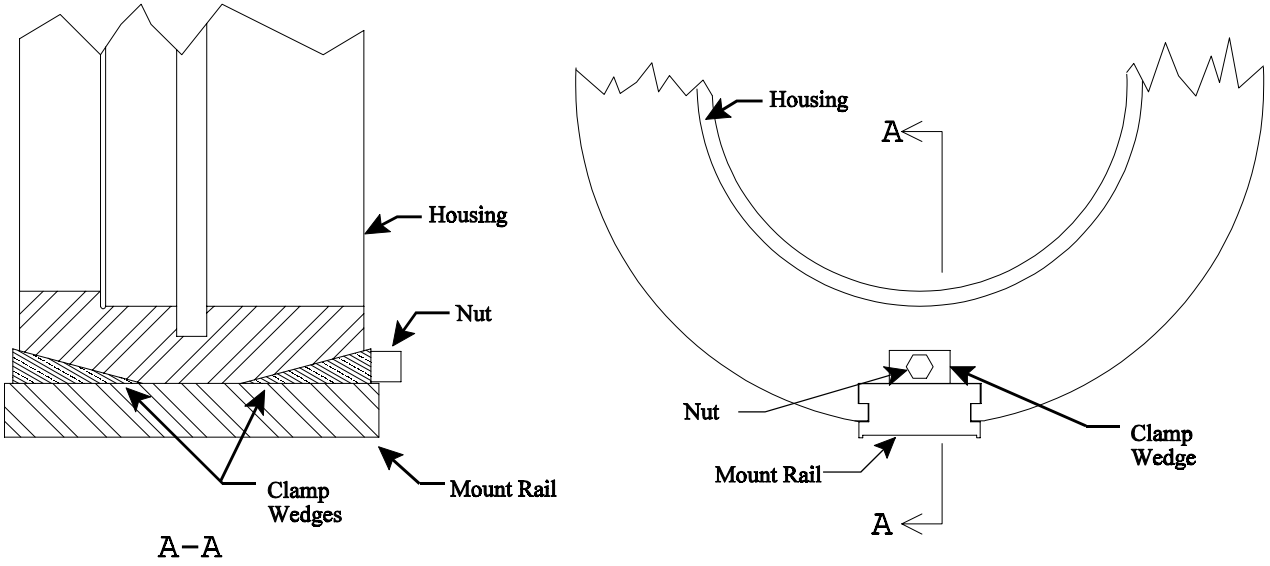

Figure 40 - Test Bearing Holder Mount System

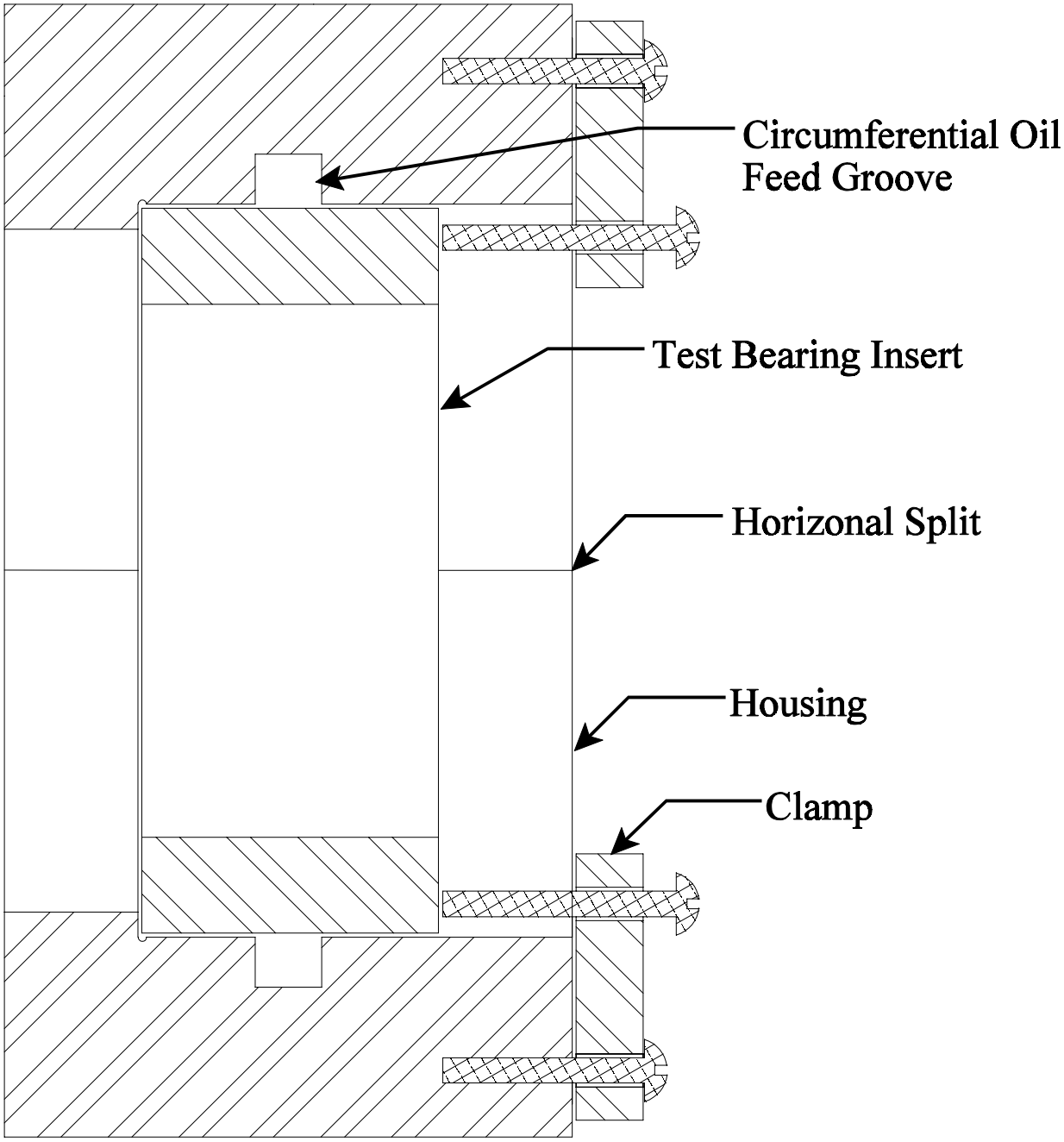

Figure 41 - Housing/Test Section

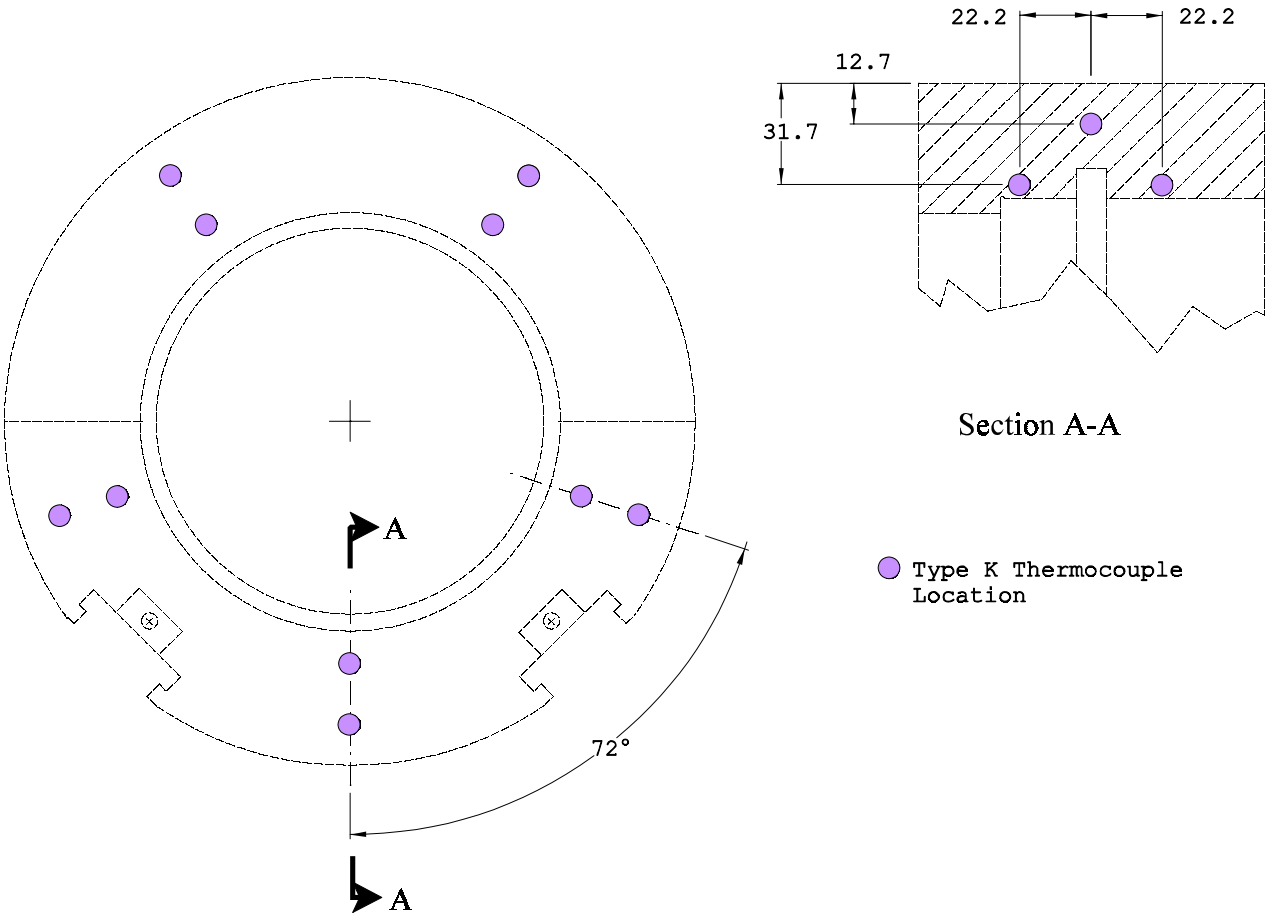

Figure 42 - Housing Thermocouple Locations

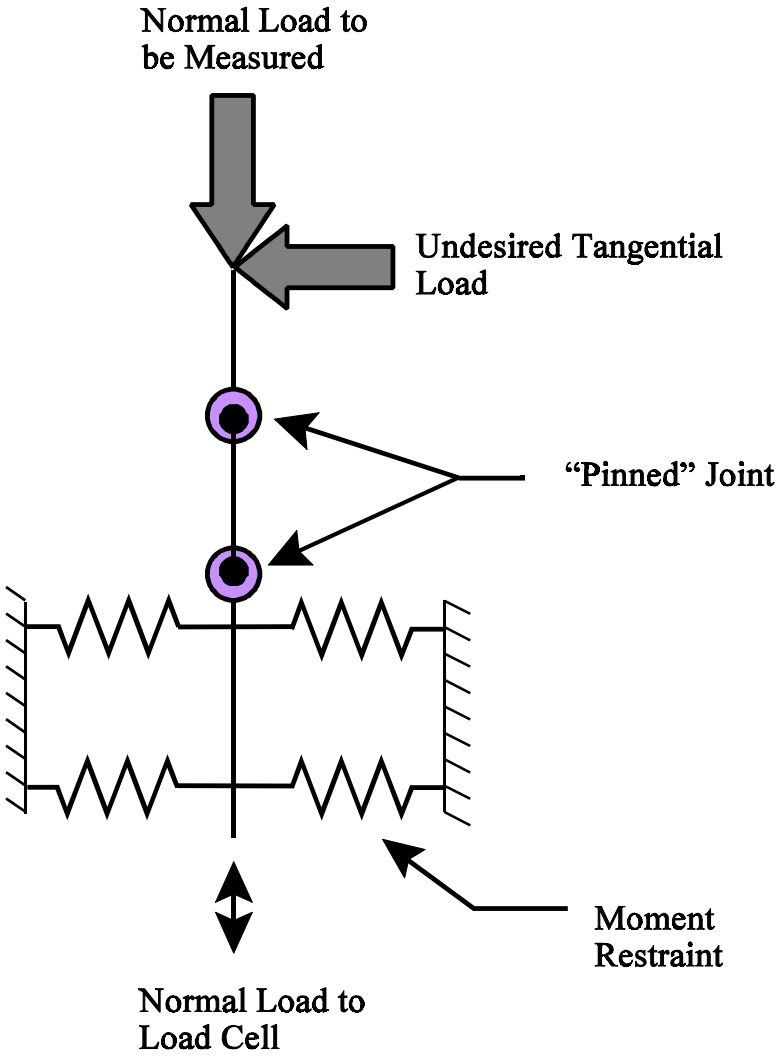

Figure 43 - Load Cell Fixture Concept

Table VIII - PCB Piezotronics Model 200A05 Force Transducer Specifications

Parameter	Specification
Range (Compression only)	22240 N
Maximum Compressive Load	44480 N
Resolution	0.8 N
Sensitivity	0.22 mV/N
Discharge Time Constant	2000 sec
Stiffness	1.75×10^{10} N/m
Linearity	1% of full scale calibration

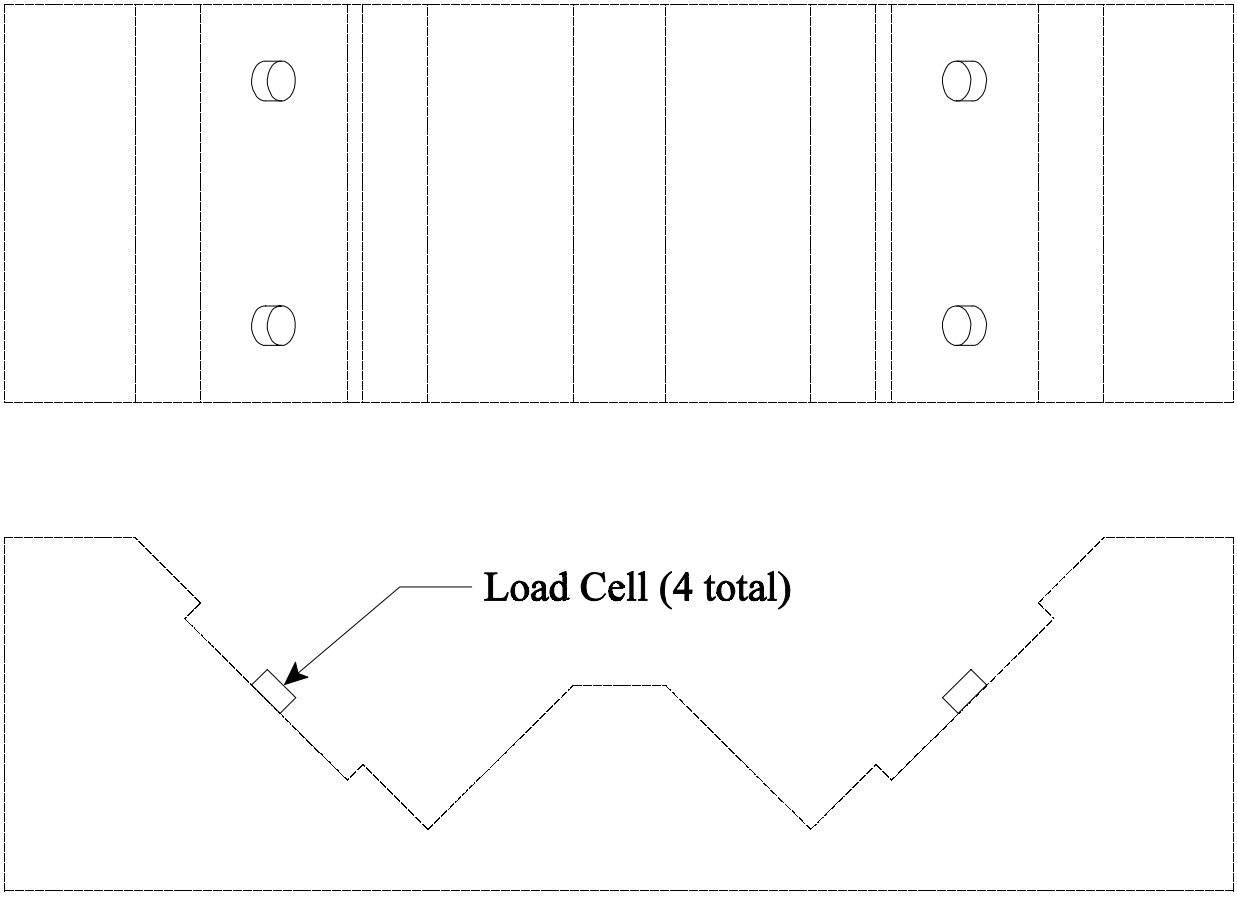

Figure 44 - Test Bearing Load Cell Locations

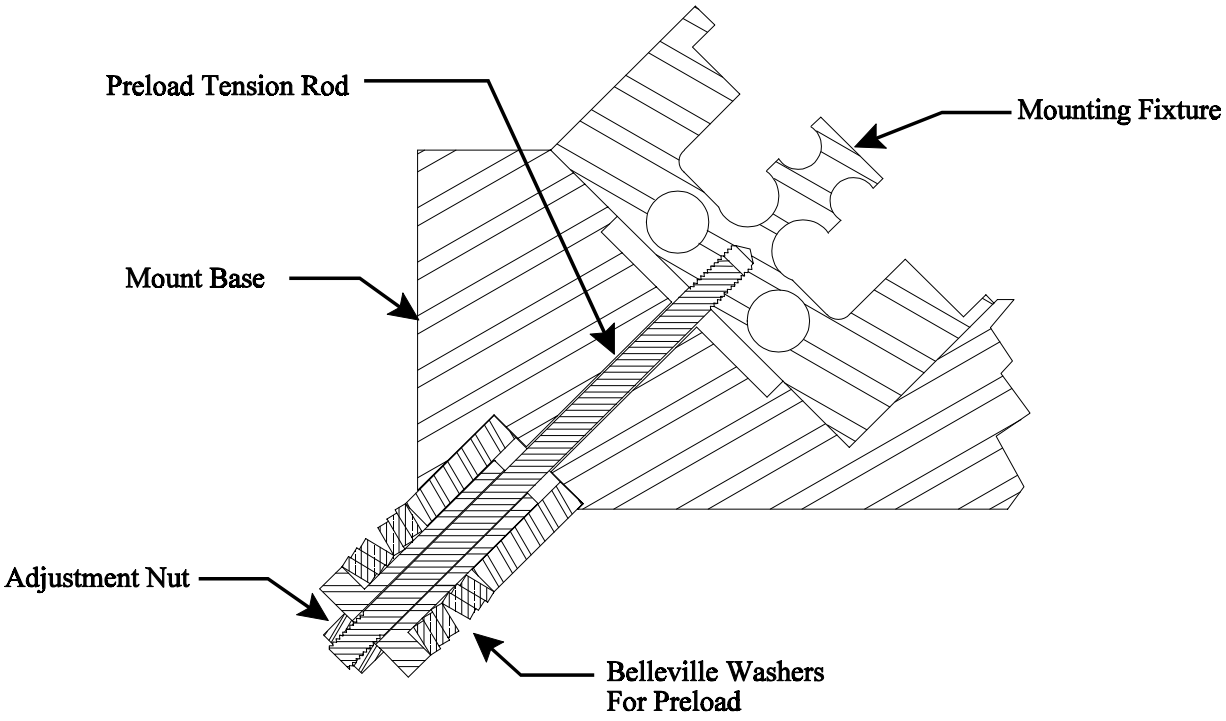

Figure 45 - Test Bearing Load Cell Preload System (1 each side)

4.4 Shaft/Bearing Displacement Measurement

The relative displacement between the shaft and test bearing is measured with eight eddy-current displacement probes as shown in Fig. 46. The probes used are Bently-Nevada 3300 series, 8 mm probes calibrated for an aluminum target. These probes are arranged as four opposing pairs to sense the vertical and horizontal positions of the shaft both inboard and outboard of the test bearing. The opposed probe arrangement was selected to obtain a reduction in measurement noise, as well as the ability to eliminate any uniform thermal growth of the housing or shaft from the measurement. The specifications of the probes are as shown in Table IX. This type of probe was selected over either optical (reflectance or laser triangulation) or capacitive probes as it is the only non-contact probe the author is aware of which can operate in an environment where oil is expected to be splashed through the sensing zone. These probes have two major disadvantages. The first is a very high sensitivity to material imperfections, including residual stresses and metallurgical and electrical non-uniformities in the shaft at the sensor location. The second is an electrical output which is centered around -10 volts DC, which is incompatible with the data acquisition system. To combat the noise problem, other researchers have used a variety of target surface modifications, including nickel coating the shaft, or using brass sensor rings. These reduce the noise magnitude by providing a target material with a higher conductivity than steel. With a higher conductivity, the eddy-current probe field does not penetrate as far into the material, which tends to improve the noise performance. In this test rig, aluminum sensor rings are used. These were selected for aluminum's combination of high strength, excellent conductivity and light weight. Probes calibrated for use against an aluminum target were also commercially available. The -10 volt offset is subtracted by a custom signal conditioner which is described in a later section.

For monitoring and debugging purposes, two similar probes (Bently Nevada 5mm, 7200 Series) are mounted inboard of the rear support bearing. These sense horizontal and vertical shaft positions at this bearing. The probes use the 17-4 PH stainless steel shaft as a target, rather than a special sensor surface. As a result, the electrical run-out signal for these two probes is as large or larger than the actual shaft motion.

There are two major error sources for these probes. The first is non-linearity. As can be seen in Table IX, the probes can have a substantial error over the full measurement range. In the test rig, only about 25 percent of the full range is used, which markedly improves the linearity specification. The error over this range could not be accurately determined, as the calibrator available could not be accurately set to calibration points to more than about ±12 μm. However, the calibration data which could be obtained, suggest that the probe linearity is probably adequate. The other potential problem with these probes concerns their temperature sensitivity. Although these probes are the de-facto standard among rotating machinery, they do exhibit a noticeable thermal shift as indicated in Table IX. Attempts at experimental determination of the probe thermal calibration shift were inconclusive.

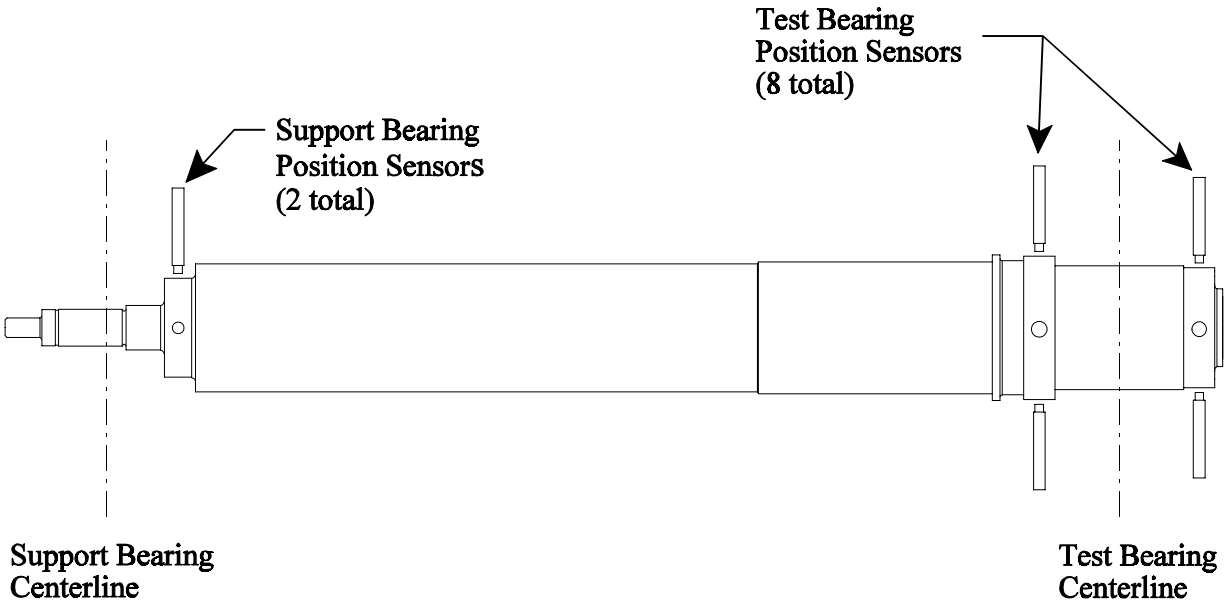

Figure 46 - Position Sensor Locations

Table IX - Bently Nevada Model 3300, 8mm dia. Position Sensor Specifications (AISI 4140 target, from Bently Nevada Catalog)

Parameter	Specification
Full Scale Range	250 µm to 2500 µm
Scale Factor	7.87 ± 0.21 mV/µm (typical)
Linearity	max ±25 µm deviation from straight line
Temperature Sensitivity	within ±76 µm, 22°C to 177°C
Frequency Range	0 - 10 kHz

4.4.1 Signal Conditioning

The test data acquisition system is shown in block diagram form in Fig. 47. There are basically two sets of signals which are measured by this system. The first are high frequency, dynamic quantities required for bearing dynamic characterization. These are the eight relative displacements, and the four bearing loads. The second group are low frequency, quasi-steady state characteristics required to define the bearing operating condition. These signals consist of thermocouple based temperature measurements and pressures as monitored by pressure taps. The average bearing load and the shaft speed measurements are made by the control system. A serial connection between the control and data acquisition computers is used to allow the data acquisition computer to access this information as required. Each of the sets of data acquisition signals has its own signal conditioning and data acquisition requirements as described in the next sections.

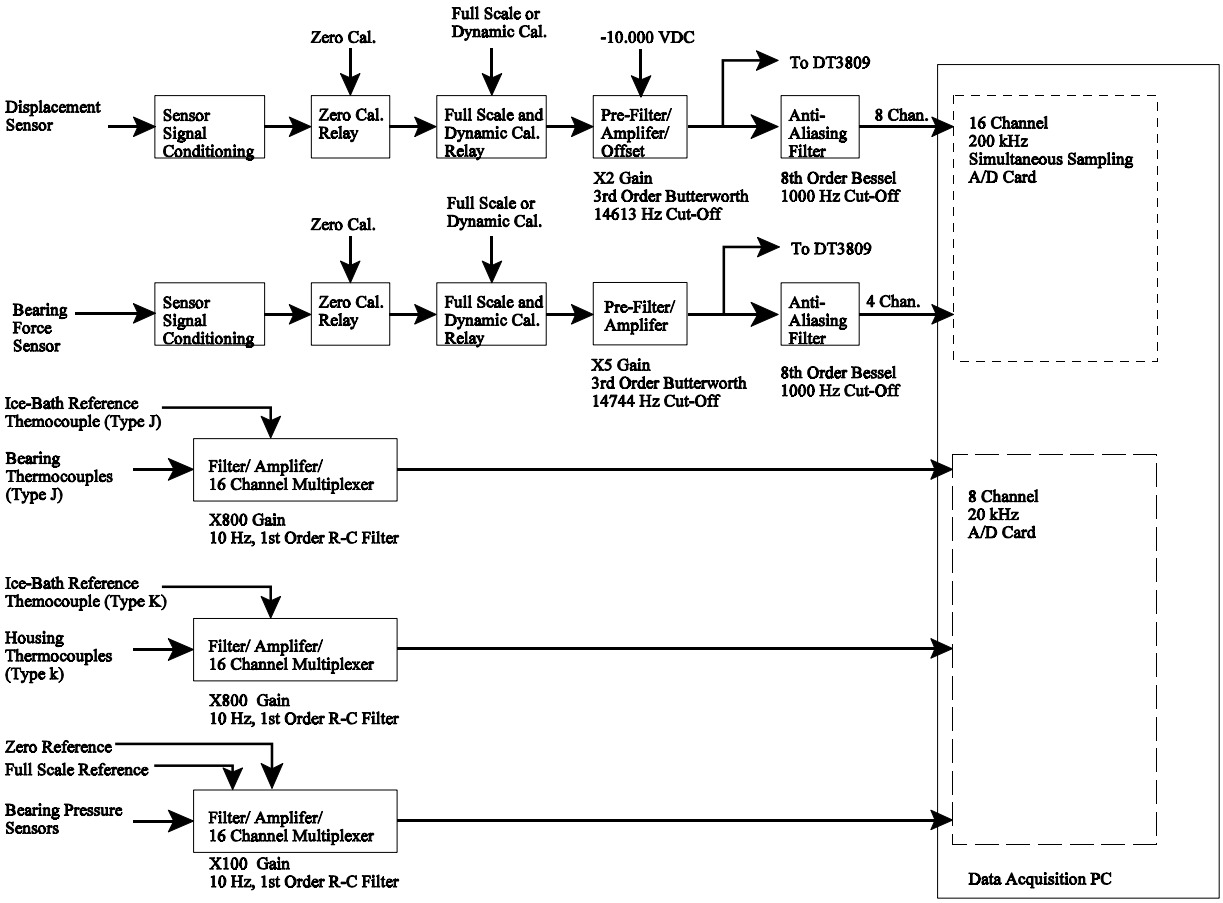

Figure 47 - Test Data Acquisition System

4.4.2 Dynamic Signals

This set of signals consists of the eight shaft/test bearing relative displacements, and the four bearing load measurements. These measurements are intended to be used as the input and output measurements required to estimate the bearing dynamic coefficients. The measurement goals for these twelve dynamic measurements are:

1) 0 to 1 kHz bandwidth
2) Simultaneous sampling
3) Interchannel amplitude matching better than 1 percent
4) Interchannel phase matching better than 1 degree
5) Linear phase response for the anti-aliasing filters
6) 12 bit minimum resolution

The high speed data acquisition system which evolved to meet these requirements includes a PC based data acquisition card, anti-aliasing filters, and amplifier/level shifters. The following sections describes these components in detail.

4.4.2.1 Data Acquisition Hardware

The data acquisition card is a United Electronic Industries model WIN3016DS. This is a 16 channel, 16 bit, simultaneous sampling, 12.5 kHz/channel PC based system. This system was selected as being the least expensive system which would meet the requirements above. The system specifications are shown in Table X. It should be noted that the card is not a true 16-bit system. Although 16 bit analog to digital converters are used, the input amplifiers are actually more appropriate for a 12 bit data acquisition system. As a result, the accuracy specification is less than 1 part in 65536 (16 bits). This inaccuracy, however, is calibrated out with the system calibration, leaving a more than adequate nonlinearity specification. The software used with this card will be described in detail in a later section. The card sample rate can be controlled in three basic modes:

Mode 1 - On board clock mode

A sample clock internal to the board is used to control sampling. This mode allows for a fairly arbitrary sample rate. The minimum appropriate sample rate is set by anti-aliasing considerations

based on the anti-aliasing filter characteristics and selected cut-off frequency. External circuitry has been provided to allow the start of sampling to be triggered by the test rig once-per-revolution signal.

Mode 2 - Controller system clock mode

This mode uses an 8192 Hz clock signal generated by the digital magnet controller system. This allows the samples to coincide with the excitation outputs driving the magnet amplifiers. This mode can also be set-up with a start trigger at the start of a block of 8192 excitation outputs (one second of excitation). This mode is especially designed to maximize the quality of the sampled data for system identification in the frequency domain. By synchronizing the data acquisition with the sampling, the sample is precisely periodic within the sample window. Hence the excitation spectrum can be represented exactly by a discrete Fourier transform of the measured data. As a result, spectral leakage does not occur in the data processing. Triggering the data at the start of an excitation block also maximizes the value of averaging the data (indeed, it becomes possible to perform time-domain rather than frequency domain averaging, thereby reducing the computational burden). Non-periodic disturbances such as shaft unbalance, shaft noise, and any control system transients will average to zero, while the excitation and response samples average to some constant value.

Mode 3 - Shaft synchronized mode

In this mode, the test rig 60 pulse-per-revolution signal is used as a data acquisition clock. Optionally, the keyphaser can be used as a trigger if desired. This mode allows the acquisition to be synchronized to shaft angular location. This mode suffers from the disadvantage that the anti-aliasing filters have a fixed cut-off of 1 kHz. At low shaft speeds, the sample rate is not high enough for the filters to prevent aliasing problems.

Table X - WIN3016DS Specifications

Parameter	Specification
Number of Inputs	16, Simultaneously Sampled
Resolution	16 bit
Maximum Acquisition Rate	12.5 kHz (for 16 channel samples)
Accuracy	0.16% (worst case)
Nonlinearity	± 2 least significant bit
Input Voltage	± 5 Volts
Gain Thermal Drift	30 ppm/degree C
Offset Thermal Drift	15 ppm/degree C

4.4.2.2.Filter/Amplifier/Level Shifting System

A filtering/amplification/level shifting system is provided by external hardware. The system block diagram was shown in Fig 47. For this system, differential input, integrated circuit, instrumentation amplifiers are used to provide gain and three-pole, Butterworth response, low-pass pre-filters. Eight-pole, switched capacitor, Bessel response low-pass filters are used as the primary anti-aliasing filters. The pre-filter/amplifier is a custom built unit, based around a Burr-Brown INA110 instrumentation op-amp. The anti-aliasing filters are model AAF-1, eighth order Bessel response filter cards, manufactured by Alligator Technology. The specifications of these filters are as shown in Table XI.

Switched capacitor filters are used as the primary anti-aliasing filters for several reasons:

- They are far less expensive than comparable analog filters
- They generally have closer inter-channel phase and amplitude matching than the analog filters
- They have a variable frequency cut-off

The variable frequency cut-off feature was important in an early configuration of the data acquisition system which synchronized the sample rate with the shaft, and varied the filter cut-off to match the shaft speed. This shaft synchronous sampling was used primarily to allow for easy time-domain run-out subtraction on the measured signals.

Switched capacitor filters do, however, have a serious drawback - they are a sampled data system, and are subject to the same aliasing phenomena as any other sampled data system. However, the sample rate is much higher than the cut-off frequency of the filter. For the filters used in the test rig, the filter sample rate is 150 kHz for a 1 kHz cut-off. This relatively high sample rate allows for a fairly simple pre-filter to prevent aliasing problems in the filters. The approach used for the data acquisition system is a third order, Butterworth response filter built around the instrumentation amplifier used to match the sensor output voltage range to the ±5 volt input range of the data acquisition card. The cut-off frequency of this filter is set about fifteen times the cut-off for the switched capacitor filter to reduce the need for precise interchannel matching of pre-filter characteristics. In the case of the displacement sensors, the amplifiers also serve as a level shifter. As discussed previously, the output

from the displacement sensor system is -5 to -15 VDC for nominal bearing displacements, and can range from about -2 to -24 VDC for motion outside the nominal range. There is no commercial PC based data acquisition system the author is aware of which is designed to be used with a voltage range essentially centered around -10 VDC. To accommodate these probes, a precision -10 VDC voltage source provides an offset voltage to the differential input of the instrumentation amplifier chip. To allow for the full displacement sensor output voltage range without damage to the amplifier, the displacement and offset voltage inputs are first attenuated by a resistive divider. This divider ensures that the voltage at each amplifier input is always less than the ±15 VDC supply voltage used. The amplifier gain then makes up for the input attenuation to provide an overall gain as desired to match up to the ±5 volt data acquisition input.

Since this data acquisition system was intended to be accurate for long testing periods, provisions for self-calibration are included in the signal conditioning system. As shown in Fig. 47, there is a relay in each of the displacement and force channels which shorts the input for calibration. This establishes a zero input condition. Any offset can then be measured and subtracted from future readings. A precision, full scale input which is common to all of the channels (again a precision voltage source) can also be selected by a relay in each channel. The calibration system is also designed to allow a dynamic calibration signal to be substituted for the full scale input to allow equalization of the channel dynamic transfer functions. As currently installed, the calibration relays are activated by a front panel switch, but could readily be controlled from the data acquisition computer so as to have a completely self calibrating signal conditioning system (the sensor systems do not have provisions for calibrating the electronics, hence they have to be calibrated by more manual methods). The goal was to use the shorting relay system to check the signal conditioning/filter/data acquisition system zero before testing, and from time to time during testing to calibrate out any zero drift. The span relays would likewise be used to periodically check the gain of the input electronics. The external circuitry for the calibration and amplifier filters was constructed on custom printed circuit boards fabricated at the Rotor Dynamics lab.

Table XI - Alligator Technology AAF-1 Lowpass Filter Specifications

Parameter	Specification
Filter Response	8th Order Bessel
Cut-Off Range	5 Hz - 50 kHz
Input Voltage Range	± 5 Volts, differential
Output Voltage Range	± 5 Volts
Harmonic Distortion	0.03%
Clock Frequency	150x cut-off
Filter Chip	Linear Technology LTC1064-3

4.4.3 Low Speed Data Acquisition System

In addition to the twelve high-speed inputs, there are also 48 channels of low speed data acquisition. These inputs correspond to the lower three signal paths in Fig. 47, which are attached to the eight channel input card. These channels include:

- 14 pressure-probe inputs
- 1 pressure probe full scale reference input
- 1 pressure probe zero input
- 15 type J thermocouple inputs
- 1 type J ice-bath reference input
- 15 type K thermocouple inputs
- 1 type K ice-bath reference

The data acquisition system for these signals consists of a Computer Boards CIO-AD08 input card, which is a 12-bit, eight channel system, and three Computer Boards CIO-MUX16 sixteen channel multiplexor/amplifier cards to expand these eight inputs to 48 input channels. The specifications of these components are shown in Table XII and XIII. The input multiplexors have built-in 10 Hz cut-off, first-order, low pass (resistor capacitor) filters on each channel. The bearing thermocouple wires are terminated with plugs which connect to a set of panel jacks on the signal conditioning rack to allow for easy bearing removal and change-over. A position for a reference thermocouple, which is immersed in an ice-bath, is also provided. The two sets of sixteen jacks are then connected to the sixteen channel multiplexor boards. This system uses an interrupt driven sampling approach to sample each input at 40 Hz. This rate was selected as a conveniently low rate which would alias all 60 Hz noise (which was expected to predominate) to the top of the sampled frequency range. In the case of 40 Hz sampling, 60 Hz noise is aliased to 20 Hz. A seventh order, digital, finite impulse response filter is employed to filter this noise out.

The two sets of sixteen thermocouple inputs function essentially the same. The only difference is the linearization routine used. Once the data are sampled, the measured ice-bath reference voltage is used to provide a reference which includes all junction effects, as well as zero-drift in the data acquisition hardware (which seems to be significant with this system). A third order linearization, derived from

standard thermocouple tables over the range of 10 to 70 °C, is then used to linearize the readings. The linearization error is less than 0.1 °C , which is an order of magnitude smaller than the typical 1°C interchangeability error for type K and J thermocouples.

The pressure probe inputs are slightly different. These are designed to work with 100 mV/V, four-arm pressure transducers. Again, jacks are provided to allow easy connection/disconnection from the inputs. An isolated, precision 10 volt power supply is also provided to drive the sensors. This supply module also contains a zero-output dummy bridge, and an unbalanced bridge to provide a full scale calibration signal. These two signals, along with the outputs of up to fourteen pressure transducers, are connected to the differential inputs of the third sixteen channel multiplexor card. This card provides a gain of 100, and a first-order, 10 Hz low-pass filter (resistor-capacitor) for each channel. After being sampled by the data acquisition card in the data-acquisition computer, a software routine uses the offset and full-scale signals as calibration references as part of the routine which converts the pressure transducer voltage signal to engineering units.

Table XII - Computer Boards AD08 Data Acquisition Card Specifications

Parameter	Specification
Inputs	8, single ended
Resolution	12 bit
Accuracy	0.01% ± 1 bit
Offset Thermal Drift	10 ppm/°C
Gain Thermal Drift	50 ppm/°C
Sample and Hold Acquisition Time	15 µs (0.01%)

Table XIII - Computer Boards Multiplexor/Amplifier Specifications

Parameter	Specification
Inputs	16, differential
Amplifier Gain Accuracy, G = 100 G = 800	0.1% 2.0%
Amplifier Gain Thermal Drift, G = 100 G = 800	20ppm/°C 80ppm/°C
Offset Thermal Drift	15 µV/°C
Multiplexer Settling Time	3.5 µs (0.01%)

4.5 Data Acquisition Software

The data acquisition software is a combination of custom C++ code, board drivers and Matlab code. There are two basic software packages developed for the data acquisition system: a set-up program, and the Matlab based data acquisition system. This section will summarize each of these in turn.

4.5.1 Set-Up Code

The first major piece of software is a set-up oriented code. This code is a C++ code developed with Microsoft Visual C++. This code runs under Microsoft Windows 3.1, and makes use of vendor supplied drivers for the high speed (WIN3016D), and low speed (AD08) data acquisition systems. It allows the user to simultaneously view all sixteen high speed inputs, the fourteen pressure probe inputs, the fifteen bearing thermocouples, and the fifteen bearing housing thermocouples in a low speed (250 ms update) digital voltmeter format. This code also allows the user to change the channel labels (names), the channel scaling, and add an offset to the scaled reading if required. This is important when changing bearings, as each bearing has a slightly different thermocouple/pressure tap configuration. The user can set-up appropriate labels in this code, which can later be saved with any data acquired. The other primary use of this code (beyond confirming functionality of a probe) is to reset the mechanical location of the displacement sensors following a bearing change. The total measurement range is only 0.51 mm, so the probes must be carefully centered in this measurement range.

This code also has the capability to communicate setpoints, etc. with the control computer. This feature allow the user to confirm that the serial link between the computers is working, as well as control the test rig from a single computer in a manual configuration if desired. This code also provides a framework for developing and testing any new software features a future user might desire. This code was used a tool to develop and debug the basic modules that form the Matlab interface described below.

4.5.2 Matlab Interface

The second major code is a collection of dynamic link libraries (DLL's) written in Visual C++ which allow Matlab to be linked to the data acquisition and control hardware. This group of tools allows standard Matlab function calls to be made which can then take data or perform a control function.

1) WIN3016.DLL — This DLL contains all of the code to allow high speed data acquisition to be performed under Matlab control. This one basic function can be called with various options to perform appropriate tasks. Enough options have been provided to allow the user to perform a variety of data acquisition tasks, as well as retrieve the set-up data stored by the set-up code.

2) AD08.DLL — This DLL allows the user to acquire the pressure and temperature data, as well as set-up information. It also provides an interface to the support bearing positioner system. The user can move the bearing in a desired direction as required to obtain or maintain a desired alignment condition.

3) Matserl.DLL — This DLL completes the set of Matlab interfaces to allow the user to interact with the control system.

With these three DLL's, it becomes possible to build a complete, automated test sequence in Matlab. This was one of the goals for this test rig. With the Matlab interface, it becomes possible for someone who is familiar with Matlab to easily develop different test situations, etc. with a minimum of training and software development time. An example of a complete test sequence for static characterization of a bearing is shown in Appendix B.

4.6 Measured System Characteristics

4.6.1 Displacement

As described previously, preliminary attempts were made to confirm both the linearity/scale factor and thermal sensitivity specifications for the eight relative displacement sensors. Due to problems

with precisely setting the calibration points, the linearity/scale factor calibration results were limited to obtaining a nominal scale factor for the probe/signal conditioning system. The thermal sensitivity results were also inconclusive. The manufacturer's claimed dynamic probe performance was not examined as part of this work.

4.6.2 Force

Figure 48 and 49 present the transfer functions between vertical impact at the top of the bearing housing to the outboard left and outboard right bearing load cells. These results suggest that the housing, mount and load cell system are probably suitable for up to almost 300 Hz, where the response begins to be affected by a resonance. This is much lower than the expected first system resonance of approximately 900 Hz, based on a two-dimensional finite element analysis of the structure. The reasons for the discrepancy have not been explored, since problems with the shaft dynamics, as will be described in chapter seven, appear to preclude use of the test rig for dynamic measurements.

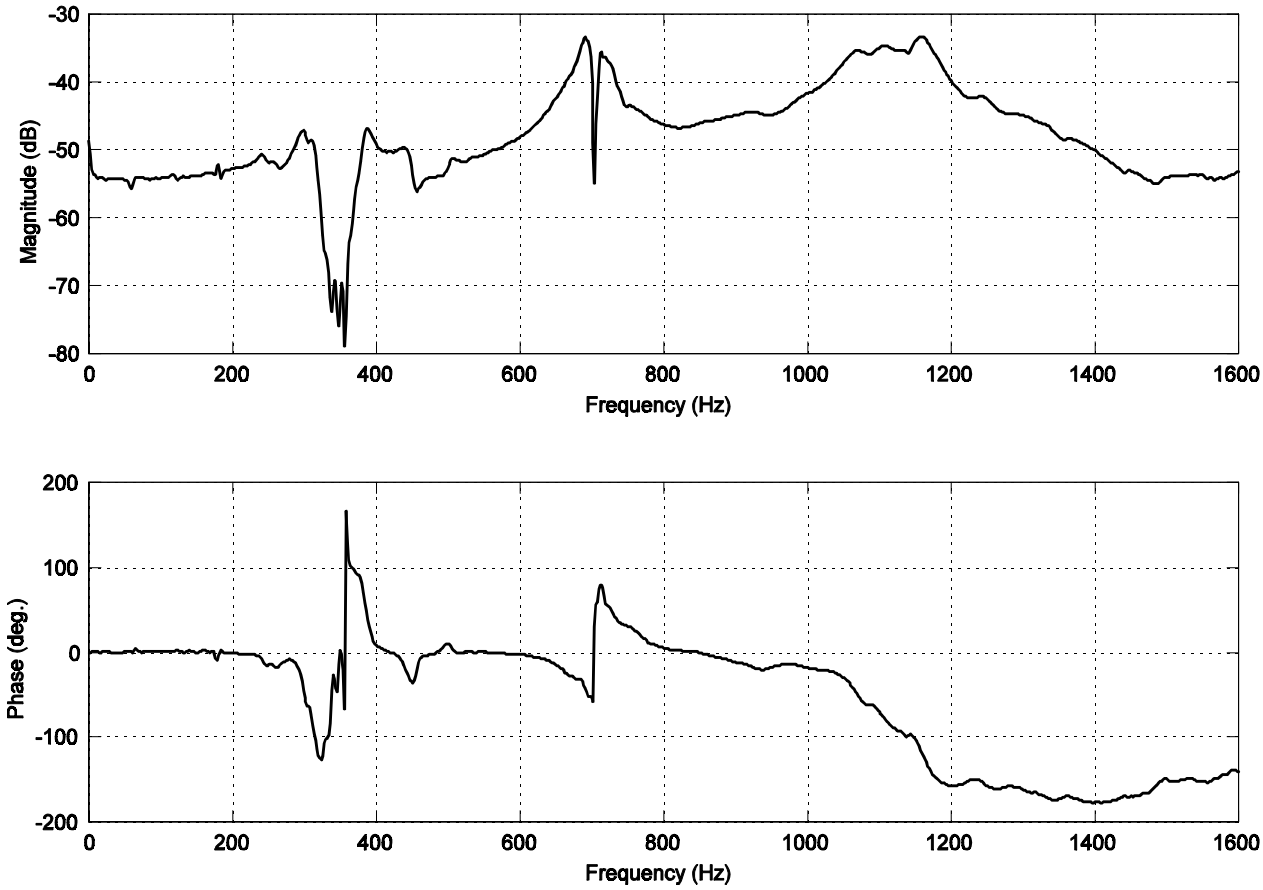

Figure 48 - Bearing Housing Vertical Impact to Outboard Left Load Cell Frequency Response

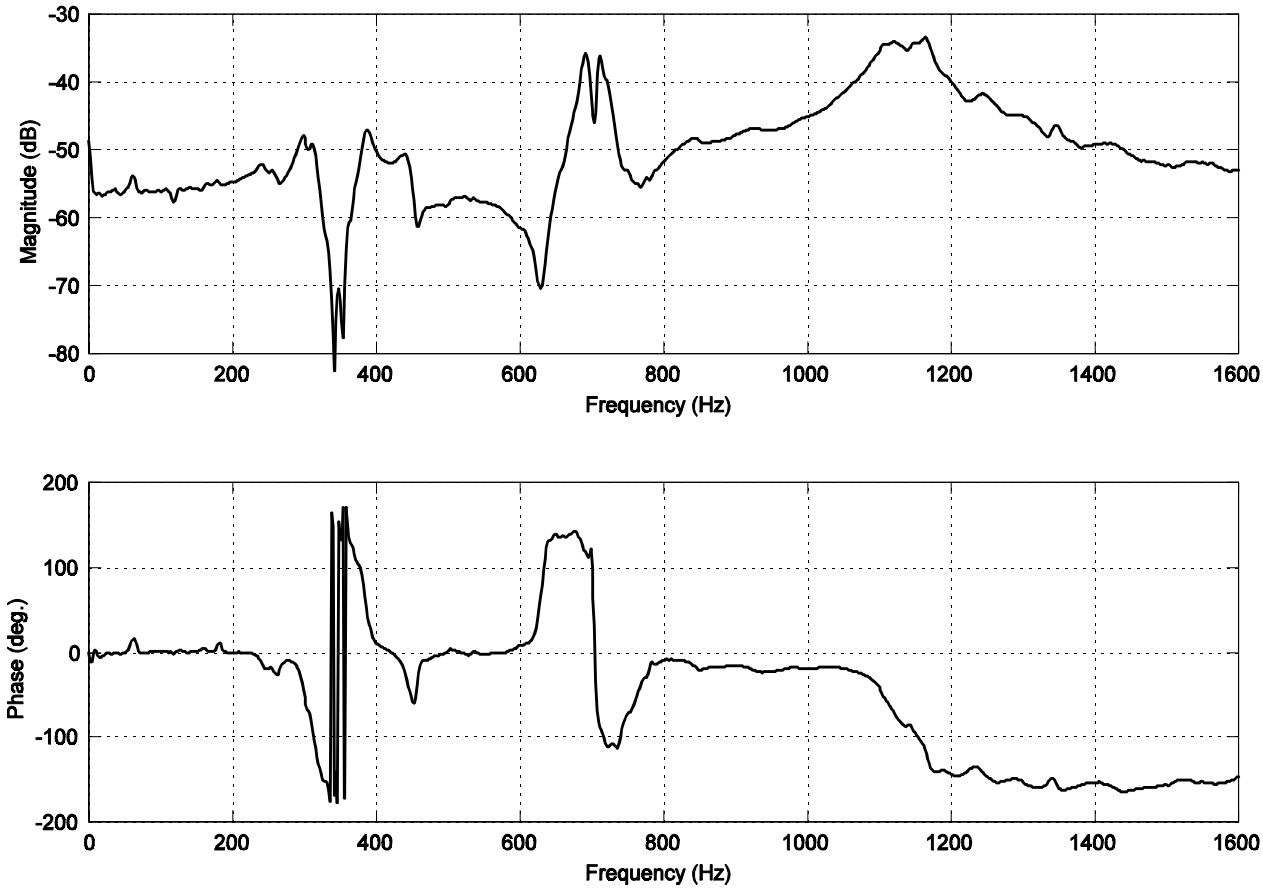

Figure 49 - Bearing Housing Vertical Impact to Outboard Right Load Cell Frequency Response

4.6.3 Signal Conditioning System

To confirm that the signal conditioning system performs as designed, an HP 35665 dynamic signal analyzer was used to inject a known test signal at a measurement system test input and measure the resulting signal conditioner output to estimate the system transfer function for each channel. Figure 50 presents the composite results for the eight displacement channels from the calibration input to the output to the data acquisition card. In this figure, the measurements for all eight displacement channels have been overlaid. Figure 51 presents the composite results for the four load cell channels, similarly overlaid. The desired goal for the system was attenuation of frequencies which would alias into the 0 to 1 kHz data range by at least 60 dB. As can be seen from the data presented in the two composite figures, this goal is more than met for all twelve dynamic data acquisition channels.

To confirm that the prefilter/amplifier attenuates frequencies above 75 kHz by at least 60 dB, to prevent aliasing in the switched capacitor filters, a wideband random input signal was used. Figure 52 presents the measured output spectrum for this input. This figure is not a transfer function since the analyzer cannot measure both input and output for this frequency range. However, the input signal is essentially flat if many (100 in this case) averages are taken. Hence, Fig. 52 is essentially a measurement of the wideband frequency response for the prefilter.

To evaluate the inter-channel characteristics, including the data acquisition card, a wide-band, random signal from the signal analyzer was used at the test input, and the data acquisition system used to collect data. Data for each channel were acquired and averaged in the frequency domain using the Matlab based data acquisition system. The frequency response functions from channel 1 to the remaining 11 channels were then estimated. The composite results are presented in Fig. 53. Note that these transfer functions should all be unity, with zero phase difference, indicating that the channels all affect the measured data in the same way. If this condition is met, than measurements made with this system can be used to estimate the bearing dynamics without problems due to data distortion in the data acquisition system. Over the desired passband of 0 to 1 kHz, the amplitudes of the signal conditioning channels match the channel 1 amplitudes to within about one percent, and show less than one degree of phase shift relative to channel 1.

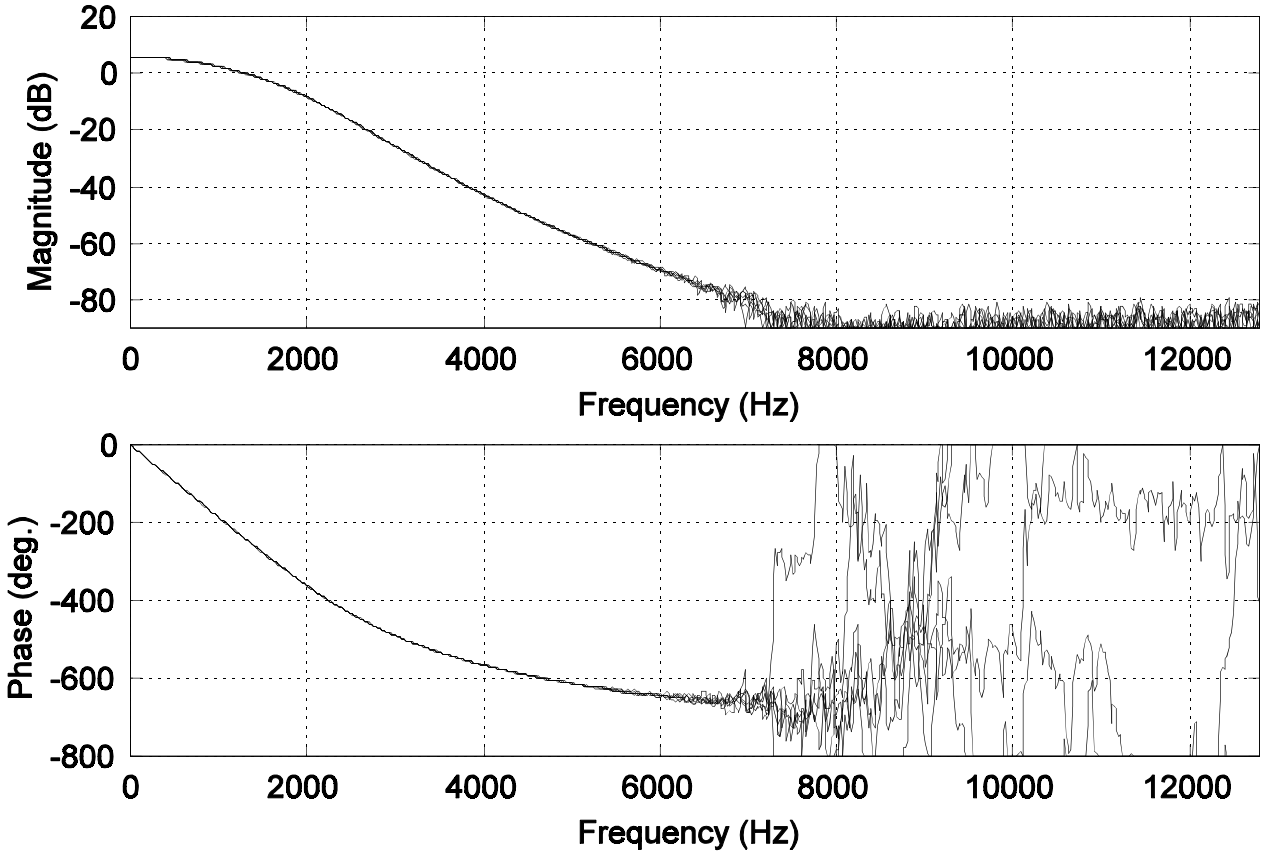

Figure 50 - Displacement Channel Signal Conditioning System Frequency Responses for all Displacement Channels

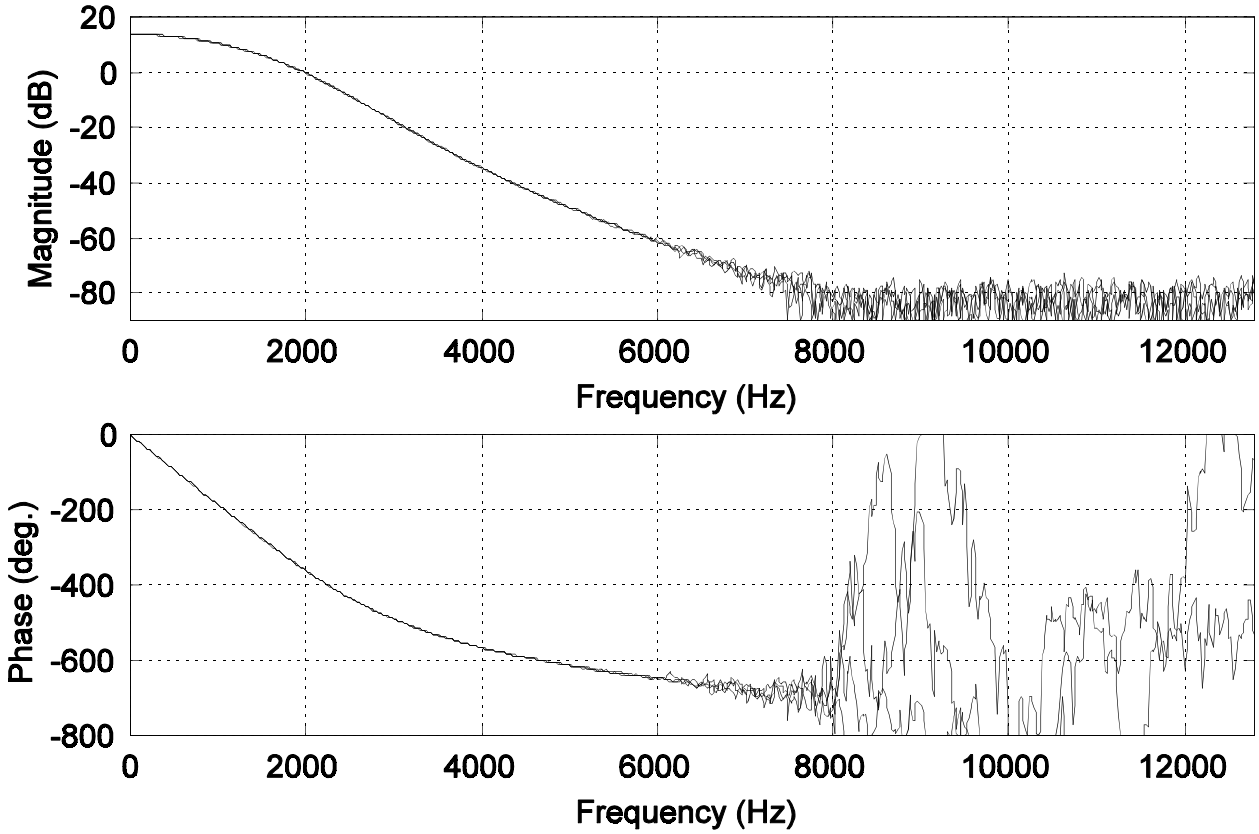

Figure 51 - Bearing Load Cell Signal Conditioning System Frequency Responses for all Force Channels

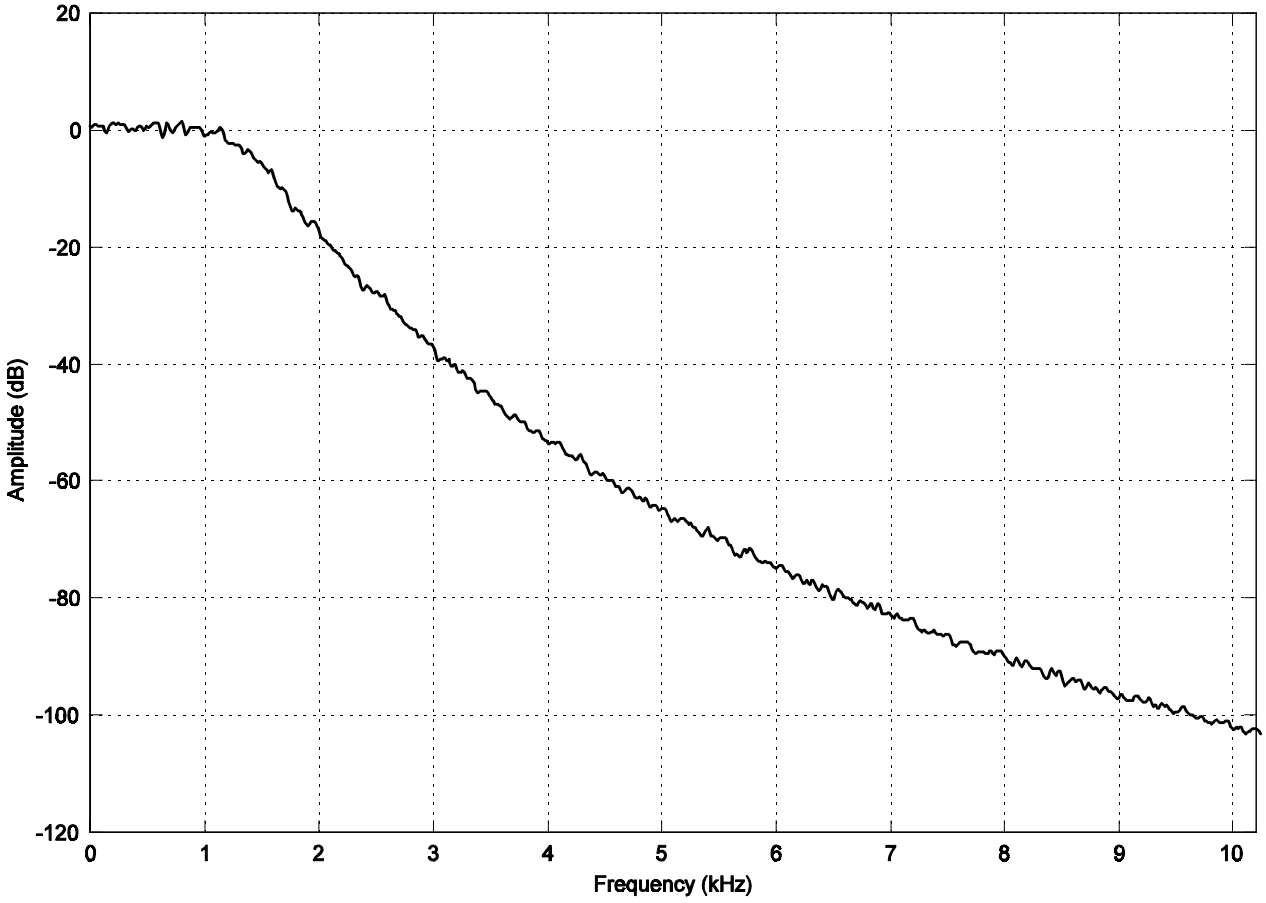

Figure 52 - Wideband Frequency Response for Pre-Filter (Inside Top Channel)

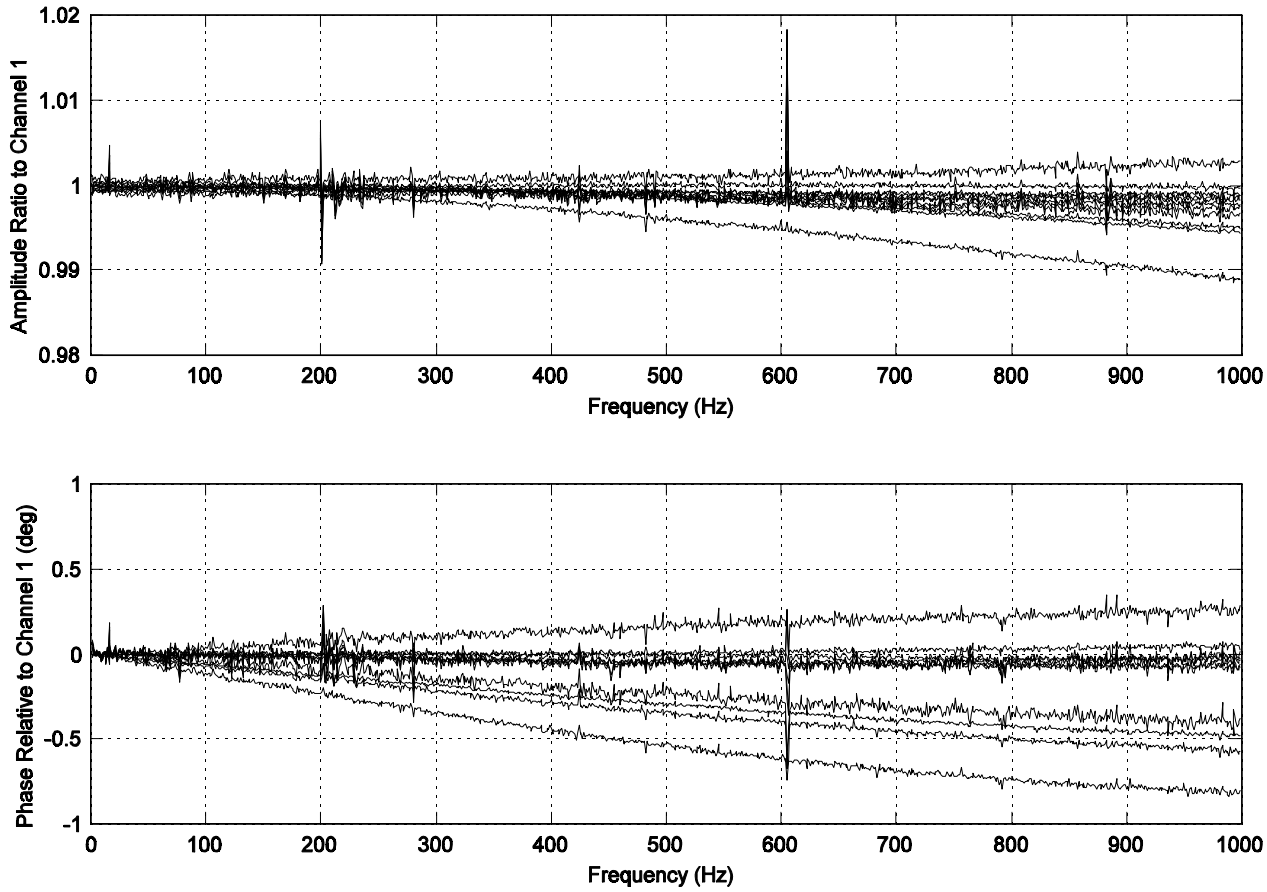

Figure 53 - Signal Conditioning System Inter-Channel Frequency Responses for all Channels

4.6.4 Noise Levels

Finally, Figs. 54 and 55 present measured time domain base noise levels for the eight displacement and four force channels respectively. The goal of these measurements was to confirm that the system noise due to sources other than test forces and motion was smaller than the desirable signals due to test forces and motion. The operating systems for each case are as enumerated in Table XIV. These data were measured by turning on the appropriate pieces of equipment for the given test case, then averaging one hundred variance estimates, each computed from one second (8192 points) samples of data. As can be seen from these data, the variance noise with the rig spinning is generally an order of magnitude larger than any other case. The next most noisy case is case 10, which corresponds to all effects except rotation.

The results suggest that the system would have been adequate for dynamic testing. Based on the results presented in the introduction, the expected displacement measurement signal variance is 2.25 μm^2, corresponding to a 9 μm peak-to-peak displacement. This signal variance is much larger than the variance measured for a non-rotating shaft (case 10, for example). If sinusoidal excitation signals had been used, the results may have been even better since most noise would not be well correlated with the excitation signal, and hence would quickly average to zero. In the case of the rotating shaft, similar comments would apply for non-synchronous excitation. For the case of synchronous excitation, some of the shaft noise associated with imbalance/non-circularity, etc., would show up as an excitation in the measurements. Averaging might or might not help, but a reasonable signal to noise ratio could probably be obtained. Similar conclusions can be drawn for the force measurements, although the final signal to noise ratio would be highly dependent on the actual bearing stiffness and damping characteristics.

Table XIV - Noise Measurement Cases

Case	Input Shorted	Bottom PWM Amp	Drive Motor, Oil System	Magnet Control System	Shaft Speed
1	Yes	Off	Off	Off	0 RPM
2	Yes	On, 8 amps	Off	Off	0 RPM
3	Yes	Off	On, 1200 RPM	Off	0 RPM
4	Yes	Off	Off	Running	0 RPM
5	Yes	On, 8 amps	On, 1200 RPM	Running	0 RPM
6	No	Off	Off	Off	0 RPM
7	No	On, 8 amps	Off	Off	0 RPM
8	No	Off	On, 1200 RPM	Off	0 RPM
9	No	Off	Off	Running	0 RPM
10	No	On, 8 amps	On, 1200 RPM	Running	0 RPM
11	No	On, 8 amps	On, 1200 RPM	Running	2880 RPM

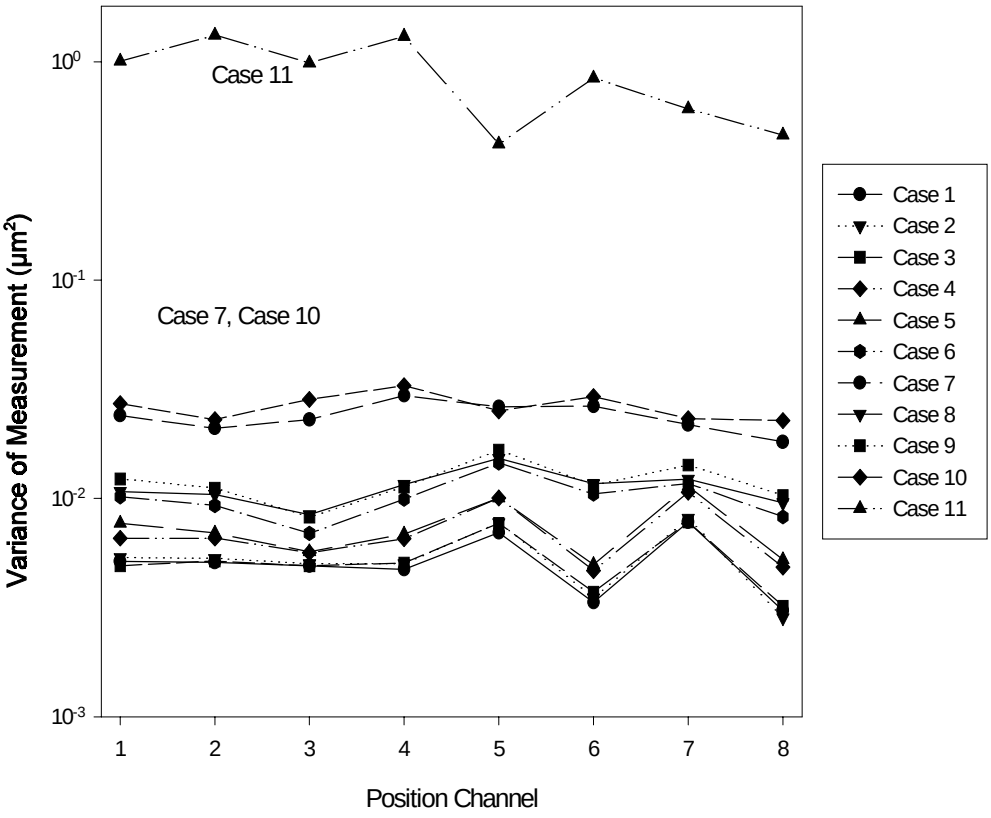

Figure 54 - Displacement Sensor Measurement Variance

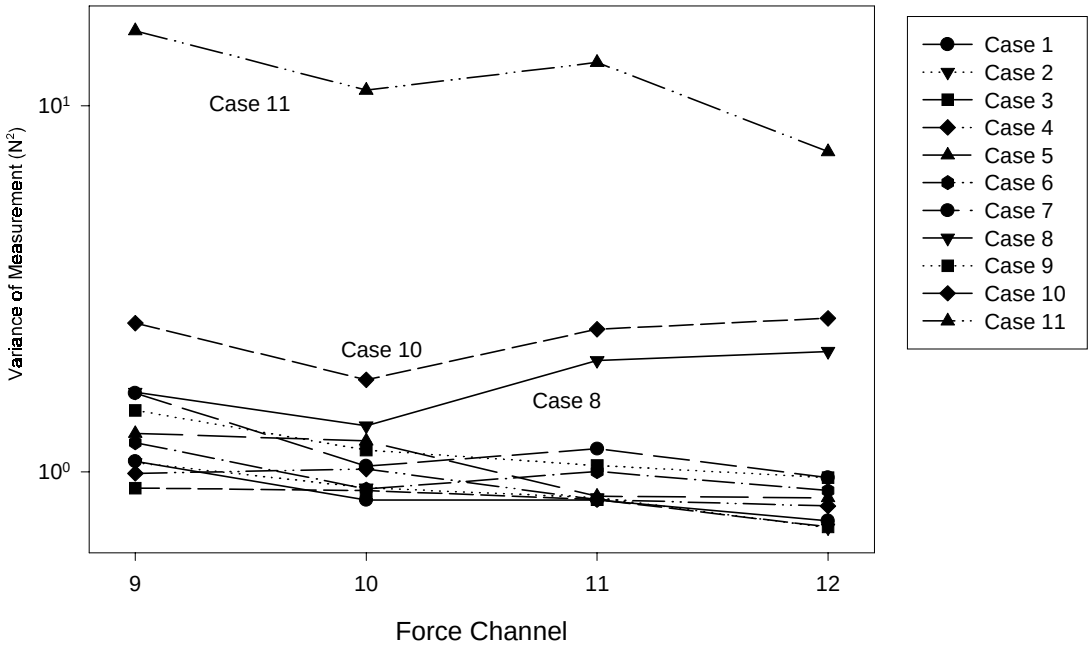

Figure 55 - Force Sensor Measurement Variance

Chapter 5

Auxiliary Rig Systems

5.1 Introduction

In addition to the major sub-systems described previously, there are a number of other systems which are required to obtain the desired operating conditions and operate the test rig. These include: the oil system, a shaft alignment system, a drive system, a foundation, rig condition monitoring instrumentation, and an electrical system. This chapter discusses these supporting systems.

5.2 Oil System

The test rig oil system is as shown in Fig. 56. This system is a fairly standard dedicated oil system. The components are as specified in Table XV. As described previously, the oil is supplied to the test bearing via the circumferential oil feed groove in the test bearing housing. It returns to the supply tank via a gravity drain passage.

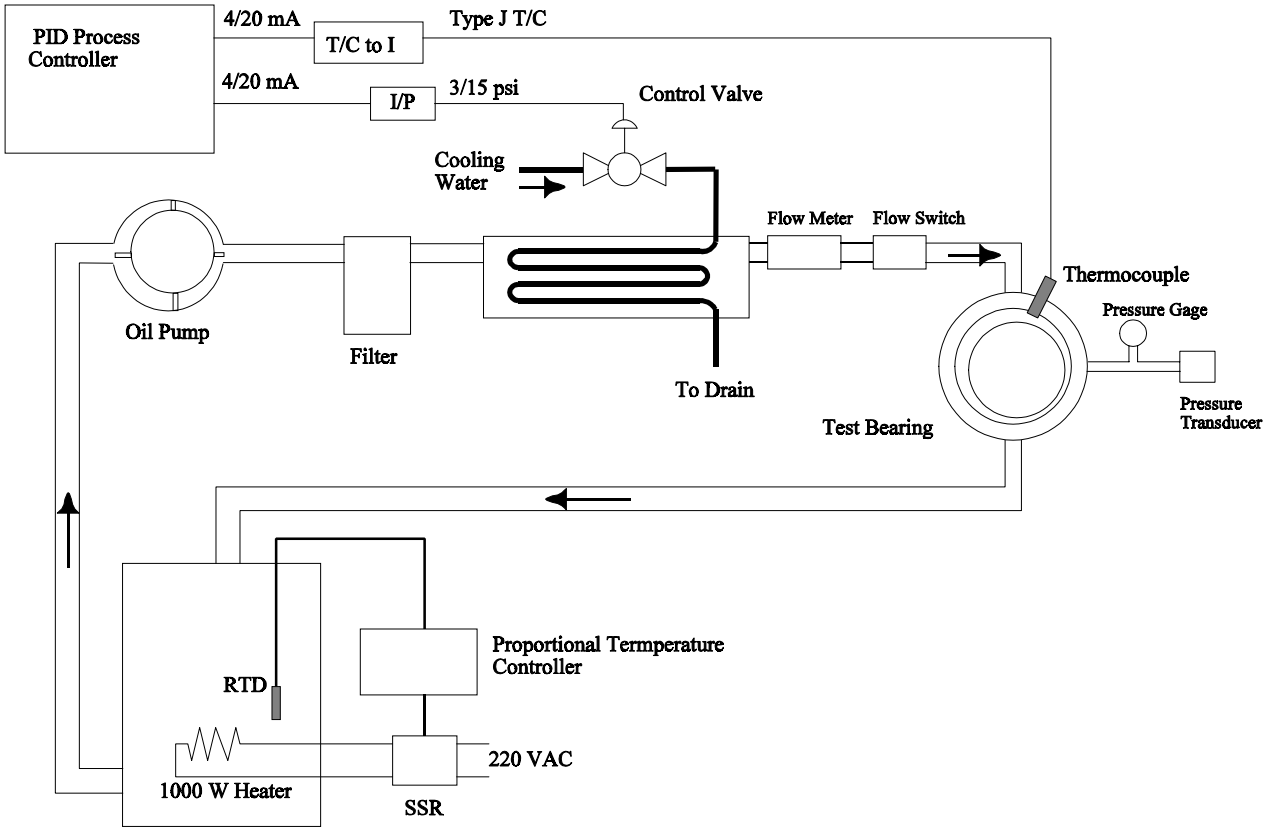

Figure 56 - Test Bearing Oil System

Table XV - Oil System Components

Item	Description
Oil Reservoir	78 L, Stainless Steel
Oil Pump	20 kPa, 38 L/min rated sliding vane pump, 0.8 kW motor
Oil Filter	15 micron
Heat Exchanger	Oil to Water, Shell and Tube, Four Pass
Flowmeter	38 L/min Rotometer
Heater	1000 w, low watt density

5.2.1 Flow/Pressure Control

The flow rate (pressure) control is provided by a manually operated, spring loaded bypass valve to provide a sufficiently constant flow of oil to the test bearing. This system is not required to have a more sophisticated and expensive feedback system, since small changes in oil inlet pressure are not expected to have a significant impact on bearing operation, except possibly at very light loads (Knight, Barrett and Cronan, 1985), or if the flow is too low for normal bearing operation. These situations were expected to be avoided in testing. Data presented in Swanson (1992) for similar test bearings also did not show a significant effect on shaft position for small variations in oil flow rate. The inlet flow rate is measured with a variable area flow meter as shown. The oil pressure in the housing feed groove is measured with an analog pressure gage, as well as a sensor which is attached to the data acquisition system.

5.2.2 Oil Temperature Control

The oil inlet temperature control system is a closed-loop feedback controlled system. To allow for temperature regulation, a separate proportional controller and electric heater are used to maintain the oil in the reservoir at least five to fifteen degrees above the desired test bearing inlet temperature. During higher speed operation, the viscous dissipation in the bearing and pump losses alone will keep the reservoir temperature sufficiently high. The hot oil is pumped through a water-cooled shell and tube heat exchanger to be cooled to the desired test bearing inlet oil temperature, as sensed via a thermocouple in the bearing oil inlet passage. The flow of cooling water is controlled by a pneumatically operated control valve, which is controlled by a commercial process controller. This controller uses the output of the thermocouple in the bearing oil inlet as feedback as shown in Fig. 56. This system works quite well. A system response to an input step and the steady-state behavior are shown in Fig. 57 and Fig. 58, respectively.

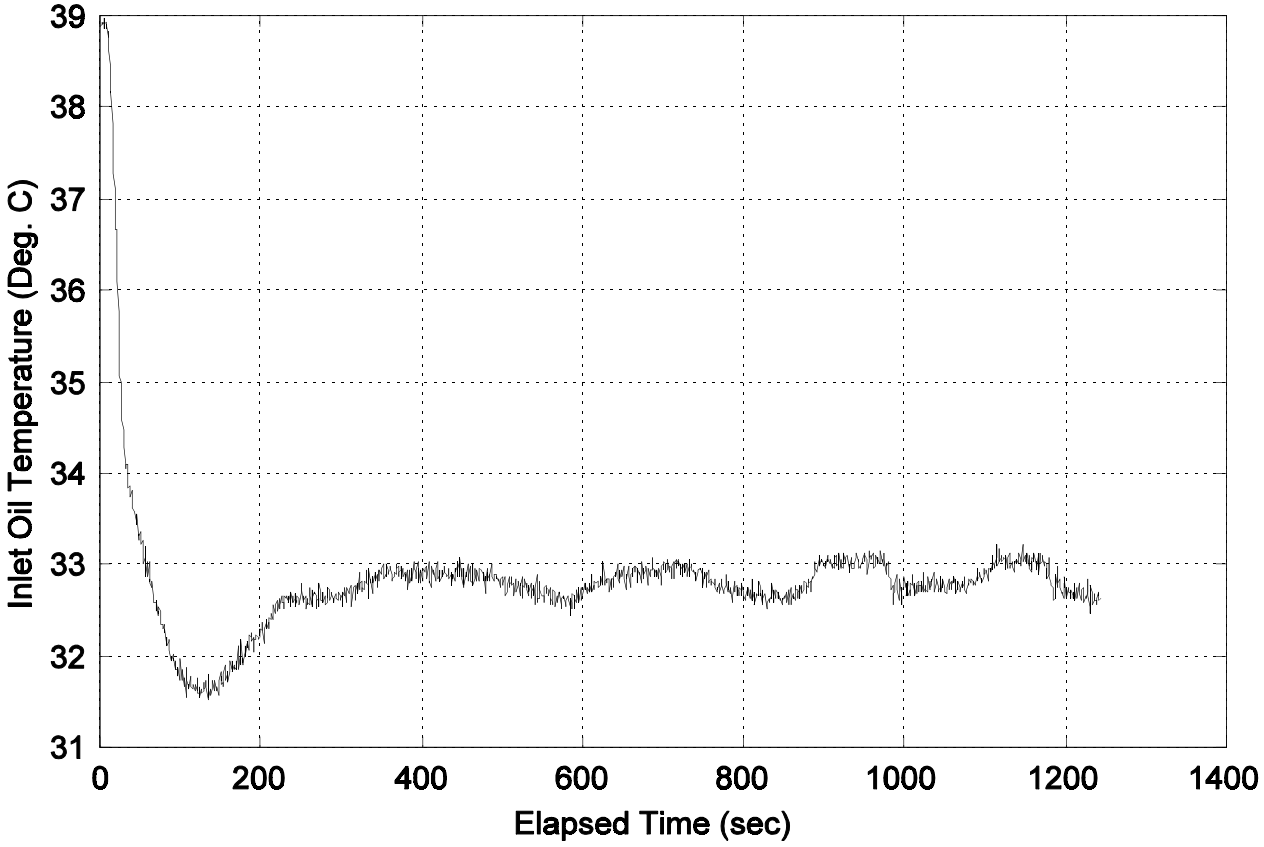

Figure 57 - Oil Temperature Step Response

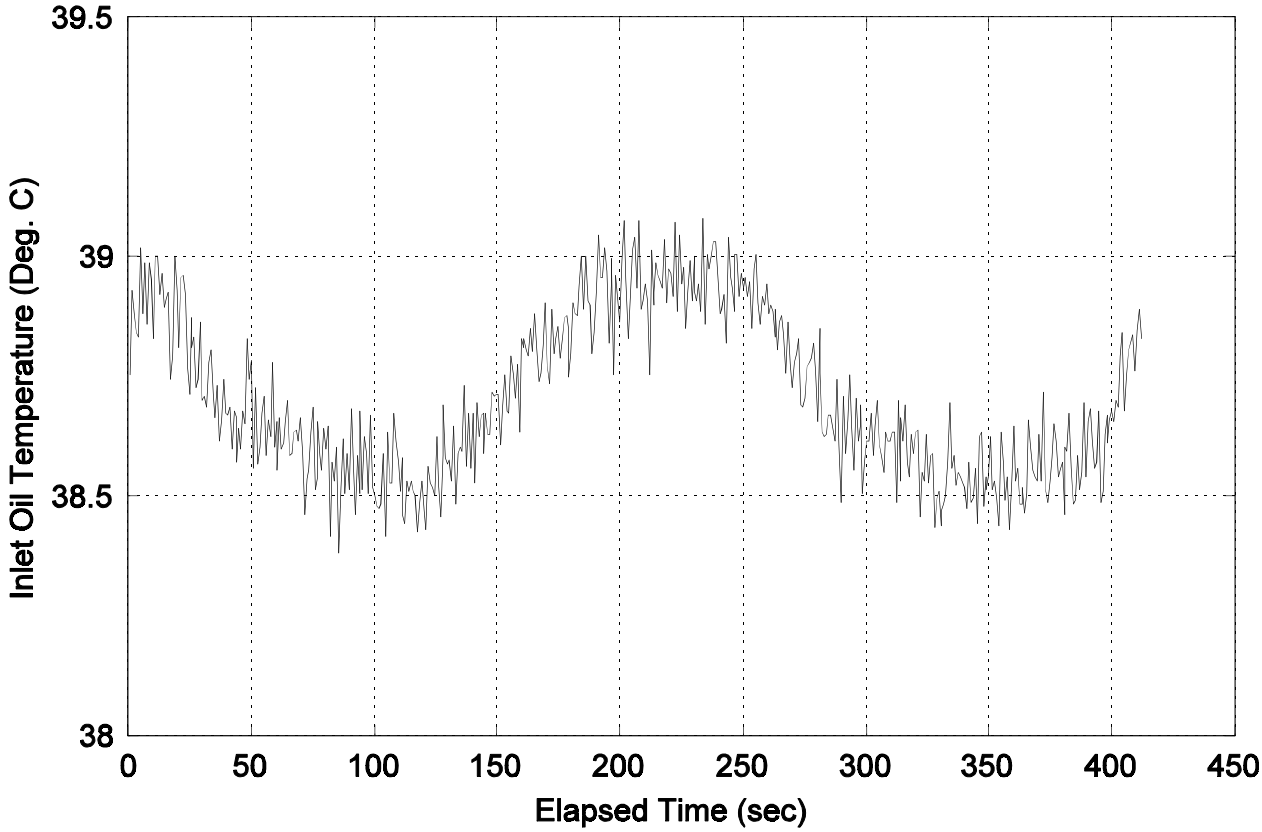

Figure 58 - Oil Temperature Steady-State Response

5.2.3 Oil Reservoir Temperature Control

As described above, the reservoir can be heated with a 1.0 kW electric heater which is controlled via a commercial proportional controller which uses an immersed resistance temperature detector (RTD) as a sensor for feedback. This system is used to raise the reservoir temperature when the rig is not running, and when the power dissipated to the bearing is not enough to maintain the desired elevated reservoir temperature. The controller is set-up to shut-down if the reservoir temperature rises too far above the setpoint. The heater system will also shut-down if the oil reservoir level falls too low, or the reservoir temperature sensor is disconnected or fails.

5.3 Shaft Alignment System

One of the usual assumptions in a bearing analysis is that the bearing and shaft axes remain parallel. Hence, the test rig needs to be able to provide this alignment for comparisons with the bearing analysis codes to be meaningful. Unfortunately, the floating shaft/fixed test bearing design of this test rig gives rise to several likely misalignment sources The largest is probably shaft bow under load (indeed, this problem should have suggested the problems with the shaft dynamics which will be discussed in chapter seven). A second problem is the fact that the test and support bearing housings are operating in different thermal environments, hence they will be at different heights in operation due to different amounts of thermal growth. Finally, there is the possibility of misalignment caused by baseplate bending, either due to load or foundation thermal effects. Hence it was necessary to provide a mechanism for automated shaft alignment during operation.

The system shown in Fig. 59 provides the needed two axis (horizontal and vertical) alignment capability. This positioner system can provide up to ±7 mm of horizontal and vertical motion at the rear test bearing. As shown in this figure, the support bearing is mounted to a plate which is supported by two wedges. Movement of one wedge moves the shaft vertically, the other moves the shaft horizontally. The wedges are moved in or out by linear actuators. The rear bearing mount plate is loaded against these wedges via a linkage and a spring in each direction. The preload system provides approximately 4500 N of preload to keep the bearing mount plate in contact with the wedges.

This wedge approach was selected to provide the highest possible stiffness, while still allowing the needed vertical and horizontal movement for alignment. The linear actuators, in turn, provide a fairly slow motion so that a simple on-off control strategy is possible. The positioner system can be controlled both manually from the operator's panel, or via a computer interface with the data acquisition computer. To prevent damage to either the magnet or test bearing, the system is provided with both electrical and mechanical motion limits. To provide axial positioning and moment restraint to the mounting plate, four 9.5mm diameter rods run from the plate to the magnet housing rear plate. This system has a very low lateral stiffness, but is designed to support significant axial and moment loads. The moment capability is required for the motor mounting system, which places a moment load on the mount plate.

During testing, the shaft alignment is measured by computing the difference between the inner and outer test bearing displacement probes in the horizontal and vertical directions. This difference is a measure of the shaft slope through the test bearing. The initial alignment is determined manually by attaching a dial indicator to the test bearing end of the shaft and sweeping the face of the test bearing housing. The rear bearing position is adjusted until the indicator run-out is zero (or some specified number if the shaft is being intentionally misaligned). Following this initial, manual alignment, the difference between the inner and outer probes in both the vertical and horizontal probes is stored.

At each desired operating point during testing, during the thermal settling phase, the test software (or operator) moves the shaft as required to return the shaft slope through the test bearing to within some tolerance of the reference position. Once the load has settled, this procedure settles rapidly. This positioning is then not disturbed while data are obtained at this test point. The procedure is then repeated at other test points. The repeatability is quite good.

Figures 60 and 61 present a comparison for both horizontal and vertical inner/outer probe differences as a vertical load of 4480 N is applied and removed, with the positioner system active and inactive. Note that although the horizontal results (Fig. 60) do show more shaft movement with the positioner active than with the system inactive, the magnitude of the misalignment is still extremely small. The increase in misalignment occurs due to the fact that the positioner system does not move the shaft

purely vertically when adjusting for the shaft deflection under load, hence some small horizontal correction is also made. Without the positioner, the vertical load results in a fairly pure vertical motion. As is noted above, however, the residual misalignment in the horizontal plane is still quite small, In the vertical plane (Fig. 61), the positioner system can be seen to substantially improve the alignment. The shaft was not rotating during these tests.

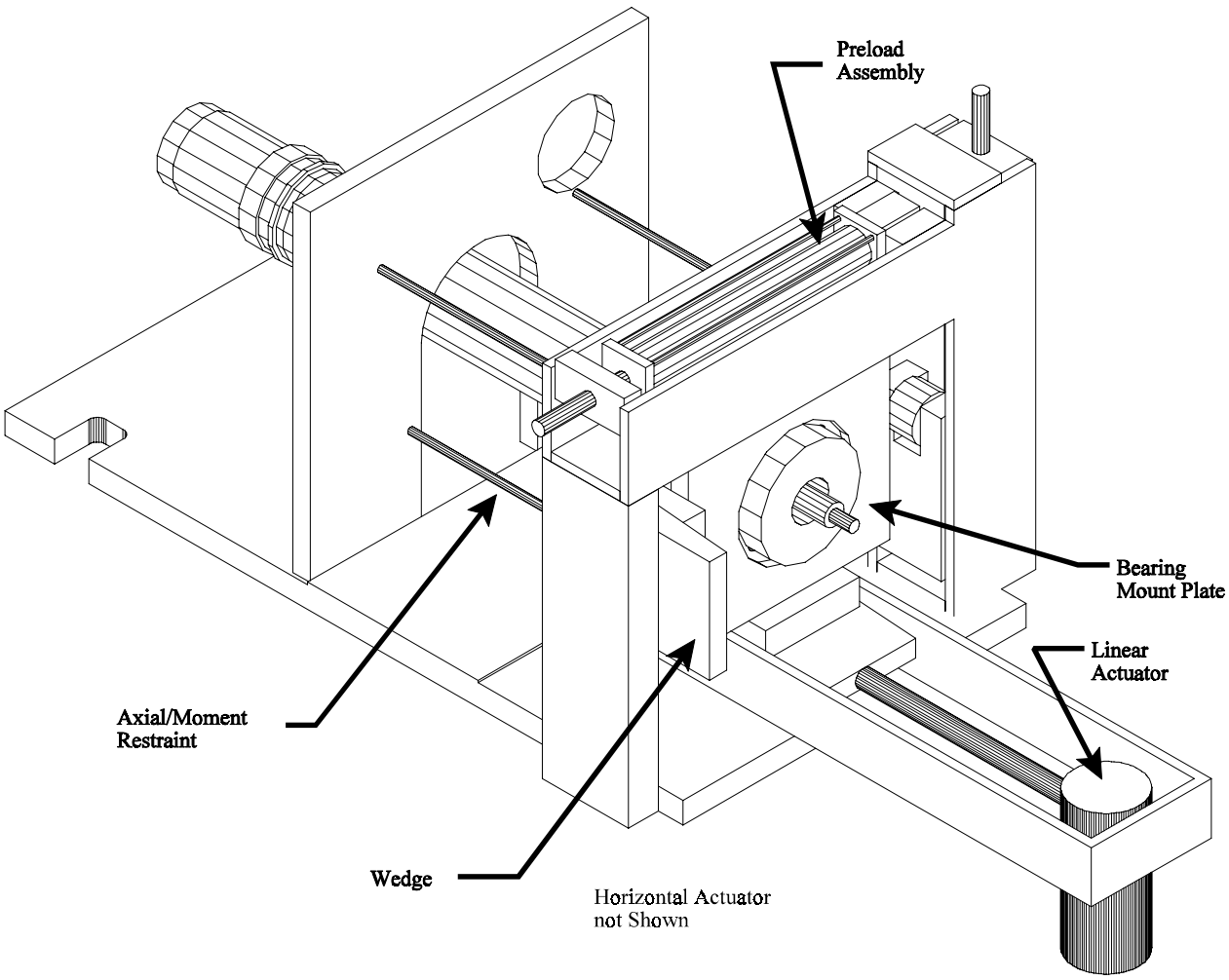

Figure 59 - Support Bearing Positioner System

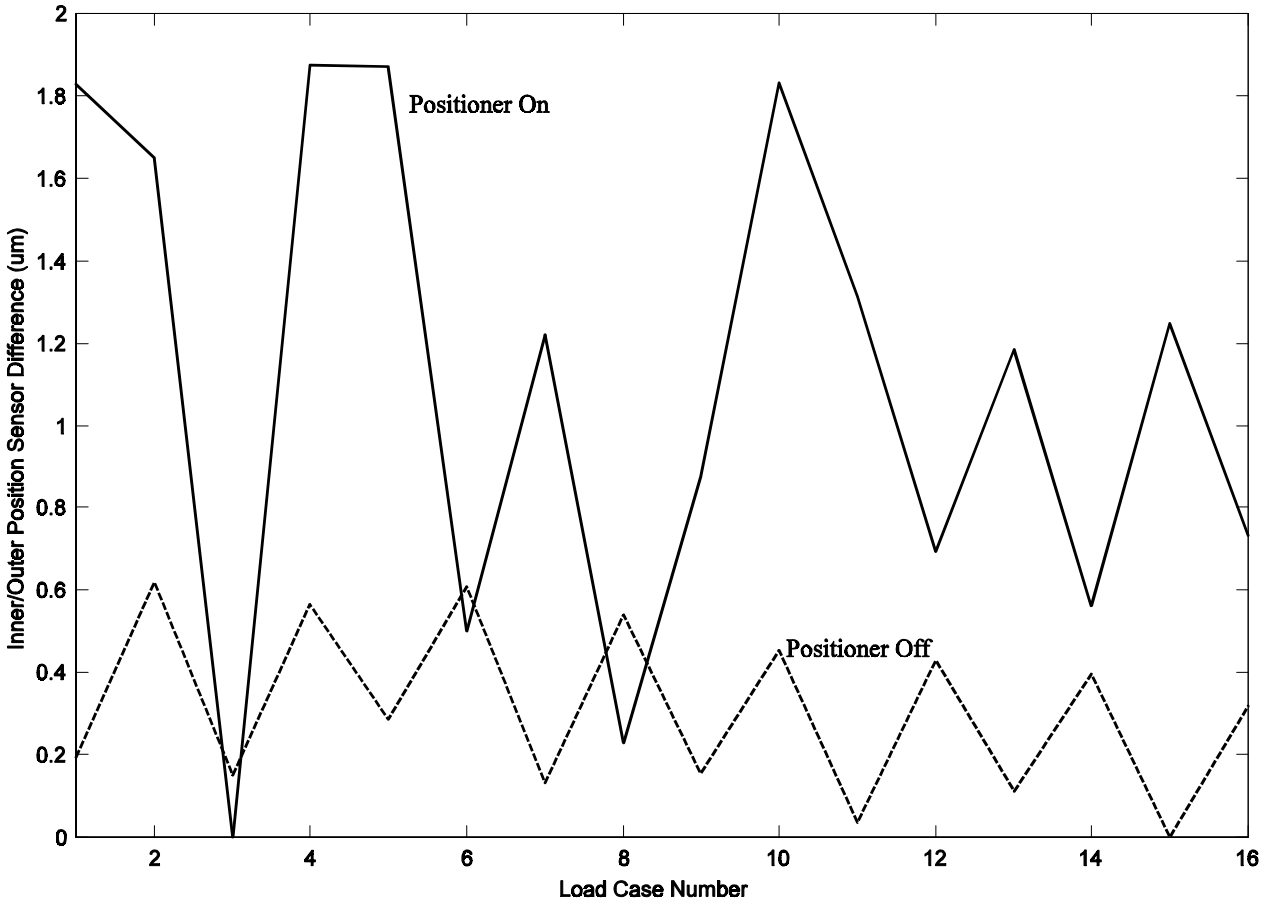

Figure 60 - Shaft Horizontal In/Out Difference for Vertical Loading, Positioner On and Off

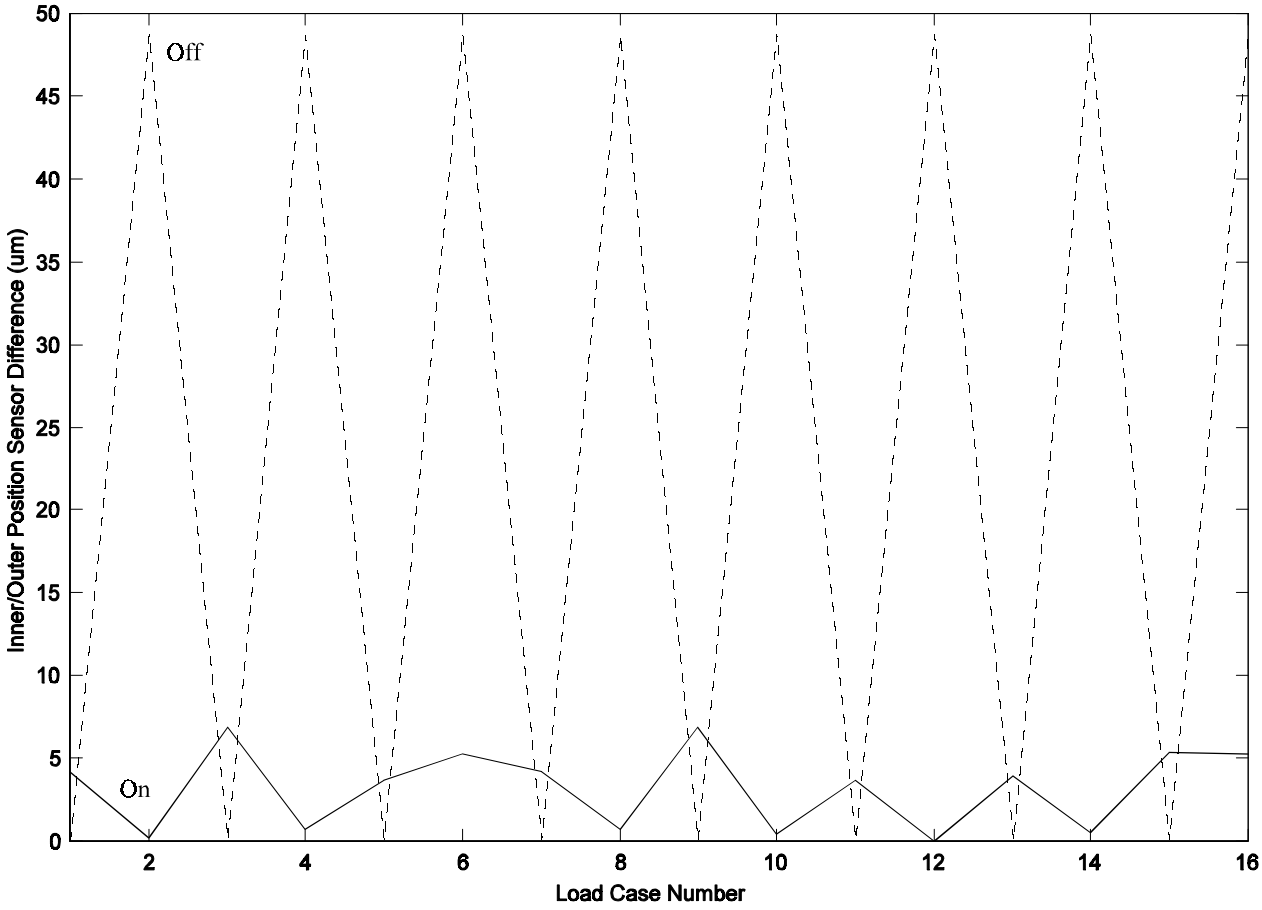

Figure 61 - Shaft Vertical In/Out Difference for Vertical Loading, Positioner On and Off

5.4 Drive System

The test rig currently has two possible drive systems. The first is the original air turbine system. The second is an electric motor based system which was built after the lab air compressor failed. Although the turbine drive system is not currently in use, it is available for future use, and is included in this work for completeness. This section describes both of these systems, as well as some common elements.

5.4.1 Air Turbine Drive

As originally designed, the test rig had an air turbine drive system. While this system does offer a very wide operating speed range, and was used quite successfully for the initial work with the test rig, it relies on a source of a substantial amount of compressed air to operate. This compressed air was provided by a surplus diesel driven sliding vane air compressor originally manufactured in 1961. This compressor suffered from some reliability problems and high cost to repair. This compressor failed, apparently as the result of a thrown vane, in the summer of 1997.

The air turbine drive supplied with the test rig is a Tech Development Co. model 50A-12. This is a small, single stage turbine originally designed to act as an equipment starter. In this application, the turbine ran at 35,000 RPM, and was fitted with a gear reducer to generate a high torque output at 2400 to 3600 RPM. The drive unit in the test rig was provided without the reduction gearing to allow rig operation at up to 35,000 RPM. Since it was produced in quantity, the cost was very low for a high speed turbine drive motor. Depending on the number of nozzles in the stator, this turbine can supply up to about 70 kW at full speed with 650 kPa supply air pressure. The turbine for the test rig has 12 nozzles, providing a maximum of 30 kW at 35,000 RPM with 650 kPa air supply. It requires approximately 25 m^3/s of air to reach this rating. The turbine is mounted to the rear support bearing mount plate via a strain gaged torque sensor. This sensor was not used due to problems with zero drift associated with temperature change and motion of the turbine air supply pipe. The turbine is coupled to the test rig through an aluminum shear shaft and a dry-diaphragm type coupling. The shear section was experimentally developed to fail at approximately 70% of the maximum coupling torque if problems arise in either the turbine or test rotor. The turbine has two speed pick-ups installed, one

which provides 30 pulses per revolution, and is used as a back-up overspeed trip. The second provides 60 pulses per revolution, and is used as the primary rig speed control sensor. The turbine also has a small thermistor temperature sensor installed adjacent to each of the two sealed ball bearings which support the turbine rotor.

Turbine speed is controlled via a 32 mm pneumatic valve and a 16 mm pneumatic valve piped in parallel as shown in Fig. 62. This arrangement provides a course and a fine air-flow adjustment. Both valves are of air-to-open design, which means if power or signal is lost to the current-to-air pressure converters (I/P) which drive the valves, they will close, thus stopping the air turbine. The I/P's are driven via a current loop by the control PC. The digital control algorithm implemented in the control PC is a modified digital proportional-integral design shown in block diagram form in Fig. 63. This system provides a way to blend the fine but limited range characteristics of the smaller control valve with the coarser, but wider range control offered by the larger valve. The system feedback signal is from a synchronous frequency counter system which measures the frequency of the pulses from the 60 pulse-per-revolution signal from the turbine pick-up. No experimental data are available for this drive system, since it is no longer in operation due to the failure of the compressor required to drive the turbine.

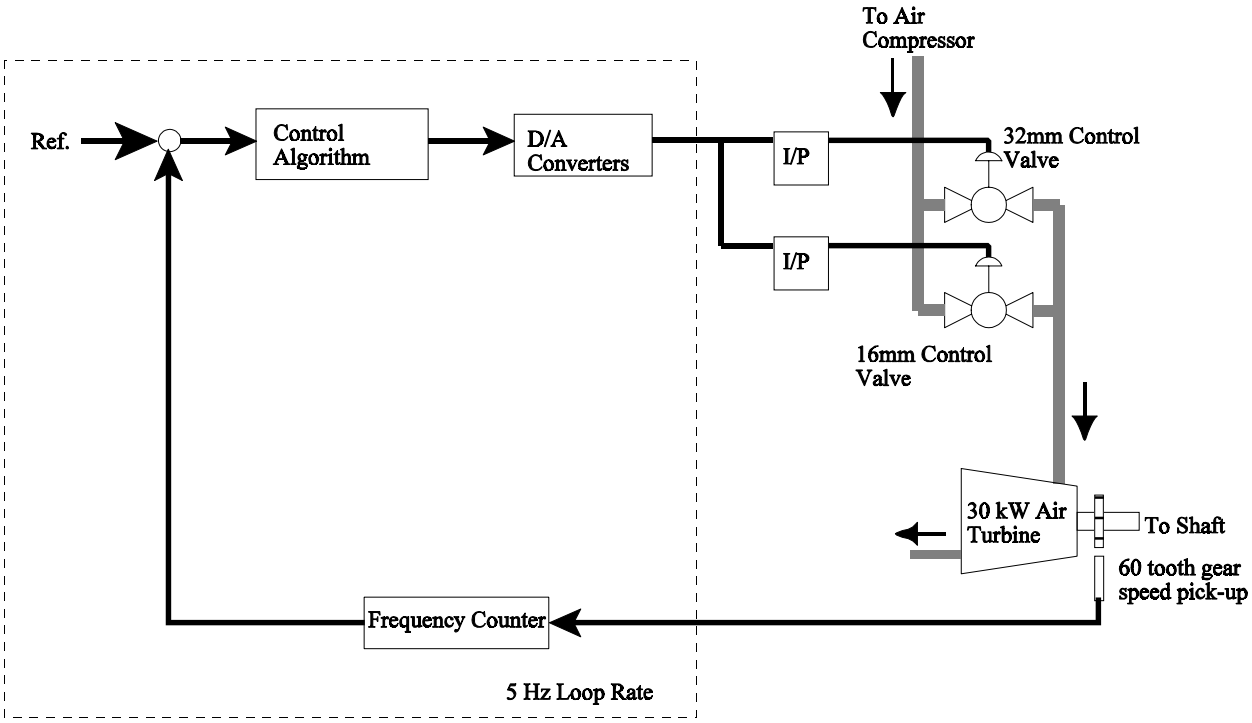

Figure 62 - Turbine Drive System

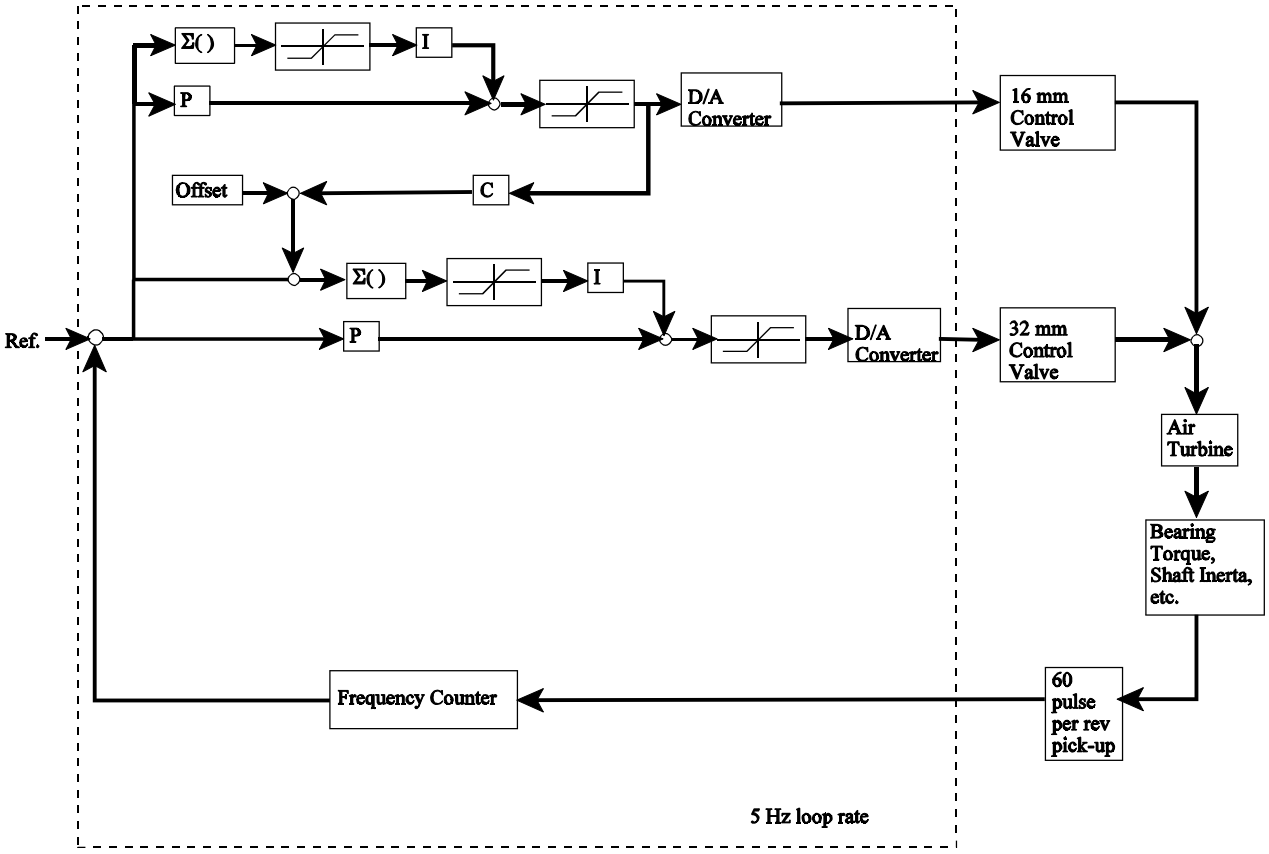

Figure 63 - Turbine Control Loop Block Diagram

5.4.2 Motor Drive System

The electric motor drive is a 15 kW belt drive system with a maximum test rotor speed capability of approximately 10,000 RPM as currently configured. Upgraded pulleys would allow a higher maximum speed. A block diagram of this system is as shown in Fig. 64. The motor is a 3-phase, 15 kW AC induction motor manufactured by Marathon Electric The motor is designed to be used with variable frequency drive systems, and is rated to 5400 RPM.

The motor speed is increased by a factor of 2.4:1 through a "poly-vee" belt drive system manufactured by Browning Inc. The belt consists of a single belt with 16 small V sections. The pulleys used in the current system are cast steel, and have not been balanced, which limits the shaft speed to less than 10,000 RPM. Operation at higher speeds is possible with balanced, machined steel pulleys. The drive sheave is attached to a short jack-shaft assembly which replaces the air turbine. This assembly uses sealed, grease packed bearings at each end. Like the air turbine, the jack-shaft is connected to the test rig rotor via a shear shaft and the dry-diaphragm coupling. As with the air turbine, a 60 tooth gear and pick-up are used to sense shaft speed.

As shown in Fig. 15, the entire drive system, including the motor, is mounted to the rear bearing support plate. This approach has the advantage that a belt tensioning idler pulley is not required to accommodate the rear bearing movement allowed by the positioner system. The drawback is a minor vibration problem. As installed, the belt vibrates far more than expected during operation. This vibration is transferred to the test rig, and is excessive at some speeds. Possible cures include another motor brace, idler pulleys, a belt guide, and/or relocating the motor to a non-moving mount. Another viable solution is to avoid speeds where the vibration causes problems.

The motor speed is varied with a variable frequency drive (VFD) manufactured by Toshiba. This drive allows control of the shaft speed by varying the frequency of the current supplied to the drive motor. The VFD is capable of driving a 30 kW motor, and should have no problem operating the15 kW motor on the test rig. The drive is controlled by a 0 to 10 volt signal from the control computer. As with the turbine, this signal is generated by a digital control loop running at 5 Hz. A conventional

PI control algorithm is used for speed control. This system is shown in block diagram form in Fig. 65.

Figure 66 presents the steady-state behavior of the system at a speed of 1000 RPM. Figure 67 shows the step response for a change in speed setpoint. As with the magnets, the response is well damped, and sufficiently consistent for the planned testing. The step response shows a slight glitch at about 32 seconds. This occurs from time to time, and is probably an artifact of noise in the frequency counter system used to measure shaft speed.

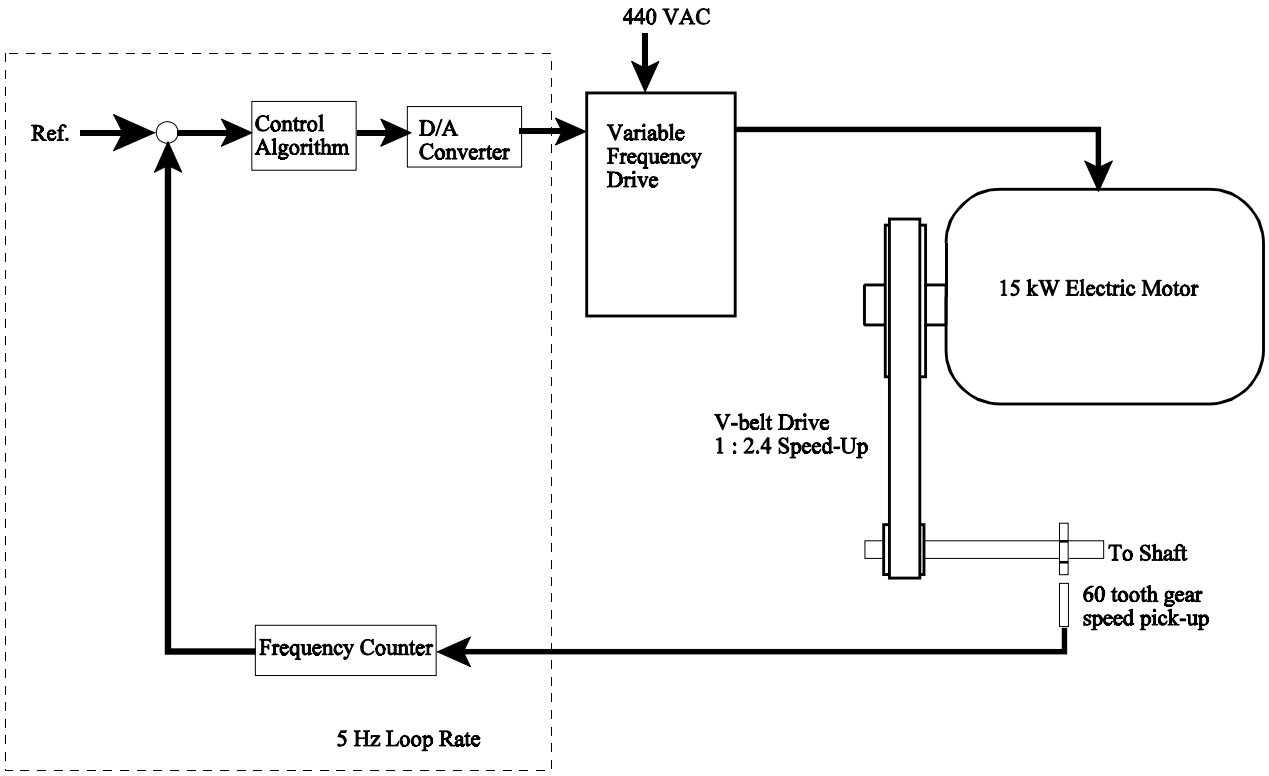

Figure 64 - Motor Drive System Block Diagram

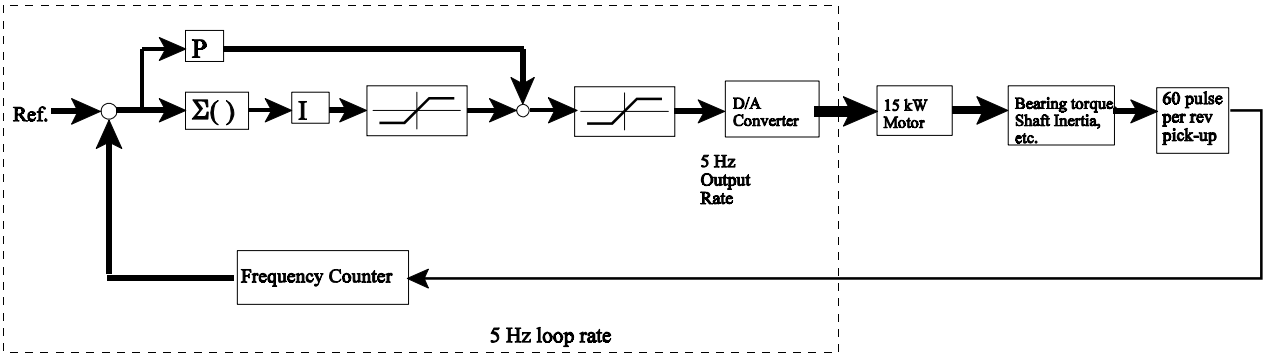

Figure 65 - Motor Drive Control Block Diagram

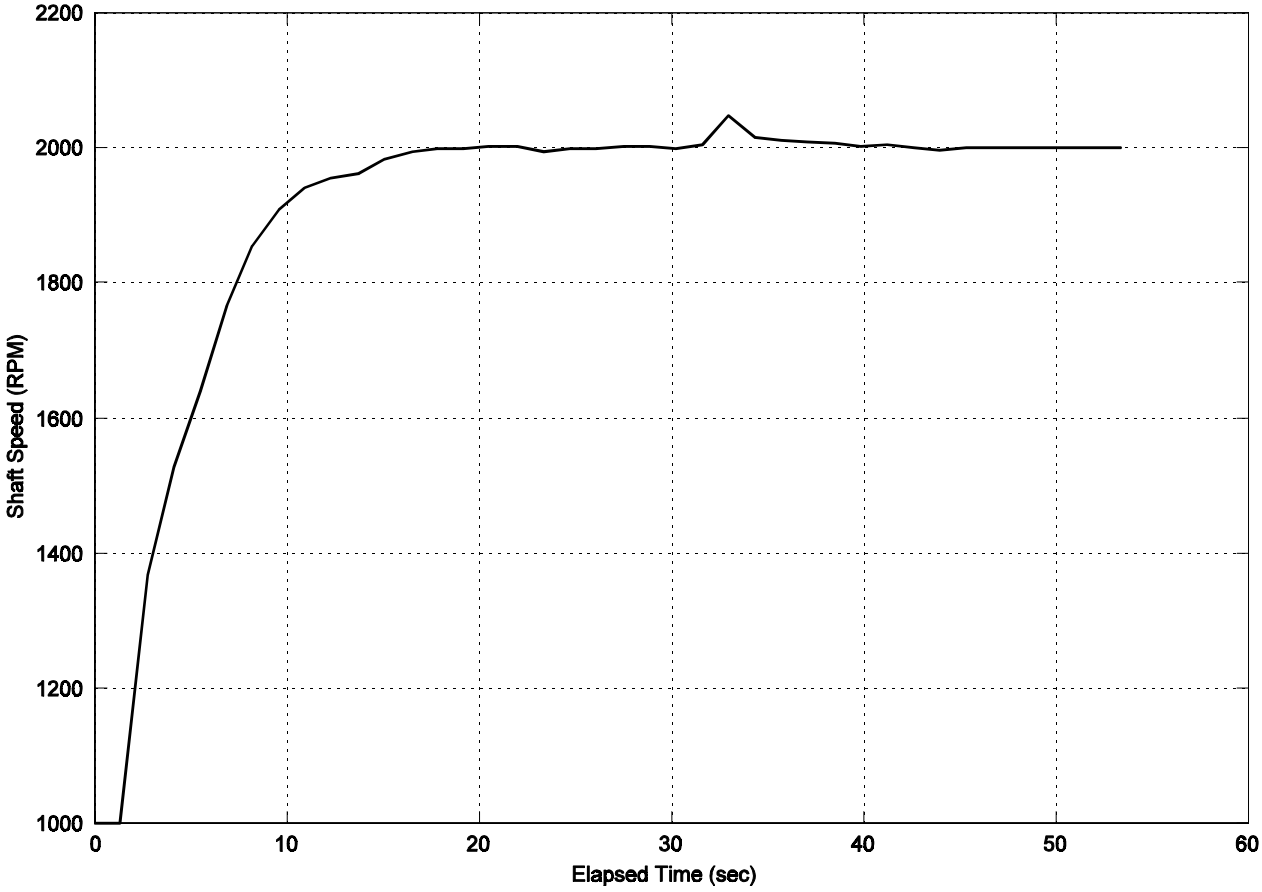

Figure 66 - Speed Control Step Response

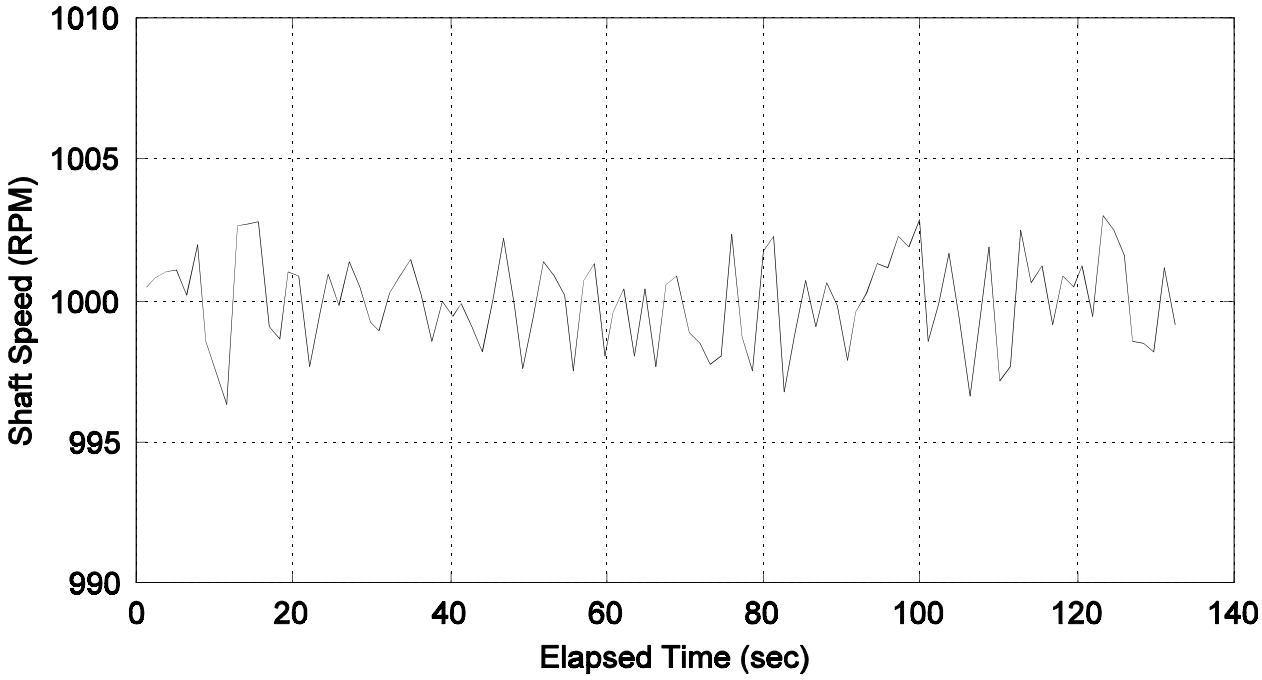

Figure 67 - Speed Steady-State Response

5.4.3 Common Drive Elements

For the purposes of rig safety, either of these drive systems will shut down in the case of problems in key rig systems. As currently configured, the drive system will shut down for:

- Low test bearing oil flow
- Low oil reservoir level (pump stops, flow stops which stops the drive)
- Low support bearing oil mister oil level
- Low support bearing mister air flow
- Loss of electrical power (turbine)

The control computer code was also designed to monitor the drive and support bearing temperatures for shut-down, but the signal conditioning hardware and computer controlled shut-down switch have not been installed. Hence, these monitoring features are not currently available.

5.4.4 Speed Sensor

Since the rig was originally designed to operate at up to 30,000 RPM, a system had to be devised which would allow measuring shaft speed with a resolution of approximately 0.5 RPM every 0.2 seconds over a speed range of 200 to 30,000+ RPM. When the rig control system was initially developed, the analog input board available had a maximum resolution of 12 bits, that is, 1 part in 4096, hence an analog solution would not have sufficient resolution. To cope with the wide operating range and sample rate requirements, a custom, synchronous frequency counter was developed. This system is implemented with a mix of custom digital hardware, counter/timer channels on the control computer analog input board, and software. A 60 tooth gear mounted to the turbine or jack-shaft and digital pick-up are used as a sensor to provide a 60 pulse per revolution signal to the system.

This system is essentially a conventional frequency counter which counts the number of events (gear tooth passing pulses) occurring over a fixed length of time. To obtain the desired resolution at low shaft speeds, while maintaining the wide (150:1) range of accurately measurable speeds, the sample time is synchronized to the input pulses to count from a starting pulse transition to an ending pulse transition. This approach avoids a potential half count error with more common non-synchronous

counter designs. This system worked extremely well when initially constructed, but suffers from occasional noise problems in the current signal conditioning cabinet.

5.5 Foundation

One of the assumptions inherent in the test set-up is a fixed boundary condition for the load cell mount. Although it is impossible for the base to be perfectly fixed in space due to finite mounting stiffness, it should be possible to have the base sufficiently rigid, with the exception of a finite number of resonance frequencies if it is securely mounted to a massive foundation. This foundation is also required to ensure safe test rig operation. The foundation used is shown in Fig. 68. It is a large reinforced concrete foundation, with an estimated mass of slightly over 7700 kg. To provide a convenient, single-point electrical ground, a 2.4 m ground rod was driven into the soil beneath the center of the foundation, and connected to the test-rig mounting anchor bolts, as well as a grounding plate via heavy wire. Figure 69 presents the results of vertical impact testing on the foundation with the rig mounted. This figure shows a well damped response to over 200 Hz.

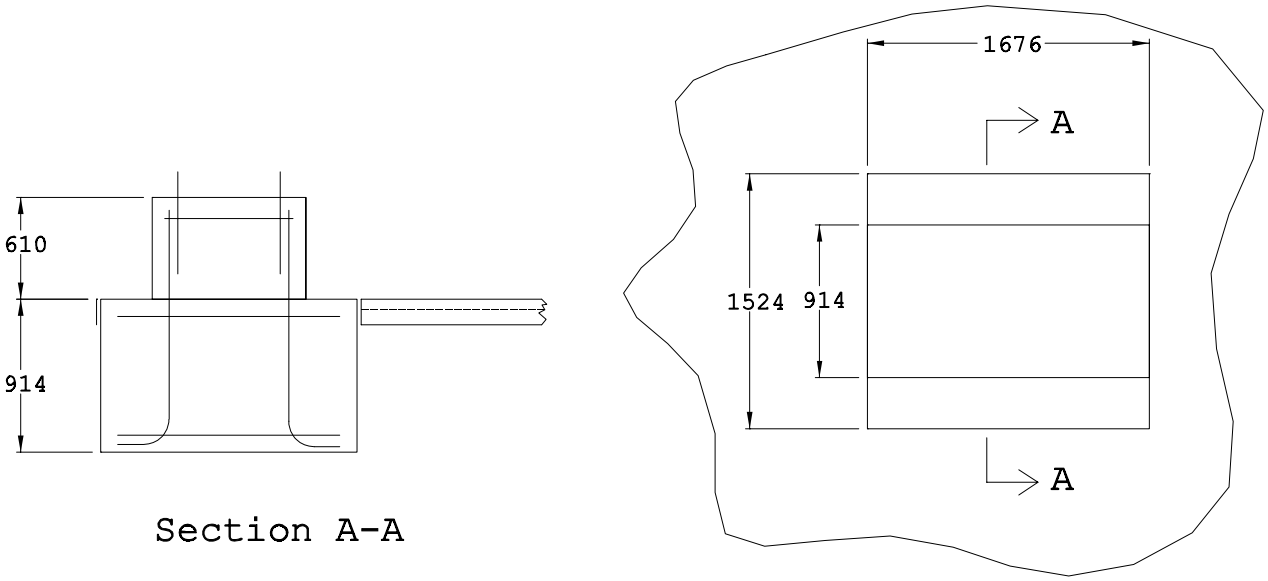

Figure 68 - Test Rig Foundation

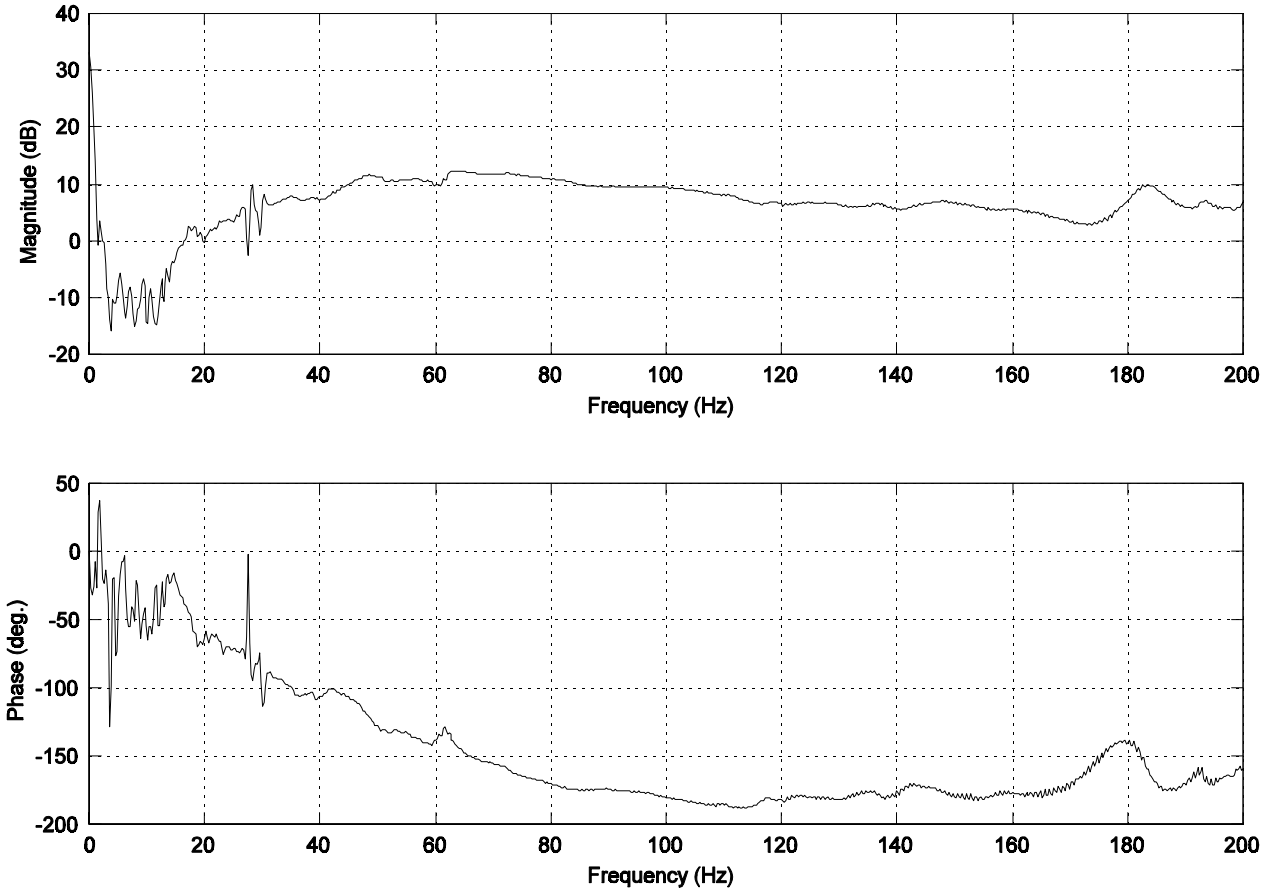

Figure 69 - Foundation Impact-Acceleration Frequency Response

5.6 Rig Electrical/Condition Monitoring

In addition to the electronic sensing and control electronic mentioned previously, there are a number of other electrical systems required to run the test rig. This section contains a brief description of each of these subsystems.

5.6.1 Rear Bearing Oil Mist Lubrication

The rear bearing is lubricated with an oil mist system. This lubrication technique is frequently used for extremely high-speed ball bearing applications, since the very fine oil mist provides a good lubrication film while the air flow provides cooling. This system is configured to stop the drive if the mister oil reservoir gets too low, or the flow through the bearing drops too low, as well as enforce a time delay between the start of oil mist flow and enabling the drive.

5.6.2 Control/Mister Air System

Both the mister system and the current to pressure converters require a source of clean, dry air. To provide a good air supply, shop air is conditioned with a prefilter, a drier and a fine post-filter. The dryer used is a desiccant system, which requires periodic maintenance to dry out the saturated desiccant. This system is provided with a solenoid valve which closes when the test rig power is turned off. This helps prolong the life of the desiccant, as well as removing the drain on the shop air system when the rig is off, in case the operator neglects to turn off the supply air valve.

5.6.3 Operator Console

One of the goals of the test rig development project was to make the rig convenient to operate. To this end, an integrated operator's console was fabricated. This console is shown in Fig. 70. This console contains all of the signal conditioning, the two computers, as well as the commercial controllers. The electrical controls (power, computer power, drive, etc.) are also located at the operator's station. The rig power control relays are mounted in a second rack located adjacent to the variable frequency drive.

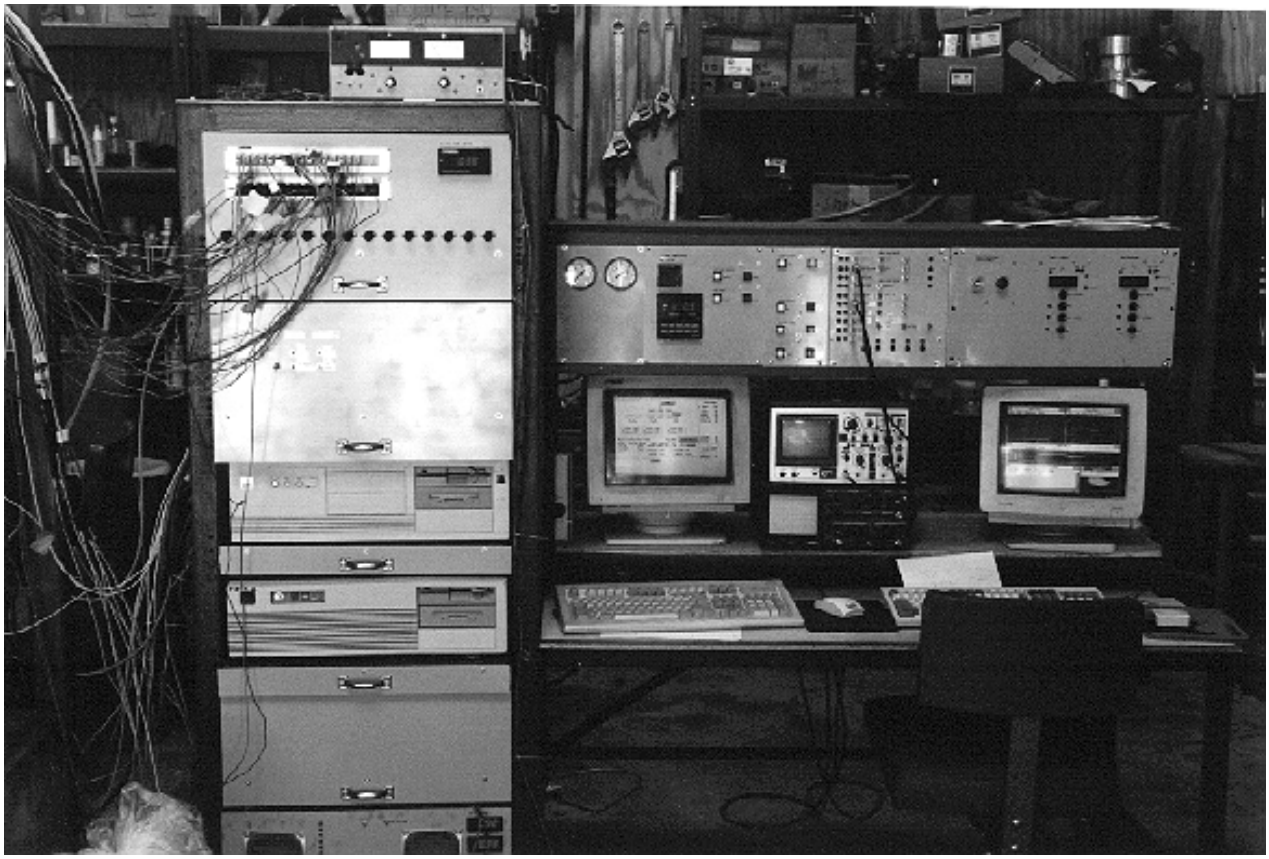

Figure 70 - Operator's Console

Chapter 6

Test Rig Operation with Steady Loads

6.1 Introduction

To demonstrate some of the test rig's current capabilities, steady-load test data for two test bearings will be presented in this chapter. These data highlight some of the features of the test rig, including repeatability, operation with light loads and automated operation. The two bearings selected are a two-axial groove bearing and a variant of this bearing known as a "pressure dam" bearing. A total of four data sets will be examined - two operating speeds for each bearing. Both shaft position and temperature data will be presented. Although the test rig also has provisions for pressure tap data, this feature was not exercised for these demonstration tests. As a point of reference, the presentation also includes a comparison with analytical predictions generated with NPADVT, the finite element based analysis code used to generate analytical bearing data in previous chapters.

6.2 Test Bearings

The two test bearings are as shown in Fig. 71 and Fig. 72. They are basically the same bearing. The pressure dam, however, has a pocket cut into the upper surface of the bearing bore. This pocket is intended to stabilize the bearing primarily by providing a hydrodynamic preload force which increases the bearing eccentricity, thus operating the bearing in a more stable region. Both bearings are steel, with a thin babbitt lining. The bearings' geometric parameters are as shown in the figures. The

locations of the thermocouples in each bearing are shown in Fig. 73 and Fig. 74. The thermocouples in each bearing are located at the bearing axial centerline, approximately 3mm from the surface of the bearing. Thermocouples 10, 11, and 12 in the two axial groove bearing are located in an axial row. Thermocouple 11 is in the center; 10 and 12 are approximately 1/4 of the length of the bearing from the edge of the bearing. The locations of the thermocouples in the bearing housing are numbered as in Fig. 75. The geometric locations of the housing thermocouples have been presented in Fig. 42. The remaining test parameters are presented in Table XVI.

Note that the oil viscosity is described as “uncertain”. Although the oil is an ISO-32 oil, with well defined viscosity-temperature characteristics, the combination of bearing cavitation and the relatively small oil reservoir results in a tremendous amount of entrained air in the oil. Figure 76 presents a photograph of a transparent section of pipe at the oil inlet to the test bearing housing immediately after the oil pump was shut down following one of the tests. As can be seen, a large number of small, but visible, air bubbles are present. Because of the presence of this entrained air, it is unclear what viscosity should be assigned to the oil. Intuition would suggest that bubbly oil would intuitively have a lower effective viscosity, but the oil film pressure in the minimum film thickness region of the bearing is very high, thus compressing the air bubbles, hence reducing the impact of the air. Even if the entrained air were modeled by the available code (NPADVT), there is no provision on the test rig to quantify the amount of entrained air.

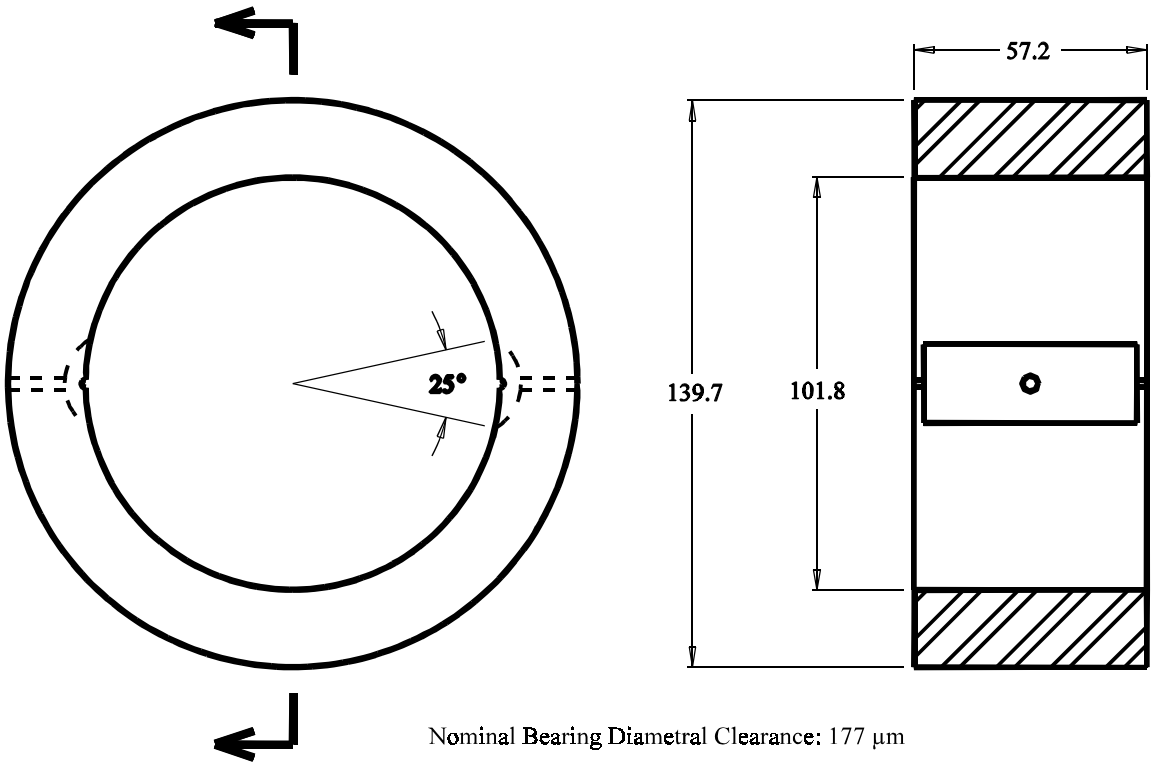

Figure 71 - Two Axial Groove Bearing Geometry

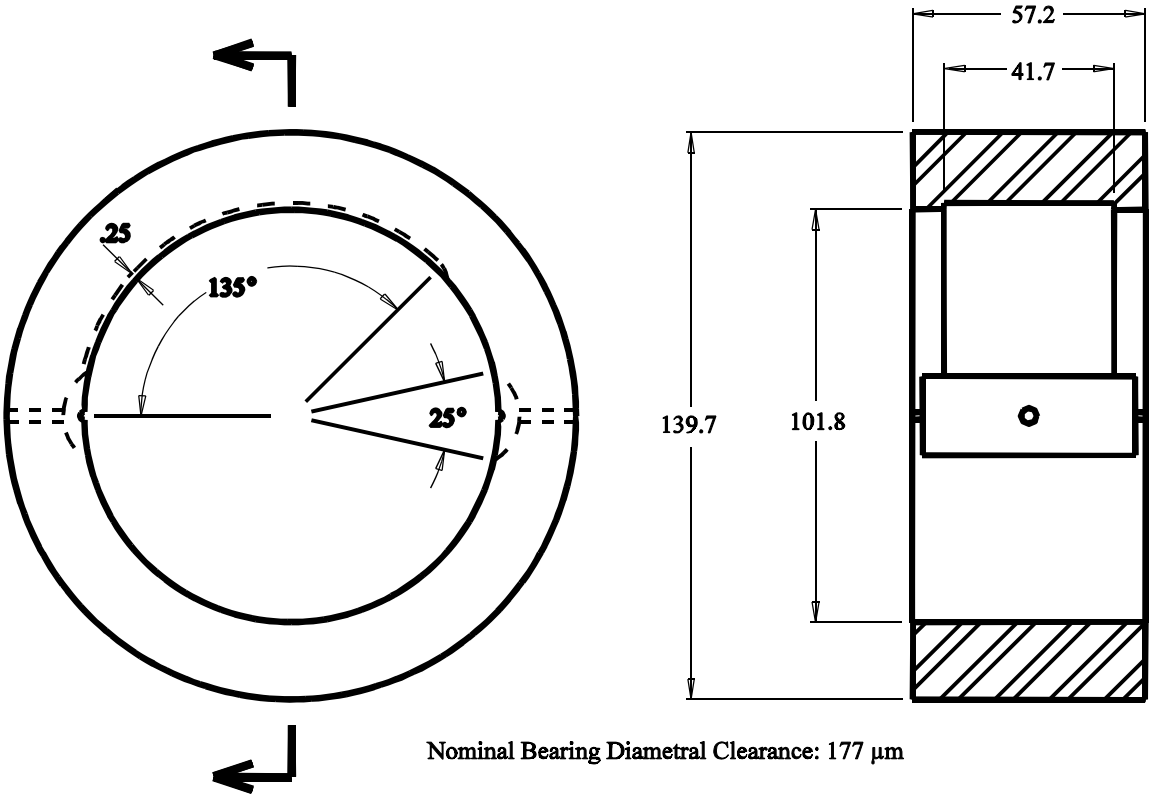

Figure 72 - Pressure Dam Bearing Geometry

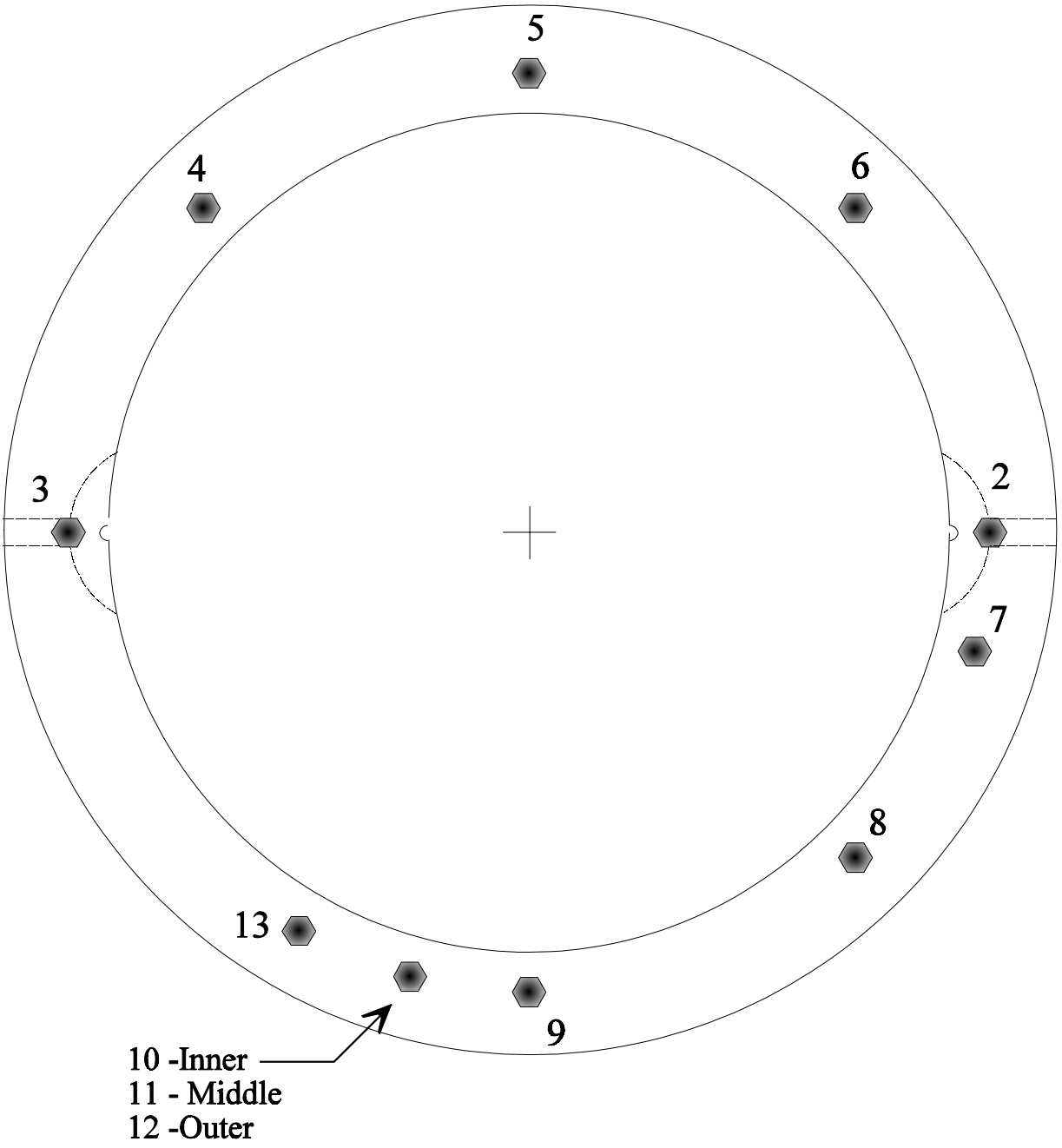

Figure 73 - Two Axial Groove Bearing Thermocouple Locations

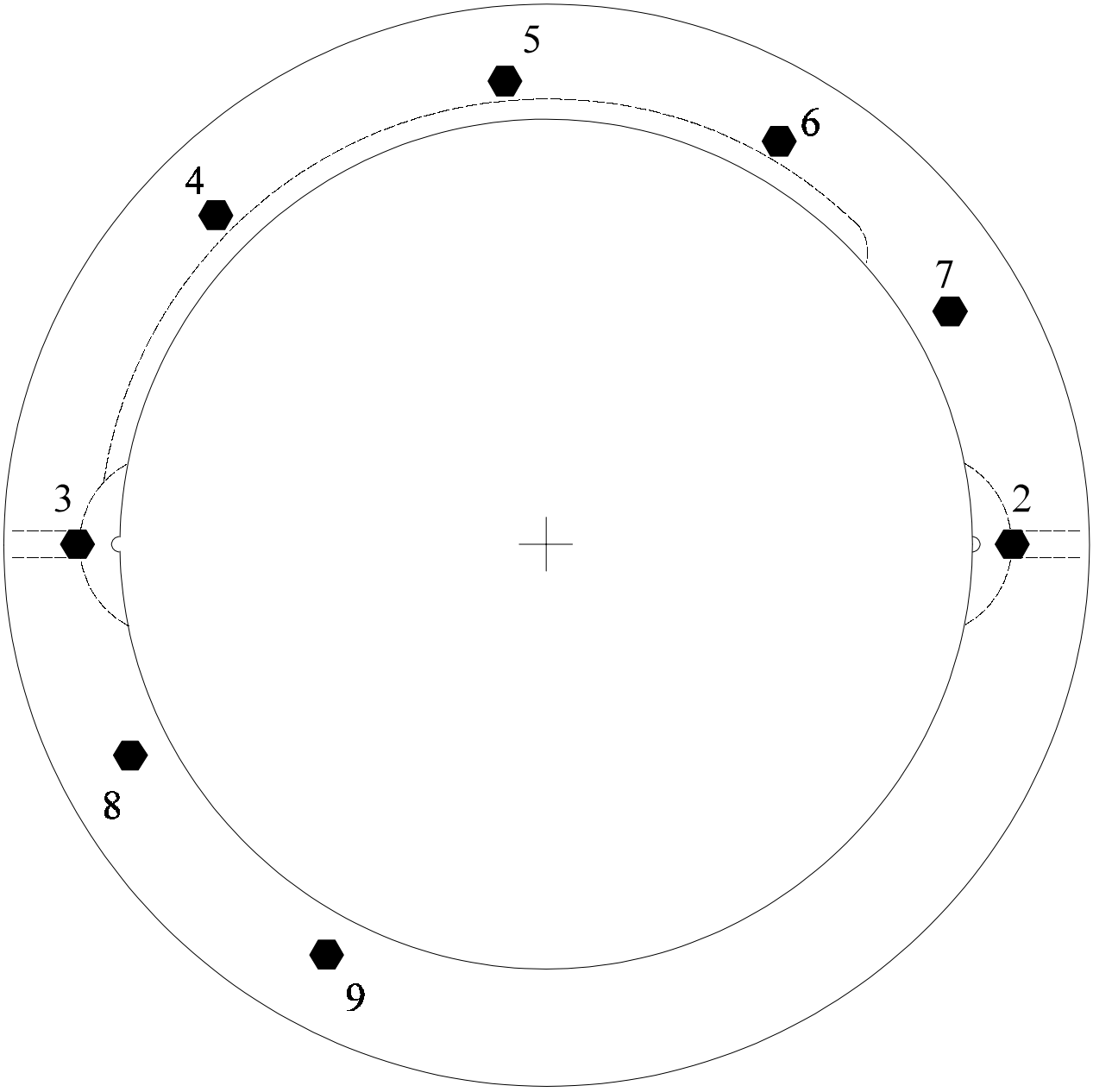

Figure 74 - Pressure Dam Bearing Thermocouple Locations

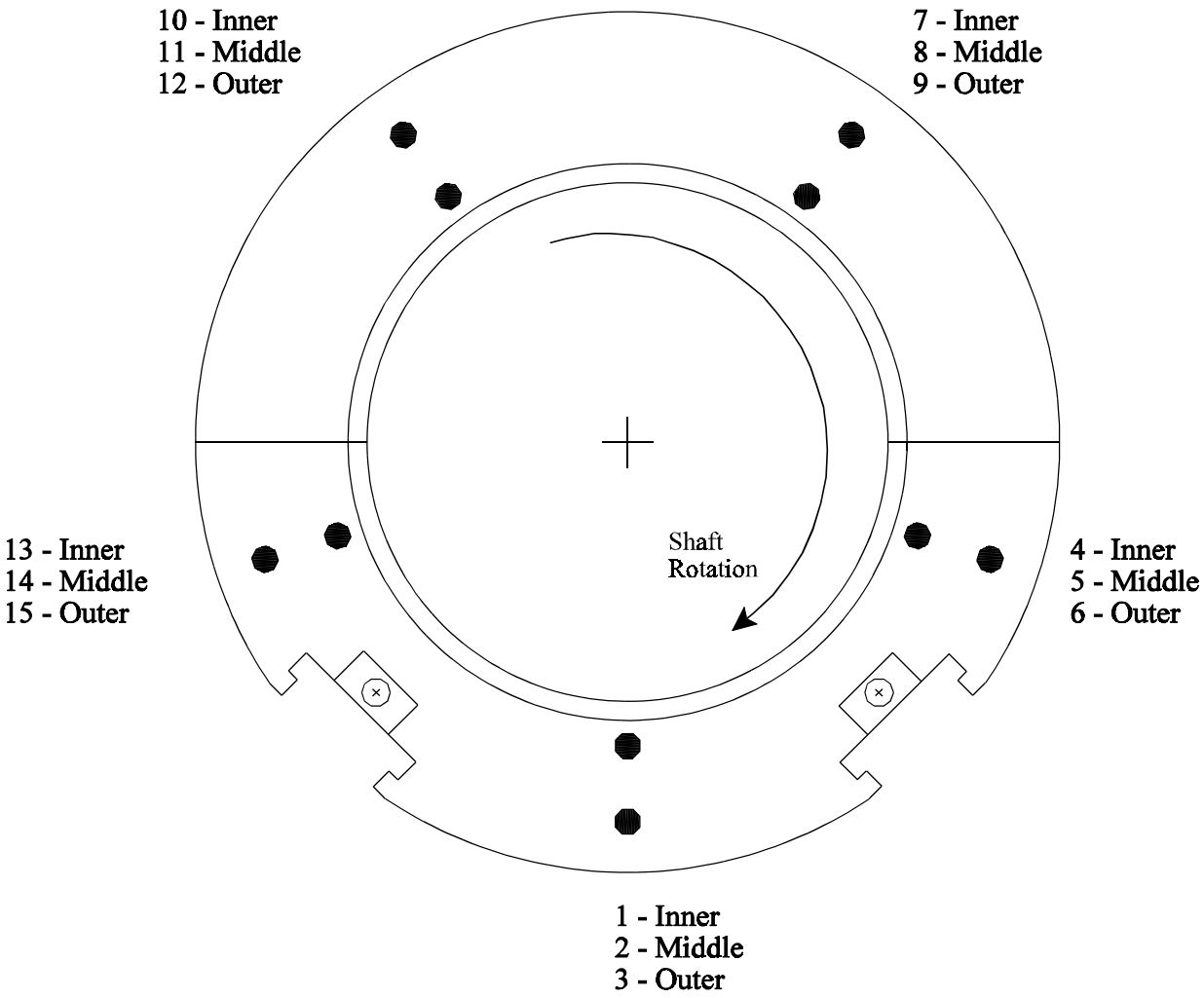

Figure 75 - Housing Thermocouple Locations

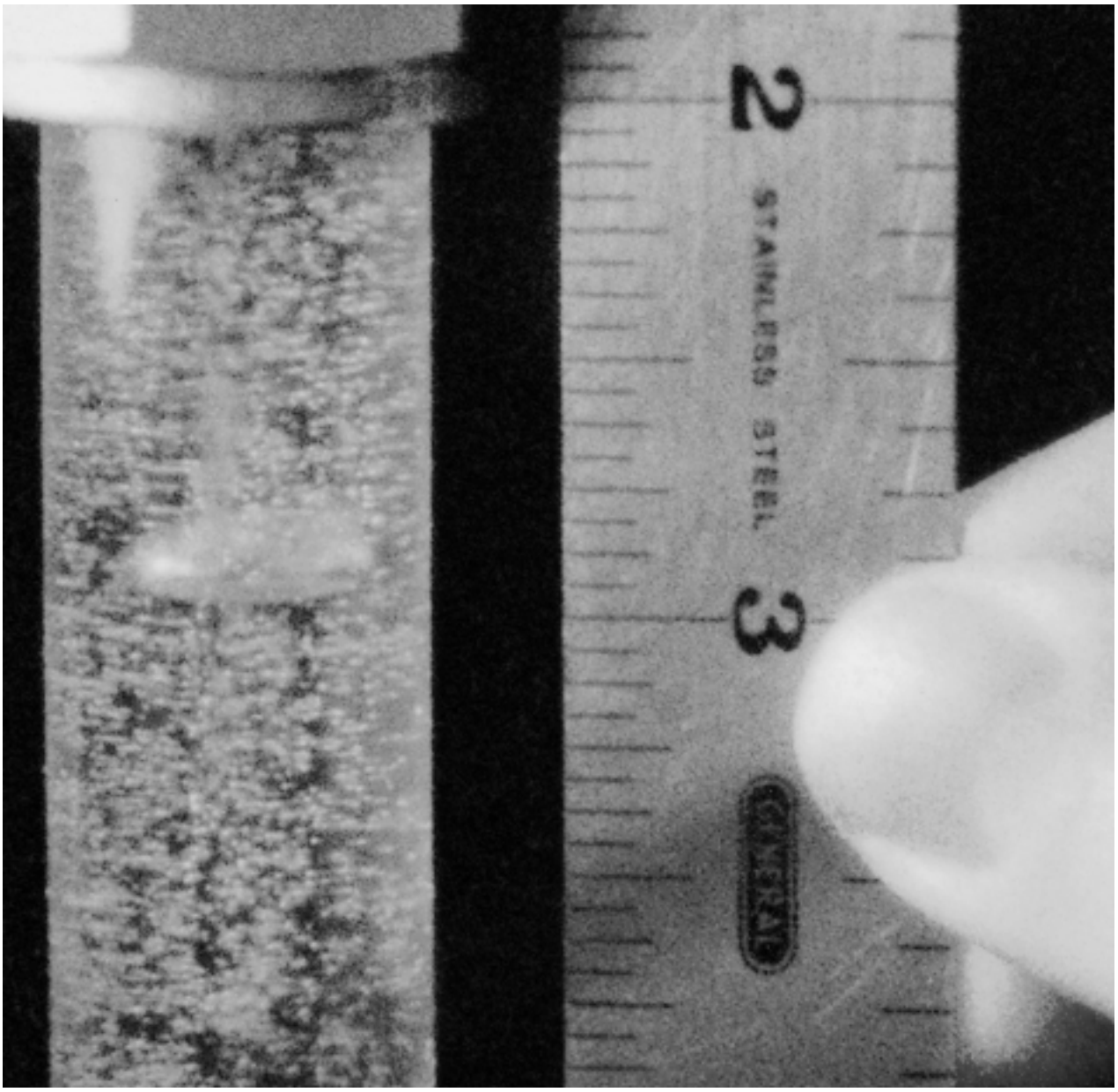

Figure 76 - Bubbles in Oil Inlet (Scale shown in inches, mm = in*25.4)

Table XVI - Test Conditions

Parameter	Value(s)
Shaft Speed	1500 RPM, 5000 RPM
Applied Load Range	2270 N to -7120 N at magnet
Oil	Exxon Teresstic-32, ISO-32
Oil Inlet Temperature	37.7 °C
Oil Flow Rate	10 l/min (2AG), 18 l/m (P.Dam)
Oil Viscosity	Uncertain

6.3 Test Sequence

The sequence followed for each bearing test is as follows:

1) Test bearing insert installed in holder, oil system started and rig operated at 1500 to 5000 RPM under medium load to bring insert temperature to operating temperature (if rig was not at temperature from a previous test run).
2) Reference thermocouple for housing and bearing placed in ice bath
3) Rig an oil system shut down to allow shaft alignment to be checked mechanically
4) Alignment set and rig restarted under program control (Matlab .m file, as in Appendix B)
5) Program starts rig, sets speed, and steady load for desired test condition
6) Program resets shaft alignment based on difference between inner and outer position sensors to restore alignment as required once operating speed and first load are reached
7) Program waits 500 seconds for thermal settling, shaft alignment is checked and reset during wait
8) Position and thermocouple data are acquired, load and speed are obtained from control computer, and all data are stored to file
9) Next test point is set and 500 second settling period begins.
10) After all test points have been acquired, rig may be stopped or next test sequence started.

The nominal vertical magnet loads for the loading sequences used for the results presented in this chapter are as shown in Table XVII. The loading cycle begins at the top of the list, and proceeds downward until data are recorded at all desired loads for a given operating speed. All of the horizontal loads for these tests are set to zero.

Table XVII - Nominal Magnet Vertical Load Settings for Tests (Loads in N)

Two Axial Groove		Pressure Dam	
1500 RPM	5000 RPM	1500 RPM	5000 RPM
1380	1380	1380	1380
2270	2270	2270	2270
-1110	-1110	-1110	-1110
-2000	-2000	-2000	-2000
-3115	-3115	-3115	-3115
-4450	-4450	-4450	-4450
-7120	-7120	-7120	-7120
-3115	-3115	-3115	-3115
-2000	-2000	-2000	-2000
-1110	-1110	-1110	-1110
-2000	(restart)	-2000	-2000
-3115	1380	-3115	-3115
-4450	2270	-4450	-4450
-7120	-1110	-7120	-7120
-3115	-2000	-3115	-3115
-2000	-3115	-2000	-2000
-1110	-4450	-1110	-1110
1380	-7120	1380	1380
2270	-3115	2270	2270
	-2000		
	-1100		
	1380		
	2270		

6.4 Measurement Uncertainty

As has been noted in previous chapters, the precise calibration of the test bearing displacement and force sensors and the magnet force sensors is not part of this work; hence, it is difficult to assign an appropriate uncertainty to these measurements. However, it is unlikely that the measurements are in error by more than 10 percent of the full range, based on preliminary calibration data which were obtained (but not presented as part of this work). Therefore, for the magnet force sensors, a reasonable estimate of the measurement uncertainty upper bound is ±800 N. The load cell specifications presented in chapter three result in a combined nonlinearity/non-repeatability/hysteresis error specification of ±23 N (root-sum-of-squares combination), which is probably a reasonable lower bound for the magnet force transducer. These uncertainty measurements apply only to the magnet force measurement. No statement will be made regarding the load at the test bearing in this work. Also, due to the high pass nature of the piezo-electric sensors used for at the test bearing, no data from these sensors will be presented for the steady-load tests presented in this chapter.

With regards to the test bearing displacement measurements, an appropriate measurement uncertainty upper bound is probably on the order of ±12 μm. Again, the non-repeatability of the measurement is probably an order of magnitude better than this figure, but no data are available to assign a more precise number.

The thermal measurements are probably accurate to within ±2°C, although this figure has not been verified beyond noting that the measurements agree at room temperature equilibrium to this accuracy.

6.5 Test Data

Figure 77 presents the shaft position data for the two-axial groove bearing in polar form. The data for 5000 RPM is the combination of the two data sets as indicated in Table XVII. This combination was required after the data acquisition computer locked-up while taking the data for 5000 RPM. It is unclear if this was a random problem, or the result of trying to take both the 1500 RPM and 5000 RPM data sets without restarting the test rig. This problem did not occur during the pressure dam

tests, which were run separately from one another. The experimental data points correspond to increasing vertical load, with +2270 N at the top, -7120 N at the bottom.

In this figure, the experimental shaft position data have been centered by taking the average of two sets of loads applied both vertically up as well as vertically down (i.e., average the measured vertical position for ±1380 N and the ±2270 N vertical loading to establish the vertical center, then likewise for the horizontal data and position). This procedure, which has been employed by several other researchers, locates the operating center for a symmetric bearing such as the two-axial groove bearing with vertical loading. The NPADVT predictions for the shaft locus for vertical loading for both speeds have also been plotted on this figure. Figure 78 presents the corresponding temperature data for the bearing for 1500 RPM for three different load cases as indicated on the figure. In this figure, the data recorded during the test are indicated by points. The average temperatures for each load/thermocouple location are connected by lines as indicated. Figure 79 presents the corresponding temperature data for the housing thermocouples for 1500 RPM operation. Figures 80 and 81 present the measured bearing and housing temperatures for 5000 RPM. The results for housing thermocouple number 9 are omitted due to problems with the sensor.

Figure 82 presents the shaft position data for the pressure dam bearing in polar form. Since this bearing does not exhibit the vertical symmetry of the two-axial groove bearing, these data could not be centered as with the two axial groove bearing data sets. Instead, since the goal of this test was not a rigorous comparison between analysis and experiment, the zero for the experimental data has been adjusted vertically and horizontally as required to achieve some degree of similarity with the curve generated by NPADVT. Note that the shaft locus for this bearing is more nearly vertical, indicating a lower amount of stiffness cross-coupling in the bearing. This reduction in the cross-coupled stiffness is responsible for this bearing' s increased region of stable operation (lower loads, and higher speeds) relative to the two axial groove design. Figures 83 and 84 presents the temperature data for the bearing and housing for 1500 RPM operation. The same load cases as were presented for the two axial groove bearing are shown. Again, the data are indicated by points, and the average of the load/thermocouple readings are connected by lines as indicated. Figures 85 and 86 presents the

temperature data for the bearing and housing for 5000 RPM operation. As with the two axial groove data, housing thermocouple 9 has been omitted due to problems with the sensor.

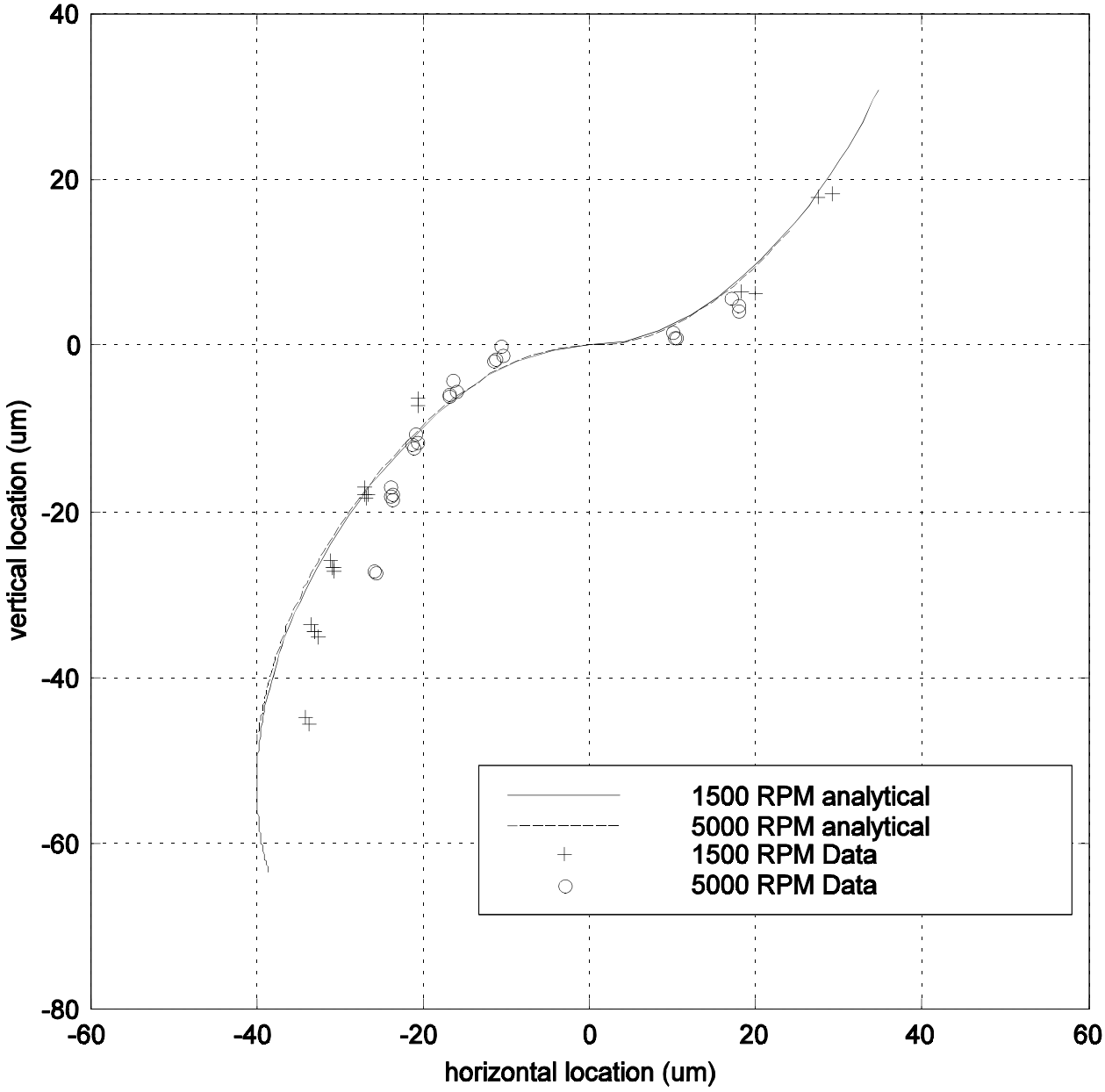

Figure 77 - Shaft Locus for Two Axial Groove Bearing

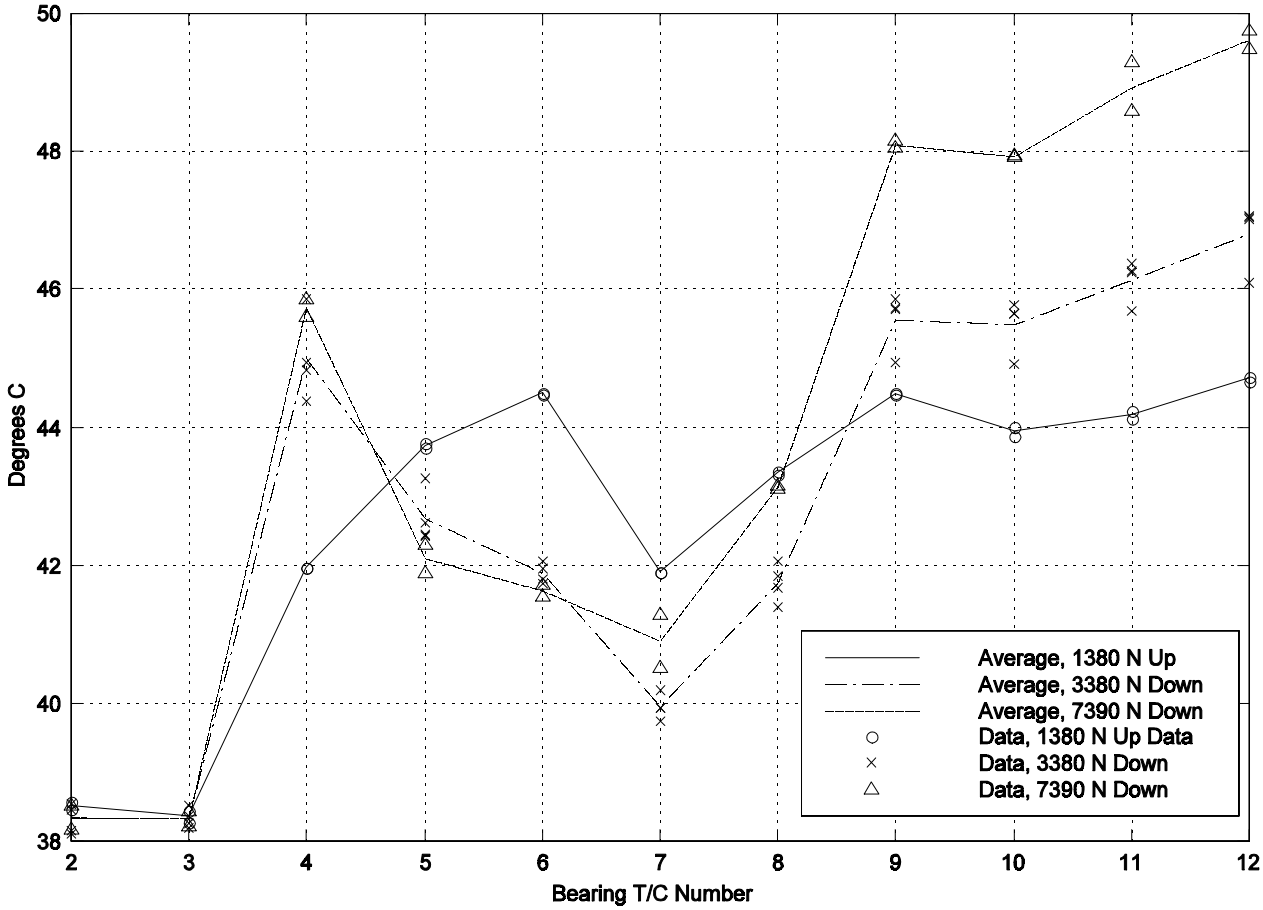

Figure 78 - Bearing Temperatures, 1500 RPM Two Axial Groove Bearing

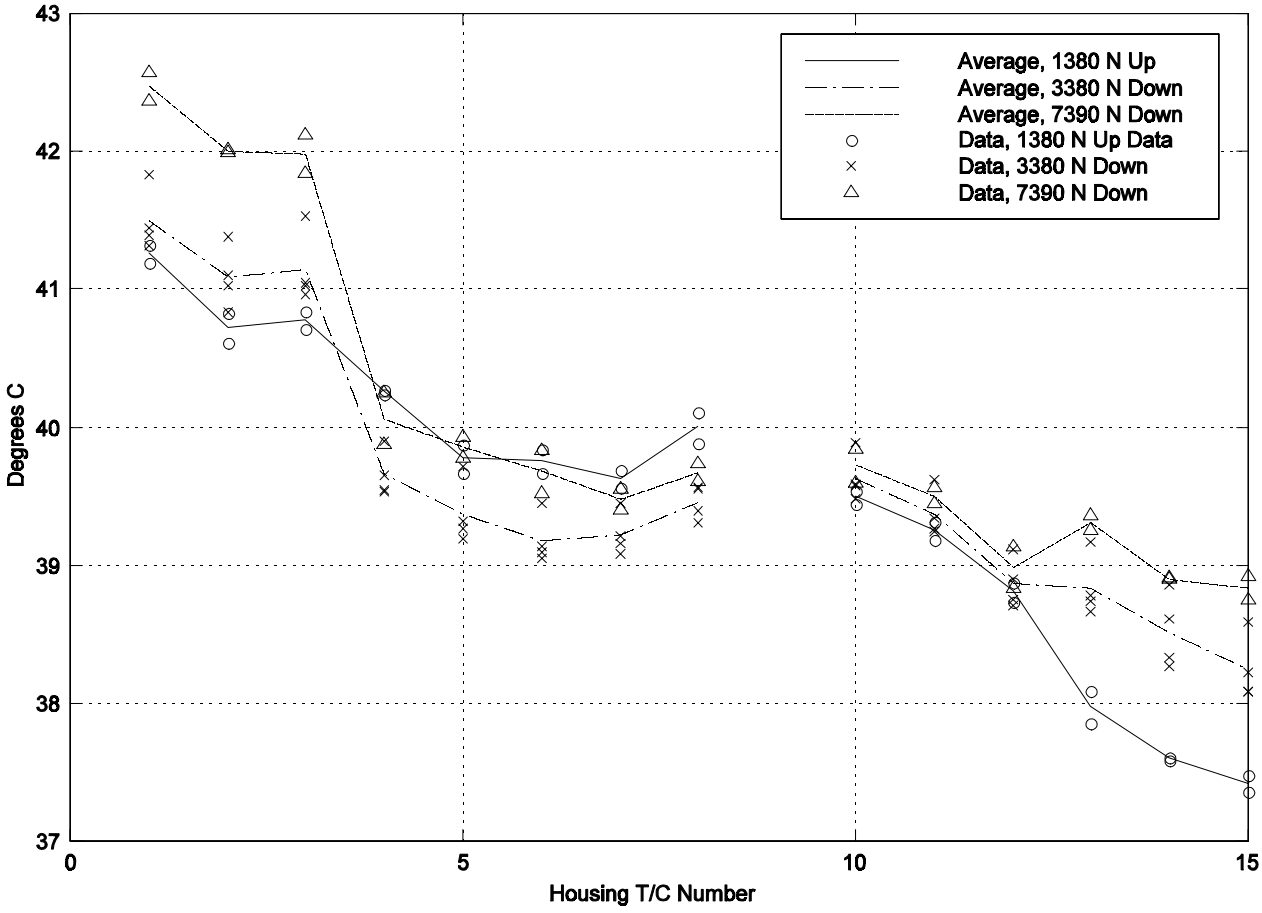

Figure 79 - Housing Temperatures, 1500 RPM Two Axial Groove Bearing

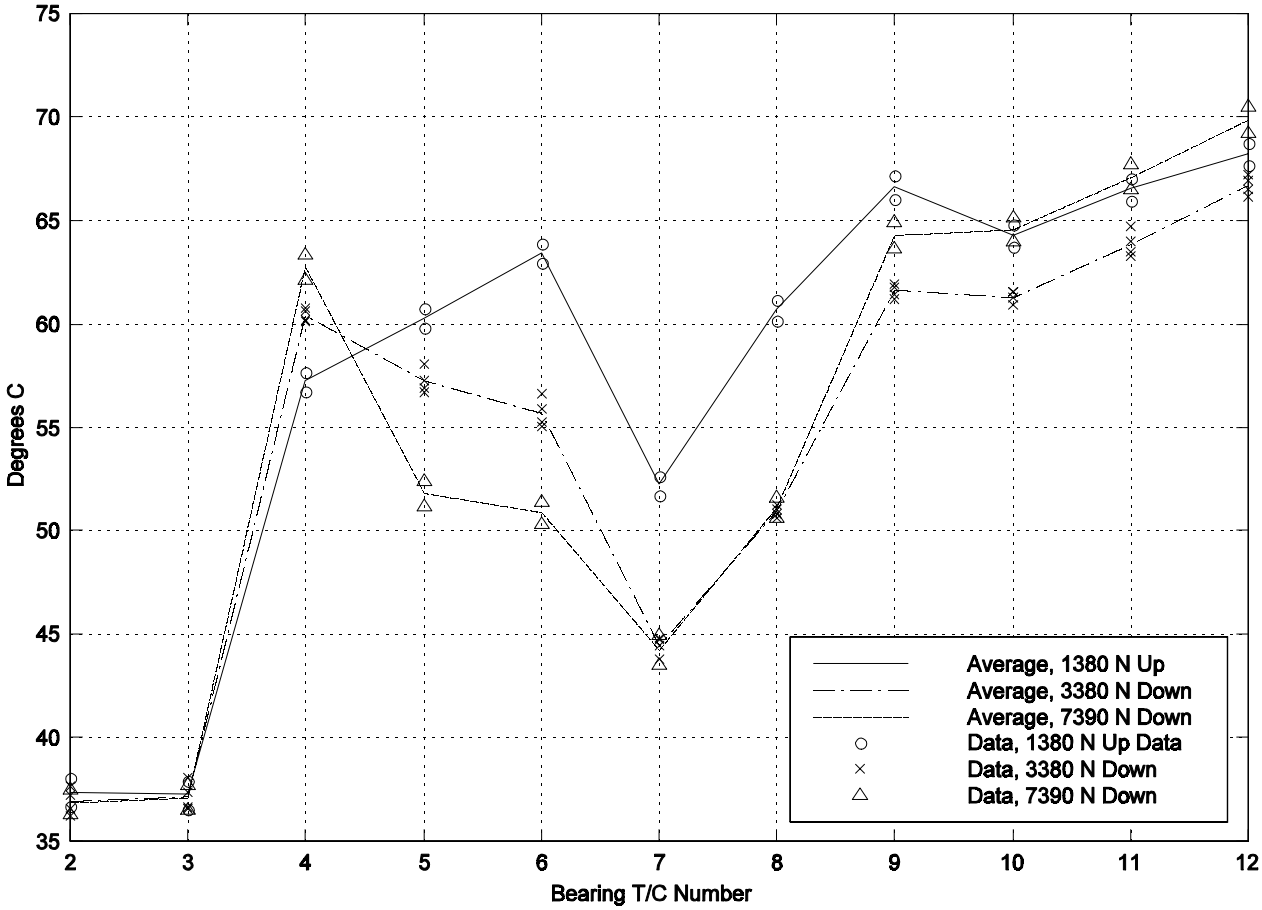

Figure 80 - Bearing Temperatures, 5000 RPM Two Axial Groove Bearing

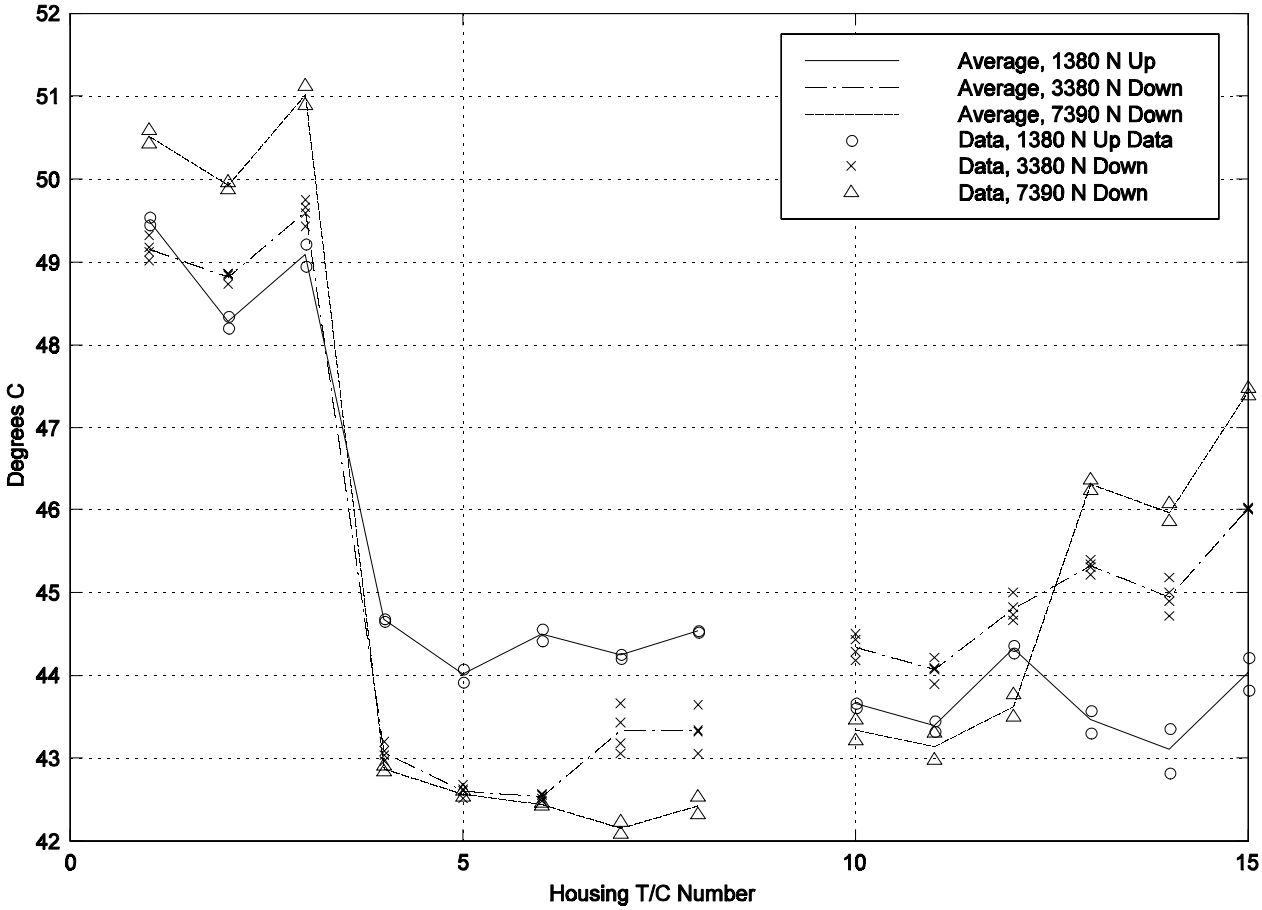

Figure 81 - Housing Temperatures, 5000 RPM Two Axial Groove Bearing

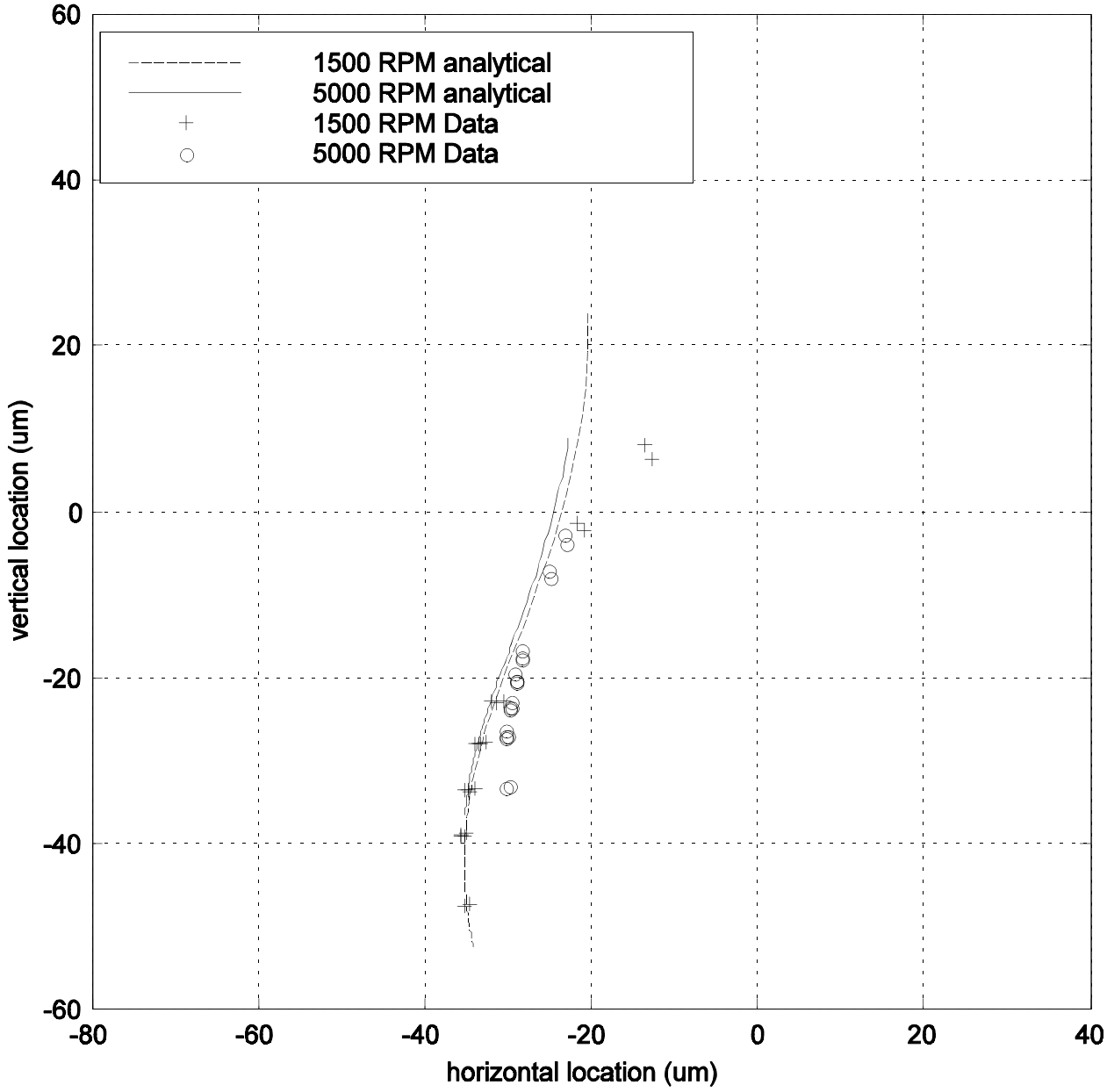

Figure 82 - Shaft Locus for Pressure Dam Bearing

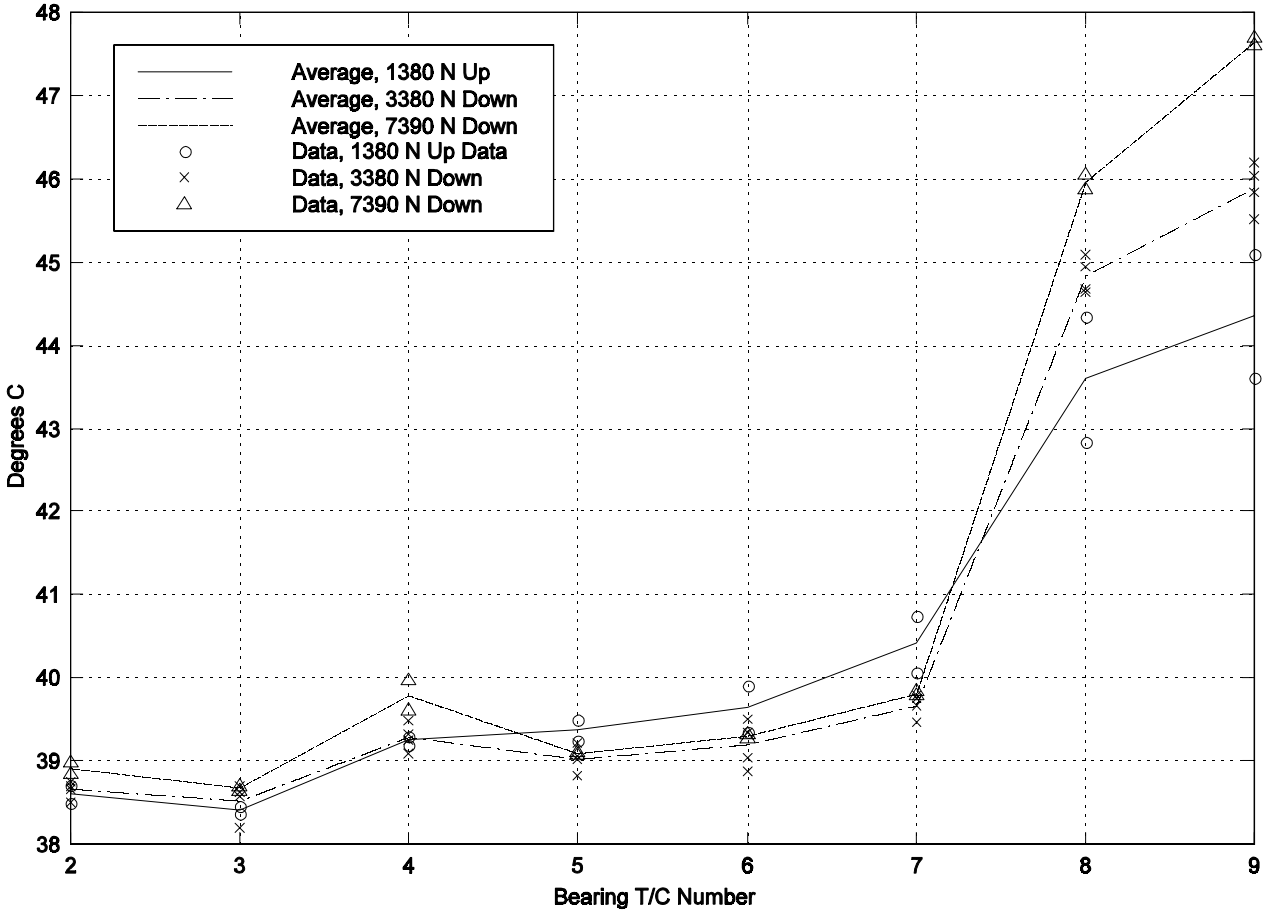

Figure 83 - Bearing Temperatures, 1500 RPM Pressure Dam Bearing

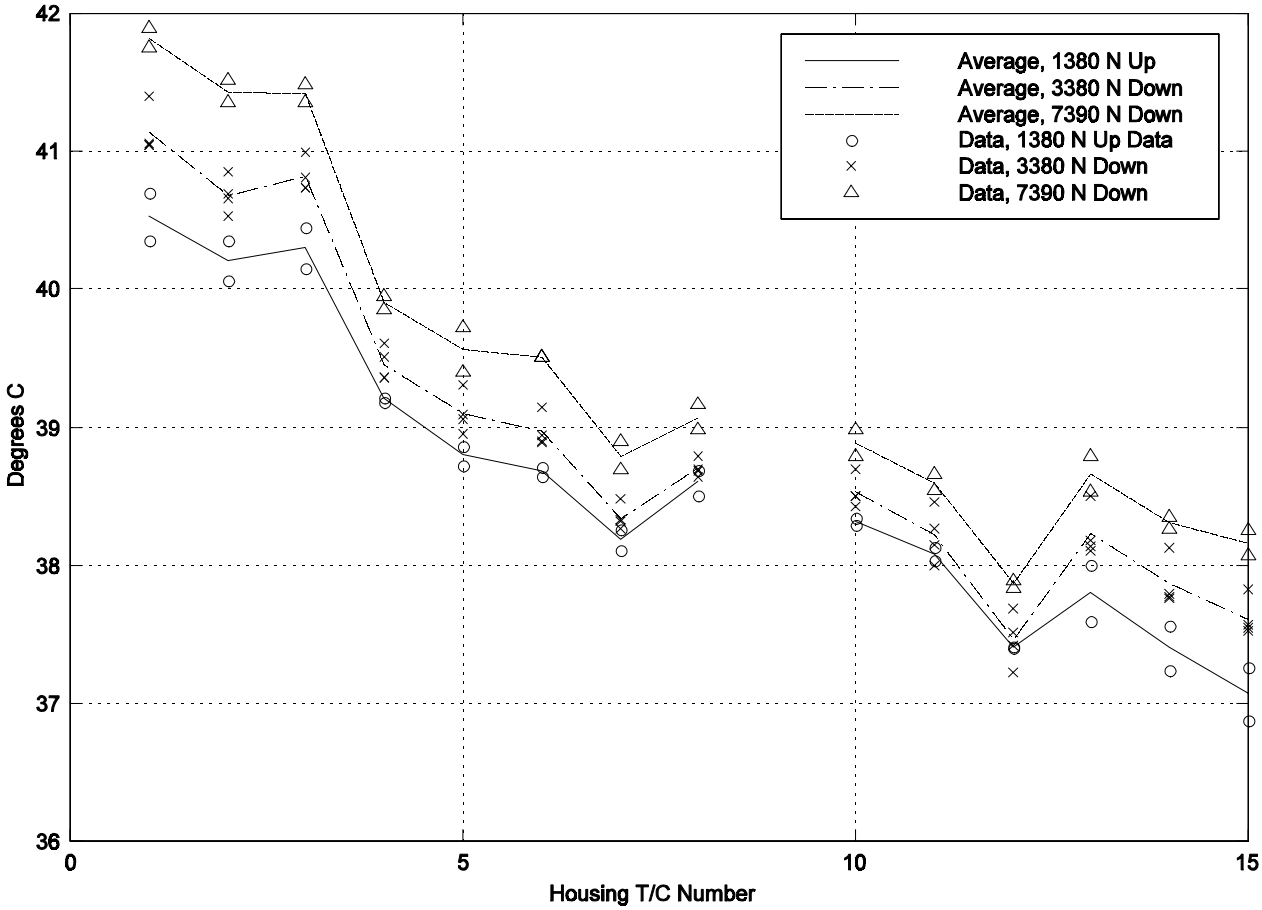

Figure 84 - Housing Temperatures, 1500 RPM Pressure Dam Bearing

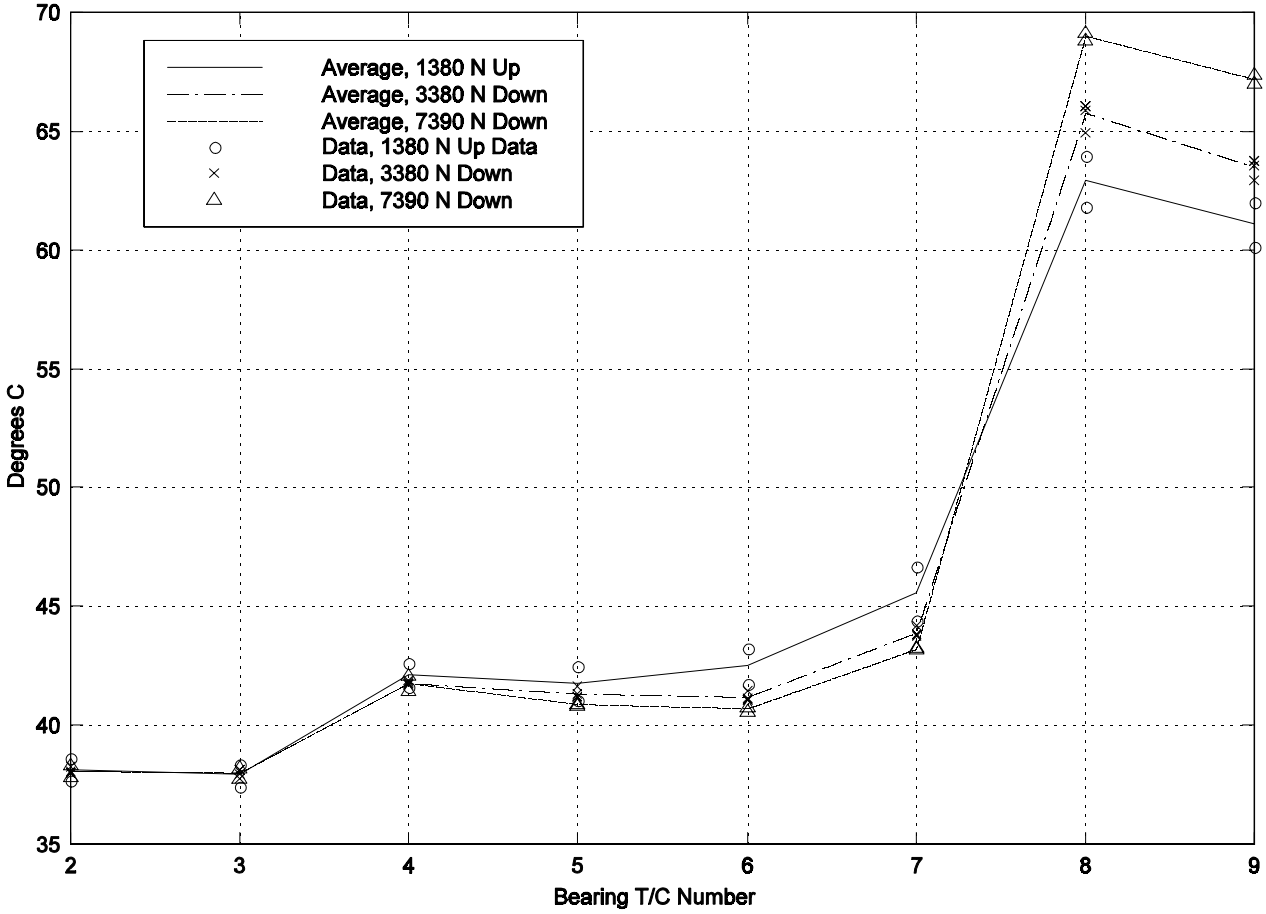

Figure 85 - Bearing Temperatures, 5000 RPM Pressure Dam Bearing

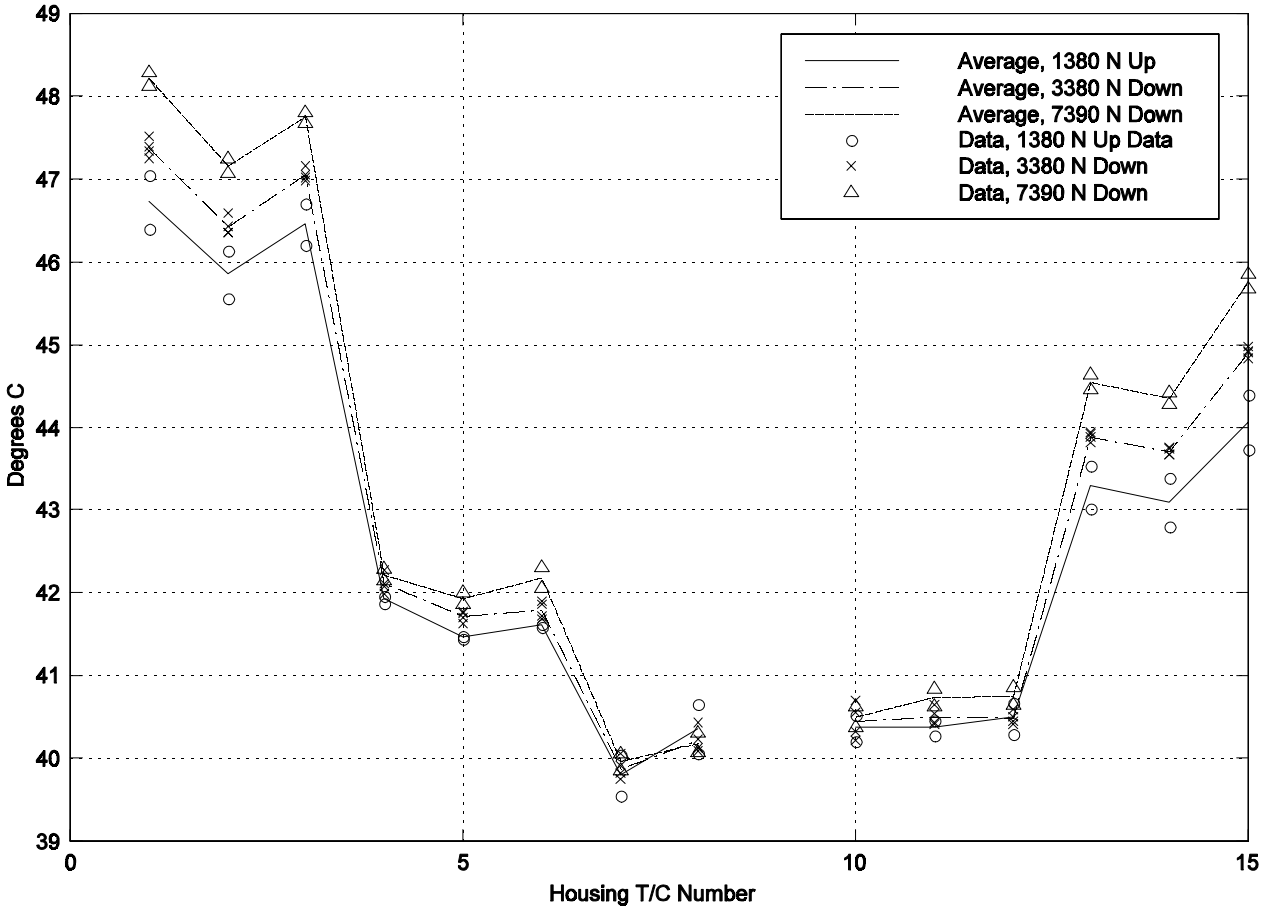

Figure 86 - Housing Temperatures, 5000 RPM Pressure Dam Bearing

6.6 Discussion

The experimental data presented above for the two axial groove bearing, show qualitative agreement in trend and curve shape between the analytical and theoretical results. The pressure dam results do not appear to agree as well. Precise point by point comparisons are not possible, as the actual bearing load and the operating center for the pressure dam bearing could not be accurately measured. The experimental results also show a speed effect on the shaft locus which is not predicted by the model implemented in NPADVT. For both bearings, the experimental shaft locus for 5000 RPM is closer to the bearing vertical centerline than the results for 1500 RPM. This effect is not predicted by the analytical results. One likely cause is thermal deformations to the bearing and shaft, which act to reduce the clearance due to the increase in shaft diameter over room temperature, as well as to change the bearing surface geometry somewhat due to temperature gradients within the bearing insert. Analytical results presented in Morton and Keogh (1986), which are based on a more sophisticated analysis which includes thermal and elastic deformations, show a similar effect. Experimental evidence showing a shift towards the bearing centerline due to thermal deformations has also been presented in Swanson (1994).

The repeated data points also show that the rig does take very consistent measurements. The repeated data points are almost all within less than ±1.5 μm of the average measurement. This is true even for the 5000 RPM, two axial groove results, which are for a briefly interrupted test. This level of agreement is probably on the order of the instrumentation uncertainty. Given a longer settling time at each test point, along with a longer test run which would include significantly more repetitions, it should be possible to reduce the uncertainty due to experimental scatter for each averaged data to point to a level well below the instrumentation uncertainty.

The thermal data, in general, show a slightly larger amount of scatter in some qualitative sense. This suggests that a longer settling time would probably be appropriate. The trends for the bearing results are what would be expected for the loading cases presented, in that the highest temperatures are generally at the regions where the minimum film thickness would be expected. The housing temperatures show similar trends, although the data for the groups of three probes indicate small axial

temperature gradients. The results generally show slightly higher temperatures at the inboard set of probes. This was not expected, as the symmetric bearing should be evenly loaded, which should result in a symmetric temperature distribution.

6.7 Shaft Loading Path

In the case of the 1500 RPM tests for both bearings, there is some indication of a thermal transient. Figures 87 and 88 present the shaft locus for these two tests, with the data points connected by a line indicating the shaft path followed as the load was cycled up and down. The hysteretic behavior shown is not predicted by the model implemented in NPADVT. One possible explanation could be inadequate thermal settling time. Figures 89 through 92 present the temperature versus load for selected bearing and housing thermocouples. The path of the line traces out the changes in measured temperature observed during the course of the test. These data are typical of the bearing thermocouples and show some signs of thermal behavior which is similar to the load path results; however, the thermal data do not show the clear trend shown in the shaft path for the loading sequence. Hence, it is unclear what might prevent the loading path from repeating.

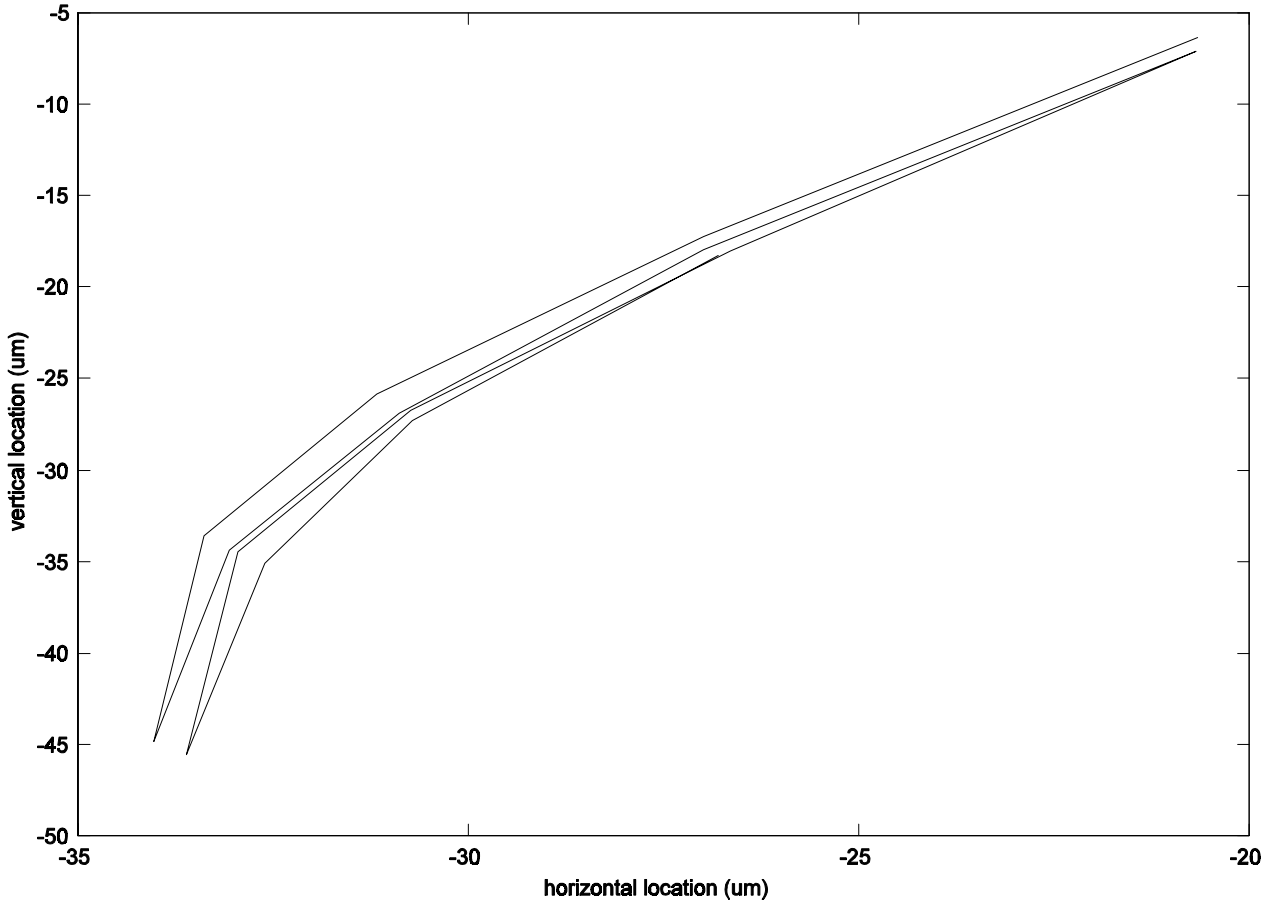

Figure 87 - Shaft Path. 1500 RPM, Two Axial Groove Bearing

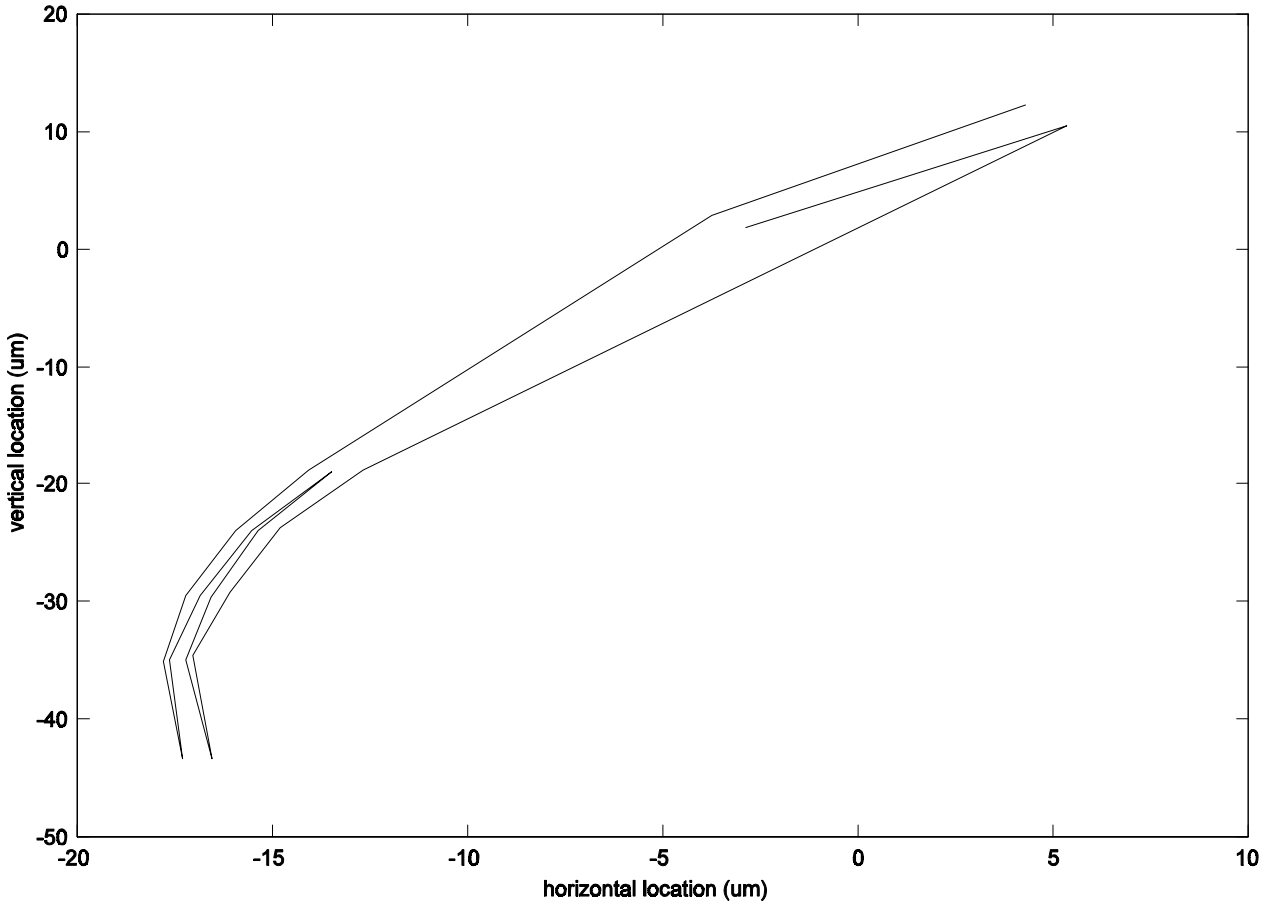

Figure 88 - Shaft Path, 1500 RPM Pressure Dam Bearing

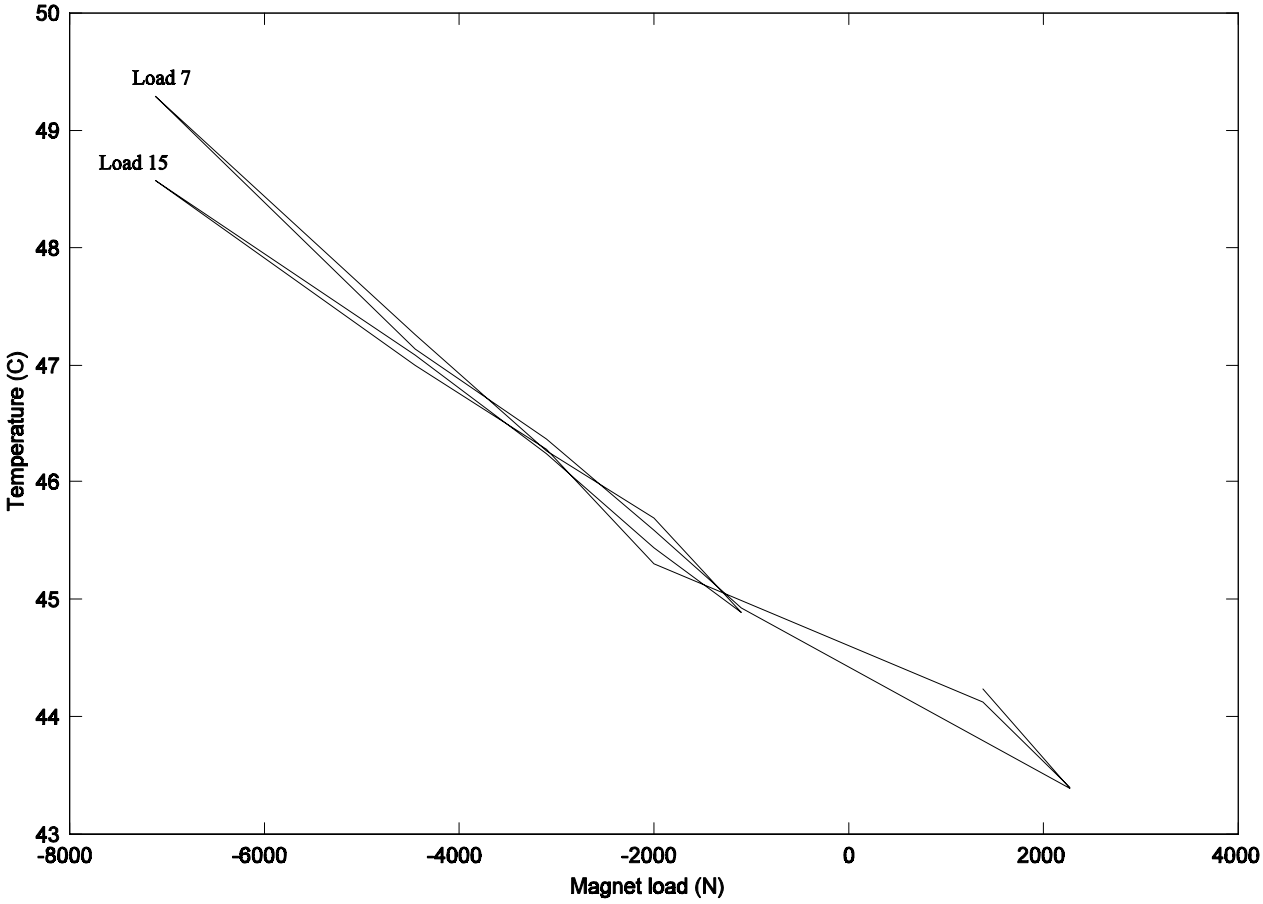

Figure 89 - Temperature vs. Load, Two Axial Groove Bearing, Brg. T/C 11, 1500 RPM

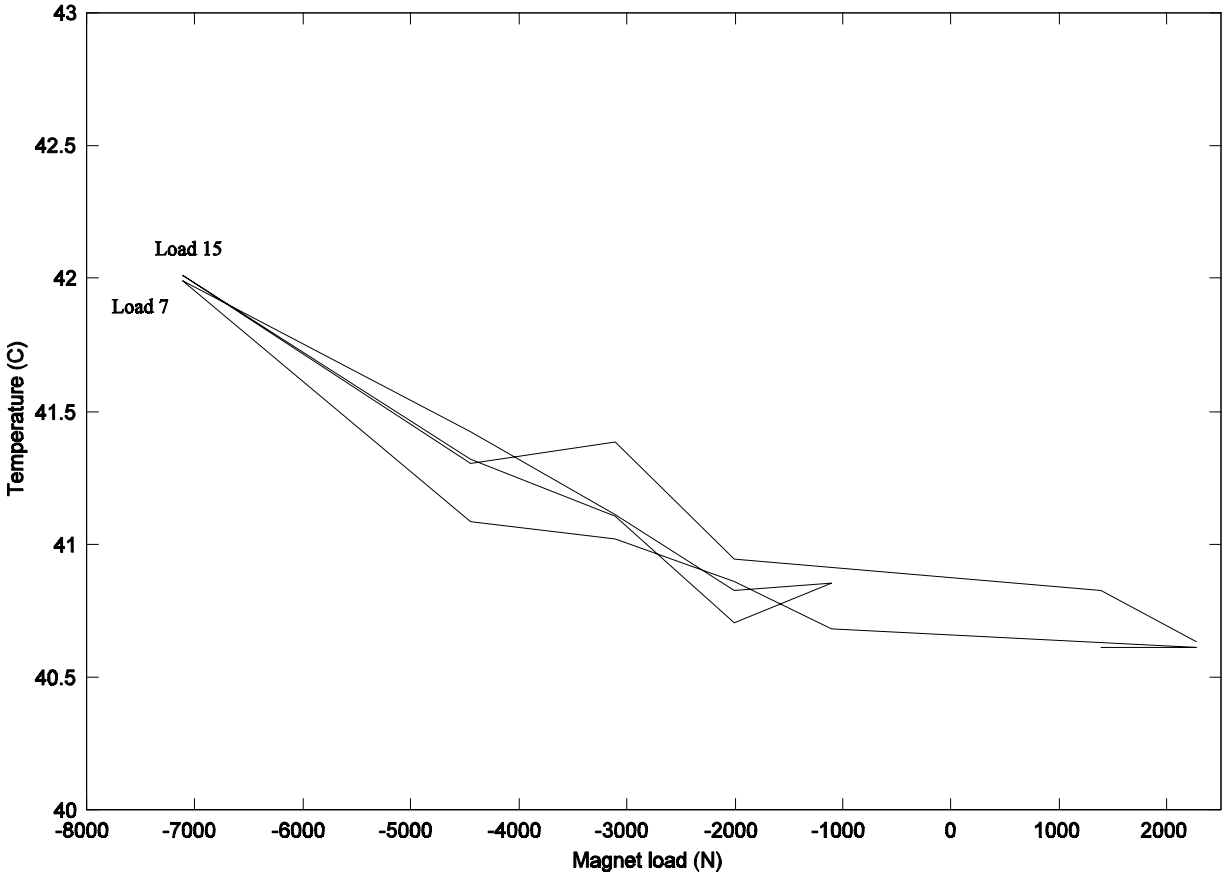

Figure 90 - Temperature vs. Load, Two Axial Groove Bearing, Housing TC 2, 1500 RPM

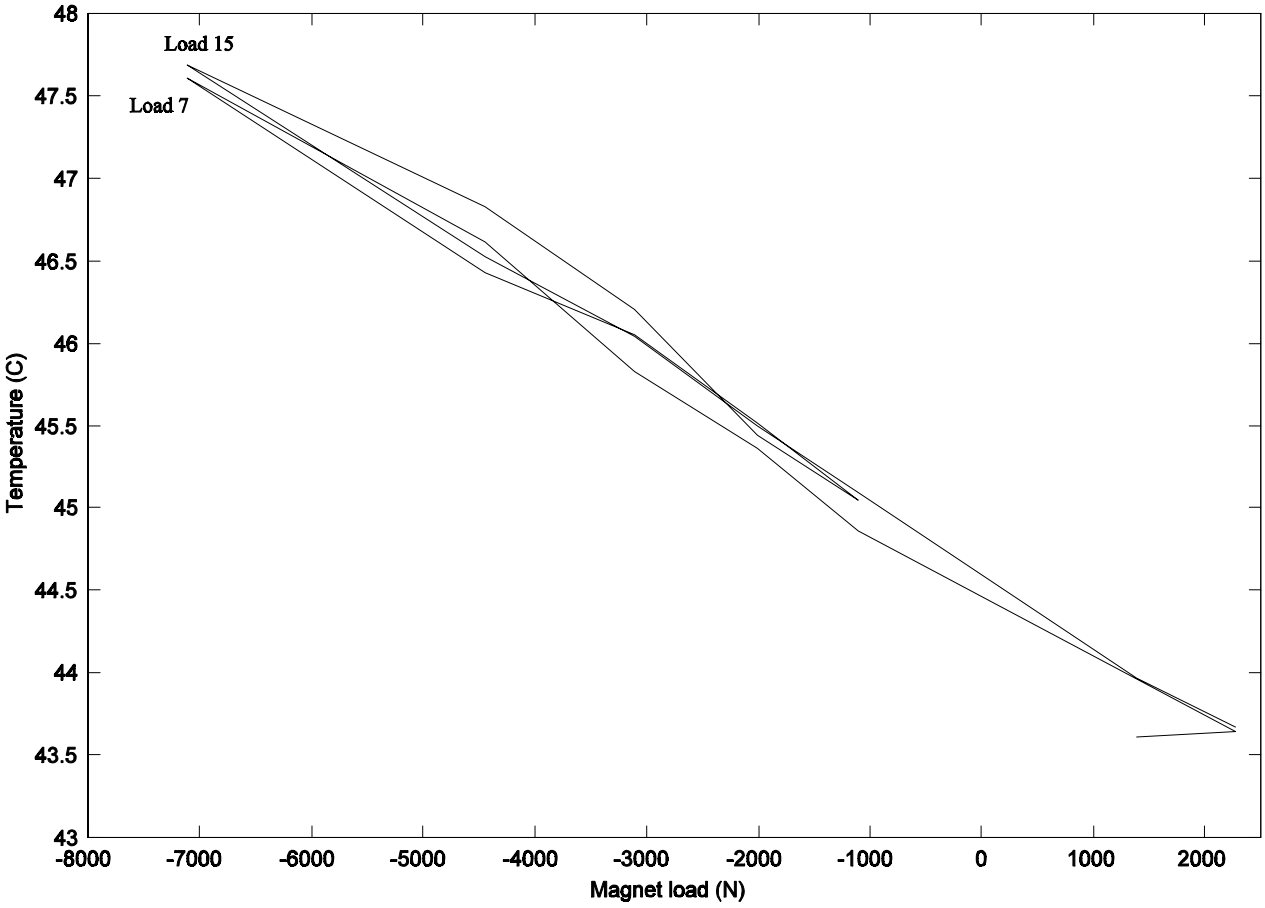

Figure 91 - Temperature vs. Load, Pressure Dam Bearing, Brg T/C 9, 1500 RPM

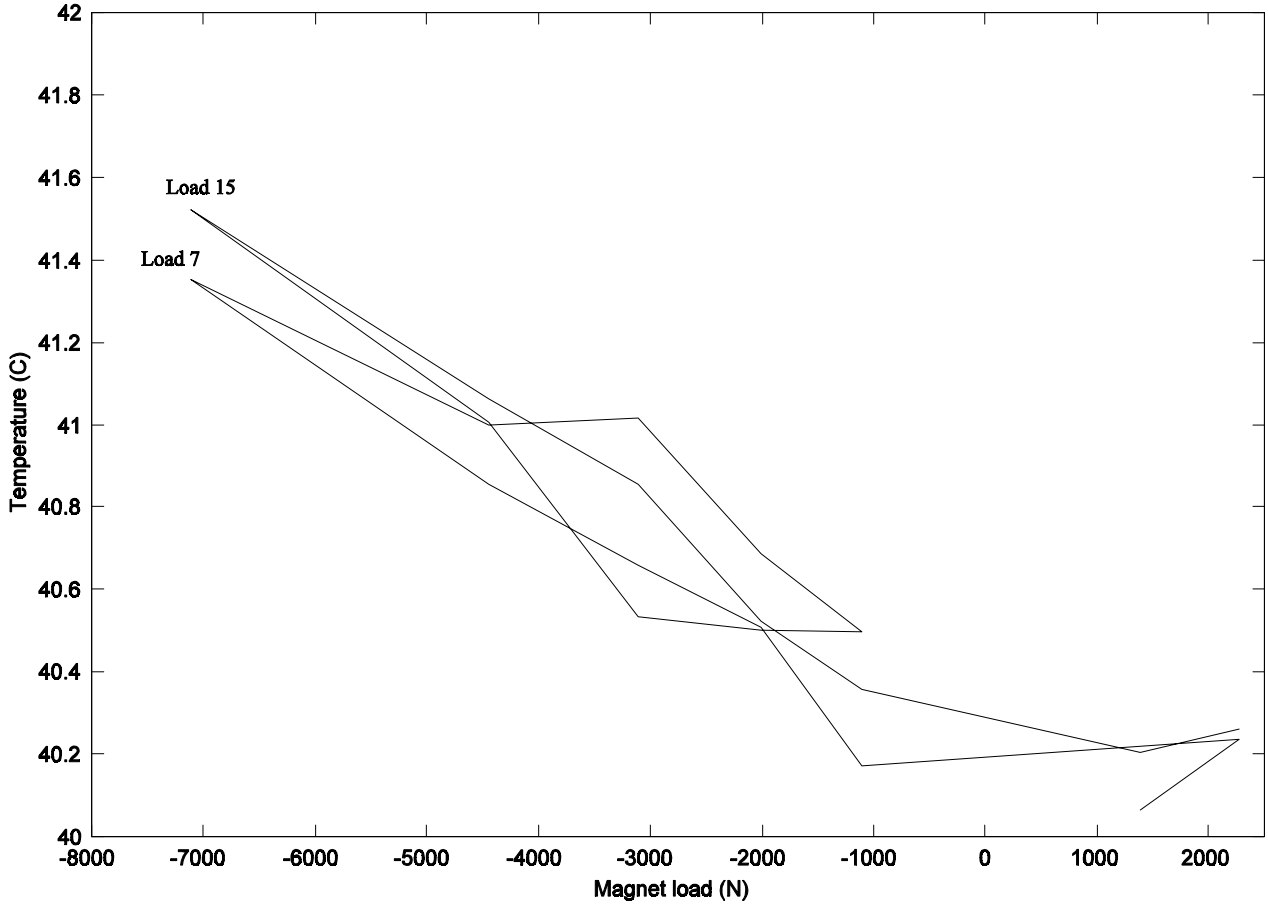

Figure 92 -Temperature vs. Load, Pressure Dam Bearing, Housing T/C 2, 1500 RPM

6.8 Summary

The results for the two bearings tested under steady loads confirm that the test rig is operating generally as expected. The test rig automation functioned essentially as expected. The only major glitch was a system crash during the initial 5000 RPM two axial groove bearing test. The results are quite repeatable over the course of a test, and generally agree with the analytical predictions from NPADVT. The results do show an unexpected path dependence, which may be indicative of insufficient thermal settling time at each test point.

Chapter 7

Test Rig Operation with Dynamic Loading

7.1 Introduction

As described previously, one of the primary goals of the development of this test rig was to be able to make the force and displacement measurements required for estimation of bearing linearized stiffness and damping coefficients. To reach this goal, the original rig was greatly modified. The loading magnets were replaced with magnets suitable for dynamic excitation, the test bearing was mounted on load cells, the test section was lengthened, the shaft was redesigned (see Fig. 93) and a digital control system was added along with a data acquisition system. Despite successes in all of these items, initial dynamic tests revealed a fatal flaw in the upgraded test rig design. This chapter will discuss the nature of the problem, as well as recent modeling which was able to explain the problem.

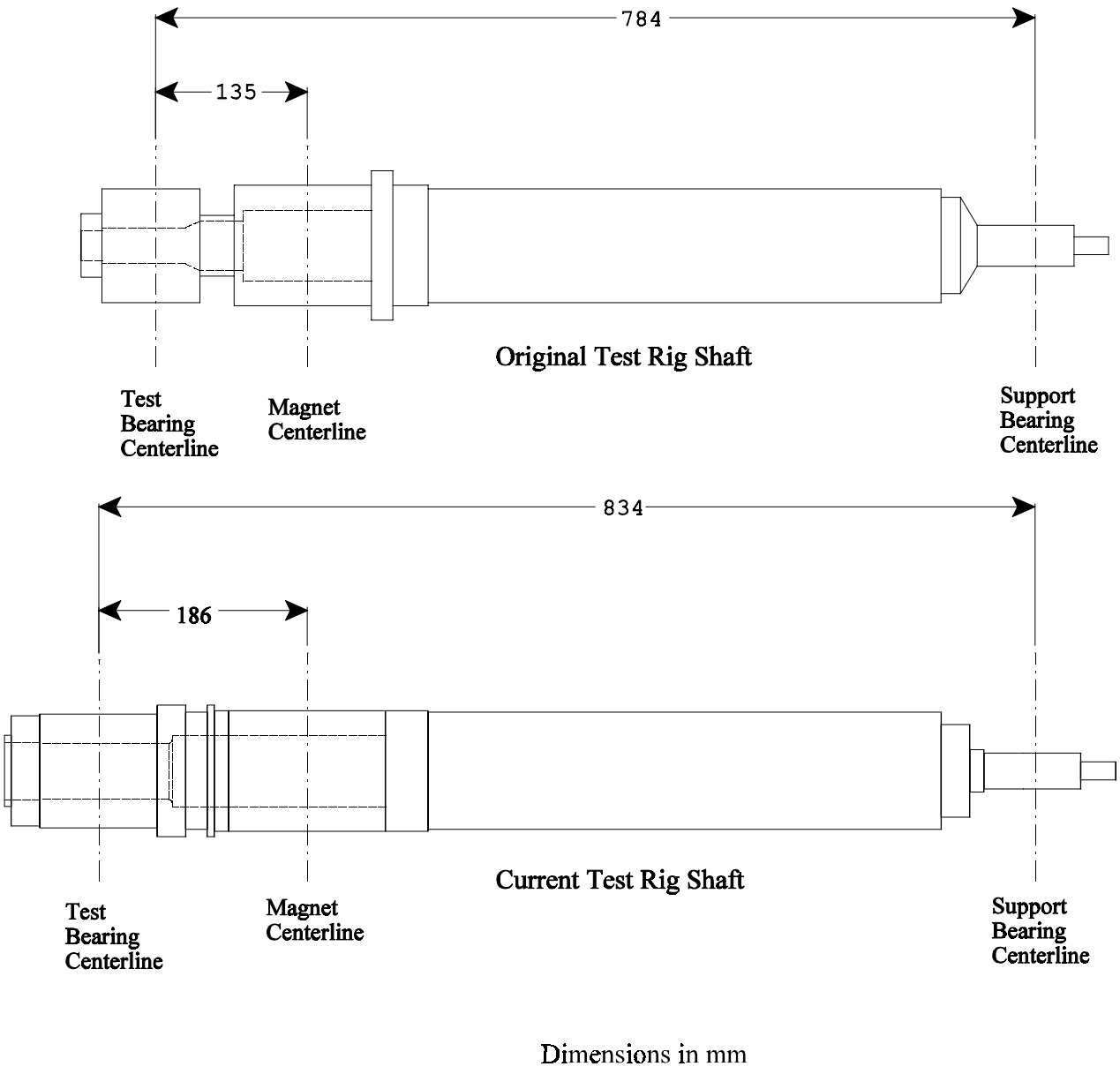

Figure 93 - Comparison of Original and Current Test Rig Shafts

7.2 Modeling Software

The results presented below were obtained through the use of two software packages. The first is NPADVT, which was discussed previously in this work. This program was used to estimate the test bearing stiffness and damping characteristics. The second is a commercial code named "DyRoBes", which is a finite element based structural analysis code developed especially to meet the needs of rotor dynamic modeling. Although the system natural frequencies, mode shapes, forced response, etc. could be obtained with a general purpose structural analysis code such as Ansys or Ideas, it would be extremely time consuming to build the model, run the required analyses and format the data for presentation. A code such as DyRoBes includes pre- and post- processing modules to allow the analyst to enter the data in a convenient form, and view the results in a useful form.

7.3 Test Rig Rotor Dynamics

7.3.1 Undamped Critical Speed Analysis

To start the discussion of the test rig shaft/bearing dynamics, the first analysis which will be considered is the "critical speed" analysis. This is generally the first analysis examined when evaluating a rotating machine. It is an examination of rotor-bearing system undamped natural frequencies (eigenvalues) and mode shapes (eigenvectors) for a spinning shaft, as a function of bearing stiffness. This is generally referred to as a "critical speed" analysis. The primary goal of this analysis is to ensure that normal operating speed is not likely to coincide with a system natural frequency. The undamped natural frequencies are plotted as a function of bearing stiffnesses, as shown in Fig. 94 and Fig. 95. These figures present the variation in system undamped natural frequencies for two different support bearing stiffnesses, as a function of test bearing stiffness. The predicted test bearing stiffness range and expected operating speed range are as indicated by horizontal and vertical bands, respectively. The bearing characteristics used to generate these figures are uncoupled and symmetric. Figure 96 shows the variation in the first undamped mode shape as the test bearing stiffness is varied for the stiffer support bearing case (corresponding to Fig. 95). Note that these mode shapes are undamped. The addition of bearing damping (which can be

substantial in oil lubricated, hydrodynamic bearings) will tend to pull the test bearing end of the rotor down to a node for a lower test bearing stiffness.

Accepted practice would suggest that the test bearing rotor design is fairly conservative. The expected maximum testing speed was in the range of 1000 to 5000 RPM, which is below the first "rigid" mode natural frequency of approximately 10,000 RPM. It is well below (by about an order of magnitude) the first bending mode, which is approximately 35,000 RPM. Hence, from this analysis there are no expected problems.

7.3.2 Model Tuning

The free-free natural frequencies and mode shapes from this analysis may also be used to tune the shaft model by comparing the predicted undamped, free-free frequencies and mode shapes to measured data taken with the shaft hanging in a quasi-free-free state. This technique was used to tune the model used for the analysis. Figure 97 presents a force- acceleration frequency response for the "free-free" shaft for excitation and response at the test bearing end of the shaft. Based on this data, it was determined that the first two natural frequencies in this quasi-free configuration are approximately 400 Hz and 1085 Hz. Figures 98 and 99 present corresponding shaft velocity mode shapes as measured by a scanning laser (Doppler) velocimeter down the length of the hanging shaft. An electrodynamic shaker was used at the at the test bearing end as a source of sinusoidal excitation. The data correspond to the first two resonances. Overlaid on top of the experimental data in each case are the predicted mode shape for a model which has been tuned as described below. Since these results were obtained after the shaft was assembled, the duplex pair, rolling element support bearing and inner housing are also on the rotor during the tests. The presence of the bearing and housing did not seem to adversely affect the 400 Hz results. In the case of the 1082 Hz data, the loosely attached housing was moving out of phase with the rotor, and the data for this region of the scan have been suppressed in Fig. 99.

To tune a rotor model, the experimental results are used in an iterative process to adjust model stiffness mass to match the prediction to measurement. In the case of the test rig rotor, one of the

major uncertainties in the model concerns the effective stiffness of a section of the rotor which was cut to a smaller diameter to accommodate the stack of approximately 450 thin, disk shaped laminates required at the magnetic actuator location. Hence, the first adjustment to the nominal geometry was to assume reduced amounts of effective stiffness in this location. By reducing the effective stiffness of the laminate stack to zero, the tuned model closely agreed with the experimental data, as shown in Figs. 98 and 99. This rotor model is shown schematically in Fig. 100. In this figure, the shaft is split about the centerline. The diameters shown on the top are the diameters used to develop the mass matrix for the model. The diameters shown below the centerline are the diameters used to develop the stiffness matrix. Note that in the region of the magnetic actuator, the stiffness diameters are much less than the mass diameter. For the final model, the stack of laminates at the magnetic actuator location are assumed to only have a mass, with no stiffness. The critical speed results for the test rig with a model which has been tuned based on data from the actual shaft are as presented previously in Fig. 94 and 95.

The analytical data from similar analyses during the original redesign should have raised warning flags. The goal of the test program was to estimate the bearing stiffness and damping characteristics by applying a force at the location indicated as “magnet centerline”, and measuring the resulting bearing reaction force and the shaft/bearing relative motion at the left-hand bearing. Although the model used in the original analysis made the more optimistic assumption of a stiffness contribution from the laminate section, the problem of not-so-rigid modes with significant shaft bending appears in these results as well. That this problem escaped notice during the original redesign is probably partially the result of the visualization tools available at this time, as well as a case of not quite asking the right questions of the data and the optimistic laminate region stiffness assumption.

7.3.4 Other Analyses

In the original analytical work for the redesign, several other results were also examined. These included the natural frequencies and mode shapes with the non-symmetric stiffness and damping

characteristics of the bearing included, as well as the rotor response to unbalance at various locations on the rotor. These results will not be presented here, as they add little new information. Another analysis which was examined was the loader to bearing centerline frequency response. A modification to the analysis code used at that time for the stability analysis, which allowed for non-shaft synchronous excitation, allowed an examination of the frequency response. Unfortunately, the results examined were amplitude transfer functions from magnet centerline to bearing centerline. Hence, they do not directly show the phase shift across the test bearing location, and did not point out the problem with the shaft dynamics.

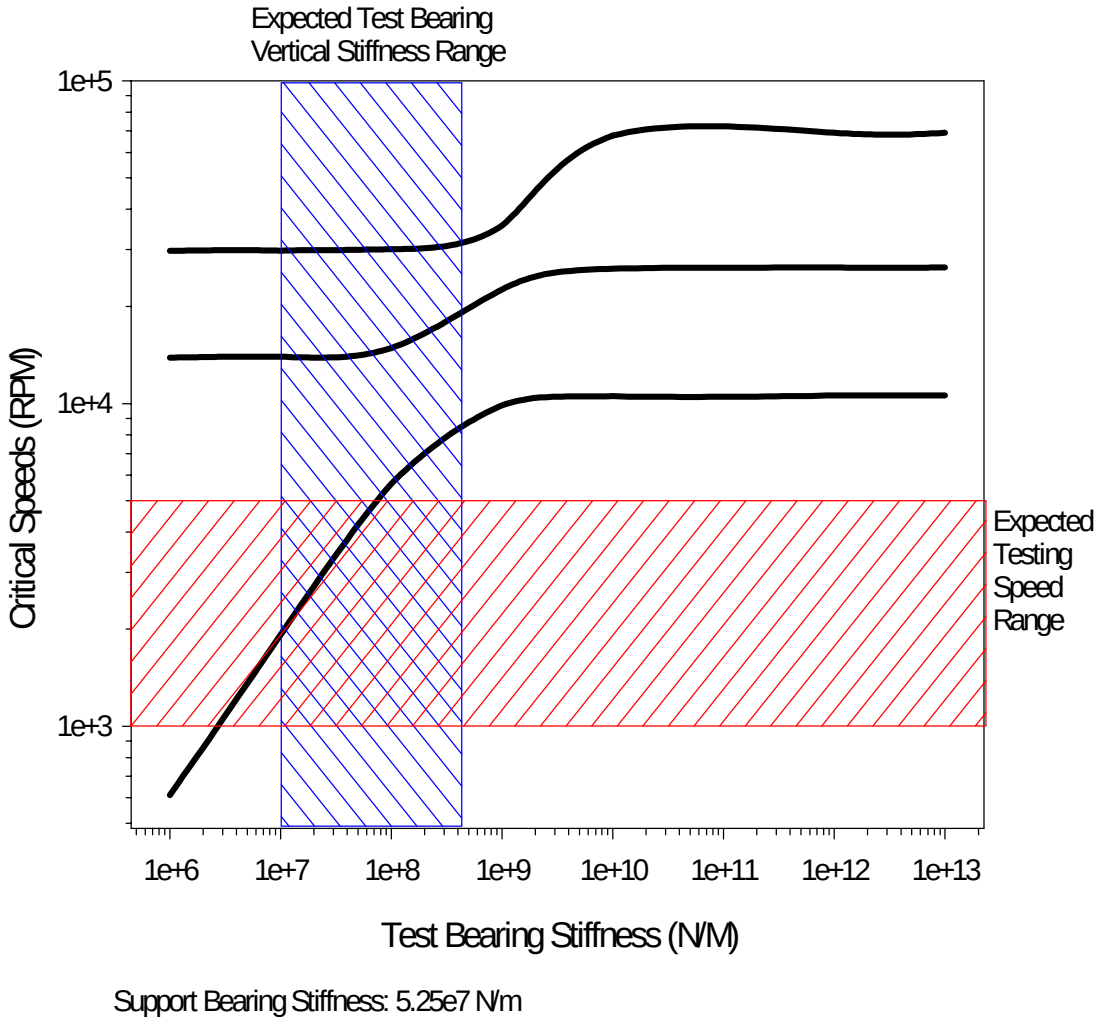

Figure 94 - Critical Speed (Undamped Natural Frequencies), Soft Support Bearing

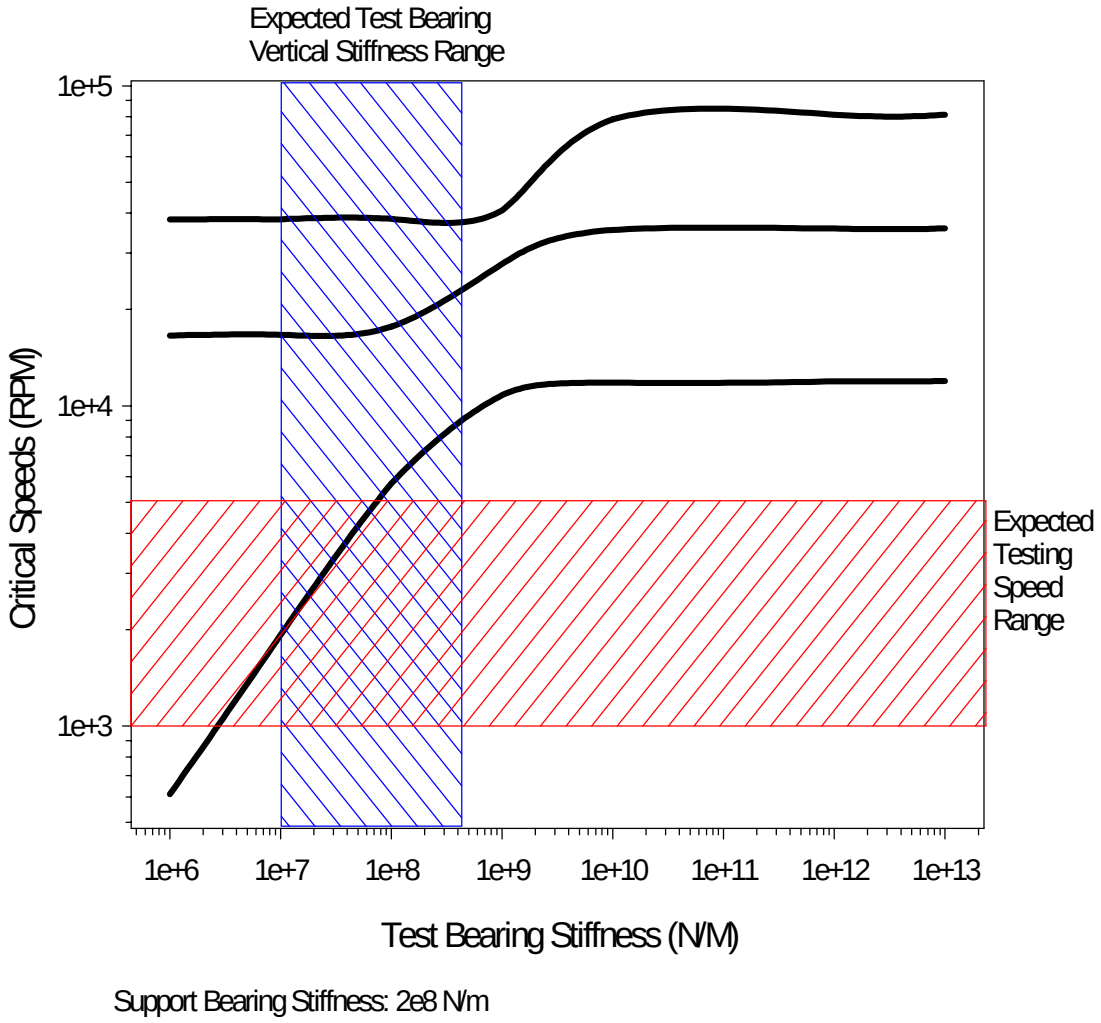

Figure 95 - Critical Speed (Undamped Natural Frequencies), Stiff Support Bearing

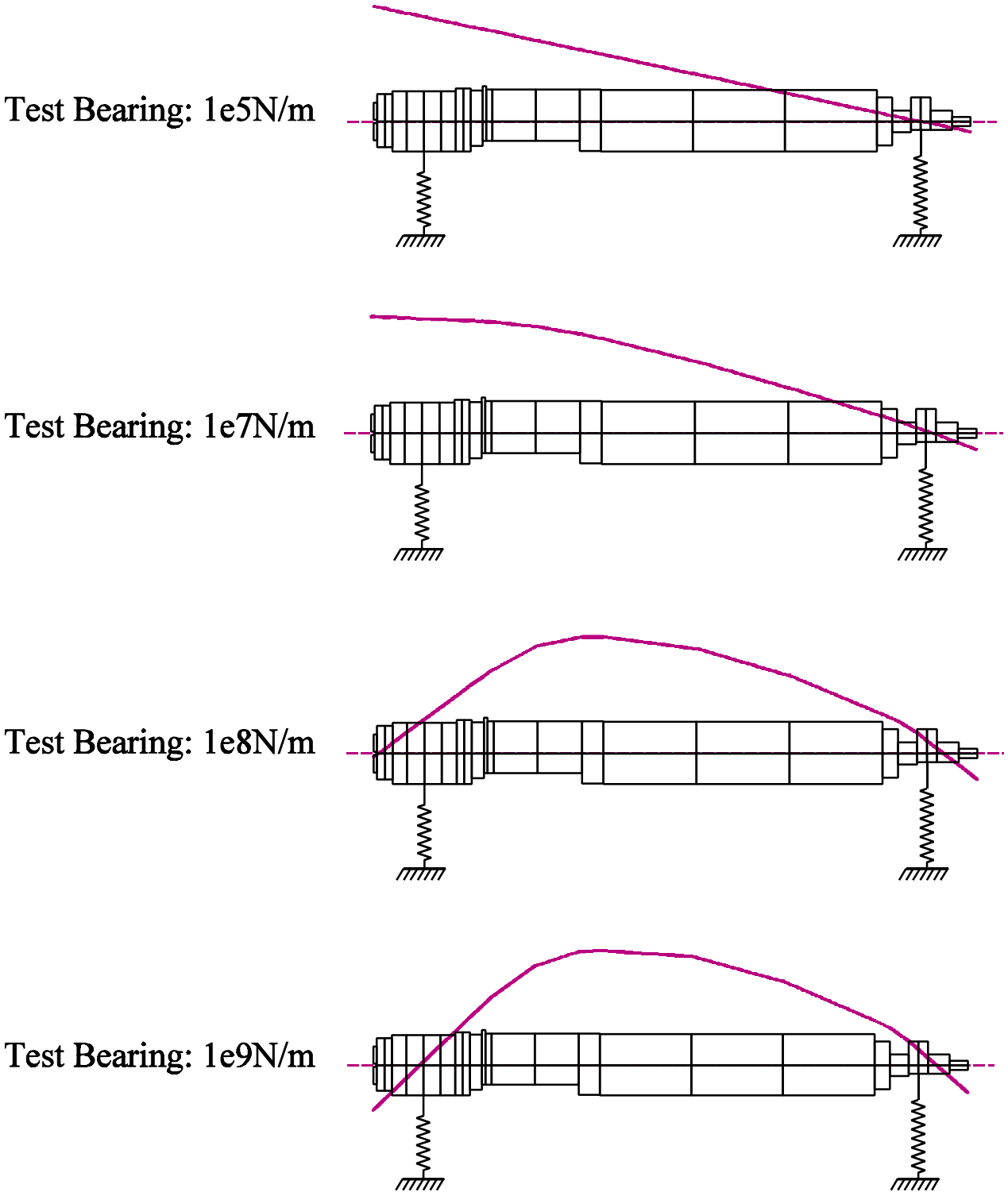

Figure 96 - Undamped First Mode Mode Shape for Stiff Support Bearing vs. Test Bearing Stiffness

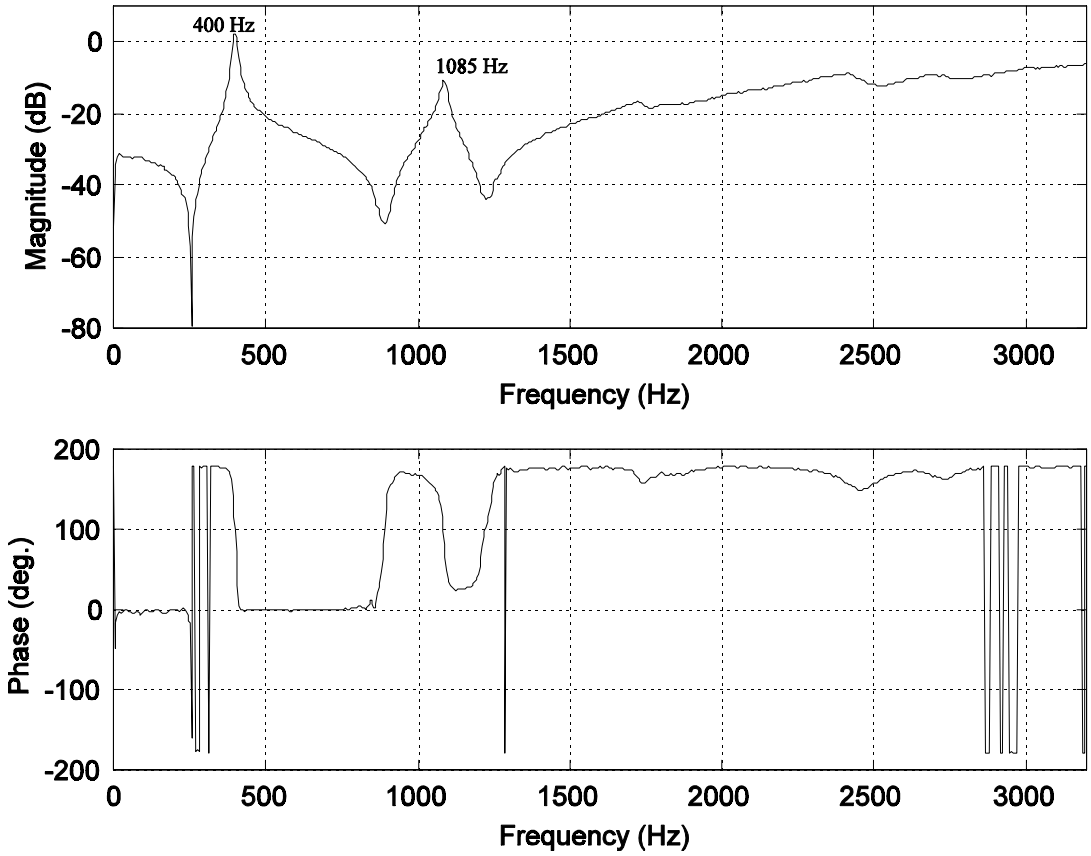

Figure 97 - Shaft Free-Free Impact to Acceleration Frequency Response

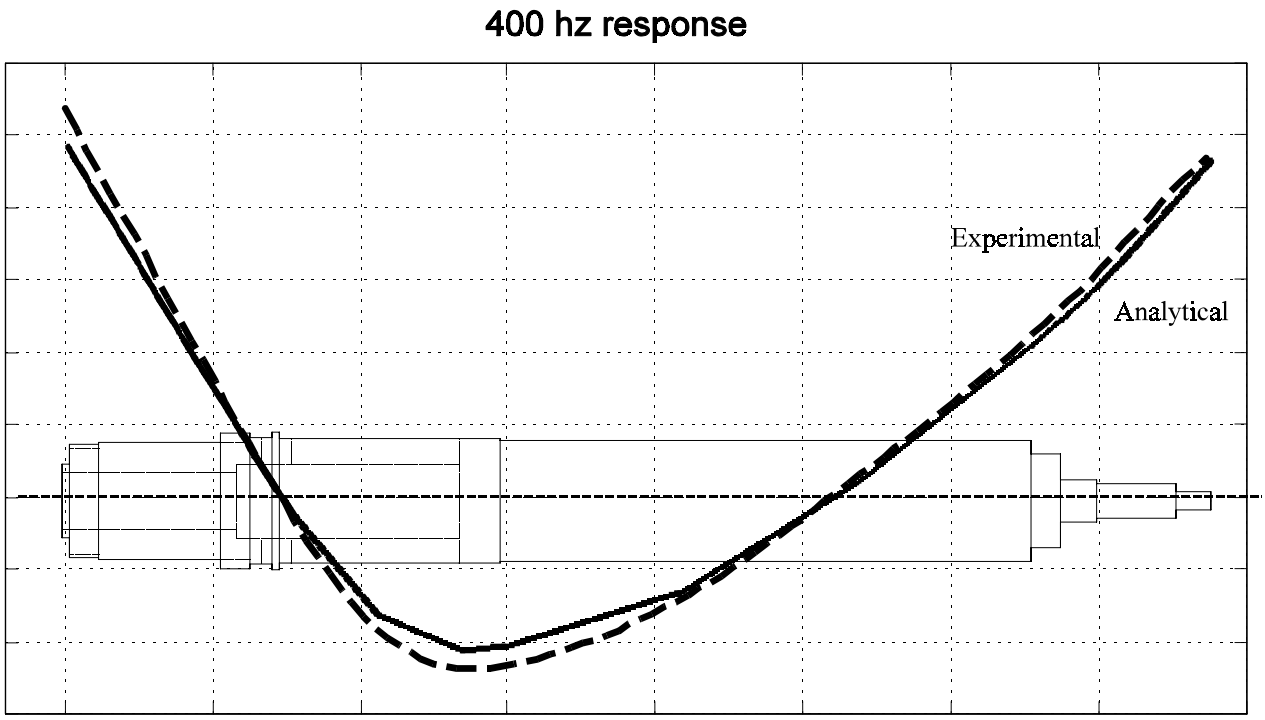

Figure 98 - Shaft First Free-Free Mode, Experimental and Tuned Analytical

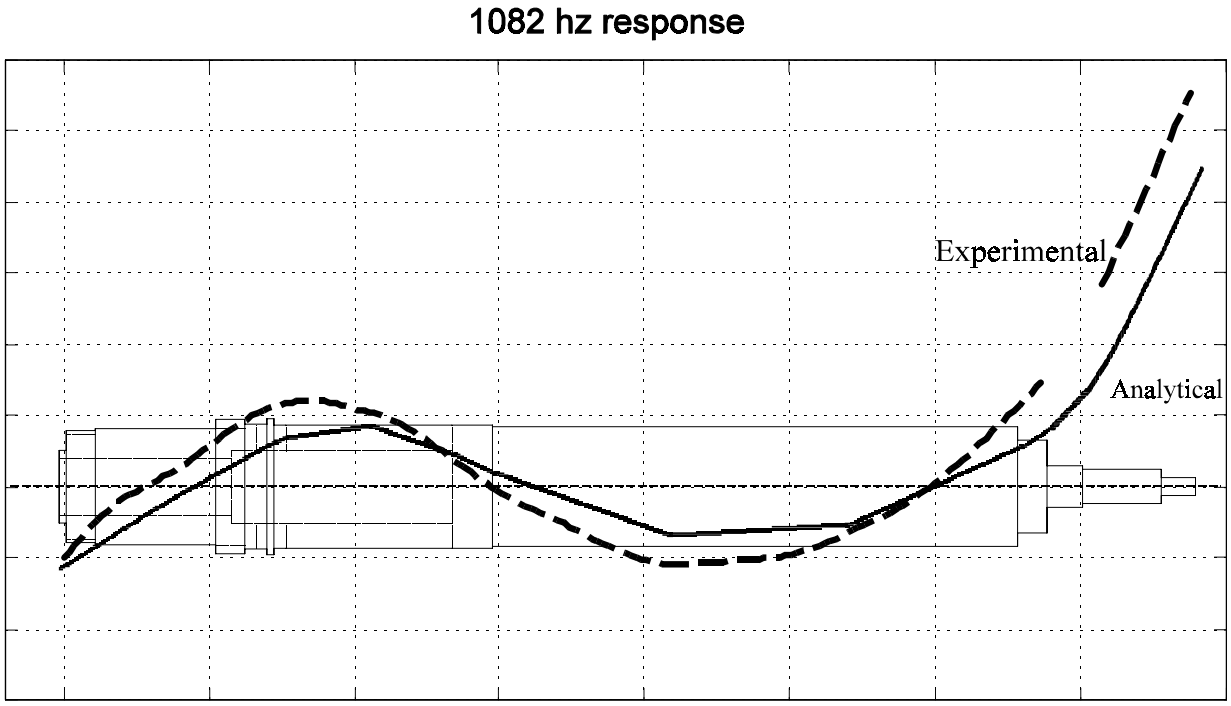

Figure 99 - Shaft Second Free-Free Mode, Experimental and Tuned Analytical

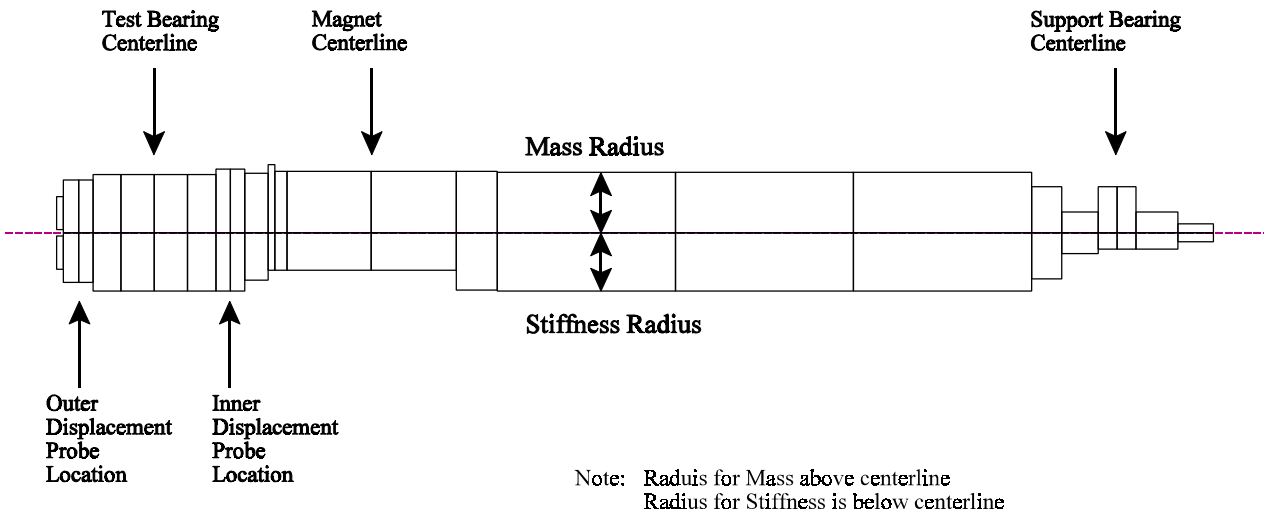

Figure 100 - Rotor Model for Dynamic Analysis, Mass (upper) and Stiffness (lower) Diameters as Shown

7.4 Diagnosis of the Problem

7.4.1 Initial Indications

The initial attempts to estimate dynamic coefficients with the test rig after the magnetic actuator was built and all the other required upgrades were complete were not very successful. During this debugging process, it was noted that the data from the inside position sensors was shifted 180 degrees relative to the outer probes (see Fig. 100 for probe locations). This data indicated that the shaft was definitely not moving parallel to the bearing surface. After confirming that the displacement probes were reading real motion, a very large clearance test bearing which was predicted to have a much lower stiffness than the shake-down bearing was installed in the test rig. With this bearing, the relative phase shift between the inner and outer test bearing sensors was examined as a function of frequency and applied load. The results of one of these tests are summarized in Fig. 101. This plot shows an increasing phase lag shift between inner and outer bearing, which ultimately becomes 180 degrees in all cases. The phase lag increases both with increasing frequency as well as increasing applied load (which is essentially the same as examining the effect of increasing the test bearing stiffness, since this bearing has a hardening spring characteristic). The only possible explanation was a nodal point between the two planes of displacement probes.

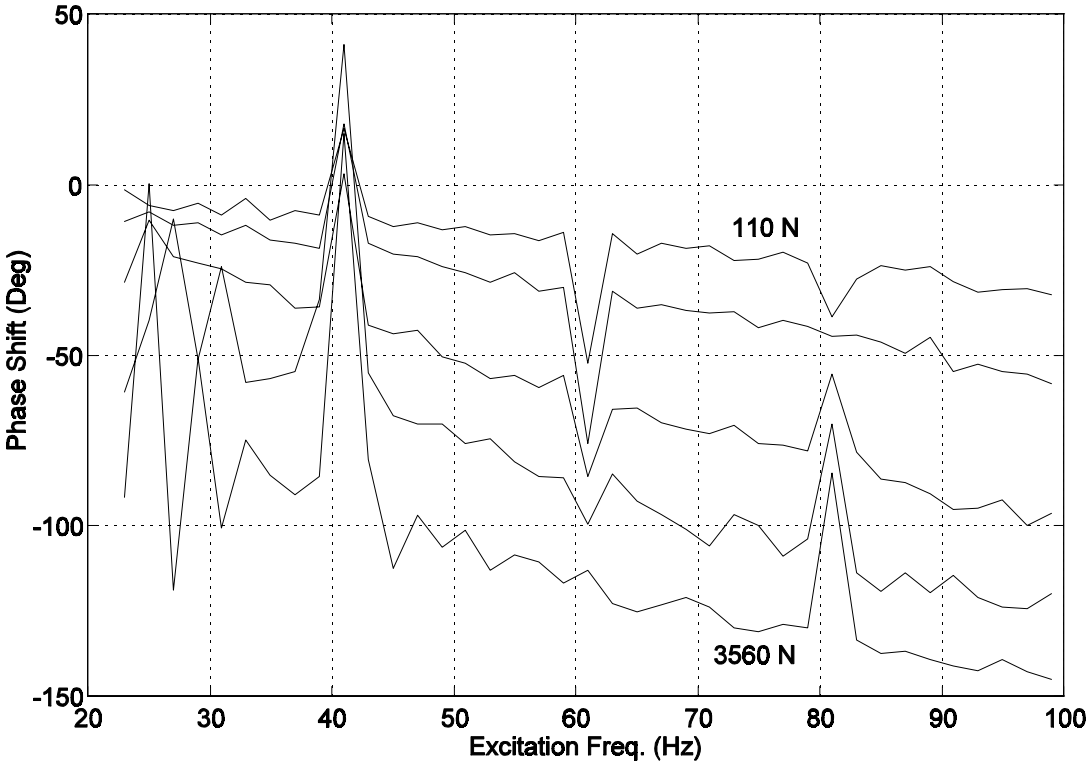

Figure 101 - Measured Inner to Outer Probe Phase Shift for Increasing Load

7.4.2 Analytical Confirmation

To confirm the experimental results, Figs. 102 and 103 present analytical shaft deflection shapes for increasing test bearing load (and hence increasing stiffness) for unbalance excitation at the magnet location for an operating speed of 5000 RPM, as predicted by DyRoBes. Note, that unlike the previous analytical results, these figures include the effects of test bearing damping. These figures show an increasing phase shift between the inner and outer probe locations similar to the experimental results presented previously.

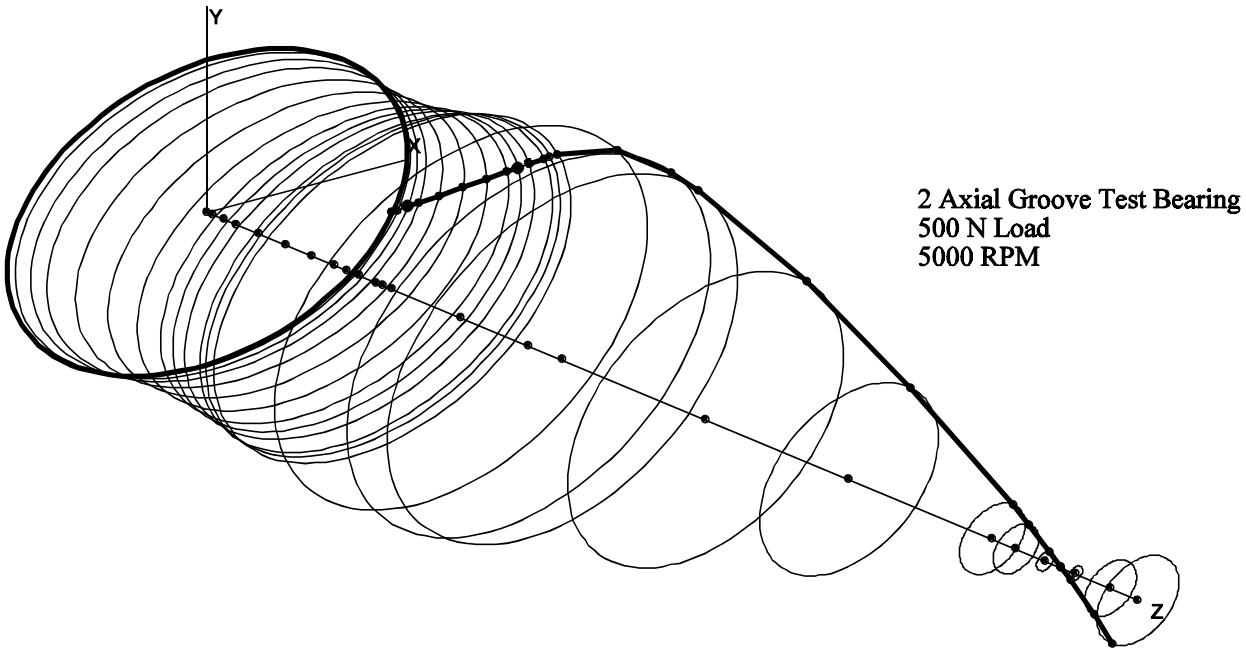

Figure 102 - Forced Response for Unbalance at Magnet, 500 N Bearing Load

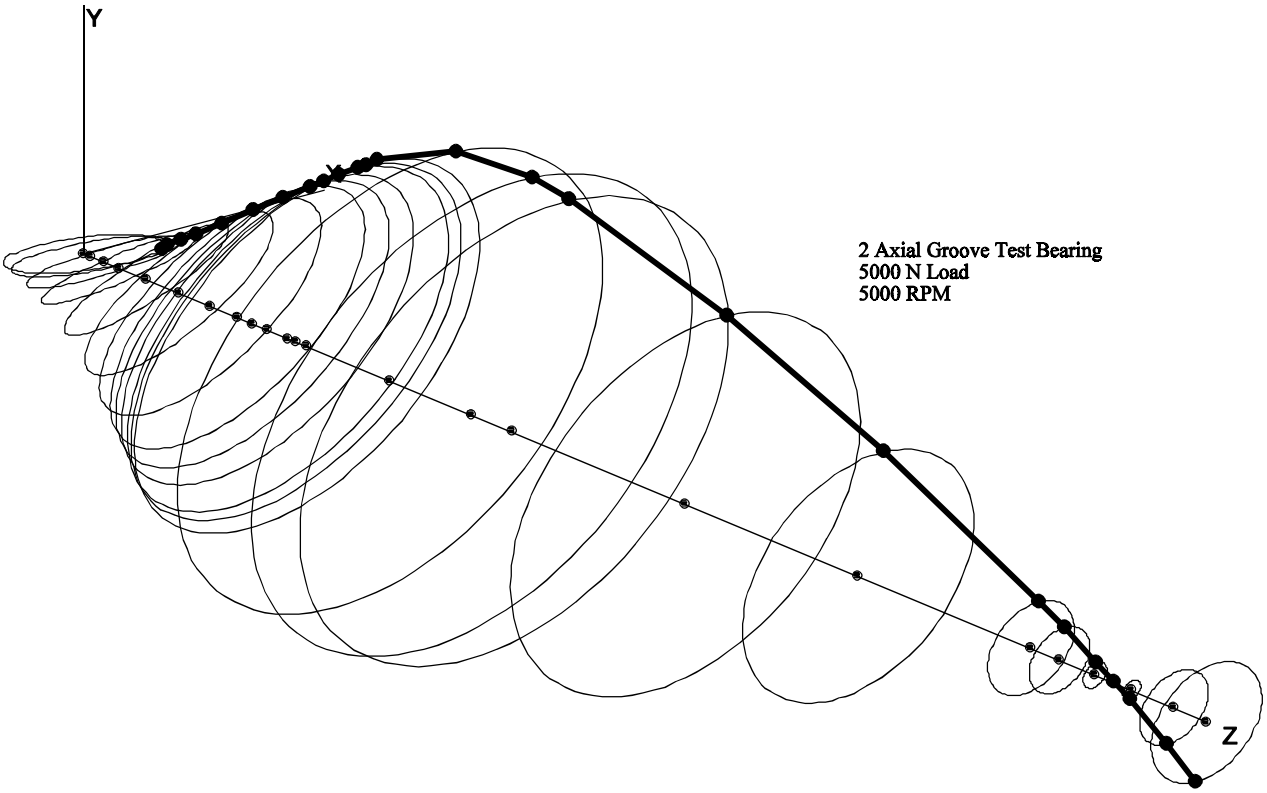

Figure 103 - Forced Response for Unbalance at Magnet, 5000 N Bearing Load

7.4.3 Analysis of Problem

To estimate what bearing stiffness would be required to place a node between the two probes and the resulting shaft response, a number of responses for an imbalance at the magnetic actuator location could be examined. However, these results are not in the most convenient form, since the forcing function magnitude is proportional to frequency squared. To obtain a forcing function with a constant magnitude, a second, dummy rotor was added to the model, and connected to the magnetic actuator location through very soft springs. This dummy rotor is also connected to ground with very soft springs. Figure 104 shows the resulting rotor model. When the unbalance response of the system above the first resonance of the dummy rotor (about 500 RPM in this case) is examined, the forcing function applied to the real rotor has a constant magnitude, independent of frequency. To further clarify the results (in particular, to avoid complex modes), symmetric, undamped bearing coefficients were used for the parametric study. Due to a quirk in the program, it was necessary to also ignore gyroscopic effects during this study. The use of undamped bearings and ignoring shaft gyroscopic effects does not markedly change the conclusions which will be drawn from this study.

With this technique, a number of test cases were examined. Figures 105 through 109 present the ratio of motion between the inner and outer probe locations, as well as the phase shift between the probes versus excitation frequency. Based on these results, it appears that the shaft dynamics will cause serious problems for dynamic testing with a test bearing stiffness greater than approximately 9e7 N/m, assuming that the support bearing effective stiffness is the same as the measured static stiffness of approximately 2.0e8 N/m (which agrees well with the approximate stiffness formula for this type of bearing). If the support bearing stiffness is lower, problems can be expected for lower test bearing stiffnesses. This result has a certain intuitive appeal, since there would be a node for a pinned support condition, which is the same as an infinitely stiff bearing.

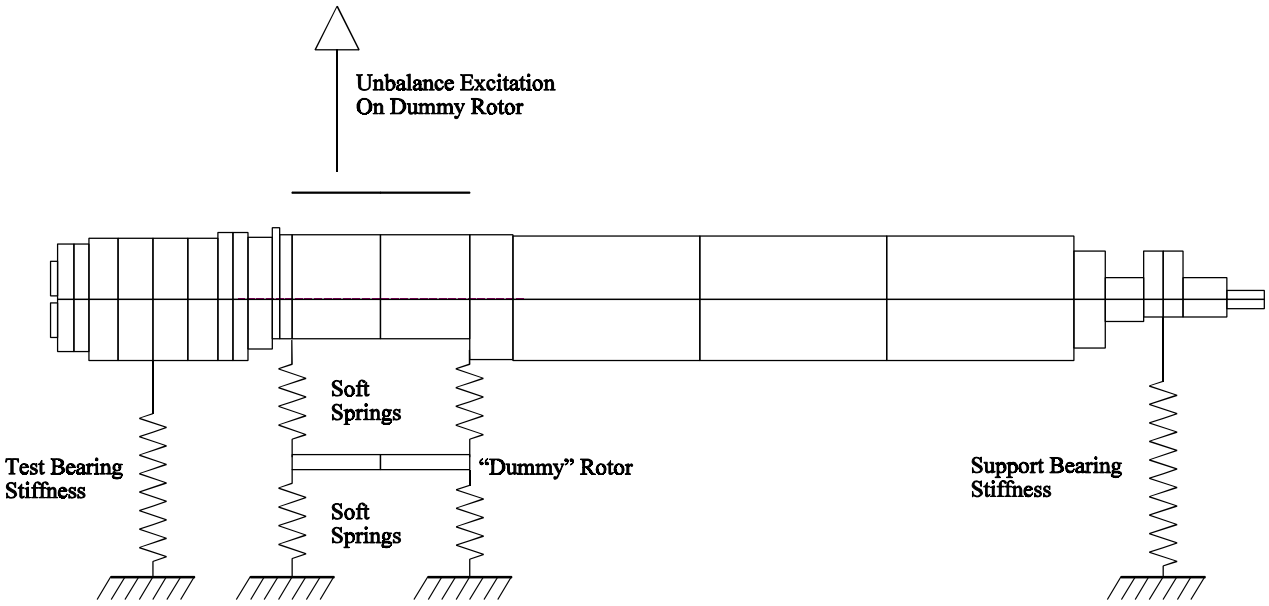

Figure 104 - Rotor Model with Dummy Exciter Rotor

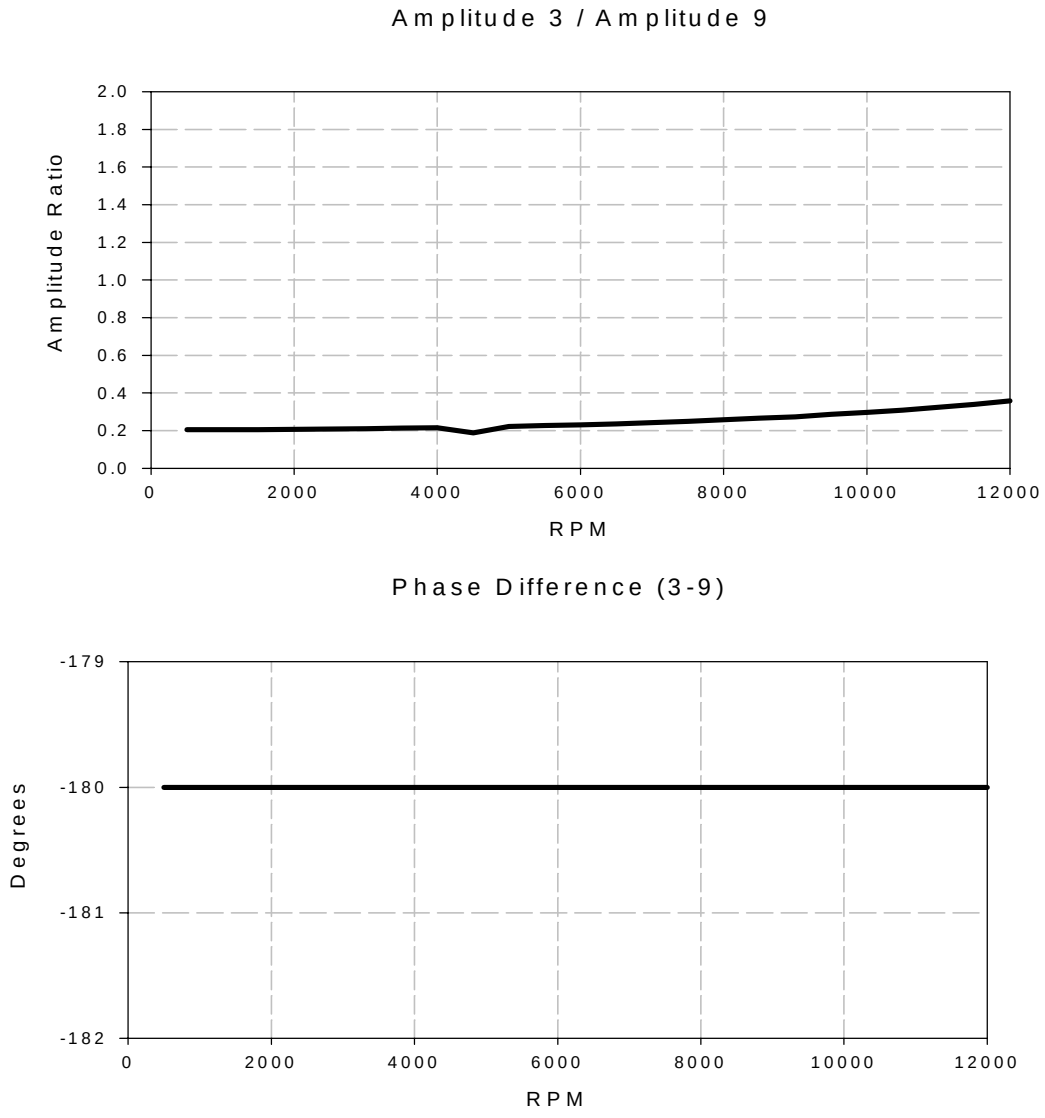

Figure 105 - Inner-Outer Probe Response, Ktest = 2e8 N/M, Ksupport = 2e8 N/M

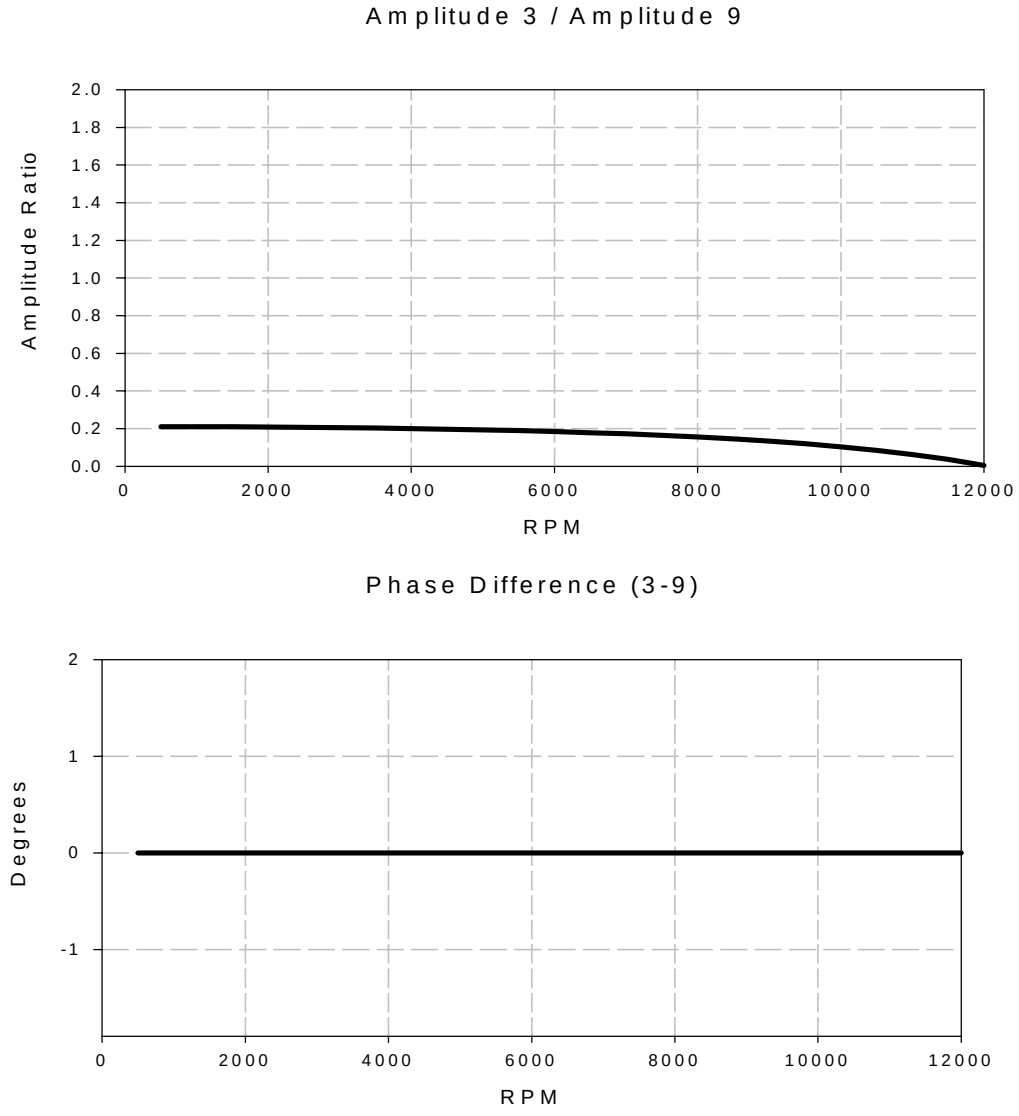

Figure 106 - Inner-Outer Probe Response, Ktest = 9e7 N/M, Ksupport = 9e7 N/M

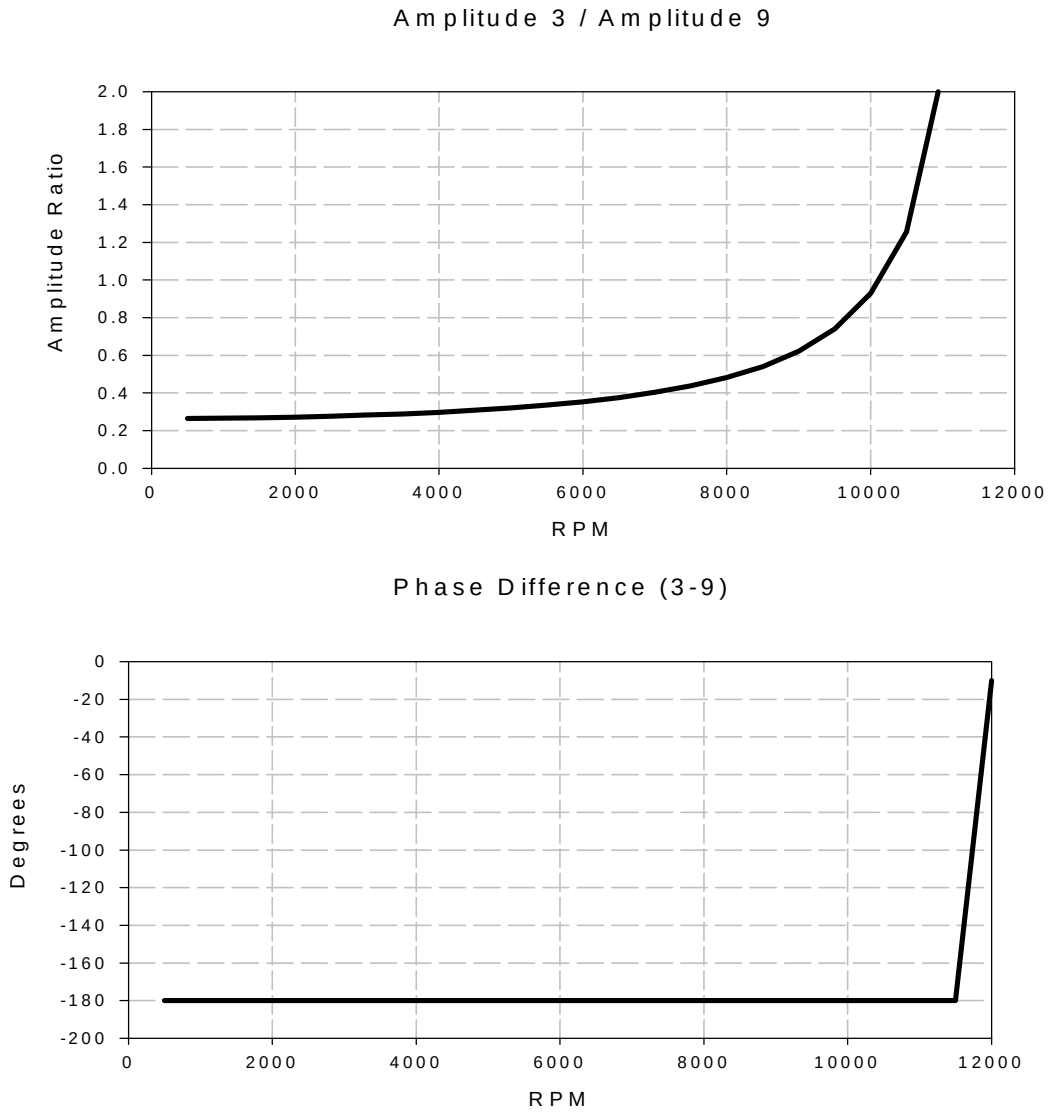

Figure 107 - Inner-Outer Probe Response, Ktest = 2e8 N/M, Ksupport = 2e7 N/M

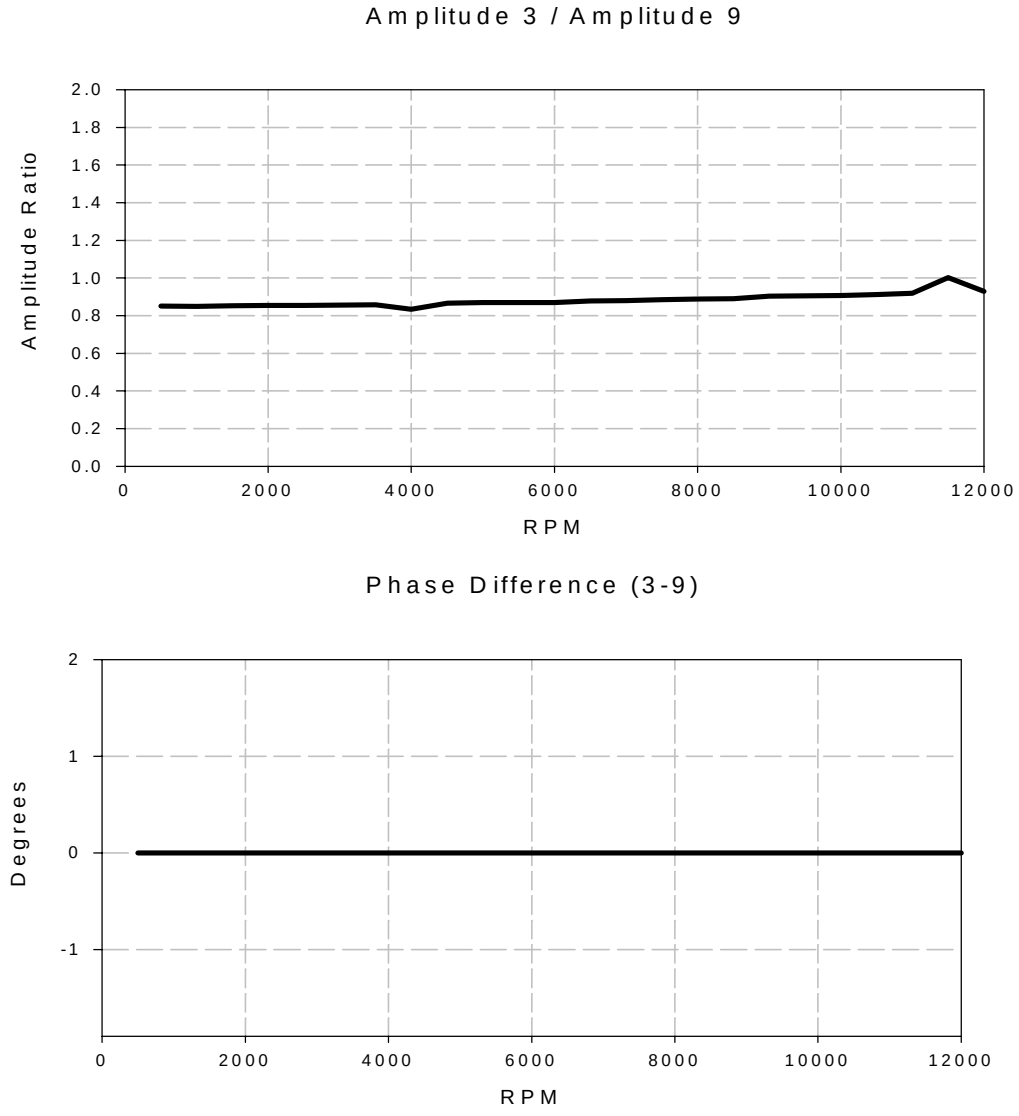

Figure 108 - Inner-Outer Probe Response, Ktest = 2e7 N/M, Ksupport = 2e8 N/M

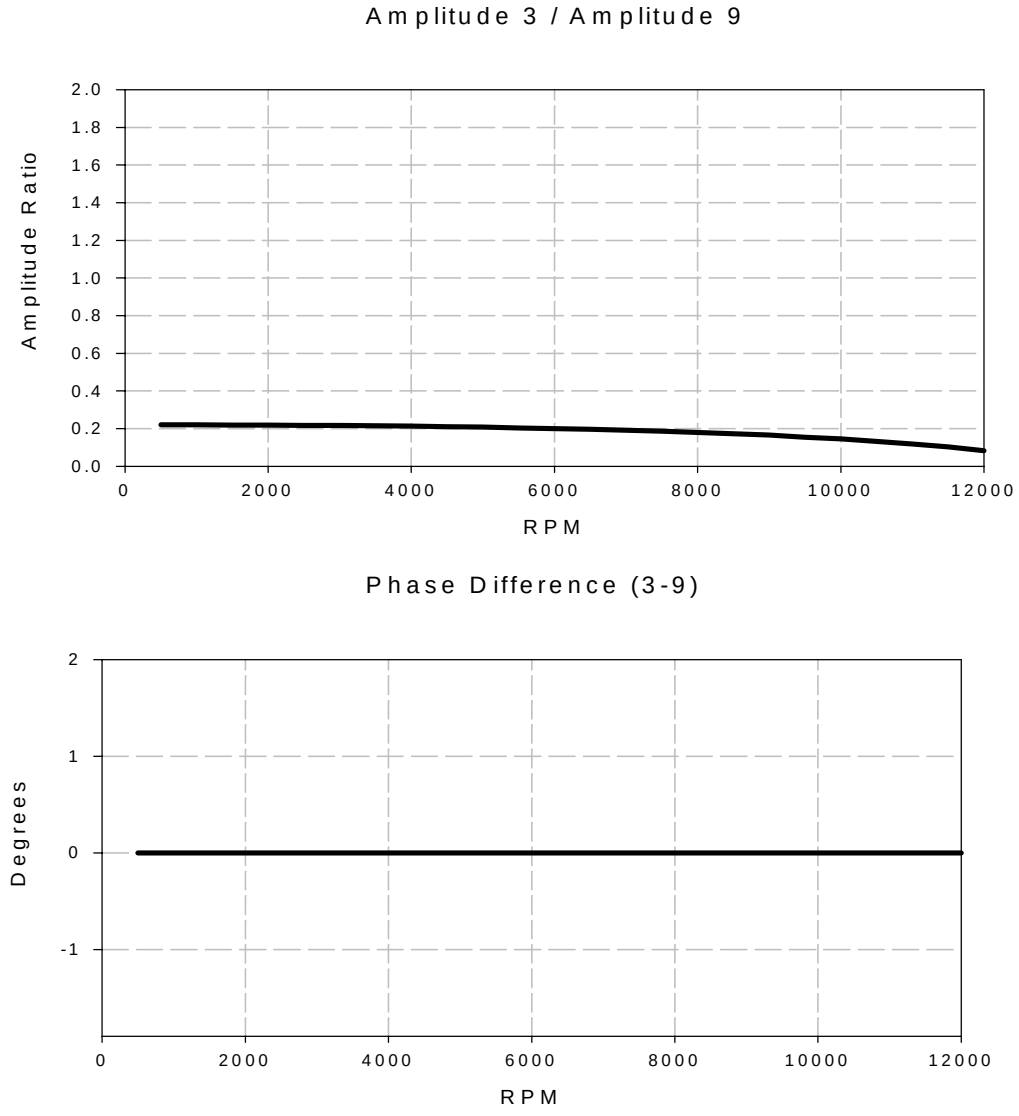

Figure 109 - Inner-Outer Probe Response, Ktest = 9e7 N/M, Ksupport = 2e8 N/M

7.5 Significance of Phase Shift

To develop a better understanding of the impact of the phase shift between the inner and outer probes, and determine if it could be ignored at low frequencies with only minor impact on the estimated dynamic coefficients, a simple, single degree of freedom system as described by equation 2 was considered.

$$c\dot{x} + kx = f \tag{2}$$

This equation can be re-written in complex form in the frequency domain as:

$$\frac{X}{F} = \frac{1}{k + i\omega c} \tag{3}$$

Based on this equation, an amplitude ratio and a phase shift measurement at a single frequency are sufficient to uniquely determine the stiffness (k) and damping (c) coefficients as the real and imaginary components of the inverse transfer function. Suppose, however, an error is made in the

$$F_{measurement} = F' = F\left(\cos(\phi) + i\sin(\phi)\right) \tag{4}$$

phase measurement. For example, suppose the input measurement (F) has a measurement phase error.

Then the transfer function shown in equation 3 becomes:

$$\frac{X}{F'} = \frac{1}{\left(k\cos(\phi) - \omega c\sin(\phi)\right) + i\left(\omega c\cos(\phi) + k\sin(\phi)\right)} \tag{5}$$

Obviously, if the real and imaginary parts of the inverse of this transfer function are taken to be the stiffness and damping coefficients of the system, the estimated coefficients would be incorrect. The error is a function of the frequency, the phase error and the ratio of the stiffness to damping

coefficients (k/c). For a two axial groove bearing with the geometry of the bearing tested in chapter six, NPADVT predicts stiffness to damping ratios for direct stiffness and direct damping (the diagonal terms of equation 1), ranging from approximately 10 to 500 depending on the operating speed and applied load. Figures 110 through 112 present the percent error in estimated stiffness and damping coefficients versus frequency for ratios of 10, 100, and 500. Note that the percentage errors go to zero at 0 Hz. This is a bit misleading, since the concept of phase does not apply at 0 Hz. Indeed, the lower the frequency, the greater the error in damping coefficient estimation.

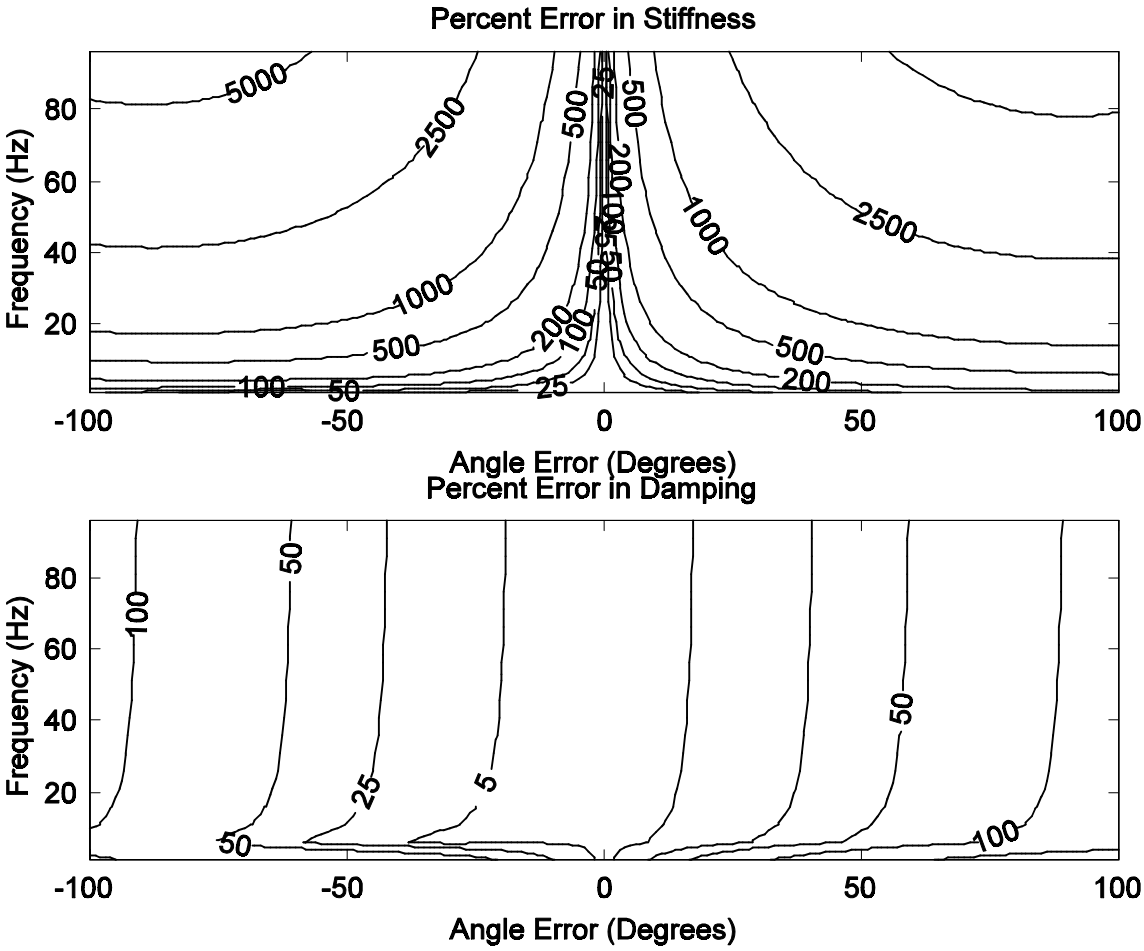

Figure 110 - First Order System Coefficient Percent Error for K/C = 10

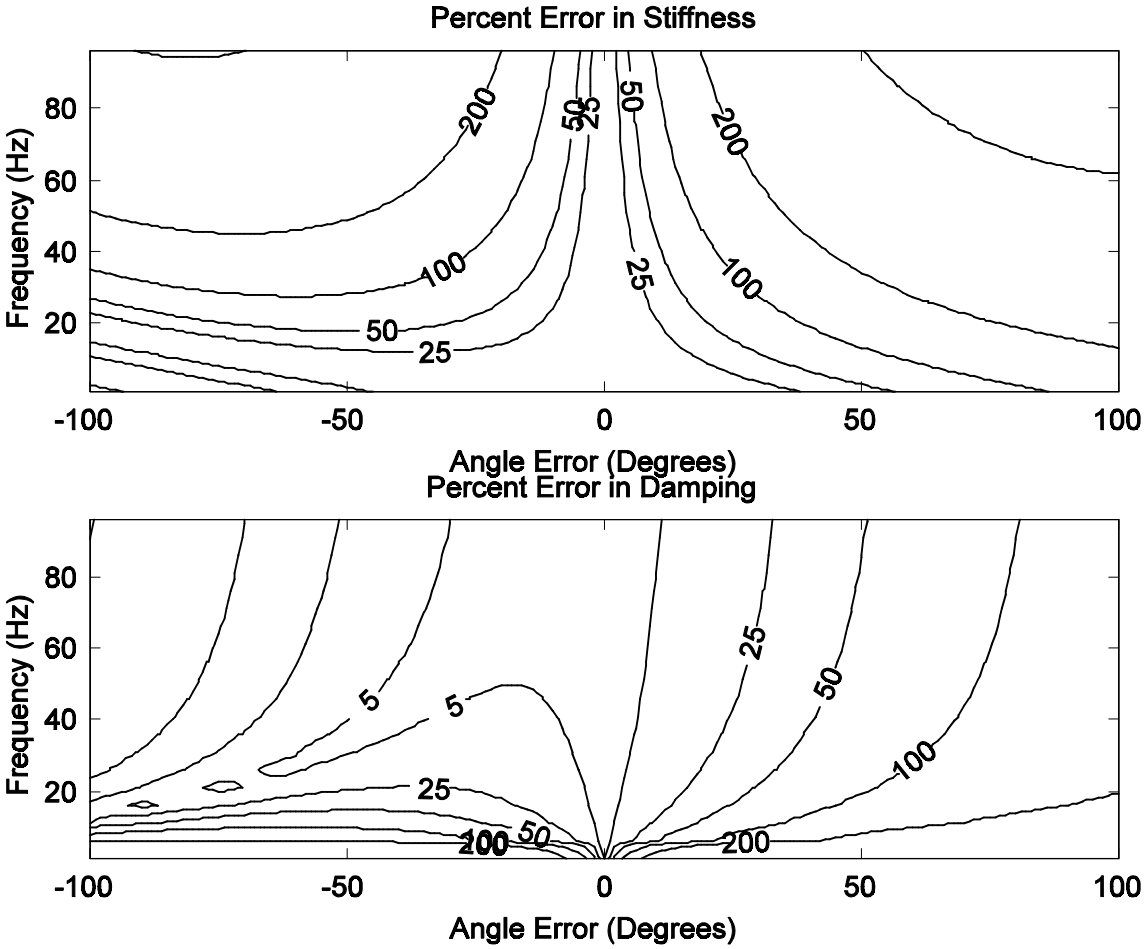

Figure 111 - First Order System Coefficient Percent Error for K/C = 100

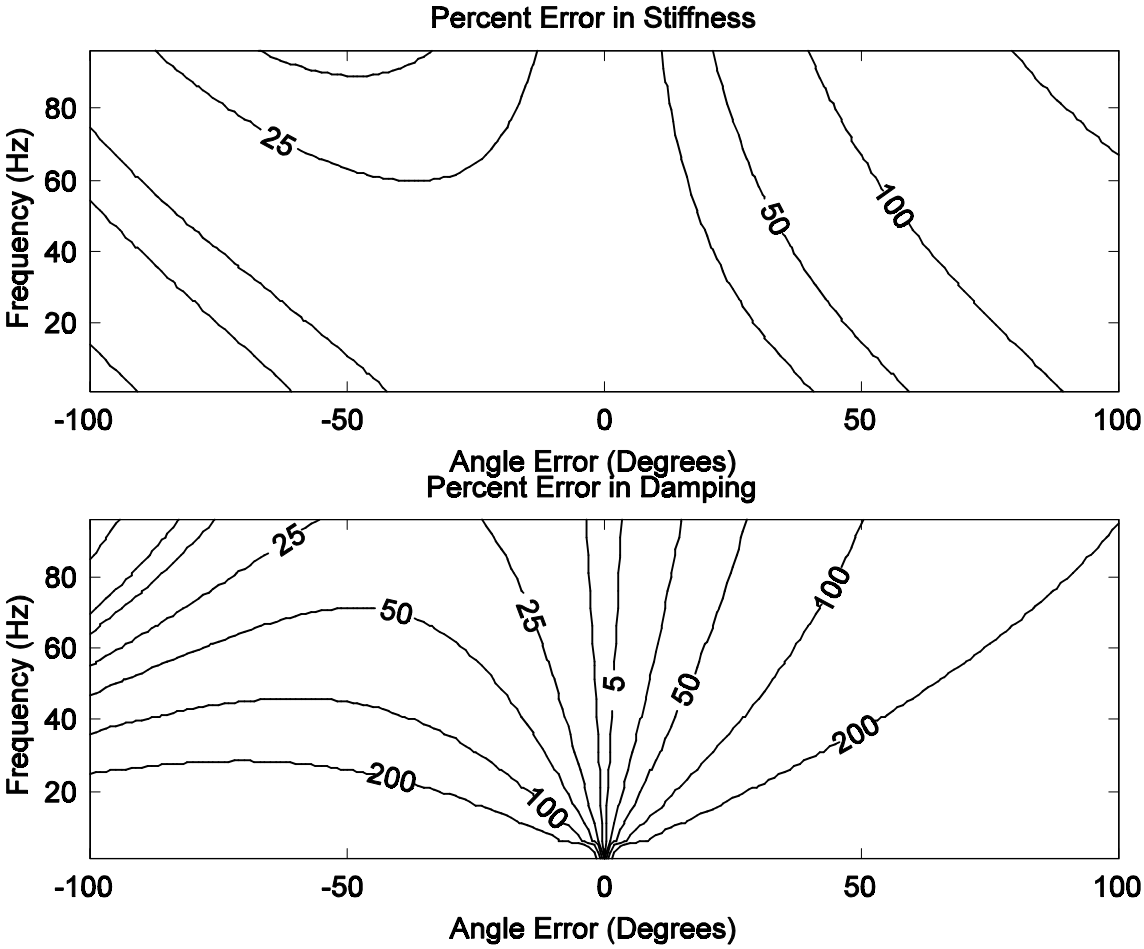

Figure 112 - First Order System Coefficient Percent Error for K/C = 500

7.6 Summary

This then is the problem with the test rig dynamics - the stiffness of the shaft is much too low relative to a typical test bearing of industrial interest. As a result, even for very low frequency loads, the bearing behaves more like a pinned support, causing a 180 degree phase change from inside to outside displacement probes. This motion does not match the assumptions inherent in the bearing analysis model, which assumes motion parallel to the bearing surface. This phase shift will also result in erroneous coefficient estimates if the coupled first-order system model of equation 1 is used in the data reduction process.

Thus, the test rig is not suitable for dynamic coefficient estimation with typical industrial test bearings. It does, however, have a number of features which will allow it to function admirably in other measurement tasks. For example, the magnetic loading system can be run in displacement mode, which would allow bearing thermal characteristics to be mapped from unstable, lightly loaded, centered operation, to heavily loaded operation. Alternately, the capability for stable rig operation with very light bearing loads could be employed to study the "Morton Effect", wherein a lightly loaded, unbalanced rotor will develop an increasing shaft bow due to local thermal expansion from a stationary hot spot on one side of the shaft. The excitation feature could also be used for other purposes. One example would be examining the pad motion for a tilting pad bearing. The rig could be used to examine the characteristics of much softer systems, such as magnetic bearings, or process lubricated, compliant surface bearings. The displacement feedback mode could also be used to look at soft, non-load supporting elements such as dry gas seals. Hence, there is a tremendous amount of work which can now be done with the test rig.

Chapter 8

Summary And Recommendations

8.1 State of Test Rig

The test rig is currently an extremely useful and flexible test rig for characterizing the steady-load characteristics of a variety of bearing types. The electric drive system is adequate for operation up to approximately 10,000 RPM as configured, and can readily be upgraded to somewhat higher speeds if required. This system is generally quite reliable, and allows long duration testing with enough repetitions for statistically meaningful conclusions to be drawn from tests. The magnet loading system can operate in both displacement and force feedback modes. The test bearing housing/load sensing system provides a solid bearing support, allows sensing of dynamic loads, and allows fairly quick test bearing changes. The oil system provides a well regulated supply of test oil to enable quality testing. The data acquisition system is capable of taking the data required, and features a Matlab interface which a new operator can readily reconfigure for different test schemes. The test rig includes a number of self-protective features to reduce the likelihood of major test rig damage.

The test rig's capability to perform steady load tests for thermal characteristics and shaft position versus load has been demonstrated.

Due to an early design/manufacturing flaw, which was not identified until after the rig was almost fully developed, the rig is not capable of making the measurements required for estimation of bearing dynamic characteristics for fluid-film bearings as currently configured.

During the initial shakedown tests, a few weak points which need attention were noted. These will be identified in the recommendations for future work.

8.2 Recommendations for Test Rig Development Work

From experience obtained during recent work with the test rig, as well as from the original goals of the test rig upgrade project, recommendations for future test rig improvements were developed. These are as follows:

1) The major missing piece for making accurately calibrated measurements is a dead-weight (or other) calibration system for the magnet load measurement system. Some system should be added to the test rig to provide a reliable method of accurately calibrating the magnet assembly load cells. In addition, some means to confirm the magnet to bearing load percentage scaling factor needs to be provided. One approach would be to provide a way of calibrating the bearing load cells.
2) The displacement probes and signal conditioning need to be calibrated more precisely to check the system non-linearity. It would also be desirable to confirm that the probe thermal sensitivity shift will not cause problems during testing.
3) The test bearing oil reservoir should be replaced with a larger tank. The current system does not allow enough latency time for entrained air due to bearing cavitation to escape. A larger capacity, 380 l, stainless steel tank was fabricated for this purpose, but has not been installed.
4) The source of the signal conditioner amplifier instability associated with turning on the DSP control system digital outputs should be resolved. The problem probably has something to do with the op-amps and capacitive loads.
5) The precision power supply fabricated for the pressure probe input panel instability needs to be fixed, or a reliable commercial unit substituted.
6) Further study of the load control system would probably result in improved performance, possibly allowing levitation without oil in the bearing.
7) The serial communication routines between the two computers are very crash-prone, and need attention.

8) The possibility of reducing the drive system belt vibration through guides, idler pulleys, etc. should be explored.
9) If frequent unattended operation is anticipated, the ball bearing temperature monitoring system and computer shut-down should be considered.

8.3 Recommendations for Future Work

In the current configuration, the test rig has the promise of measuring a number of parameters of interest to researchers developing advanced journal bearing models. Some of these items are inspired by the discussions of Pinkus (1990). These include:

1) Oil temperature in the pockets of stabilized bearings (pressure dam, pocket, etc.). This could include both the feed pockets as well as the stabilizing pockets.
2) Oil pressures in the pockets of stabilized bearings (pressure dam, pocket, etc.).
3) Transient thermal behavior for changes in load magnitude and/or vector and/or operating speed.
4) Tilting pad bearing operating temperatures for various feed designs
5) Tilting pad bearing pivot friction studies
6) Shaft locus versus load for stabilized bearing designs not available in the literature.
7) The bearing centered node could also be possibly used to allow some work to be performed on the evaluation of moment coefficients in these bearings
8) Operation with extremely light bearing loads might allow the rig to be useful for studies on the “Morton Effect”

References

Adams, M.L., and Abu-Mahfouz, I.A., 1994, "Exploratory Research On Chaos Concepts as Diagnostic Tools for Assessing Rotation Machinery Vibration Signatures." *Proceedings 4th International Conference on Rotor Dynamics*, IFToMM, pp. 29-39.

Arumugam, P., Swarnamani, S., and Prabhu, B.S., 1997, "Effects of Journal Misalignment on the Performance Characteristics of Three-Lobe Bearings." *Wear*, **206**, pp. 122-129.

Arumugam, P., Swarnamani, S., and Prabhu, B.S., 1996, "An Experimental Investigation on the Static and Dynamic Characteristics of Journal Bearings Under the Influence of Twisting Misalignment." ASME Preprint 96-TRIB-11.

Childs, D., and Hale, K., 1993, "A Test Apparatus and Facility to Identify the Rotordynamic Coefficients of High-Speed Hydrostatic Bearings." ASME preprint 93-Trib-48.

Crooijmans, M.T.M., et al., 1990, "Limit Cycle Predictions of a Nonlinear Journal-Bearing System." *Journal of Engineering for Industry*, **112**, pp 168-171.

Elkholy, A.H., and Elshakweer, A., 1995, "Testing Evaluation of Journal Bearings." *Experimental Techniques*, November/December, pp. 20-23.

El-Shafei, A., 1993, "Modeling Fluid Inertia Forces of Short Journal Bearings for Rotordynamic Applications." *Vibrations of Rotating Systems*, **DE-Vol 60**, ASME, pp. 129-137.

Gethin, D.T., 1996, "Modeling the Thermohydrodynamic Behavior of High Speed Journal Bearings." *Tribology International*, **29**, pp.579-596.

Gondhalekar, V., and Holmes, R., 1984, "Design of a Radial Electromagnetic Bearing for the Vibration Control of a Supercritical Shaft." *Proceedings of the Instn. of Mech. Engrs.*, **198**, part C, pp. 235-242.

Heshmat, H., 1989, "The Mechanism of Cavitation in Hydrodynamic Bearings." STLE Preprint 89-TC-5B-1.

Hollis, P., Taylor, D.L., 1986, "Hopf Bifurcation to Limit Cycles in Fluid Film Bearings." *Journal of Tribology*, **108**, pp. 184-189.

Kato, T., Koguchi, K., and Hori, Y., 1992, "Seismic Response of a Linearily Stable Multirotor System." *Vibrations in Rotating Machinery*, Instn. of Mech. Engrs., pp. 359-363.

Knight, J.D., Barrett, L.E., and Cronan, R.D., 1985, "The Effects of Supply Pressure on the Operating Characteristics of Two-Axial-Groove Journal Bearings." *ASLE Transactions*, **28**, pp. 336-342.

Kostrzewsky, G.J., Flack, R.D., and Barrett, L.E., 1996, "Comparison Between Measured and Predicted Performance of a Two-Axial-Groove Bearing." *Tribology Transactions*, **39**, pp. 571-578.

Ma, M.T.,and Taylor, C.M., 1996, "An Experimental Investigation of Thermal Effects in Circular and Elliptical Plain Journal Bearings." *Tribology International*, **29**, pp. 19-26.

Makino, T., and Taniguchi, S., 1996, "Thermohydrodynamic Performance of High-Speed Journal Bearings." *Proceedings of the Instn. of Mech. Engrs, Part J - Journal of Engineering Tribology*, **210**, pp. 179-187.

Morton, P.G., and Keogh, P.S., 1986, "Thermoelastic Influences in Journal Bearing Lubrication." *Proceedings of the Royal Society of London, Series A*, **403**, pp. 111-134.

Myers, C.J., 1984, "Bifurcation Theory Applied to Oil Whirl in Plain Cylindrical Journal Bearings." *Journal of Applied Mechanics*, **51**, pp 244-250.

Nataraj, C., Ashrafiuon, H., and Arakere, N.K., 1994, "Effect of Fluid Inertia on Journal Bearing Performance." *Tribology Transactions*, **37**, pp 784-792.

Nicholas, J.C., 1977, "A Finite Element Dynamic Analysis of Pressure Dam and Tilting Pad Bearings." PhD Dissertation, University of Virginia, Charlottesville, VA.

Ogrodnic, P.J., et. al., 1996, "A Novel Variable Impedance Hydrodynamic Oil-Film Bearing Part 2: Experimental Identification of the Steady State and Dynamic Characteristics." *Proceedings of the Instn. of Mech. Engrs, Part J - Journal of Engineering Tribology*, **206**, pp. 65-74.

Pinkus, O., 1990, *Thermal Aspects of Fluid Film Tribology*, ASME, New York.

Prabhu, B.S., 1997, "An Experimental Investigation on the Misalignment Effects in Journal Bearings." *Tribology Transactions*, **40**, pp. 235-242.

Qiu, Z.L., and Tieu, A.K., 1996a, "The Effect of Perturbation Amplitudes on Eight Force Coefficients of Journal Bearings." *Tribology Transactions*, **39**, pp 469-475.

Qiu, Z.L., and Tieu, A.K., 1996b, "Experimental Study of Freely Alignable Journal Bearings - Part 2: Dynamic Characteristics." *Journal of Tribology*, **118**, pp. 503-508.

Reinhardt, E., and Lund, J.W., 1975, "The Influence of Fluid Inertia on the Dynamic Properties of Journal Bearings." *Journal of Lubrication Technology*, **97**, pp. 159-167.

Someya, T. (ed), 1988, *Journal Bearing Databook*, Springer-Verlag, Berlin.

Sundararajan, P., and Noah, S.T., 1997, "Dynamics of Forced Nonlinear Systems Using Shooting/Arc-Length Continuation Methods - Application to Rotor Systems." *Journal of Vibration and Acoustics*, **119**, pp. 9 - 20.

Swanson, E.E., 1992, *Evaluation of the VPI & SU Fluid Film Bearing Test Rig*, MS Thesis, VA Tech.

Swanson, E.E., Kirk, R.G., and Mondy, R.E., 1992, "An Examination and Comparison of the Maximum Film Temperature in a Journal Bearing for 13 Synthetic, Mineral and Viscosity Index Enhanced Oils." *Rheology and Tribology of Engine Oils, SAE SP-936*, Warrendale, SAE, pp. 137-146.

Swanson, E.E., and Kirk, R.G., 1994, "An Experimental Comparison of Two Steadily Loaded Plain Journal Bearings." *Tribology Transactions*, **37**, pp. 843-849.

Swanson, E.E., and Kirk, R.G., 1995, "Experimental Temperature and Pressure Profiles for Two Steadily Loaded Journal Bearings." *Tribology Transactions*, **38**, pp. 601-606.

Swanson, E.E., and Kirk, R.G., 1997, "Survey of Experimental Data for Fixed Geometry Hydrodynamic Journal Bearings." *Journal of Tribology*, **119**, pp. 704-710.

Tichy, J.A., 1983, "The Effect of Fluid Inertia in a Squeeze Film Damper Bearings: A Heuristic and Physical Description." ASME Paper 83-GT-177.

Tieu, A.K., and Qiu, A.L., 1996, "Experimental Study of Freely Alignable Journal Bearings - Part 1: Static Characteristics." *Journal of Tribology*, **118**, pp. 498-502.

Appendix A

Matlab Codes

A.1 WIN3016.DLL

This DLL contains all of the code to allow high speed data acquisition to be performed under Matlab control. This one basic function can be called with various options to perform appropriate tasks as follows:

mat3016('init') - initializes system
mat3016('close') - closes system
mat3016('sample', xxx) - samples and stores xxx samples per channel
mat3016('sample', xxx, 'trg3808') - 3808 triggered sampling
mat3016('sample', xxx, 'clk3808') - 3808 clock sampling
mat3016('sample', xxx, 'clktrg3808') - 3808 clock and trigger sampling
mat3016('sample', xxx, 'clk60t') - 60 tooth clocked sampling
mat3016('sample', xxx, 'clk60ttrgkey') - 60 tooth clock, key phase trig.
mat3016('sample', xxx, 'trgkey') - keyphaser trigger
mat3016('sample', xxx, 'norm') - normal mode
L = mat3016('getchan', xx) - return samples for channel xx
[Names, Gains, Offsets] = mat3016('getsetup') - returns setup info

As can be seen, enough options have been provided to allow the user to perform a variety of data acquisition tasks, as well as retrieve the set-up data stored by the set-up code.

A.2 AD08.DLL

This DLL allows the user to acquire the pressure and temperature data, as well as set-up information. It also provides an interface to the support bearing positioner system. The user can move the bearing in a desired direction as required to obtain or maintain a desired alignment condition. This one basic function can be called with various options to perform appropriate tasks as follows:

matad08('init') - initializes system
matad08('close') - closes system
[Names, Gains, Offsets] = matad08('getsetup') - returns setup info
data = matad08('sample') returns 48 channels of data
[Press(1:16); TC0(1:16); TC1(1:16)]
matad08('up', xxx) moves positioner up for xxx milliseconds

matad08('down', xxx) moves positioner down for xxx milliseconds
matad08('left', xxx) moves positioner left for xxx milliseconds
matad08('right', xxx) moves positioner right for xxx milliseconds

A.3 Matserl.DLL

This DLL contains all of the code to allow interaction with the control computer to be performed under Matlab control. This one basic function can be called with various options to perform appropriate tasks as follows:

matserl('init') initializes
matserl('setload', [xxx, yyy]) sets x and y loads
matserl('setspd', xxx) sets speed to xxx rpm
matserl('excoff') turns excitation off
matserl('excon') turns excitation on
matserl('setexc', ch#, excvect) sends an excitation to output
channel ch#, excvect is complex
1x4096
matserl('close') closes system
S = matserl('getspd') reads current speed
Sp = matserl('getspdsp') gets current speed setpoint

Appendix B

Sample Matlab Test Script

The following is a sample Matlab script file (.M file), which implements a steady state test at 1500 RPM

```
% stest1.m implements a steady-state test at 1500 RPM

% define test parameters


loads = [0 (300+61);
        0  (500+61);
        0 -300;
        0 -500;
        0 -1000;
        0 -1500;
        0 -1500;
        0 -1000;
        0 -500;
        0 -300;
        0 (300+61);
        0 (500+61);
        0 -1500;
        0 -1000;
        0 -500;
        0 -300;
        0 -1500;
        0 -300;
        0 -1000;
        0 -500;
        0 -1000;
        0 -300;
        0 -500;
        0 -1500];
```

```
rpm = 1500;

%zero data
raw3016 = zeros(length(loads(:,1)),16);
feedpress = zeros(length(loads(:,1)),1);
tcdata = zeros(length(loads(:,1)),28);
xdata = zeros(length(loads(:,1)),1);
ydata = zeros(length(loads(:,1)),1);
actrpm = zeros(length(loads(:,1)),1);
actload = zeros(length(loads(:,1)),2);

%initialize systems
matserl('init');
matad08('init');
mat3016('init');

%get set-up info
[ad08names ad08scf ad08oset] = matad08('getsetup');
[w3016names w3016scf w3016oset] = mat3016('getsetup');

%draw plots, pause to arrange
figure(1)
plot(xdata,ydata,'o');
title('averaged x, y');
axis('square');

figure(2)
subplot(211)
plot(loads,xdata,'+');
title('x versus load');
ylabel('xpos');
xlabel('load (lb)');

subplot(212)
plot(loads,ydata,'+');
title('y versus load');
ylabel('ypos');
xlabel('load (lb)');

figure(3)
plot(tcdata(:,2:11)')
title('brg tcs vs load');
```

```
ylabel('deg f');
xlabel('load');

figure(4)
title('averaged orbit');

pause;

for i=1:length(loads(:,1))

%set load, speed
  matserl('setspd',rpm);
  matserl('setload',loads(i,:));
  loadnow = matserl('getload');
  while( (abs(loadnow(1) - loads(i,1)) > 5) & ...
         (abs(loadnow(2) - loads(i,2)) > 5))
   loadnow = matserl('getload')
  end;

%adjust positioner
  dummy = pzreset([2.2059    4.0815]);

% start timer
  tic;

  while (toc < 60)
% display orbits while waiting
    wdata = samp3016(5000);
    figure(4)
    clg;
    plot( (wdata(:,6)+wdata(:,8)+wdata(:,2)+wdata(:,4))/4,...
          (wdata(:,7)+wdata(:,5)+wdata(:,3)+wdata(:,1))/4);
    title('average orbit');
    drawnow;
    dummy = pzreset([2.2059    4.0815]);
  end;

%grab data, plot, save
  wdata = samp3016(8192);
  actrpm(i) = matserl('getspd');
  actload(i,:) = matserl('getload')';
  ad08data = matad08('sample');
  raw3016(i,:) = mean(wdata);
```

```
  feedpress(i) = ad08data(1);
  tcdata(i,:) = [ad08data(17:28) ad08data(33:48)];
  xdata(i) =(raw3016(i,6)+raw3016(i,8)+raw3016(i,2)+raw3016(i,4))/4;
  ydata(i) =(raw3016(i,7)+raw3016(i,5)+raw3016(i,3)+raw3016(i,1))/4;

   figure(1)
   clg;
   plot(xdata,ydata,'o');
   title('averaged x, y');
   axis('square');

   figure(2)
   clg;
   subplot(211)
   plot(loads,xdata,'+');
   title('x versus load');
   ylabel('xpos');
   xlabel('load (lb)');

   subplot(212)
   plot(loads,ydata,'+');
   title('y versus load');
   ylabel('ypos');
   xlabel('load (lb)');

   figure(3)
   clg
   plot(tcdata(:,2:11)')
   title('brg tcs vs load');
   ylabel('deg f');
   xlabel('load');

   save

end;
```

Vita

Erik Swanson entered Virginia Polytechnic Institute and State University in the Fall of 1985. He spent five years as an undergraduate student. During this time, he was also a co-op student at the Hopewell, Virginia paper mill owned by Stone Container Corporation. He graduated Magna Cum Laude with a Bachelor of Science Degree in Mechanical Engineering, and a minor in Philosophy, in the spring of 1990. He immediately entered his graduate program, and defended his Masters of Science thesis in March of 1992. Finally, after 8 years as a professional student, he defended his dissertation in the summer of 1998. Prior to defending, he accepted a position at Mohawk Innovative Technology, Inc. in Albany NY in January of 1998. He is a member of Tau Beta Pi, Pi Tau Sigma, Sigma Xi, ASME and STLE.